



**HAL**  
open science

# Toward high-precision measurements of neutrino oscillations in the future long baseline experiments

Anna Ershova

► **To cite this version:**

Anna Ershova. Toward high-precision measurements of neutrino oscillations in the future long baseline experiments. High Energy Physics - Phenomenology [hep-ph]. Université Paris-Saclay, 2023. English. NNT : 2023UPASP060 . tel-04267631

**HAL Id: tel-04267631**

**<https://theses.hal.science/tel-04267631>**

Submitted on 2 Nov 2023

**HAL** is a multi-disciplinary open access archive for the deposit and dissemination of scientific research documents, whether they are published or not. The documents may come from teaching and research institutions in France or abroad, or from public or private research centers.

L'archive ouverte pluridisciplinaire **HAL**, est destinée au dépôt et à la diffusion de documents scientifiques de niveau recherche, publiés ou non, émanant des établissements d'enseignement et de recherche français ou étrangers, des laboratoires publics ou privés.

# Toward high-precision measurements of neutrino oscillations in the future long baseline experiments

*Vers des mesures de haute précisions des oscillations des neutrinos dans  
les futures expériences à longues bases de vol*

## Thèse de doctorat de l'université Paris-Saclay

École doctorale n° 576, Particules, hadrons, énergie et noyau :  
instrumentation, imagerie, cosmos et simulation (PHENIICS)  
Spécialité de doctorat: physique des particules  
Graduate School : Physique  
Référent : Faculté des sciences d'Orsay

Thèse préparée dans l'unité de recherche  
**Département de Physique Nucléaire** (Université Paris-Saclay, CEA),  
sous la direction de **Alain LETOURNEAU**, Ingénieur-chercheur,  
la co-direction de **Sara BOLOGNESI**, Ingénieure-chercheuse

Thèse soutenue à Paris-Saclay, le 26 juin 2023, par

**Anna ERSHOVA**

## Composition du Jury

Membres du jury avec voix délibérative

<b>Fabien CAVALIER</b> Directeur de recherche, Université Paris-Saclay	Président
<b>Maria Benedetta BARBARO</b> Professeure, Université de Turin	Rapporteuse & Examinatrice
<b>Anselmo MEREGAGLIA</b> Chargé de recherche, HDR, Université de Bordeaux	Rapporteur & Examineur
<b>Margherita BUIZZA-AVANZINI</b> Chargée de Recherche, Institut Polytechnique de Paris	Examinatrice
<b>Alessandra TONAZZO</b> Professeure, Université Paris Cité	Examinatrice

**Titre :** Vers des mesures de haute précisions des oscillations des neutrinos dans les futures expériences à longues bases de vol

**Mots clés :** neutrinos accélérateurs, modèles nucléaires, oscillation des neutrinos, T2K

**Résumé :** Alors que la physique de l'oscillation des neutrinos entre dans l'ère de la précision, la modélisation des interactions neutrino-noyau constitue un défi grandissant comme source d'incertitude systématique pour les nouvelles mesures. Pour réduire ces incertitudes, une nouvelle génération de détecteurs est en cours de développement, qui vise à mesurer l'état final complet (exclusif) de l'interaction des neutrinos. Des simulations précises des effets nucléaires sur l'état final des nucléons sont alors nécessaires pour bénéficier pleinement des capacités améliorées des détecteurs. Dans ce travail de thèse, j'ai abordé ce problème en étudiant l'état final des interactions des neutrinos et des antineutrinos sur le noyau de carbone avec les modèles nucléaires INCL et ABLA. Au cours de ma thèse, j'ai également contribué au développement de l'amélioration du détecteur proche de l'expérience T2K. Le travail expérimental se concentre sur l'éta-lonnage de l'électronique et sur l'effet de la non-uniformité du champ magnétique pour les nouvelles chambres de projection temporelle à haut angle. Les études nucléaires se concentrent sur les interactions des particules de l'état final avec le milieu nucléaire en comparant les modèles de cascade NuWro et INCL et en considérant le modèle de désexcitation d'ABLA. INCL est un code de cascade nucléaire très avancé et principalement conçu principalement conçu pour simuler les réactions induites par les nucléons, les pions et les ions légers sur les noyaux. ABLA est un code de désexcitation couplé à INCL et capable de simuler toutes les particules émises par désexcitation. Cette thèse est la première étude utilisant le modèle INCL dans le cadre des interactions avec les neutrinos. C'est également la première étude utilisant ABLA pour les interactions

de neutrinos. Elle met en évidence plusieurs nouveautés dans la modélisation de cette interaction, notamment la production de particules composites (par exemple, deutérons, particules  $\alpha$ ) dans l'état final et la modélisation de la libération complète de l'énergie d'excitation. La caractérisation de l'état final hadronique est présentée avec un accent particulier mis sur les variables de cinématique transverses et les comparaisons avec les mesures expérimentales disponibles. Les seuils des expériences actuelles sont trop hauts pour être sensibles aux différences entre les modèles et pour voir l'impact de la désexcitation, mais j'ai démontré qu'ils auront un impact lorsque la sensibilité des expériences s'améliorera. L'observabilité des particules composites sous forme de traces à l'intérieur du détecteur et leur contribution à l'activité du vertex sont également évaluées dans ce travail. J'ai démontré que leur modélisation peut avoir un impact significatif sur l'analyse et l'interprétation des données expérimentales, notamment pour l'identification des particules à faible inertie et la mesure des dépôts d'énergie autour du vertex des neutrinos. J'ai également utilisé INCL, implémenté dans Geant4, pour étudier les interactions secondaires des neutrons dans le détecteur en montrant qu'elles sont cruciales pour avoir une détection non-biaisée.

L'étude présentée dans cette thèse introduit d'importantes nouveautés et constitue donc un jalon vers la simulation précise de re-interactions nucléaires et de la de-excitation nucléaire dans les interactions neutrino-noyau et, par conséquent, sur l'estimation des incertitudes dans la modélisation des états finaux exclusifs qui sont ciblés par la prochaine génération de détecteurs pour les expériences de longue durée.

**Title :** Toward high-precision measurements of neutrino oscillations in the future long baseline experiment

**Keywords :** accelerator neutrinos, nuclear models, neutrino oscillations, T2K

**Abstract :** As neutrino oscillation physics enters the precision era, modeling neutrino-nucleus interactions constitutes an increasingly challenging source of systematic uncertainty for new measurements. To confront such uncertainties, a new generation of detectors is being developed, which aim to measure the complete (exclusive) final state of neutrino interaction. Precise simulations of the nuclear effects on the final-state nucleons are needed to fully benefit from the improved detector capabilities. In this thesis work, I addressed this problem by studying the final state of the neutrino and antineutrino interactions on Carbon nucleus with INCL and ABLA nuclear models. During my thesis, I also contributed to the development of the upgrade of the T2K near detector. The experimental work is focused on electronics calibration and the effect of the non-uniformity of the magnetic field for the new High-Angle Time Projection Chambers. The nuclear studies focus on the re-interactions of final state particles with the nuclear medium (FSI) by comparing NuWro and INCL cascade models and considering the de-excitation model from ABLA. INCL is an evolved nuclear cascade code primarily designed to simulate nucleon-, pion- and light-ion-induced reactions on nuclei. ABLA is a de-excitation code coupled to INCL that can simulate all the particles emitted by de-excitation. This is the first study using the INCL model in the framework of neutrino interactions. It is also the first study using ABLA for neutrino interactions. It highlights various novelties in the neutrino interaction mo-

deling, including the production of nuclear clusters (e.g., deuterons,  $\alpha$  particles) in the final state and the simulation of the full release of excitation energy. The characterization of the hadronic final state after FSI is presented with a particular focus on the single transverse variables and comparisons to available experimental measurements of transverse kinematic imbalance. The thresholds of the current experiments are too large to be sensitive to the differences between the models and to see the impact of the de-excitation, but I show that they will have an impact when the sensitivity of the experiments will improve. The observability of nuclear clusters as tracks inside the detector and as a contribution to the vertex activity is also assessed in this work. Their modeling may significantly impact the analysis and interpretation of the experimental data, notably for identifying low-momentum particles and measuring energy deposits around the neutrino vertex. I also employed INCL implemented in Geant4 to study the neutron secondary interactions in the detector, showing they are crucial for an unbiased detection of neutrons.

The study presented in this thesis introduces some important novelties, and it is, therefore, a milestone toward the precise simulation of FSIs, secondary interactions and de-excitation in neutrino-nucleus interactions and, thus, on the estimation of the uncertainties in the modeling of exclusive final states which are targeted by the next generation of detectors for long-baseline experiments.



## Acknowledgements

This thesis was a joint multilevel effort of many people with various backgrounds who have been there for me to advise, review, or give a pat on the back. It might be challenging to thank everyone as they deserve it properly, but I will try to do it here.

First, I would like to express my deepest gratitude to my supervisors, Alain and Sara, for their unwavering guidance, expertise, and continuous support throughout my journey. Their invaluable insights and constructive feedback have been instrumental in shaping the direction of my research and the overall quality of this thesis. I arrived in France in the midst of Covid. Because of Covid restrictions, social activities were limited, so I was very lonely. I cannot express enough how much I appreciate the times Sara invited me to spend time with her amazing family. It helped me a lot to start getting used to my new environment.

I am profoundly grateful to my thesis reviewers, Maria Barbaro and Anselmo Meregaglia, for their insightful comments, valuable suggestions, and rigorous examination of my work. Their expertise and diverse perspectives have enriched my research and contributed to its rigor and academic integrity. I would also like to thank the jury members, Fabian Cavalier, Alessandra Tonazzo, and Margherita Buizza-Avanzini, for their thoughtful questions during my defense.

I am delighted to have been a part of the T2K collaboration—not only a fantastic experiment with an impressive scientific program and world-class experts but also an amicable place to work. I am happy to have met many amazing people who share my passion for science. I want to highlight the contribution of the Physics and Performance working group and its conveners, Stephen and Laura.

I am thrilled to have been a member of the INCL group in DPhN. I am deeply grateful to Jean-Christophe David and Jason Hirtz for their help in understanding INCL. Every time I visited them, I knew I would learn something new that day. I also want to thank Jose-Luis for being responsible for ABLA and handling all corresponding questions.

My work would not be possible without the help of the NuWro group, Jan, and Kajetan. It is difficult to underestimate the importance of their expertise and more theoretical vision of my work. Kajetan was also there to support or oppose me in my doubts and views on the

working process. Maybe his comments were not always pleasant, but I believe they pushed me and my research toward excellence.

I want to express my appreciation to the DPhP accelerator neutrino group. I truly enjoyed being a part of it. I am grateful for the hands-on detector experience I gained. I want to thank Samira, Guillaume, and David for helping me broaden my knowledge.

I extend my heartfelt appreciation to Isabelle, who handled my numerous issues, like organizing a work trip or printing my poster. My French could be better, and I acknowledge her speaking the way I can understand. She made my bureaucracy adventures less challenging.

I would also like to thank my officemates, Tristan, Shivam, and Demid, for constructive (and not really) conversations. I greatly appreciate my family and friends for their unwavering support, encouragement, and understanding throughout my doctoral journey. Their love, patience, and belief in me have been a constant source of inspiration and motivation. Despite the pandemics, I met many wonderful people, and I am grateful to Adam, Lorenzo, Sara, Frances, Sergey, Ksenia, Anastasia, Sasha, Yulia, Vlad, Kostia, Katharina, Masha, Vlada, and many others for all the fun we had together that made sure I had a healthy work-life balance.

Finally, I would like to extend my gratitude to all whose names may not be mentioned but who have played a big or small role in completing this thesis. Your contributions, whether through discussions, feedback, or support in various forms, have been invaluable, and I am sincerely thankful. Your unwavering support, encouragement, and belief in my abilities have been pivotal in my academic growth and the successful completion of this milestone. Thank you all for being an integral part of this journey.

# Résumé

Les oscillations des neutrinos ont été découvertes pour la première fois grâce à l'étude des neutrinos atmosphériques et solaires. Depuis lors, le modèle basé sur la matrice de mélange PMNS des oscillations des neutrinos a été établi, grâce aux mesures des neutrinos de réacteurs et d'accélérateurs. De plus, la statistique croissante des expériences de neutrinos atmosphériques ont contribué à ce modèle. Les expériences de la génération actuelle, notamment T2K et NOVA, repoussent les limites de la précision dans les oscillations des neutrinos. Elles ont également le potentiel d'atteindre une signification de  $3\sigma$  pour une éventuelle mesure de violation de la charge et parité (CP) et une détermination de l'ordre des masses. La découverte de la phase de violation non nulle de CP indiquera la violation de la symétrie de charge et de parité dans le secteur leptonique—un effet qui a le plus grand potentiel pour expliquer l'asymétrie matière-antimatière dans l'univers. En regardant vers l'avenir, la prochaine génération d'expériences d'accélérateur à longue ligne de base, DUNE et Hyper-Kamiokande, vise à établir l'ordre des masses et éventuellement à découvrir la violation de CP avec une signification de  $5\sigma$ , ainsi qu'à mesurer la valeur de la phase de paramétrisation CP ( $\delta_{CP}$ ) avec une précision meilleure que 15 degrés.

Alors que la physique des oscillations des neutrinos entre dans l'ère de la précision, la modélisation des interactions neutrino-noyau constitue une source d'incertitude systématique de plus en plus difficile à relever pour de nouvelles mesures. Pour faire face à de telles incertitudes, une nouvelle génération de détecteurs est en cours de développement, visant à mesurer l'état final complet (exclusif) des interactions neutrino. Des simulations précises des effets nucléaires sur les nucléons de l'état final sont nécessaires pour tirer pleinement parti des capacités améliorées du détecteur.

L'objectif principal de cette thèse est d'évaluer en détail les incertitudes possibles inhérentes à la simulation des interactions de l'état final (FSI, pour *final state interactions*) dans la diffusion neutrino-noyau. Cette étude constitue également une étape vers une implémentation plus précise et complète des effets de FSI dans les simulations Monte Carlo des interactions neutrino-noyau. Étant donné les besoins des expériences en cours, notamment l'analyse des données du détecteur ND280 amélioré, nous nous concentrons sur la modélisation des interactions de l'état final avec des outils actuellement disponibles et nouveaux. Cette

thèse présente l'étude des FSI avec deux modèles nucléaires différents : le code IntraNuclear Cascade Liège (INCL), un nouvel outil pour la physique des neutrinos, et NuWro, un générateur de neutrinos largement utilisé dans la communauté des neutrinos. Les interactions fondamentales neutrino-noyau sans production de pions sont étudiées, où les pions dans l'état final ne peuvent être produits que par le biais des FSI avec les nucléons.

Les chapitres 1 et 2 contiennent une introduction générale, le principe de fonctionnement des expériences de neutrinos à longue distance, en mettant l'accent sur l'expérience T2K. L'expérience T2K au Japon est une expérience d'oscillation des neutrinos à longue distance qui vise à mesurer les paramètres d'oscillation des neutrinos, et notamment à rechercher la violation de CP. Elle comporte également une large gamme d'analyses exotiques, par exemple la recherche de neutrinos stériles aux détecteurs éloignés et proches. Le faisceau de neutrinos est produit au Complexe de Recherche sur les Accélérateurs de Protons du Japon (J-PARC, pour *Japan Proton Accelerator Research Complex*) à Tokai, préfecture d'Ibaraki. J-PARC produit un faisceau de protons, qui est dirigé vers une cible en graphite pour créer des pions et des kaons qui se désintègrent en neutrinos et antineutrinos. Le flux de neutrinos et d'antineutrinos est choisi en sélectionnant le courant de l'aimant magnétique, qui est utilisé pour focaliser les pions et les kaons positivement ou négativement chargés. T2K utilise le détecteur Cherenkov à eau Super-Kamiokande comme détecteur éloigné, situé à 295 km de la source de neutrinos. Le détecteur éloigné et certains détecteurs du complexe du détecteur proche sont placés hors de l'axe du faisceau de neutrinos. Cette configuration diminue légèrement le taux de neutrinos mais resserre le spectre d'énergie des neutrinos dans la région d'oscillation maximale. Pour caractériser le flux de neutrinos et les interactions des neutrinos, T2K utilise les détecteurs proches situés à 280 mètres de la cible de production de flux de neutrinos, qui sont constitués des détecteurs INGRID (Interactive Neutrino GRID) et MUMON sur l'axe du faisceau, ainsi que les détecteurs hors axe WAGASCI-BabyMIND et ND280. INGRID et MUMON sont utilisés pour mesurer précisément la direction et la position du flux de neutrinos. WAGASCI possède une cible d'eau enrichie (80% d'eau et 20% de CH) et permet de mesurer les sections efficaces des neutrinos sur une cible d'eau (la même cible que le détecteur éloigné Super-Kamiokande) à un angle hors axe différent. Le détecteur hors axe ND280 est conçu pour mesurer le flux de neutrinos et les sections efficaces des neutrinos sur les noyaux. Comme WAGASCI, ND280 est également équipé d'un module de cible d'eau et effectue des mesures à la même inclinaison hors axe que le détecteur éloigné.

Actuellement, dans l'analyse de l'oscillation T2K, l'énergie du neutrino est reconstruite en se basant uniquement sur la cinématique du muon :

$$E_{QE} = \frac{m_p^2 - m_\mu^2 - (m_n - E_B)^2 + 2E_\mu(m_n - E_B)}{2(m_n - E_B - E_\mu + p_\mu^z)}, \quad (1)$$

où  $m_{p/\mu/n}$  est la masse d'un proton/muon/neutron;  $E_\mu$  et  $p_\mu^z$  sont l'énergie et l'impulsion du muon sortant projetées dans la direction du neutrino entrant; et  $E_B$  est l'énergie de liaison du nucléon frappé. Cette formule approximative fonctionne raisonnablement bien pour les interactions quasi-élastiques (CCQE), la plus grande partie des interactions avec les neutrinos à l'énergie T2K. D'autre part, à proximité du détecteur, une autre stratégie d'analyse pourrait être poursuivie, qui utiliserait également l'information sur le nucléon sortant principal et fournirait une meilleure résolution :

$$E_{vis} = E_\mu + T_N, \quad (2)$$

où  $T_N$  est l'énergie cinétique du proton sortant (neutron) dans les interactions neutrino (antineutrino), et  $E_\mu$  est l'énergie totale du muon sortant. Le détecteur proche actuel n'a pas été conçu pour détecter les neutrons et ne peut détecter les protons que au-dessus d'un seuil de moment relativement élevé (300–400 MeV). De plus, ND280 a été conçu pour mesurer principalement les particules allant vers l'avant (étant donné la nature fortement accélérée des interactions neutrino provenant du flux de neutrinos). D'autre part, le détecteur éloigné a une acceptation de  $4\pi$ , couvrant également les interactions moins fréquentes produisant des muons à angle élevé ou rétrogrades. Une mise à niveau du détecteur ND280 est en cours pour résoudre ces limitations : elle améliorera l'acceptation angulaire pour les traces à grand angle et rétrogrades ainsi que l'acceptation pour les hadrons de faible impulsion (protons, pions); elle permettra également la détection des neutrons et la reconstruction de l'énergie pour la première fois dans les interactions neutrino. Toutes ces améliorations nous permettront d'utiliser l'équation 2, et ainsi fourniront une meilleure reconstruction de l'énergie des neutrinos.

Le chapitre 3 décrit les caractéristiques des différents modes d'interaction des neutrinos (principalement la réaction CCQE) et les effets nucléaires à prendre en compte. De nombreux modèles d'interaction des neutrinos utilisent l'approximation d'impulsion d'onde plane (PWIA, pour *plane-wave impulse approximation*), en supposant qu'il n'y a pas d'impact du potentiel nucléaire sur les particules de l'état final (hadrons et leptons), qui sont donc caractérisées par des ondes planes. La PWIA permet de factoriser la section efficace lepton-noyau, c'est-à-dire que la section efficace est modélisée comme une convolution de la section efficace de l'interaction sur le nucléon individuel et d'un modèle nucléaire décrivant la dynamique de ces nucléons cibles. Dans ce cas, les réinteractions ultérieures des hadrons sortants dans le milieu nucléaire sont simulées séparément. Les interactions de l'état final sont généralement simulées avec des modèles de cascade. Grâce à l'approche de factorisation, il est possible d'utiliser INCL avec le vertex neutrino simulé avec NuWro, un autre générateur d'événements Monte Carlo largement utilisé dans la communauté des neutrinos, et de comparer ensuite les résultats de leur simulation en cascade.

INCL est présenté en détail dans le chapitre 4. INCL est principalement un modèle nucléaire dédié à la simulation des réactions induites par des baryons (nucléons,  $\Lambda$ ,  $\Sigma$ ), des mésons (pions et kaons) ou des noyaux légers ( $A \leq 18$ ) sur un noyau cible. Le neutrino ne fait pas partie des projectiles disponibles dans INCL, nous utiliserons donc le vertex neutrino simulé par NuWro. Le modèle nucléaire INCL est principalement classique, avec l'inclusion de certains ingrédients supplémentaires pour imiter les effets quantiques. Contrairement au modèle de cascade NuWro, où les particules sont propagées dans le milieu continu (modèle de cascade de type espace-temps), chaque nucléon dans INCL est doté d'une position et d'une impulsion et se déplace librement dans le puits de potentiel. Dans INCL, la position et l'impulsion sont corrélées, mais cette corrélation est rendue moins stricte en utilisant le formalisme de Hartree-Fock-Bogoliubov (HFB), également pour tenir compte des propriétés quantiques des fonctions d'onde. Il existe deux principales options pour la modélisation du blocage de Pauli dans INCL : le modèle strict qui interdit toute interaction en dessous du moment de Fermi et le modèle statistique qui ne prend en compte que les nucléons proches et n'agit que dans l'espace des phases donné. L'option par défaut applique un blocage de Pauli strict à la première interaction et un blocage de Pauli statistique aux interactions consécutives. Étant donné que dans l'étude présentée, la première interaction est une interaction neutrino prise à partir de NuWro, nous utilisons uniquement un modèle statistique de blocage de Pauli dans INCL. À l'intérieur de la cascade, il existe plusieurs scénarios possibles d'événements. Le participant peut interagir avec les nucléons du noyau cible et, pour certaines particules, peut se désintégrer. S'il tente de quitter le milieu nucléaire, la particule peut soit être déviée vers l'intérieur du milieu nucléaire, soit être émise du noyau. Si le nucléon est sur le point d'être éjecté du noyau, avec une certaine probabilité, il peut se regrouper avec des nucléons proches et quitter le noyau en tant que groupe nucléaire. La production de groupes nucléaires est une caractéristique remarquable d'INCL, connue et calibrée pour les besoins de la physique nucléaire mais absente dans tout générateur de neutrinos actuel. INCL peut être couplé à des modèles de désexcitation. Nous avons choisi ABLA parmi tous les codes de désexcitation possibles, car il s'est révélé précis pour les noyaux légers.

Les chapitres 5, 6 et 7 contiennent les principaux résultats de la thèse. La plupart des résultats sont obtenus pour les interactions neutrino muoniques du courant chargé quasi-élastique (CCQE, pour *Charged-Current Quasi-Elastic*) sur le carbone en utilisant le flux d'énergie neutrino du détecteur proche T2K. Le chapitre 5 est consacré à la comparaison des mécanismes de la cascade FSI d'INCL et de NuWro dans la simulation des interactions neutrino et antineutrino CCQE. L'analyse est axée sur les particules produites et les changements cinématiques du nucléon principal induits par la FSI. En particulier, nous avons utilisé les variables transverses simples (STV, pour *Single Transverse Variables*) pour comparer les effets des différents modèles de cascade. Une différence significative entre les deux modèles est qu'INCL simule la production de groupes nucléaires dans la FSI des interactions

neutrino. En ce qui concerne l'impact de la FSI sur le nucléon principal, le modèle nucléaire d'INCL présente une transparence beaucoup plus faible que NuWro. La transparence est une mesure qui permet d'estimer la force de la FSI dans un modèle donné. De tels résultats proviennent d'une combinaison caractéristique des sections efficaces nucléon-nucléon, du blocage de Pauli et des spécificités du modèle nucléaire utilisé. Notamment, la simulation de la FSI d'INCL présente une fraction importante d'événements sans proton dans l'état final, en particulier lors de la propagation de protons de faible impulsion à partir du vertex primaire. De plus, le modèle INCL a tendance à réabsorber les autres particules produites pendant la cascade FSI : les événements avec des protons de faible impulsion sont principalement accompagnés d'autres nucléons dans NuWro mais pas dans INCL. Nous montrons également les différences fondamentales entre les interactions neutrino et antineutrino et leur impact sur la distribution du neutron principal. Avec un transfert d'énergie plus faible, les interactions antineutrino sont davantage affectées par le blocage de Pauli.

Le chapitre 6 pousse plus loin l'étude présentée dans le chapitre précédent en ajoutant une simulation de désexcitation au-dessus de la simulation en cascade d'INCL. Même si les hadrons sortant du vertex neutrino ne subissent aucune interaction de diffusion finale (FSI), le noyau aura une énergie d'excitation non nulle résultant de l'interaction fondamentale du neutrino. La FSI augmentera davantage l'énergie stockée dans le noyau, en particulier en cas d'absorption de nucléons, et cette énergie sera ensuite libérée lors de l'étape de désexcitation. Pendant la désexcitation, ABLA génère une quantité importante de différentes particules, principalement des protons et des particules alpha. La simulation INCL+ABLA montre une production de protons presque triplée et une production de particules alpha multipliée par dix. La désexcitation induit également la production de protons dans certains événements où le proton de la cascade FSI a été absorbé, mais la cinématique de ces protons diffère considérablement de celle des protons produits par la FSI. La présence de la simulation de désexcitation convertit l'énergie de liaison en énergie d'excitation, qui est libérée sous forme de particules supplémentaires. Par conséquent, l'énergie du neutrino peut être reconstruite de manière impartiale en utilisant toutes les particules produites dans les événements neutrino. La reconstruction précise de l'énergie du neutrino est une étape essentielle pour la nouvelle génération d'expériences d'oscillation. La méthode calorimétrique de la reconstruction de l'énergie du neutrino, qui prend en compte toutes les particules émises après l'interaction du neutrino, permet une meilleure résolution de l'énergie du neutrino, mais nécessite également une meilleure modélisation du composé hadronique des interactions neutrino-noyau.

La compréhension de la production et des propriétés cinématiques des amas nucléaires est cruciale pour améliorer les modèles d'interaction neutrino-noyau existants et contrôler les incertitudes systématiques correspondantes. Les amas nucléaires sont détaillés dans le chapitre 7, ainsi que la comparaison des résultats de simulation avec les données existantes. Nous avons comparé les résultats de simulation avec les données expérimentales fournies par

les collaborations T2K et MINERvA. Il est difficile de différencier les deux modèles de FSI en raison de la sensibilité limitée des données disponibles et du seuil de moment du proton des détecteurs actuels. Les amas nucléaires peuvent être détectés sous forme de traces fortement ionisantes ou contribuer à l'énergie déposée autour du vertex (activité du vertex) s'ils sont en dessous du seuil de suivi. À bien des égards, ces amas se comportent différemment des protons, car ils libèrent plus d'énergie par ionisation. Pour être reconstruits, ces amas doivent avoir un moment plus élevé que les protons. Lorsqu'ils sont identifiés comme des traces, leur moment peut être mesuré par leur courbure, et leur énergie cinétique correspondante dépend de la masse réelle de la particule. L'énergie cinétique d'un amas quittant le noyau diffère de celle du proton initial produisant l'amas. Nous avons présenté les résultats de notre algorithme d'identification des particules, qui ont montré que les protons ne peuvent pas être confondus avec des amas nucléaires. Cependant, une simulation complète tenant compte des interactions secondaires et de la réponse électronique est nécessaire. INCL+ABLA présente une production significative de plusieurs nucléons et de fragments nucléaires contribuant à l'activité du vertex. La proportion de l'énergie du neutrino transférée à l'énergie cinétique des hadrons secondaires n'est pas négligeable, en particulier lors de la prise en compte de la désexcitation. Parallèlement, la partie de l'énergie visible dans le détecteur est plus petite en raison des effets d'extinction. Il est donc essentiel d'avoir des modèles capables de modéliser avec précision une telle fraction d'énergie, qui doit être corrigée pour parvenir à une reconstruction complète de l'énergie du neutrino.

Nous avons également étudié les interactions secondaires des neutrons en simulant la propagation des neutrons dans le détecteur à l'aide des deux modèles. Nos résultats ont montré que les modèles de Bertini et d'INCL prédisent de manière cohérente la cinématique des neutrons, tandis que l'efficacité présente une différence de 4%, ce qui correspondrait à d'importantes systématiques sur la détection des neutrons.

Le chapitre 8 couvre les efforts en vue de la mise à niveau de ND280 : l'étalonnage de la réponse électronique des ASIC AFTER de l'électronique HA-TPC et les études  $E \times B$  réalisées avec le faisceau de test HA-TPC de DESY. L'étalonnage électronique vise à garantir une mesure précise de la charge et une linéarité de réponse entre les canaux. Les coefficients de linéarité électronique sont homogènes au sein d'un ASIC, avec une différence de linéarité inférieure à 3% entre les ASIC voisins. La non-linéarité globale sur tous les canaux peut atteindre 7%. Les études  $E \times B$  utilisant les données du faisceau de test DESY ont été réalisées pour étudier les distorsions de l'image de la trace projetée sur les modules de lecture. L'amplitude de l'effet observé dans les données est cohérente avec l'estimation théorique obtenue à partir d'un calcul analytique. Cette analyse a été d'une aide essentielle pour extraire les performances appropriées du TPC à partir de ces données.

Les résultats obtenus à partir de cette étude amélioreront notre compréhension des effets nucléaires, conduisant finalement à des mesures plus précises des oscillations des neutrinos

et à une compréhension plus approfondie des propriétés fondamentales des neutrinos. Les conclusions présentées ici contribuent aux efforts en cours visant à améliorer notre compréhension des neutrinos et ouvrent la voie à des expériences de neutrinos futures plus précises et fiables.



# Contents

<b>Résumé</b>	<b>vii</b>
<b>List of Figures</b>	<b>xix</b>
<b>List of Tables</b>	<b>xxix</b>
<b>List of abbreviations</b>	<b>xxxii</b>
<b>1 Introduction</b>	<b>1</b>
1.1 The dawn of neutrino oscillations . . . . .	2
1.2 The definitive experimental establishment of neutrino oscillations . . . . .	6
1.3 Present and future of long-baseline neutrino experiments at accelerators . . . . .	10
1.4 Thesis outline . . . . .	12
References . . . . .	14
<b>2 Neutrino long baseline experiments: T2K and beyond</b>	<b>19</b>
2.1 Long-baseline accelerator experiments . . . . .	19
2.2 The T2K experiment . . . . .	24
2.2.1 The Far Detector . . . . .	25
2.2.2 The Near Detector . . . . .	26
2.3 ND280 upgrade for T2K . . . . .	30
2.3.1 The SuperFGD detector . . . . .	30
2.3.2 HA-TPC . . . . .	31
2.4 Future experiments . . . . .	32
References . . . . .	34
<b>3 Neutrino-nucleus interactions</b>	<b>39</b>
3.1 Neutrino primary vertex . . . . .	40
3.2 Initial state models . . . . .	45
3.3 Final state interactions . . . . .	52
3.4 Neutrino MC generators . . . . .	53

---

References . . . . .	58
<b>4 Liège Intranuclear Cascade code</b>	<b>65</b>
4.1 The INCL code . . . . .	65
4.1.1 Model ingredients . . . . .	66
4.1.2 Elementary collisions in INCL . . . . .	73
4.2 Coupling to the de-excitation models . . . . .	77
4.2.1 The de-excitation code ABLA . . . . .	78
4.3 INCL distribution within other softwares . . . . .	79
4.4 CCQE implementation in INCL . . . . .	81
References . . . . .	85
<b>5 FSI modelling with INCL and NuWro cascade models</b>	<b>91</b>
5.1 Implementation of the NuWro input . . . . .	91
5.2 Proton FSI modelling . . . . .	94
5.2.1 Leading proton kinematics . . . . .	95
5.2.2 Single Transverse Variables . . . . .	97
5.3 Neutron FSI modelling . . . . .	102
5.3.1 Leading neutron kinematics . . . . .	103
5.3.2 Single Transverse Variables . . . . .	106
5.4 Beyond factorization approach: spectral function FSI . . . . .	107
5.5 Summary . . . . .	109
References . . . . .	111
<b>6 De-excitation role in <math>\nu</math>-nucleus scattering</b>	<b>113</b>
6.1 Excitation energy calculation . . . . .	113
6.2 Particle production in de-excitation . . . . .	115
6.3 Proton kinematics . . . . .	117
6.3.1 Single Transverse Variables . . . . .	118
6.4 Neutrino energy reconstruction . . . . .	120
6.5 Summary . . . . .	122
References . . . . .	124
<b>7 Experimental observables</b>	<b>125</b>
7.1 Proton kinematics: comparison to the available data . . . . .	125
7.2 Nuclear clusters and vertex activity . . . . .	129
7.2.1 Modelling of clusters using Geant4 . . . . .	129
7.2.2 Identification of the nuclear clusters as tracks . . . . .	132
7.2.3 Vertex activity . . . . .	135

---

7.3 Neutron measurements . . . . .	138
7.4 Summary . . . . .	145
References . . . . .	147
<b>8 New detectors: the case of the High-Angle TPC for the ND280 upgrade</b>	<b>149</b>
8.1 Electronics calibration . . . . .	150
8.2 The $E \times B$ effect . . . . .	154
8.3 Summary . . . . .	159
References . . . . .	160
<b>9 Conclusion</b>	<b>163</b>
References . . . . .	166
<b>Appendix A Initial state nuclear model</b>	<b>167</b>
References . . . . .	169



# List of Figures

1.1	The original letter of Wolfgang Pauli [12] with the proposal of the new particle that will be later called a neutrino. . . . .	2
1.2	Scheme of the two distinct neutrino mass hierarchy. The picture is taken from [27].	5
1.3	Appearance probability of $\nu_e$ for initial $\nu_\mu$ as a function of energy E. Left: neutrinos, right: antineutrinos. The picture is taken from [33]. . . . .	6
1.4	Neutrino-oscillation experiments using neutrinos from nuclear reactors or accelerator beams as a function of the distance from source to detector and the peak energy of the neutrinos. Open markers indicate future projects (for detectors above 5 kton, the area of the marker is proportional to the detector mass), and italics indicate completed experiments. The experiments are colored according to the target material. The picture is taken from Ref. [39]. . . . .	8
1.5	Expected flavor composition of the reactor neutrino flux for 4 MeV neutrinos as a function of distance to the reactor cores. The picture is taken from Ref. [23]. .	9
1.6	The predicted solar neutrino energy spectrum. The picture is taken from Ref. [46].	10
1.7	Left: the reconstructed neutrino energy spectra for the SK samples containing electron-like events in neutrino-mode ( <b>a</b> ) or antineutrino-mode ( <b>b</b> ) beam running. The solid stacked chart corresponds to $\delta_{CP=0}$ , and the dashed lines represent predictions of the total predicted number of events for the two extreme CP-violating cases. Right: constraints on PMNS oscillation parameters $\theta_{13}$ and $\theta_{23}$ . The plots are taken from Ref. [57]. . . . .	12
2.1	The schematic view of the T2K beamline. . . . .	20
2.2	Timeline of the long-baseline neutrino experiments. The baseline L and the peak neutrino energy E are indicated. For all the experiments the schematic views of the near detectors are shown, but for the Hyper-Kamiokande detector, the far detectors scheme is used since the near detector will be an upgraded near detector facility used by T2K. The figures were adapted from [13–19]. . . .	22
2.3	Factors that contribute to the neutrino rate calculation at the far detector. Most of them depend on the true neutrino energy. . . . .	23

2.4	The schematic view of the T2K experiment, including its far detector and the near detector complex. Figures are adapted from [30–32]. . . . .	24
2.5	Muon neutrino survival probability and the neutrino fluxes at different off-axis angles. The figure is taken from [35]. . . . .	25
2.6	Schematic overview of the Super-Kamiokande experiment. The picture is taken from [47] . . . . .	26
2.7	Example of reconstructed T2K events in Super-Kamiokande for (a) a muon-like ring and (b) an electron-like ring. The figures show the projection of the cylindrical detector onto a plane. Each point is a PMT, and the color corresponds to the amount of charge. Reconstructed light cone is depicted as a white line. The picture is taken from [32]. . . . .	27
2.8	The schematic view of the T2K near detector ND280. The picture is taken from [32].	28
2.9	The neutrino energy reconstruction resolution and bias calculated for $E_{vis}$ and $E_{QE}$ for $\pm 10$ MeV shifts to the nominal removal energy distribution (denoted by the red and blue colors respectively). The calculation is done for the CCQE events. The picture and the description are adapted from [55]. . . . .	29
2.10	The schematic view of the T2K ND280 upgrade detector. The picture is taken from [16]. . . . .	30
2.11	The schematic view of the SuperFGD structure. The picture is taken from [16].	31
2.12	The schematic view of the HA-TPC. The picture is taken from [16]. . . . .	32
2.13	The schematic view of the bulk MicroMegas (left) used in current TPCs and the resistive MicroMegas (right). The picture is taken from [56]. . . . .	33
3.1	The factorization scheme of the neutrino-nucleus interaction modeling. . . . .	39
3.2	Examples of the neutrino quasi-elastic CC (left) and elastic NC (right) neutrino interactions. . . . .	40
3.3	Total neutrino and antineutrino per nucleon CC cross sections divided by neutrino energy and plotted as a function of neutrino energy. Contributions of different channels are shown: quasi-elastic (dashed line), resonance (dash-dotted line) production, and deep inelastic scattering (dotted line). The experimental data coming from different measurements are also added. The figure is adapted from [5]. . . . .	41
3.4	Example of the multinucleon knock-out production. . . . .	42
3.5	Example of the neutrino resonance production. . . . .	43
3.6	Example of the neutrino deep inelastic scattering. . . . .	44
3.7	Example of the coherent pion production. . . . .	44

3.8	Total cross section for charged current coherent pion production. Data are scaled to $^{12}\text{C}$ assuming the $A^{1/3}$ dependence. NC data are multiplied by factor 2 assuming $\sigma_{COH}^{CC} = 2\sigma_{COH}^{NC}$ . The figure is taken from Ref. [24]. . . . .	45
3.9	Nuclear potential wells for protons and neutrons. $E_F^p$ and $E_F^n$ are the Fermi energies of protons and neutrons, $E_B$ is a binding energy. The inspiration for the figure is taken from [24]. . . . .	46
3.10	A shell model picture used to describe the nucleus, $^{16}\text{O}$ example. $E_{1s_{1/2}}$ , $E_{1p_{3/2}}$ , and $E_{1p_{1/2}}$ are the binding energies of shells $1s_{1/2}$ , $1p_{3/2}$ , and $1p_{1/2}$ , respectively. . . . .	49
3.11	Three-dimensional plot of the oxygen spectral function. Here $k$ is the nucleon momentum. The figure is adapted from [46]. . . . .	51
3.12	The initial nucleon momentum distribution within a Carbon nucleus simulated using the Spectral function, Local Fermi Gas (LFG), and Relativistic Fermi Gas (RFG) implemented in NuWro. The geometrical factor $p_n^2$ is implied. . . . .	52
3.13	Schematic view of a nuclear cascade induced by an incident neutrino. . . . .	53
4.1	Proton induced reaction cross section on $^{12}\text{C}$ as a function of the proton momentum calculated with INCL and NuWro models: comparison of the INCL and NuWro models to available experimental data [18–36]. Results of the NuWro 19.02.2 simulation were taken from Ref. [37]. . . . .	67
4.2	The scheme of the impact parameter $b$ definition. Deflection because of the classical Coulomb field is also shown. . . . .	68
4.3	Illustration of the correlation between the spatial and momentum distributions implied by the phase space distribution from Eq. 4.3. Particles with momentum between $p$ and $p + dp$ can reach a maximum radial distance between $R(p)$ and $R(p + dp)$ . Figure and the caption are adapted from [38]. . . . .	69
4.4	The considered clusters for the maximal allowed mass number $A_{cl}^{max} = 12$ are identified by their charge $Z$ (vertical ordering), and neutron $N$ (horizontal ordering) numbers and are displayed inside the perimeter delineated by the heavy line. Stable clusters are depicted inside the yellow cells. Time-displaying cells represent clusters with a lifetime larger than 1 ms, which are considered to be detectable. Other cells (in blue) correspond to clusters with a lifetime smaller than 1 ms and are forced to decay. The picture and description are adapted from [44]. . . . .	71
4.5	Elementary nucleon-nucleon cross sections. The lines represent the parametrization used in INCL [38, 47]. Experimental data are taken from Ref. [48]. The plot and the description are adapted from [49]. . . . .	74

4.6	Parametrization for the $\pi^+ p$ and $\pi^- p$ total cross sections. The crosses represent experimental data coming from Particle Data Group [52]. Continuous lines and dotted lines stand for the total reaction cross section and the $\Delta$ recombination cross section used in INCL. The plot and the description are adapted from [49].	76
4.7	ABLA diagram of de-excitation processes, where $E^*$ and $T$ represent the excitation energy and temperature of the nuclear system, respectively, $S_{min}$ is the minimum particle separation energy, and $T_{freeze-out} = \max \left[ 5.5, 9.33 e^{(-2.82 \times 10^{-3} A_{rem})} \right]$ is the freeze-out temperature; $A_{rem}$ is the mass number of the remnant. The picture and description are adapted from [55].	78
4.8	Model map for the INCL-based physics lists. The first two columns represent nucleon- and pion-induced reactions. The fourth column represents nucleus-nucleus reactions where at least one of the partners is below $A=18$ . The fifth column represents other nucleus-nucleus reactions. The picture is adapted from [63].	80
4.9	$\left[ A(q^2) \mp B(q^2) \frac{(s-u)}{M^2} + \frac{C(q^2)(s-u)^2}{M^4} \right]$ simulated with NuWro and standalone CCQE code for different neutrino energies. The standalone CCQE code does not have the energy transfer constraints implemented yet. It, therefore, is extended to the nonphysical $q^2$ region.	83
4.10	The transition scheme from the laboratory frame to CMS for the final state kinematics generation. The picture is adapted from [71].	84
5.1	Neutrino CCQE interaction.	91
5.2	The scheme of neutrino-nucleus reaction implementation.	92
5.3	Radial coordinate and momentum distribution inside the nucleus for INCL (left), and NuWro LFG (right) nuclear models ( $z$ axis in arbitrary units).	93
5.4	Left: Momentum distribution of neutrons in the nucleus for NuWro SF and RFG and INCL nuclear models (shape comparison). Right: Position distribution of neutrons in INCL and NuWro and of the INCL neutron chosen to match the SF neutron simulated in NuWro in our matching algorithm.	93
5.5	Nuclear transparency of $^{12}\text{C}$ (percentage of events without FSI) as a function of proton momentum modelled by NuWro and INCL.	96
5.6	Nuclear transparency of $^{12}\text{C}$ (ratio of number of events without FSI to all events) dependence on the position of the neutrino interaction inside the nucleus. $Y$ -coordinate is averaged out to the 5 slices. The $Z$ -coordinate corresponds to the initial neutrino direction.	96

5.7	Top: proton momentum before FSI for INCL (left), and NuWro (right) cascade models in CCQE events with T2K neutrino energy flux. Sub-processes correspond to the fate of the proton after FSI. The shape of proton momentum before FSI is by definition identical for INCL and NuWro cascades. Bottom: leading proton momentum after FSI for INCL (left), and NuWro SF (right) nuclear models. The fractions of different FSI sub-processes as listed in Tab. 5.1 are also shown. The 0 proton channel in NuWro includes muon only and pion and neutron production. There is no cluster production in NuWro. . . . .	98
5.8	Distribution of leading proton's momentum in NuWro SF and NuWro+INCL before and after FSI (top left, shape comparison). Distribution of difference in proton's momentum before and after FSI ( $\Delta P = P_{after} - P_{before}$ ) in NuWro SF and NuWro+INCL (bottom left, shape comparison). Distribution of leading proton $\cos(\theta)$ in NuWro SF and NuWro+INCL before and after FSI (top right, shape comparison). Distribution of difference in proton's $\cos(\theta)$ before and after FSI ( $\Delta \cos(\theta) = \cos\theta_{after} - \cos\theta_{before}$ ) in NuWro SF and NuWro+INCL (bottom left, shape comparison). The "no FSI" channel is excluded. CCQE events with T2K neutrino energy flux are simulated. . . . .	99
5.9	Schematic illustration of the single-transverse kinematic imbalance. $\vec{p}_{N'}$ and $\vec{p}_{l'}$ are momenta of the outgoing nucleon and lepton (in the neutrino CCQE case proton and $\mu^-$ , in the antineutrino case—neutron and $\mu^+$ ). $\vec{p}_T^{N'}$ and $\vec{p}_T^{l'}$ are their projection on the transverse plane. On the right side of figure, the two-dimensional projection on the transverse plane is shown. The figure is adapted from [4]. . . . .	100
5.10	Top: $\delta\alpha_T$ simulated with the INCL+NuWro SF (left), and NuWro (right) cascade models in CCQE events with T2K neutrino energy flux. Bottom: $\delta p_T$ for the INCL+NuWro SF (right) and Nuwro SF(left) nuclear models. . . . .	101
5.11	$\delta\alpha_T$ distribution in NuWro SF and NuWro+INCL (shape comparison). The effect on $\delta\alpha_T$ shape of including also the leading nuclear cluster in INCL events is shown. . . . .	101
5.12	Antineutrino CCQE interaction. . . . .	102
5.13	Left: Neutrino and antineutrino CCQE reaction cross sections modeled with NuWro. Right: energy transfer for neutrino and antineutrino CCQE interactions simulated with NuWro with T2K neutrino and antineutrino flux. . . . .	102

---

5.14	Top: neutron momentum before FSI for INCL (left), and NuWro (right) cascade models in CCQE events with T2K antineutrino energy flux. Sub-processes correspond to the fate of the neutron after FSI. The shape of neutron momentum before FSI is by definition identical for INCL and NuWro cascades. Bottom: leading neutron momentum after FSI for INCL (left), and NuWro SF (right) nuclear models. The fractions of different FSI sub-processes as listed in Tab. 5.2 are also shown. The 0 neutron channel in NuWro includes muon only and pion and proton production. There is no cluster production in NuWro. . . . .	104
5.15	Distribution of leading neutron's momentum in NuWro SF and NuWro+INCL before and after FSI (top left, shape comparison). Distribution of difference in neutron's momentum before and after FSI ( $\Delta P = P_{after} - P_{before}$ ) in NuWro SF and NuWro+INCL (bottom left, shape comparison). Distribution of leading neutron $\cos(\theta)$ in NuWro SF and NuWro+INCL before and after FSI (top right, shape comparison). Distribution of difference in neutron's $\cos(\theta)$ before and after FSI ( $\Delta \cos\theta = \cos\theta_{after} - \cos\theta_{before}$ ) in NuWro SF and NuWro+INCL (bottom left, shape comparison). The "no FSI" channel is excluded. CCQE events with T2K antineutrino energy flux are simulated. . . . .	105
5.16	NuWro simulation of the $\cos(\theta)$ before (left) and after (right) FSI for protons (top) and neutrons (bottom). . . . .	106
5.17	Top: $\delta\alpha_T$ simulated with the INCL+NuWro SF (left), and NuWro (right) cascade models in CCQE events with T2K antineutrino energy flux. Bottom: $\delta p_T$ for the INCL+NuWro SF (right) and Nuwro SF(left) nuclear models. . . . .	107
5.18	$\delta\alpha_T$ simulated with NuWro using the Llewellyn-Smith formula without (left) and with (right) Pauli Blocking. . . . .	108
5.19	Proton momentum before FSI simulated with INCL+NuWro SF (left) and NuWro SF (right). "SF FSI" option in NuWro simulation was used. . . . .	108
5.20	$\delta\alpha_T$ simulated with INCL+NuWro SF (left) and NuWro SF (right). . . . .	109
6.1	Excitation energy calculated for transparent events simulated with NuWro. The mass of the remnant is simulated with constant potential and with the mass table. . . . .	116
6.2	Excitation energy after INCL and NuWro cascades. . . . .	116
6.3	Average number of different particles in NuWro, INCL and INCL+ABLA simulations. . . . .	117
6.4	Comparison of the momentum distribution of $\alpha$ , deuterons and protons produced during cascade and de-excitation (left) and energy spectrum of the top 9 produced particles during de-excitation (right). The $\gamma$ -ray distribution was additionally scale down to 25%, so its peak is comparable to the energy spectra peaks of the emitted hadrons. . . . .	118

6.5	Proton momentum before (left) and after (right) FSI. Simulated with INCL+ABLA (top), INCL (center), and NuWro (bottom) cascade models in CCQE events with T2K neutrino energy flux. Sub-processes correspond to the fate of the proton after FSI. The shape of proton momentum before FSI is by definition identical for INCL and NuWro cascades. The plots with the INCL and NuWro results are the same as in Chapter 5. . . . .	119
6.6	$\delta\alpha_T$ (left) and $\delta p_T$ (right) simulated with INCL+ABLA (top), INCL (center) and NuWro (bottom) cascade models in CCQE events with T2K antineutrino energy flux. The plots with the INCL and NuWro results are the same as in Chapter 5. .	121
6.7	Shape comparison of the neutrino energy reconstruction resolution using proton and muon only (left) or the sum of the kinetic energy of all the final state particles (right). . . . .	122
6.8	Shape comparison of the neutrino energy reconstruction resolution using with proton and muon only and with all outgoing particles. Left: all events simulated with NuWro, INCL and INCL+ABLA; center: INCL+ABLA simulation of the FSI events; right: INCL+ABLA simulation of the no FSI events. . . . .	122
7.1	Top to bottom: NuWro SF comparison to T2K data; INCL + NuWro SF comparison to T2K data; comparison of NuWro, INCL + NuWro SF and data; ratio of NuWro SF and INCL + NuWro SF models of QE channel. Left: $\delta\alpha_T$ , right: $\delta p_T$ . .	127
7.2	Top to bottom: NuWro SF comparison to MINERvA data; INCL + NuWro SF comparison to T2K data; comparison of NuWro, INCL + NuWro SF and data; ratio of NuWro SF and INCL + NuWro SF models of QE channel. Left: $\delta\alpha_T$ , right: $\delta p_T$ . . . . .	128
7.3	INCL, INCL+ABLA and NuWro comparison to the T2K data, superimposed. Left: $\delta\alpha_T$ , right: $\delta p_T$ . . . . .	129
7.4	INCL, INCL+ABLA and NuWro predictions if various cuts applied. Left: $\delta\alpha_T$ , right: $\delta p_T$ . . . . .	130
7.5	Energy distributions used for particle gun. Fit function is $\exp(p_0 + p_1 \cdot E) + \exp(p_2 + p_3 \cdot E)$ , for low energies of the proton: 2 order polynomial. . . . .	131
7.6	Left: momentum distribution of clusters produced by FSI in INCL (solid line) and visible energy loss by ionization (with Birks correction) as a function of their momentum (scatter plot). Right: total track length of nuclear clusters as a function of visible energy of the particles. The $^3\text{He}$ distribution overlaps with the $\alpha$ distribution and almost cannot be seen on the plot. . . . .	132

7.7	Scheme of the particles simulation and identification algorithm in a segmented scintillating detector. The shaded line indicates the cluster track traversing multiple scintillating cubes. The cluster has initial kinetic energy $E^0$ and deposits energy $E_i^d ep$ in each cube. The last cube, where the cluster stops, is not considered in the identification algorithm. . . . .	133
7.8	Visible energy deposited by ionization by different particles in a sphere of 1 (left) and 3 cm (right) radius around the vertex in events simulated with INCL+ABLA.	136
7.9	Total visible energy deposited by ionization by all the particles in a sphere of 1 (3) cm radius around the vertex. Distributions from events simulated with INCL and NuWro are compared with the same overall normalization. The tail with low statistics is not shown. . . . .	136
7.10	Vertex activity as a fraction of the initial neutrino energy depending on the neutrino energy simulated with NuWro, INCL and INCL+ABLA. The bands correspond to the $1\sigma$ uncertainty. ABLA does not shift the mean ratio much but gives a larger spreading of this ratio distribution for the given neutrino energy.	137
7.11	Sum of the kinetic energy of all clusters, neutrons and non-leading protons in the event as a fraction of the initial neutrino energy depending on the neutrino energy simulated with INCL and INCL+ABLA. The bands correspond to the $1\sigma$ uncertainty. . . . .	138
7.12	Left: the efficiency to detect protons, muons and neutrons in ND280. Right: the reconstructed $\delta p_T$ distribution for selected $CC0\pi$ and anti-neutrino interactions split by interaction mode and target for $1 \times 10^{22}$ POT. The plots are taken from [13].	139
7.13	The scheme of merging trajectories to estimate the neutron multiplicity. The primary particle has track 1. It produced particles with tracks 2, 3, 4, and 5. Assigning new tracks to the initial particles is impossible, so no merging is applied. The particle with track 5 has participated in interaction with no production of extra particles, but its track number has changed to 6 and then to 7. In this case, the algorithm merges all these trajectories into one trajectory 5. Then, this neutron 5 interacts and produces two more particles. Again, no merging is applied. In the end, out of 9 tracks in the event, after applying the algorithm, there will be only 7. . . . .	140
7.14	Possible scenarios of the neutron interaction with a potential number of secondary neutrons. . . . .	140
7.15	Left: secondary neutrons multiplicity simulated with Bertini and INCL. Right: secondary neutrons multiplicity with various energy cuts applied for the Bertini simulation. . . . .	141

---

7.16 Neutron parents (left) and neutron daughters (right) simulated with INCL and Bertini. "Vertex" means that the neutron was produced in the neutrino interaction vertex. . . . .	141
7.17 Geant4 processes (left) and sub-processes (right) in which participate primary and secondary neutrons. The simulation is performed with the physics list that includes INCL. . . . .	142
7.18 Probability of different neutron processes as a function of neutron energy. These processes were simulated with INCL and Bertini physics lists. . . . .	143
7.19 Number of interactions (left), $\Delta E$ (middle) and $\Delta \cos\Theta$ (right) for primary (top) and secondary (bottom) neutrons. . . . .	144
7.20 $\Delta E$ vs. $\Delta \cos(\theta)$ for primary (left) and secondary (right) neutrons. For the bottom plots, the cut on the kinetic energy $E > 5$ MeV is applied. Such a cut application suggests that large scattering angles correspond to the low-energy particles. . .	144
7.21 Number of visible interactions for primary (left) and secondary (right) neutrons; INCL cascade model. . . . .	145
7.22 Kinetic energy reconstruction resolution of the primary neutrons, simulated with INCL and Bertini cascades. . . . .	145
8.1 The HA-TPC structure and the structure of a Micromegas module with its associated electronics and mechanical structure. . . . .	150
8.2 Photographs of the setup. . . . .	150
8.3 Example of calibration signals: signals on an ERAM (each bin represents a pad) (left) and distribution of all signals collected in a single pad (right). . . . .	151
8.4 Pedestal test. ASICs are separated with gray dashed lines. . . . .	151
8.5 Example of the maximum of amplitude of injected signals in two different channels. . . . .	152
8.6 Example of the calibration line. After subtracting the pedestal, its intercept must be around zero. . . . .	153
8.7 Map of the electronic linearity coefficients. . . . .	153
8.8 Left: 1D distribution of the pedestal dispersion of two FECs. Right: 1D distribution of the electronic linearity coefficients of two FECs. . . . .	154
8.9 When a particle passes through the Micromegas detector, it ionises several atoms in the conversion volume, and the primary electrons drift to the amplification region. In the amplification region, an electron avalanche is formed. The picture and description are taken from [8]. . . . .	154
8.10 Scheme of the DESY test beam setup. The figure is adapted from Ref. [10]. . . .	155

---

8.11	Map of the magnetic field. Left: radial component, top view. Central: longitudinal component, top view. Right: radial component, front view. The black boxes represent the contours of the TPC's drift volume. Notice the non-negligible radial component of the field, especially in the rear of the TPC. The figure and description are adapted from Ref. [6]. . . . .	156
8.12	Event display of nominally horizontal beam. (a) single track; (b) accumulation plot of the tracks from the same dataset ( $B = 0.2$ T). The figure and description are adapted from Ref. [6]. . . . .	157
8.13	Schematic view of the drift velocity components according to the Langevin equation. . . . .	157
8.14	Top: examples of rejected tracks; bottom: examples of accepted tracks. . . . .	159
8.15	Slope coefficients depending on the value of the magnetic field, superimposed.	160
A.1	Top to bottom: NuWro RFG comparison to T2K data; INCL + NuWro RFG comparison to T2K data; comparison of NuWro RFG, INCL + NuWro RFG and data; ratio of NuWro RFG and INCL + NuWro RFG models of QE channel. Left: $\delta\alpha_T$ , right: $\delta p_T$ . . . . .	168
A.2	Neutron momentum distribution inside the nucleus: standard INCL nucleus (left) and INCL nucleus built around NuWro neutron (right) as a function of radius. . . . .	169
A.3	$\delta\alpha_T$ for NuWro RFG (left), INCL+NuWro RFG (middle) and INCL+NuWro RFG reweighted to INCL initial momentum and position (right). . . . .	169

# List of Tables

4.1	List of considered reactions involving strangeness based on experimental data.	77
4.2	List of the reactions involving strangeness and requiring information that has been taken exclusively from models. The X stands for all possible reactions, excluding the reaction summarised in Table 4.1. . . . .	77
5.1	Fractions of the different FSI channels, i.e. fraction of events with different final state particles after the FSI cascade, in CCQE events with T2K neutrino energy flux. Fractions of events with and without protons in the final state are quoted separately. . . . .	95
5.2	Fractions of the different FSI channels, i.e. fraction of events with different final state particles after the FSI cascade, in CCQE events with T2K neutrino energy flux. Fractions of events with and without protons in the final state are quoted separately. . . . .	103
7.1	Signal phase space restriction for the T2K and MINERvA measurements. For T2K, the cuts apply to the proton with the highest momentum. For MINERvA, event passes the cuts if any proton corresponds to the allowed phase space. . .	126
7.2	Percentage of clusters travelling more than 1 and 3 cm, for INCL only and INCL+ABLA simulations. . . . .	134
7.3	Percentage of misidentified clusters simulated with INCL. . . . .	135
7.4	Percentage of misidentified clusters simulated with INCL+ABLA. . . . .	135
A.1	Fractions of events with and without protons in the final state, fractions of different channels in events with and without protons in the final state. . . . .	169



# List of abbreviations

<b>ABLA</b>	the ablation model
<b>ADC</b>	Analog-to-Digital Converter
<b>ADS</b>	Accelerator-Driven Systems
<b>ARFG</b>	Asymmetric Relativistic Fermi Gas
<b>ASIC</b>	Application Specific Integrated Circuit
<b>BabyMIND</b>	Magnetized Iron Neutrino Detector
<b>CC</b>	Charged Current
<b>CCQE</b>	Charge Current Quasi-Elastic
<b>CDPP</b>	Coherent Dynamical Pauli Principle
<b>CKM matrix</b>	Cabibbo-Kobayashi-Maskawa matrix
<b>CMS</b>	Center-of-Mass
<b>COH</b>	COHerent pion production
<b>CVC</b>	Conserved Vector Current
<b>DIS</b>	Deep Inelastic Scattering
<b>DUNE</b>	the Deep Underground Neutrino Experiment
<b>ENUBET</b>	Enhanced NeUtrino BEams from kaon Tagging
<b>ERAM</b>	Encapsulated Resistive Anode Micromegas
<b>FD</b>	Far Detector
<b>FEC</b>	Front-End Card
<b>FEM</b>	Front End Module
<b>FGD</b>	Fine Grained Detector
<b>FHC</b>	Forward Horn Current
<b>FSI</b>	final state interactions
<b>FTF</b>	the Fritiof model
<b>GALLEX</b>	The Gallium Experiment
<b>GENIE</b>	Generates Events for Neutrino Interaction Experiments
<b>GiBUU</b>	the Giessen Boltzmann-Uehling-Uhlenbeck model
<b>HA-TPC</b>	High-Angle Time Projection Chamber

---

<b>HFB</b>	Hartree-Fock-Bogoliubov
<b>HK</b>	the Hyper-Kamiokande experiment
<b>HV</b>	high voltage
<b>IMF</b>	Intermediate-Mass Fragment
<b>INC</b>	Intra-Nuclear Cascade
<b>INCL</b>	IntraNuclear Cascade Li'ege
<b>INGRID</b>	Interactive Neutrino GRID
<b>IO (IH)</b>	inverted ordering (inverted hierarchy)
<b>IWCD</b>	the Intermediate Water Cherenkov Detector
<b>JUNO</b>	Jiangmen Underground Neutrino Observatory
<b>J-PARC</b>	the Japan Proton Accelerator Research Complex
<b>K2K</b>	the KEK to Kamioka experiment
<b>LBL</b>	Long Baseline
<b>LDA</b>	Local Density Approximation
<b>LFG</b>	Local Fermi Gas
<b>LTF</b>	the Local Thomas-Fermi approximation
<b>MC</b>	Monte Carlo
<b>MCNP</b>	Monte Carlo N-Particle
<b>MF</b>	Mean-Field
<b>MFA</b>	Mean-Field Approximation
<b>MHO</b>	Modified-Harmonic-Oscillator
<b>MINERvA</b>	the Main Injector Experiment for $\nu$ -A
<b>MO (MH)</b>	mass ordering (mass hierarchy)
<b>MPPC</b>	Multi-Pixel Photon Counter
<b>MSW effect</b>	the Mikheyev–Smirnov–Wolfenstein effect
<b>MUMON</b>	the MUon MONitor detector
<b>MiniBooNE</b>	the Mini Booster Neutrino Experiment
<b>NC</b>	Neutral Current
<b>ND</b>	Near Detector
<b>NMBT</b>	Nuclear Many-Body Theory
<b>NO (NH)</b>	normal ordering (normal hierarchy)
<b>nuSTORM</b>	Neutrinos from Stored Muons
<b>PCAC</b>	Partially Conserved Axial Current
<b>PHITS</b>	Particle and Heavy Ion Transport code System
<b>PMNS matrix</b>	Pontecorvo–Maki–Nakagawa–Sakata matrix
<b>PMT</b>	Photo-Multiplier Tube
<b>PRISM</b>	Precision Reaction-Independent Spectrum Measurement
<b>PWIA</b>	Plane-Wave Impulse Approximation

---

<b>QEL</b>	Quasi-ELastic
<b>QGS</b>	the Quark-Gluon String model
<b>RES</b>	RESonance production
<b>RFG</b>	Relativistic Fermi Gas
<b>RHC</b>	Reverse Horn Current
<b>RMF</b>	Relativistic Mean Field
<b>SAGE</b>	The Soviet–American Gallium Experiment
<b>SBN program</b>	Short Baseline Neutrino program
<b>SF</b>	Spectral Function
<b>SI</b>	Secondary Interactions
<b>SK</b>	the Super-Kamiokande experiment
<b>SMRD</b>	Side Muon Range Detector
<b>SNO</b>	Sudbury Neutrino Observatory
<b>SRC</b>	Short-Range Correlations
<b>SRN</b>	Supernova Relic Neutrinos
<b>SSM</b>	Standard Solar Model
<b>STV</b>	Single Transverse Variables
<b>SuSA</b>	SUper SCALing Approach
<b>SuperFGD</b>	Super Fine Grained Detector
<b>T2K</b>	the Tokai to Kamioka experiment
<b>TDCM</b>	Trigger and Data Concentrator Module
<b>TOF</b>	the Time-of-Flight detector
<b>TPC</b>	Time Projection Chamber
<b>VA</b>	Vertex Activity
<b>WLS fiber</b>	Wave-Length Shifting fiber



# 1

## Introduction

The journey of the study of elementary particles and their interactions dates back more than two and a half thousand years. It stems from the ideas of ancient Greek natural philosophers about the structure of the world. It is stunning how antique philosophers Leucippus and Democritus, in the 5th century BC with no modern scientific tools, invented the idea that the matter consists of an infinite number of *atoms*—non-dividable particles invisible to the human eye [1]. The philosophical atomism found its continuation in modern science when in the early 19th century, English chemist John Dalton introduced an atomic theory to chemistry [2]. However, serious scientific development of the question started only at the end of the 19th century. In 1897, the eminent English experimental physicist J. J. Thomson determined that all the particles forming the cathode rays are identical, as they have the same charge-to-mass ratio and are part of the matter [3]. This discovery finally gave the *electron* the status of an actual physical object and became the first known elementary particle in the history of humanity. Thomson also proposed a model of the atom, sometimes called a "plum pudding" model. According to this model, the atom is a positively charged body with electrons enclosed inside. This model did not explain the discrete nature of the radiation of atoms and was later disproved by Ernest Rutherford, who later discovered a *proton*, with the mass of  $\sim 1836$  electrons [4], that was considered to be an elementary particle at the time. These discoveries were followed by a century of fruitful breakthroughs, including radioactivity [5], atom structure [6], wave–particle duality [7], development of the theory of relativity [8, 9] and quantum mechanics [10].

One of the major problems in nuclear physics in the twenties and thirties was the problem of beta decay: the spectrum of electrons produced by beta decay, measured by the English physicist James Chadwick as early as 1914, was continuous [11]. It was already known from quantum mechanics that the particles emitted during the decay process should have a discrete spectrum, as, for example, the spectrum of  $\alpha$ -particles during the  $\alpha$ -decay. The continuous

nature of the beta decay electron spectrum thus called the energy conservation law into question. The question was so acute that in 1931 Niels Bohr, at the Rome Conference, proposed the idea of non-conservation of energy. However, there was also another explanation: some unknown, invisible particle carried away the lost energy. The hypothesis of the exceedingly weakly interacting particle was proposed by Wolfgang Pauli in his illustrious letter to the participants of the Tübingen conference in 1930, which is presented in Fig. 1.1. After the discovery in 1932 of the neutron, Enrico Fermi proposed to name Pauli's particle *neutrino*.

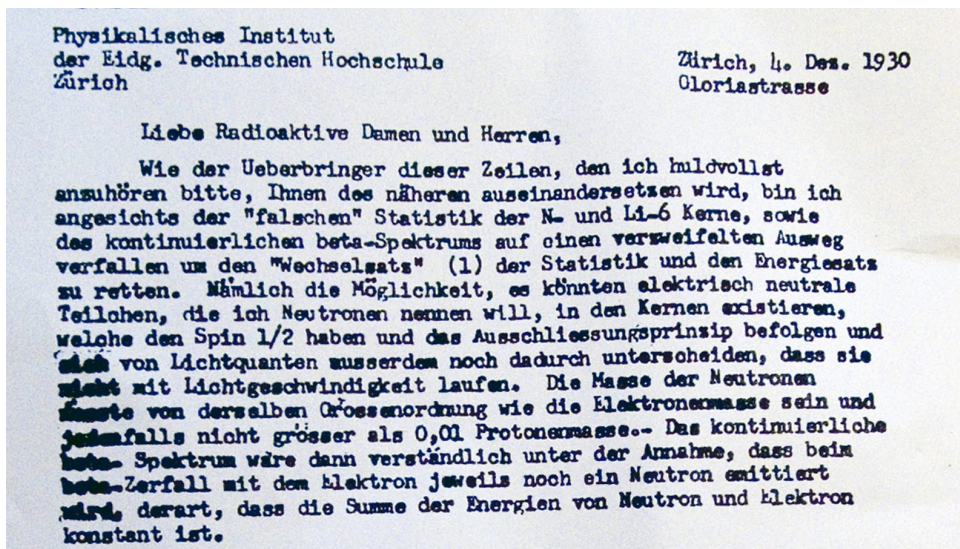


Figure 1.1 The original letter of Wolfgang Pauli [12] with the proposal of the new particle that will be later called a neutrino.

Direct neutrino detection occurred more than 20 years later in the Cowan–Reines neutrino experiment in 1953 [13]. Since then, neutrino physics has been one of the fastest-growing fields of particle physics.

## 1.1 The dawn of neutrino oscillations

The observations of the Homestake experiment, led by R. Davis and J.N. Bahcall [14, 15], dictated the path of neutrino physics development. The primary goal was solar neutrino detection based on B.M. Pontecorvo's proposal of the neutrino capture reaction (inverse beta decay reaction):



This experiment reported a shortage of the recorded electron neutrinos, as only about  $1/3$  of the predicted by Standard Solar Model (SSM) flux was detected.

The Soviet–American Gallium Experiment (SAGE) [16, 17] and the Gallium Experiment (GALLEX) [18] were designed to cross-check the results of the Homestake experiment. These

experiments are based on the reaction:



that has a low threshold for the neutrino detection (233.2 KeV) allowing for the low-energy neutrino detection, unlike the  ${}^{37}\text{Cl}$ -based experiments. These experiments only confirmed the previous results from Homestake.

Bruno Pontecorvo's idea that neutrinos have mass and can mix, analogously to the  $K^0 \leftrightarrow \bar{K}^0$  oscillations, was proposed as a solution. Since only one neutrino flavor was known back then, the sole feasible oscillation would happen between neutrinos and antineutrinos. As more neutrino flavors were discovered, Pontecorvo extended his initial concept to incorporate two neutrino flavors, predicting oscillations of the solar neutrinos even before the Homestake measurements [19]. In parallel, Z. Maki, M. Nakagawa, and S. Sakata proposed the two-neutrino mixing [20] in 1962. Sometime after, in 1969, V. Gribov and B. Pontecorvo published their theoretical model of the two-flavor neutrino oscillations [21]. Once the paradigm of the three generations of the charged leptons and the three neutrino flavors was established, the original neutrino mixing theory was extended to the three families. The lepton mixing matrix of three neutrinos has been named after Pontecorvo, Maki, Nakagawa, and Sakata (PMNS).

The concept of neutrino oscillations considers that neutrino has a non-zero mass. Neutrino flavor eigenstates ( $\nu_e, \nu_\mu, \nu_\tau$ ) are a linear combination of their mass states ( $\nu_1, \nu_2, \nu_3$ ):

$$|\nu_\alpha\rangle = \sum_{i=1}^3 U_{\alpha i}^* |\nu_i\rangle, \quad (1.3)$$

where  $U_{\alpha i}$  is the mixing matrix,  $\nu_\alpha$  are the weak eigenstates, and  $\nu_i$  are the mass states. Flavor states are the eigenstates of the neutrino (weak) interactions with matter, while the mass states are the eigenstates of the free propagation Hamiltonian. The PMNS matrix can be parametrized as follows:

$$U = \underbrace{\begin{pmatrix} 1 & 0 & 0 \\ 0 & c_{23} & s_{23} \\ 0 & -s_{23} & c_{23} \end{pmatrix}}_{\text{atmospheric and accelerator}} \underbrace{\begin{pmatrix} c_{13} & 0 & s_{13}e^{-i\delta_{CP}} \\ 0 & 1 & 0 \\ -s_{13}e^{i\delta_{CP}} & 0 & c_{13} \end{pmatrix}}_{\text{accelerator and reactor}} \underbrace{\begin{pmatrix} c_{12} & s_{12} & 0 \\ -s_{12} & c_{12} & 0 \\ 0 & 0 & 1 \end{pmatrix}}_{\text{solar and reactor}}, \quad (1.4)$$

where  $c_{ij} \equiv \cos(\theta_{ij})$ ,  $s_{ij} \equiv \sin(\theta_{ij})$ ,  $\theta_{ij} \in [0, \pi/2]$  are the mixing angles, and  $\delta_{CP} \in [0, 2\pi]$  is the CP-violation phase. This matrix is similar to the Cabibbo-Kobayashi-Maskawa (CKM) matrix from the quark sector, but the lepton mixing is much stronger (indeed, all the mixing angles of the CKM matrix are small, with the Cabibbo angle being the largest:  $\sin(\theta_C) =$

0.225 [22]. For the PMNS matrix,  $\theta_{23}$  measured in atmospheric and accelerator neutrino experiments is consistent with  $45^\circ$  that corresponds to the maximal mixing, and  $\theta_{12}$  measured in solar neutrino experiments and by KamLAND is consistent with  $33^\circ$  [23]). In equation 1.4, the neutrino sources allowing to probe various oscillation parameters are also indicated.

This parametrization of the PMNS matrix is just one of the many possible (in fact, the only physical observable is the Jarlskog invariant [24]). This parametrization is common since it represents the different experimental domains (i.e., different regimes of neutrino oscillation baseline and energy).

In a vacuum, taking into account plane-wave impulse approximation, the neutrino state evolves as [22]:

$$|\nu_\alpha(t)\rangle = e^{-iHt} |\nu_\alpha(0)\rangle = \sum_{i=e,\mu,\tau} e^{-iE_i t} U_{\alpha i}^* |\nu_i(0)\rangle, \quad (1.5)$$

where  $E_i = \sqrt{p_i^2 + m_i^2} \simeq p + \frac{m_i^2}{2E}$ . The probability of changing the flavor in a vacuum in a time  $t$  is:

$$\begin{aligned} P(\nu_\alpha \rightarrow \nu_\beta) &= |\langle \nu_\beta | \nu_\alpha(t) \rangle|^2 = \left| \sum_{i,j=1}^3 U_{\beta j} e^{-iE_i t} U_{\alpha i}^* \langle \nu_j | \nu_i \rangle \right|^2 \\ &= \left| \sum_{i,j=1}^3 U_{\beta j} e^{-iE_i t} U_{\alpha i}^* \delta_{ji} \right|^2 = \left| \sum_{i=1}^3 U_{\beta i} e^{-iE_i t} U_{\alpha i}^* \right|^2 \end{aligned} \quad (1.6)$$

The final result for the oscillation probability of the three neutrino flavors at distance  $L$  and energy  $E$  will be:

$$\begin{aligned} P(\nu_\alpha \rightarrow \nu_\beta) &= \delta_{\alpha\beta} - 4 \sum_{i<j} \text{Re} \left[ U_{\alpha i} U_{\beta i}^* U_{\alpha j}^* U_{\beta j} \right] \sin^2 \frac{(m_i^2 - m_j^2)L}{4E} + \\ &\quad + 2 \sum_{i<j} \text{Im} \left[ U_{\alpha i} U_{\beta i}^* U_{\alpha j}^* U_{\beta j} \right] \sin \frac{(m_i^2 - m_j^2)L}{2E} \end{aligned} \quad (1.7)$$

In the simplest case of two neutrino flavors oscillations, the oscillation probability can be presented as follows:

$$P(\nu_\alpha \rightarrow \nu_\beta) = \frac{1}{2} \sin^2(2\theta) \left( 1 - \cos \left( \frac{\Delta m^2}{2E} L \right) \right) = \sin^2(2\theta) \sin^2 \left( \frac{\Delta m^2}{4E} L \right). \quad (1.8)$$

The amplitude of the oscillation only depends on the mixing angle  $\theta$ , and its frequency is a function of  $L/E$ , and it depends on  $\Delta m^2$ . Oscillations only depend on the difference in masses squared  $\Delta m^2$ , so they do not allow for absolute neutrino mass measurements. To directly measure the neutrino mass, experiments utilize the electron capture processes or the kinematics of single  $\beta$ -decays [25]. For example, the KATRIN experiment [26] exploits the

reaction:



Neutrino mass constrains the minimal energy they carry away, leading to a drop in the electron spectrum and the slight distortion of its shape close to the endpoint. Its measurement is a goal of KATRIN.

Because of the  $\sin^2$  dependence, oscillations in a vacuum are only sensitive to the absolute values of  $\Delta m^2$  and, therefore, the neutrino mass ordering  $m_1 < m_2 < m_3$  (normal hierarchy) or  $m_3 < m_1 < m_2$  (inverted hierarchy) is unknown (the scheme of the neutrino mass ordering is shown in Fig. 1.2). Measuring the neutrino mass hierarchy is one of the flagship tasks of current and future neutrino experiments.

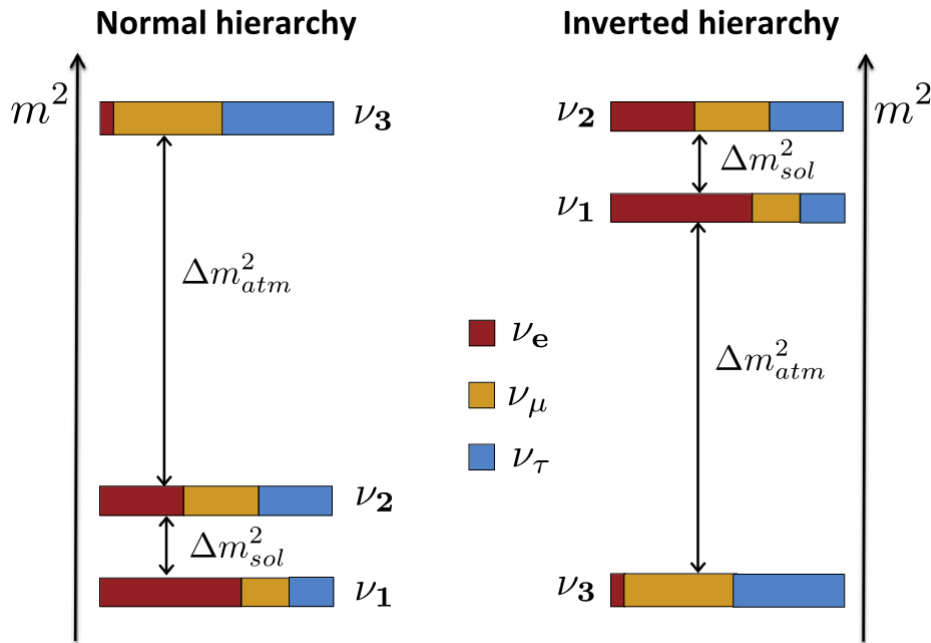


Figure 1.2 Scheme of the two distinct neutrino mass hierarchy. The picture is taken from [27].

In the case of in-medium neutrino propagation, neutrinos can interact with the particles of the medium, especially electrons [28]. To obtain the oscillation probability for the neutrinos propagating through the Earth matter (that is the case for most neutrino experiments), these "matter effects" can be parametrized as if neutrinos in the matter had a different effective mass than neutrinos in a vacuum. For the 2-flavor oscillations, we can write analogously to the oscillations in a vacuum:

$$P_m(\nu_\alpha \rightarrow \nu_\beta) = \sin^2(2\theta_m) \sin^2\left(\frac{\Delta m_m^2 L}{4E}\right), \quad (1.10)$$

where effective  $\Delta m_m^2$  is:

$$\Delta m_m^2 = \Delta m^2 \sqrt{(\Delta V / \Delta m^2 - \cos(2\theta))^2 + \sin^2(2\theta)} \quad (1.11)$$

and the mixing angle:

$$\sin(2\theta_m) = \frac{\sin(2\theta)}{\sqrt{(\Delta V / \Delta m^2 - \cos(2\theta))^2 + \sin^2(2\theta)}} \quad (1.12)$$

In these formulas  $\Delta V$  is the difference of the flavor potentials:  $\Delta V = V_\alpha - V_\beta$ . One can notice that if  $\Delta V / \Delta m^2 = \cos(2\theta)$ ,  $\sin(2\theta_m) = 1$  independently on the mixing angle in vacuum. Therefore, there is such an electron density where oscillations in the matter are maximal, even if the oscillations in the vacuum are small. This effect is known as the *Mikheyev–Smirnov–Wolfenstein* (MSW) effect [28, 29].

The matter effect stems from the charged current interactions that differ for the neutrinos and antineutrinos. Therefore, the matter effect also affects neutrinos and antineutrinos differently, and it is dependent on the sign of  $\Delta m^2$ , and thus on the mass ordering (MO). With a longer baseline, the sensitivity to the MO becomes higher [30]. Figure 1.3 shows the appearance probability of  $\nu_e$  for initial  $\nu_\mu$  in the NOvA [31] experiment. The future experiment DUNE [32] with the 1300 km baseline is expected to determine the neutrino mass ordering.

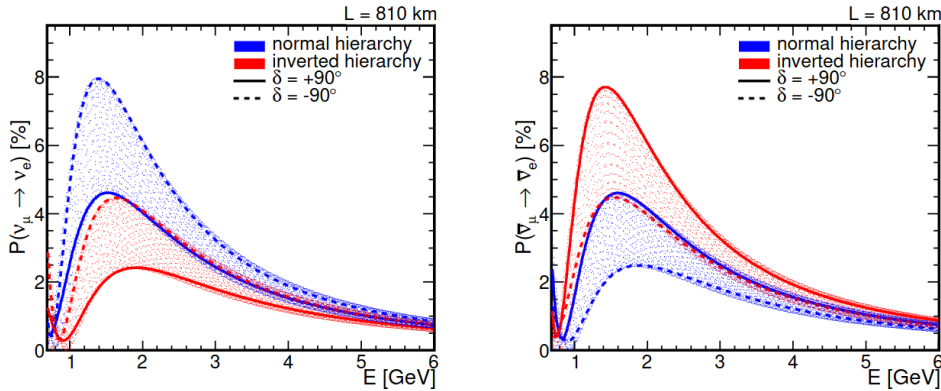


Figure 1.3 Appearance probability of  $\nu_e$  for initial  $\nu_\mu$  as a function of energy  $E$ . Left: neutrinos, right: antineutrinos. The picture is taken from [33].

## 1.2 The definitive experimental establishment of neutrino oscillations

The dominant contribution to the neutrino oscillation discovery was made by the Super-Kamiokande [34], and Sudbury Neutrino Observatory (SNO) [35] experiments. Super-Kamiokande,

a successor of the Kamiokande experiment, could register atmospheric neutrinos from different directions: from directly above and the ones "from below", that traversed the whole Earth. Super-Kamiokande observed that fewer muon neutrinos were coming from directions where neutrinos traveled more (from the bottom). These results suggested that the number of neutrinos of a given flavor depends on the path they travel, which may be a consequence of the transformation of neutrinos from one species to another. SNO involves detecting the three flavors of solar neutrinos in a heavy-water-based detector. The flux of electron solar neutrinos was in disagreement with the model, along the line of previous experimental measurements; however, the flux of the sum of all neutrino types was consistent with the theoretical predictions. The joint efforts of SNO and Super-Kamiokande [36, 37] resulted in the Nobel Prize in 2015 "for the discovery of neutrino oscillations, which shows that neutrinos have mass" [38].

After the discovery of oscillations by the SNO and Super-Kamiokande experiments, neutrino physics became one of the most actively developing areas of particle physics. Fig. 1.4 shows sensitivity to various neutrino energies and oscillation distances of reactor and accelerator neutrino experiments. Experiments are sensitive to the different oscillation parameters depending on the neutrino source, energy, and oscillation distance, so modern neutrino oscillation experiments probe solar, reactor, atmospheric, and accelerator neutrinos.

Reactor neutrino experiments, a very intense source of neutrinos, play a crucial role in measuring neutrino oscillation parameters. The fission products of the chain reaction are neutron-rich and decay through a  $\beta^-$  reaction, producing a flux of the electron antineutrinos. As indicated in Fig. 1.5, a non-zero  $\theta_{13}$  is responsible for the deficit of  $\nu_e$  at  $\sim 1 - 2$  km baseline that is proportional to  $\sin^2(2\theta_{13})$ . At the long distance, these experiments also are sensitive to  $\Delta m_{21}^2$  and  $\theta_{12}$ .

The first generation of the reactor experiments, CHOOZ [40] and PALO VERDE [41] were supposed to measure  $\theta_{13}$  but neither of them observed the  $\nu_e$  deficit, so they only set up an upper limit  $\sin^2(2\theta_{13}) < 0.1$  [40]. The second generation of experiments: Daya Bay, Double CHOOZ, and RENO, achieved great success in measuring the mixing angle  $\theta_{13}$  and  $\Delta m_{32}^2$  keeping a precision record of  $\theta_{13}$  measurement. In Ref. [42] Daya Bay reports  $\sin^2(2\theta_{13}) = 0.0851 \pm 0.0024$ . As one can see from equation 1.4 the measurement of the non-zero mixing angle  $\theta_{13}$  makes it possible to determine  $\delta_{CP}$  using neutrino oscillations in accelerator and atmospheric experiments.

The Jiangmen Underground Neutrino Observatory (JUNO) [43, 44], a 20 kton liquid-scintillator detector, will continue the reactor antineutrino measurements program started in China by the Daya Bay experiment. It is located 53 km from the Yangjiang and Taishan nuclear power plants, optimized to reach the maximal sensitivity to the neutrino mass ordering determination. With high statistics and good resolution, it aims to determine MO at  $3 - 4\sigma$

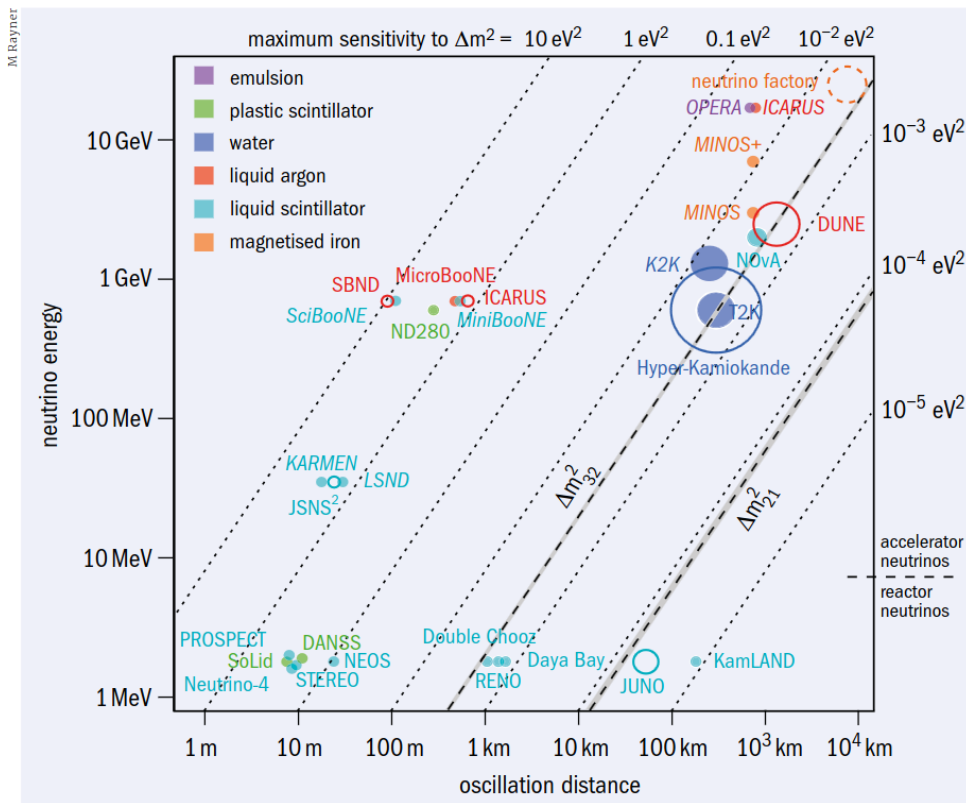


Figure 1.4 Neutrino-oscillation experiments using neutrinos from nuclear reactors or accelerator beams as a function of the distance from source to detector and the peak energy of the neutrinos. Open markers indicate future projects (for detectors above 5 kton, the area of the marker is proportional to the detector mass), and italics indicate completed experiments. The experiments are colored according to the target material. The picture is taken from Ref. [39].

significance within 6 years of data taking. While neutrino MO determination is its primary goal [44], having a longer oscillation baseline, it will be sensitive to  $\theta_{12}$  and  $\Delta m_{21}^2$ .

Solar neutrinos are mainly created through the  $pp$  chain and CNO cycle. The spectrum of solar neutrinos is shown in Fig. 1.6. For solar experiments, the sensitivity to oscillation parameters appears primarily due to the MSW effect in the Sun. SNO and Super-Kamiokande experiments significantly contributed to the precision measurements of the  $\theta_{12}$  and  $\Delta m_{21}^2$ . The SNO detector consisted of a 6-meter-radius acrylic vessel filled with 1,000 tonnes of heavy water. Its detector threshold allowed for the detection of neutrinos from the  $B^8$  and  $hep$ -reactions. Heavy water was an excellent feature that allowed for detecting all three types through elastic scattering on electrons of all types of neutrinos and the charged current interactions of electron neutrinos and neutral current interactions with deuterium. The Super-Kamiokande experiment is also sensitive to the neutrinos from the  $B^8$  reactions. Super-Kamiokande discovered the day/night asymmetry in the solar neutrino measurements, proving that oscillations of solar neutrinos are affected by the terrestrial matter effect [45]. Precise measurement of the  $\theta_{12}$  and  $\Delta m_{21}^2$  parameters with only solar neutrino measurements was challenging due to the

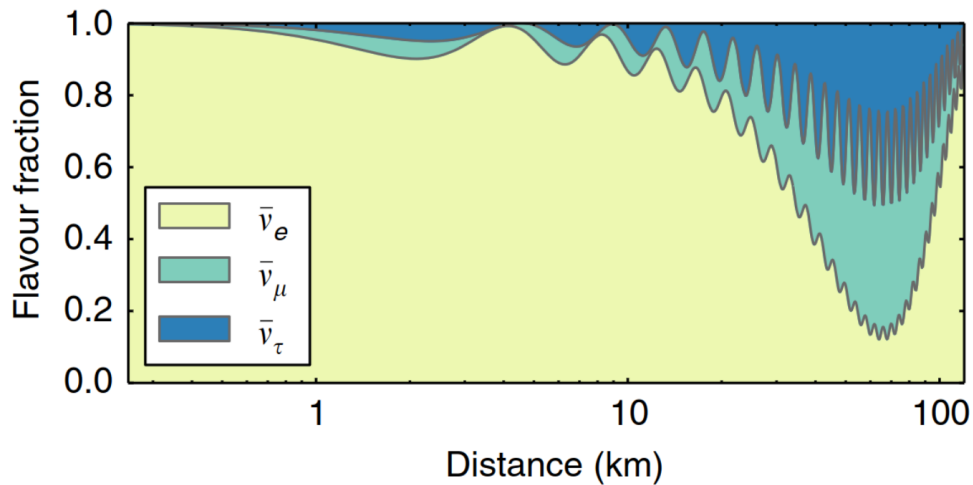


Figure 1.5 Expected flavor composition of the reactor neutrino flux for 4 MeV neutrinos as a function of distance to the reactor cores. The picture is taken from Ref. [23].

large uncertainty in the solar neutrino flux predicted by the Standard Solar Model, the strong matter effect inside the Sun, and the great distance the neutrinos travel. These challenges can be overcome by studying the same oscillation parameters from another source.

The KamLAND [47] experiment measured the  $\bar{\nu}_e$  spectrum from 55 reactors at the mean distance of 180 km. Its result confirmed the solar neutrino measurements of neutrino oscillations. Combined with the solar neutrino measurements,  $\theta_{12}$  and  $\Delta m_{21}^2$  became one of the most precisely measured oscillation parameters. It was also the first experiment to register the geoneutrino (neutrino emitted in radioactive isotope decay inside Earth) [48].

An accelerator neutrino beam is produced by colliding the proton beam with a fixed target, producing mesons (primarily pions) that later decay and produce neutrinos. The KEK to Kamioka (K2K) experiment [49] in Japan used a beam of muon neutrinos and consisted of the two detectors: near (300 meters from the target) and far (Super-Kamiokande at 250 km). The main task of the near detector was to determine the beam parameters while the far detector recorded its changes. K2K observed the disappearance of the muon neutrino flux, confirming neutrino oscillations with the parameters obtained in the Super-Kamiokande experiment with atmospheric neutrinos [50]. The Main Injector Neutrino Oscillation Search (MINOS) [51]—accelerator experiment in the USA—used a muon neutrino beam, and as K2K consisted of two near and far detectors (at the distance of 735 km). MINOS also observed the muon neutrino disappearance and confirmed oscillations of neutrinos with "atmospheric" parameters [52].

The IceCube experiment [53] located at the South Pole consist of the 86 strings with 60 spherical optical sensors each located under the Antarctic ice in a  $1 \text{ km}^3$  volume. There is also an internal DeepCore [54] part consisting of 8 strings with increased density. Although

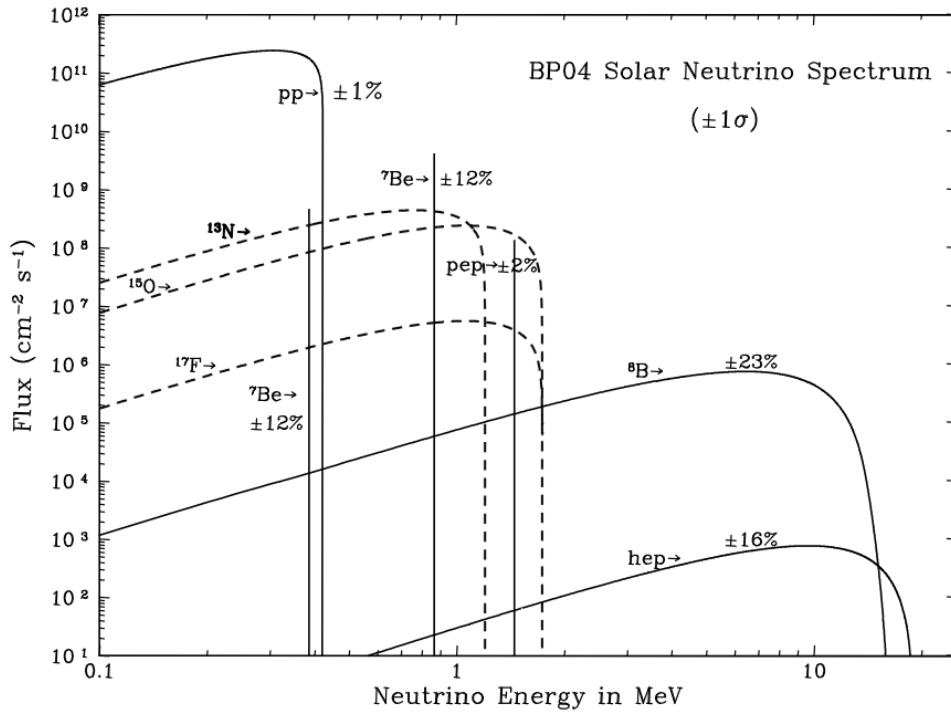


Figure 1.6 The predicted solar neutrino energy spectrum. The picture is taken from Ref. [46].

aimed at recording astrophysical neutrinos, also measures oscillation parameters, having started a data taking in 2011 [55]. With the DeepCore, IceCube is sensitive to  $\theta_{23}$  and  $\Delta m_{32}^2$ .

### 1.3 Present and future of long-baseline neutrino experiments at accelerators

The main objective of the accelerator neutrino experiments, which are the focus of this thesis and will be covered in detail in Chapter 2, is the determination of the  $\theta_{23}$  mixing angle,  $\Delta m_{32}^2$ , and the CP-violation phase  $\delta_{CP}$ . Accelerator neutrinos propagate through the Earth matter inducing matter effect, also allowing for the mass ordering measurements. Modern neutrino acceleration experiments employ a two-detector scheme to reduce systematic uncertainties. In addition to the far detectors, measurements are also carried out in the near detectors, placed near the neutrino source before any standard neutrino oscillation can occur, and designed to characterize the neutrino flux and to measure the neutrino-nucleus cross section to tune the interaction models and minimize the corresponding uncertainties.

There are currently two operating neutrino accelerator experiments: T2K [56] and NOvA [31]. In Fig. 1.7 we present the main T2K results [57] with the electron neutrino (antineutrino) appearance measured by Super-Kamiokande and the  $\delta_{CP}$  phase measurement that excludes some of its values at three standard deviations ( $3\sigma$ ).

The CP violation occurs if the oscillation probability for neutrinos and antineutrinos is different  $P(\nu_\alpha \rightarrow \nu_\beta) \neq P(\bar{\nu}_\alpha \rightarrow \bar{\nu}_\beta)$ . The oscillation probability for antineutrinos can be written the same way as in equation 1.7, but with the minus sign before the the last term. The Jarlskog invariant for the PMNS matrix is:

$$J \equiv \text{Im} \left[ U_{\alpha i} U_{\beta i}^* U_{\alpha j}^* U_{\beta j} \right] = \frac{1}{8} \cos(\theta_{13}) \sin(2\theta_{23}) \sin(2\theta_{13}) \sin(\delta) \quad (1.13)$$

Assuming  $\Delta m_{21}^2 \ll \Delta m_{32}^2$ , we can write the difference of the oscillation probabilities as:

$$P(\nu_\alpha \rightarrow \nu_\beta) - P(\bar{\nu}_\alpha \rightarrow \bar{\nu}_\beta) \simeq \pm 8J \left( \frac{\Delta m_{21}^2 L}{2E} \right) \sin^2 \left( \frac{\Delta m_{31}^2 L}{4E} \right) \sin(\delta) \quad (1.14)$$

$P(\nu_\alpha \rightarrow \nu_\beta) + P(\bar{\nu}_\alpha \rightarrow \bar{\nu}_\beta)$  is dependent on  $\cos(\delta)$ , but the real components are dominant. Therefore the final neutrino-antineutrino asymmetry:

$$A_{CP} = \frac{P(\nu_\alpha \rightarrow \nu_\beta) - P(\bar{\nu}_\alpha \rightarrow \bar{\nu}_\beta)}{P(\nu_\alpha \rightarrow \nu_\beta) + P(\bar{\nu}_\alpha \rightarrow \bar{\nu}_\beta)} \propto \sin(\delta_{CP})$$

Within the next decade, the next generation of the experiments: DUNE [32] in USA and Hyper-Kamiokande [58] in Japan will start data taking. They aim to establish mass ordering and possibly discover charge-parity violation with  $5\sigma$  significance, as well as to measure the value of the CP-parameterizing phase with a precision better than 15 degrees. The unprecedented statistics of produced and detected neutrinos, acquired with new beams and next generation far detectors, will enable such results, requiring an exceptionally robust and precise control of systematic uncertainties and therefore new near detectors.

The most significant and complex systematic uncertainty in present neutrino long-baseline experiments stems from the modeling of neutrino-nucleus interactions. To address the challenge of improved precision, the long-baseline experiments are moving from inclusive analysis, focused on the leptonic part of the neutrino-nucleus interaction final state, to exclusive analysis, including the hadronic component of the final state. To this aim, relatively new technologies for the field, like using liquid Argon Time Projection Chambers in the SBN program [59], or the highly granular scintillator detector as the target of the upgrade of the T2K near detector [60], are being deployed. The aim is to use a detailed and precise measurement of the hadronic final state to improve the understanding of nuclear effects. Notably, the exclusive reconstruction of the hadronic part of the final state of neutrino-nucleus interactions permits a more precise reconstruction of the neutrino energy on an event-by-event basis. Yet, it poses new challenges in the modeling of such interactions. We need precise simulations of the nuclear effects on the final-state nucleons to fully benefit from the improved detector capabilities.

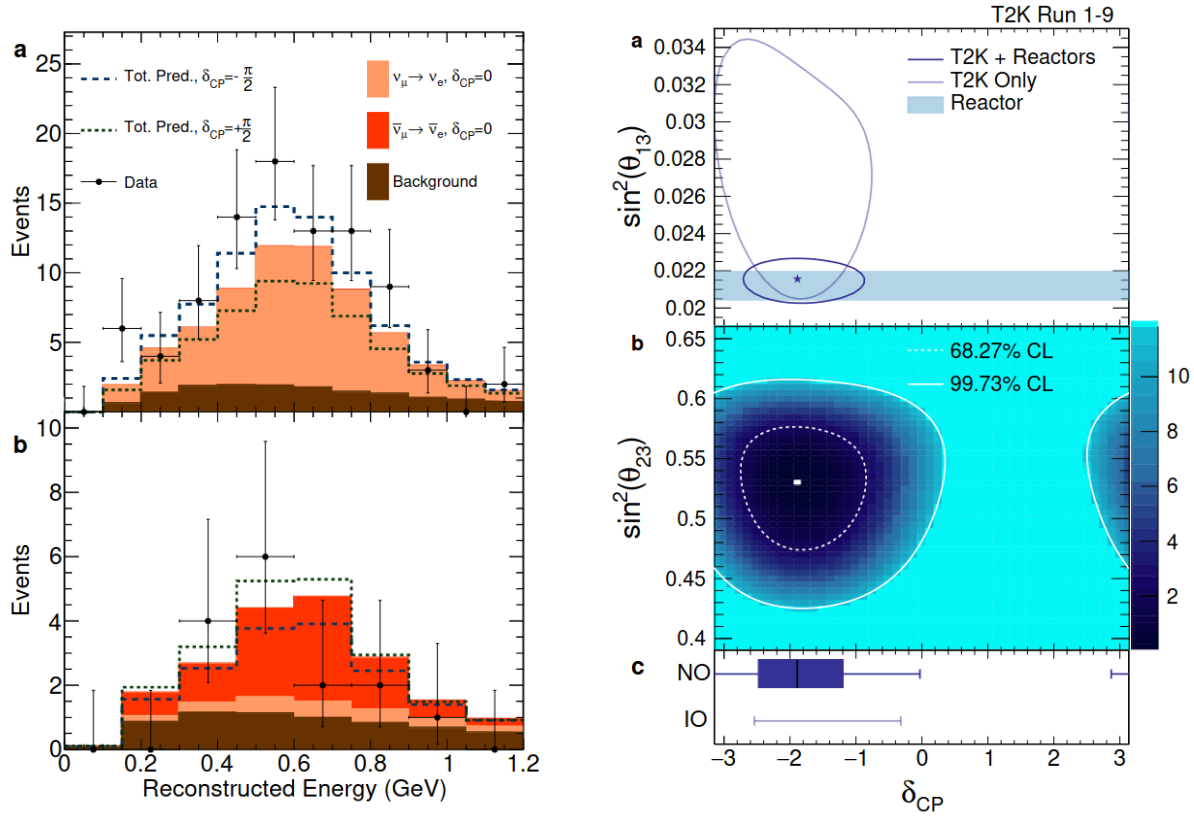


Figure 1.7 Left: the reconstructed neutrino energy spectra for the SK samples containing electron-like events in neutrino-mode **(a)** or antineutrino-mode **(b)** beam running. The solid stacked chart corresponds to  $\delta_{CP}=0$ , and the dashed lines represent predictions of the total predicted number of events for the two extreme CP-violating cases. Right: constraints on PMNS oscillation parameters  $\theta_{13}$  and  $\theta_{23}$ . The plots are taken from Ref. [57].

## 1.4 Thesis outline

The study presented here aims to evaluate in detail the possible uncertainties inherent to the FSI simulation in neutrino-nucleus scattering. This study is also a step toward a more precise and complete implementation of FSI effects in Monte Carlo simulations of neutrino-nucleus interactions. Given the needs of running experiments, notably the analysis of the data from the upgraded ND280, we focus on final state interactions (FSI) modeling with currently available and new tools. This thesis presents the study of FSI with two different nuclear models implemented in the IntraNuclear Cascade Liège (INCL) code [61–64], a new tool for the neutrino physics, and NuWro [65]. Fundamental neutrino-nucleus interactions without pion production are studied, where pions in the final state can only be produced through nucleon FSI.

In chapter 2, we present a context of the long baseline neutrino experiments, providing their technical design, history, and goals of the current and future experiments. Focusing on

the T2K experiment, we also describe the T2K near detector upgrade. Chapter 3 overviews the neutrino-nucleus interaction simulation, providing details about neutrino reaction modes, nuclear models that describe the nuclear target, and final state interaction simulation. It also provides an overview of the widely-used Monte-Carlo neutrino event generators. Chapter 4 describes in detail the INCL code and its coupling to the de-excitation models, focusing on the ABLA de-excitation code. This chapter finishes with an ongoing effort for the implementation of the CCQE neutrino-nucleus interaction in INCL. Chapter 5 contains the main results of the INCL and NuWro neutrino and antineutrino simulation comparison. We study different variables to characterize and quantify the impact of FSI on the kinematics of the leading nucleon, particle type, multiplicity, and on vertex activity. In chapter 6, we push further the INCL study by coupling INCL with ABLA. We study the kinematics of the particles produced in de-excitation and provide a comparison of the neutrino energy reconstruction resolution for the events simulated with NuWro, INCL, and INCL+ABLA. Chapter 7 focuses on the study of the experimentally observable variables. We compare the NuWro, INCL, and INCL+ABLA models to various T2K and MINERvA measurements of the kinematics of the leading proton. Then we describe in detail the simulation of the propagation of the nuclear clusters inside the detector. We study their observability and possible misidentification with protons and calculate the vertex activity for different simulations. In this chapter, we also focus on the neutron secondary interactions. Results of chapters 5 and 7, covering comparison of the INCL and NuWro leading proton kinematics, single transverse variables (STV), and comparison to T2K and MINERvA data, are published in Ref. [66]. The last chapter 8 contains work performed for the ND280 upgrade: electronics calibration for the new Time Projection Chambers (TPC) and the studies of the distortions of the track image in the TPC module in the presence of the non-uniform magnetic field ( $E \times B$  effect). The results covered in this chapter have been partially published in Refs. [67] and [68].

## References

- [1] *The atomists, Leucippus and Democritus: fragments, a text and translation with a commentary* by C.C.W. Taylor. University of Toronto Press Incorporated, 1999.
- [2] A.J. Rocke. *In Search of El Dorado: John Dalton and the Origins of the Atomic Theory*. Johns Hopkins University Press, 2005.
- [3] J. J. Thomson. “Cathode rays”. In: *Phil. Mag. Ser. 5* 44 (1897), pp. 293–316.
- [4] Friedrich Lenz. “The Ratio of Proton and Electron Masses”. In: *Phys. Rev.* 82 (4 1951), pp. 554–554.
- [5] Henri Becquerel. “On the rays emitted by phosphorescence”. In: *Compt. Rend. Hebd. Seances Acad. Sci.* 122.8 (1896), pp. 420–421.
- [6] E. Rutherford. “The scattering of alpha and beta particles by matter and the structure of the atom”. In: *Phil. Mag. Ser. 6* 21 (1911), pp. 669–688.
- [7] Albert Einstein and Leopold Infeld. *The evolution of Physics. the growth of ideas from early concepts to relativity and quanta*. Vol. 4. 1938.
- [8] A. Einstein. “Über die vom Relativitätsprinzip geforderte Trägheit der Energie”. In: *Annalen Phys.* 23.7 (1907), pp. 371–384.
- [9] Albert Einstein. “The foundation of the general theory of relativity.” In: *Annalen Phys.* 49.7 (1916). Ed. by Jong-Ping Hsu and D. Fine, pp. 769–822.
- [10] Albert Einstein. “Zur Quantentheorie der Strahlung”. In: *Phys. Z.* 18 (1917), pp. 121–128.
- [11] J. Chadwick. “The intensity distribution in the magnetic spectrum of beta particles from radium (B + C)”. In: *Verh. Phys. Gesell.* 16 (1914), pp. 383–391.
- [12] W. Pauli. “Dear radioactive ladies and gentlemen”. In: *Phys. Today* 31N9 (1978), p. 27.
- [13] C. L. Cowan et al. “Detection of the free neutrino: A Confirmation”. In: *Science* 124 (1956), pp. 103–104.
- [14] Raymond Davis Jr. “Attempt to detect the antineutrinos from a nuclear reactor by the Cl37(anti-nu,e-) A37 reaction”. In: *Phys. Rev.* 97 (1955), pp. 766–769.
- [15] John N. Bahcall and R. Davis. “Solar Neutrinos - a Scientific Puzzle”. In: *Science* 191 (1976), pp. 264–267.
- [16] J. N. Abdurashitov et al. “Measurement of the solar neutrino capture rate with gallium metal”. In: *Phys. Rev. C* 60 (1999), p. 055801. arXiv: astro-ph/9907113.
- [17] J. N. Abdurashitov et al. “Solar neutrino flux measurements by the Soviet-American Gallium Experiment (SAGE) for half the 22 year solar cycle”. In: *J. Exp. Theor. Phys.* 95 (2002), pp. 181–193. arXiv: astro-ph/0204245.

- [18] W. Hampel et al. “GALLEX solar neutrino observations: Results for GALLEX IV”. In: *Phys. Lett. B* 447 (1999), pp. 127–133.
- [19] B. Pontecorvo. “Neutrino Experiments and the Problem of Conservation of Leptonic Charge”. In: *Zh. Eksp. Teor. Fiz.* 53 (1967), pp. 1717–1725.
- [20] Ziro Maki, Masami Nakagawa, and Shoichi Sakata. “Remarks on the Unified Model of Elementary Particles”. In: *Progress of Theoretical Physics* 28.5 (Nov. 1962), pp. 870–880. eprint: <https://academic.oup.com/ptp/article-pdf/28/5/870/5258750/28-5-870.pdf>.
- [21] V. Gribov and B. Pontecorvo. “Neutrino astronomy and lepton charge”. In: *Physics Letters B* 28.7 (1969), pp. 493–496.
- [22] R. L. Workman et al. “Review of Particle Physics”. In: *PTEP* 2022 (2022), p. 083C01.
- [23] P. Vogel, L. J. Wen, and C. Zhang. “Neutrino oscillation studies with reactors”. In: *Nature Communications* 6.1 (2015), p. 6935.
- [24] C. Jarlskog. “Commutator of the Quark Mass Matrices in the Standard Electroweak Model and a Measure of Maximal  $CP$  Nonconservation”. In: *Phys. Rev. Lett.* 55 (1985), p. 1039.
- [25] M. Aker et al. “Direct neutrino-mass measurement with sub-electronvolt sensitivity”. In: *Nature Physics* 18.2 (2022), pp. 160–166.
- [26] A. Osipowicz et al. “KATRIN: A Next generation tritium beta decay experiment with sub-eV sensitivity for the electron neutrino mass. Letter of intent”. In: (Sept. 2001). arXiv: hep-ex/0109033.
- [27] S Adrián-Martínez et al. “Letter of intent for KM3NeT 2.0”. In: *Journal of Physics G: Nuclear and Particle Physics* 43.8 (2016), p. 084001.
- [28] L. Wolfenstein. “Neutrino oscillations in matter”. In: *Phys. Rev. D* 17 (9 1978), pp. 2369–2374.
- [29] S. P. Mikheyev and A. Yu. Smirnov. “Resonance Amplification of Oscillations in Matter and Spectroscopy of Solar Neutrinos”. In: *Sov. J. Nucl. Phys.* 42 (1985), pp. 913–917.
- [30] Sara Bolognesi. “Neutrino Physics with Particle Beams”. In: *PoS EPS-HEP2021* (2022), p. 042.
- [31] D. S. Ayres et al. “NOvA: Proposal to Build a 30 Kiloton Off-Axis Detector to Study  $\nu_\mu \rightarrow \nu_e$  Oscillations in the NuMI Beamline”. In: (Mar. 2004). arXiv: hep-ex/0503053.
- [32] B. Abi et al. *Deep Underground Neutrino Experiment (DUNE), Far Detector Technical Design Report, Volume II: DUNE Physics*. 2020.

- [33] Tomas Nosek. “Effects of Matter in Neutrino Oscillations and Determination of Neutrino Mass Hierarchy at Long-baseline Experiments”. Other thesis. Dec. 2016. arXiv: 1612.09132 [hep-ph].
- [34] Y. Fukuda et al. “The Super-Kamiokande detector”. In: *Nucl. Instrum. Meth. A* 501 (2003). Ed. by V. A. Ilyin, V. V. Korenkov, and D. Perret-Gallix, pp. 418–462.
- [35] J. Boger et al. “The Sudbury neutrino observatory”. In: *Nucl. Instrum. Meth. A* 449 (2000), pp. 172–207. arXiv: nucl-ex/9910016.
- [36] Q. R. Ahmad et al. “Direct Evidence for Neutrino Flavor Transformation from Neutral-Current Interactions in the Sudbury Neutrino Observatory”. In: *Phys. Rev. Lett.* 89 (1 2002), p. 011301.
- [37] Y. Fukuda et al. “Evidence for oscillation of atmospheric neutrinos”. In: *Phys. Rev. Lett.* 81 (1998), pp. 1562–1567. arXiv: hep-ex/9807003.
- [38] <https://www.nobelprize.org/prizes/physics/2015/summary/>.
- [39] M. Rayner. “Tuning in to neutrinos”. In: *CERN COURIER* (2020).
- [40] M. Apollonio et al. “Limits on neutrino oscillations from the CHOOZ experiment”. In: *Physics Letters B* 466.2-4 (1999), pp. 415–430.
- [41] A. Piepke. “Final results from the Palo Verde neutrino oscillation experiment”. In: *Prog. Part. Nucl. Phys.* 48 (2002). Ed. by A. Faessler, pp. 113–121.
- [42] F. P. An et al. “Precision measurement of reactor antineutrino oscillation at kilometer-scale baselines by Daya Bay”. In: (Nov. 2022). arXiv: 2211.14988 [hep-ex].
- [43] Angel Abusleme et al. “JUNO physics and detector”. In: *Prog. Part. Nucl. Phys.* 123 (2022), p. 103927. arXiv: 2104.02565 [hep-ex].
- [44] Fengpeng An et al. “Neutrino Physics with JUNO”. In: *J. Phys. G* 43.3 (2016), p. 030401. arXiv: 1507.05613 [physics.ins-det].
- [45] A. Renshaw et al. “First Indication of Terrestrial Matter Effects on Solar Neutrino Oscillation”. In: *Phys. Rev. Lett.* 112 (9 2014), p. 091805.
- [46] J N Bahcall. “Solar Models and Solar Neutrinos”. In: *Physica Scripta* T121 (2005), pp. 46–50.
- [47] S. Abe et al. “Precision Measurement of Neutrino Oscillation Parameters with KamLAND”. In: *Phys. Rev. Lett.* 100 (2008), p. 221803. arXiv: 0801.4589 [hep-ex].
- [48] T. Araki et al. “Experimental investigation of geologically produced antineutrinos with KamLAND”. In: *Nature* 436 (2005), pp. 499–503.
- [49] M. H. Ahn et al. “Measurement of Neutrino Oscillation by the K2K Experiment”. In: *Phys. Rev. D* 74 (2006), p. 072003. arXiv: hep-ex/0606032.

- 
- [50] M. H. Ahn et al. “Indications of neutrino oscillation in a 250 km long baseline experiment”. In: *Phys. Rev. Lett.* 90 (2003), p. 041801. arXiv: hep-ex/0212007.
- [51] E. Ables et al. “P-875: A Long baseline neutrino oscillation experiment at Fermilab”. In: (Feb. 1995).
- [52] P. Adamson et al. “Improved search for muon-neutrino to electron-neutrino oscillations in MINOS”. In: *Phys. Rev. Lett.* 107 (2011), p. 181802. arXiv: 1108.0015 [hep-ex].
- [53] M.G. Aartsen et al. “The IceCube Neutrino Observatory: instrumentation and online systems”. In: *Journal of Instrumentation* 12.03 (2017), P03012–P03012.
- [54] R. Abbasi et al. “The Design and Performance of IceCube DeepCore”. In: *Astropart. Phys.* 35 (2012), pp. 615–624. arXiv: 1109.6096 [astro-ph.IM].
- [55] M. G. Aartsen et al. “Measurement of Atmospheric Neutrino Oscillations with IceCube”. In: *Physical Review Letters* 111.8 (2013).
- [56] K. Abe et al. “The T2K Experiment”. In: *Nucl. Instrum. Meth. A* 659 (2011), pp. 106–135. arXiv: 1106.1238 [physics.ins-det].
- [57] K. Abe et al. “Constraint on the matter–antimatter symmetry-violating phase in neutrino oscillations”. In: *Nature* 580.7803 (2020), pp. 339–344.
- [58] Hyper-Kamiokande Proto-Collaboration: K. Abe et al. *Hyper-Kamiokande Design Report*. 2018.
- [59] Jonathan Asaadi et al. “A New Concept for Kilotonne Scale Liquid Argon Time Projection Chambers”. In: *Instruments* 4.1 (2020).
- [60] K. Abe et al. “T2K ND280 Upgrade - Technical Design Report”. In: (Jan. 2019). arXiv: 1901.03750 [physics.ins-det].
- [61] Alain Boudard et al. “New potentialities of the Liège intranuclear cascade model for reactions induced by nucleons and light charged particles”. In: *Phys. Rev. C* 87.1 (2013), p. 014606. arXiv: 1210.3498 [nucl-th].
- [62] Davide Mancusi et al. “Extension of the Liège intranuclear-cascade model to reactions induced by light nuclei”. In: *Phys. Rev. C* 90.5 (2014), p. 054602. arXiv: 1407.7755 [nucl-th].
- [63] Jose Luis Rodríguez-Sánchez et al. “Improvement of one-nucleon removal and total reaction cross sections in the Liège intranuclear-cascade model using Hartree-Fock-Bogoliubov calculations”. In: *Phys. Rev. C* 96.5 (2017), p. 054602.
- [64] J. Hirtz et al. “Parametrization of cross sections for elementary hadronic collisions involving strange particles”. In: *Eur. Phys. J. Plus* 133.10 (2018), p. 436. arXiv: 1805.01655 [nucl-th].

- 
- [65] Tomasz Golan, Cezary Juszczak, and Jan T. Sobczyk. “Final State Interactions Effects in Neutrino-Nucleus Interactions”. In: *Phys. Rev. C* 86 (2012), p. 015505. arXiv: 1202.4197 [nucl-th].
- [66] A. Ershova et al. “Study of final-state interactions of protons in neutrino-nucleus scattering with INCL and NuWro cascade models”. In: *Phys. Rev. D* 106.3 (2022), p. 032009. arXiv: 2202.10402 [hep-ph].
- [67] D. Attié et al. “Characterization of Charge Spreading and Gain of Encapsulated Resistive Micromegas Detectors for the Upgrade of the T2K Near Detector Time Projection Chambers”. In: (Mar. 2023). arXiv: 2303.04481 [physics.ins-det].
- [68] D. Attié et al. “Analysis of test beam data taken with a prototype of TPC with resistive Micromegas for the T2K Near Detector upgrade”. In: (Dec. 2022). arXiv: 2212.06541 [physics.ins-det].

# 2

## Neutrino long baseline experiments: T2K and beyond

This chapter covers in detail the work principles of the long baseline neutrino experiments and the challenges they face. Section 2.1 presents the production of the neutrino beam, the history of the long-baseline accelerator experiments, and their current perspectives. Sections 2.2 and 2.3 describe, respectively, the T2K experiment and the on-going upgrade of its near detector. Section 2.4 provides a perspective on the future long-baseline neutrino experiments DUNE and Hyper-Kamiokande.

### 2.1 Long-baseline accelerator experiments

Neutrino oscillations depend on the distance between the production and detection of neutrinos and on the neutrino energy. Experiments that study neutrinos produced in the Sun or atmosphere cannot control or tune these parameters. In reactor neutrino experiments, one can choose the distance from the neutrino source, but the decay of the reactor fuel will dictate the energy spectrum. On the other hand, in long-baseline experiments we can control the energy of accelerator-produced neutrinos and the distance (baseline) between the source and the detector. Such parameters could be therefore tuned to provide the maximal oscillation probability (and possibly explore its dependence on baseline and energy). This concept, independently proposed by M. Schwarz [1] and B. Pontecorvo [2], was used for the first time in the experiment that proved the existence of two neutrino types in the 1960s [3]. Modern accelerator neutrino experiments perform measurements of neutrino oscillations with unprecedented precision.

To create a flux of neutrinos, the high-intensity proton beam impinges on a target to create the secondary charged mesons ( $\pi$  and K) that then produce neutrinos by their decay. The

charge of the secondary mesons is chosen by magnetic horns, allowing one to select a neutrino or antineutrino beam. For example, for the muon neutrino beam, the main decay modes of the  $\pi$  and  $K$  mesons are  $\pi^+ \rightarrow \mu^+ \nu_\mu$  with the subsequent  $\mu^+ \rightarrow e^+ \nu_e \bar{\nu}_\mu$ ; and  $K^+ \rightarrow \pi^+ \nu_\mu$  and  $K_L \rightarrow \pi^+ e^- \nu_e$ . In the end the beam consists mostly of muon neutrinos. There is also a small ( $\sim 0.5 - 1\%$ ) admixture of electron neutrinos and muon antineutrinos from the meson decay (see, for example [4]). Fig. 2.1 shows the example of the beam produced at JPARC for the T2K experiment.

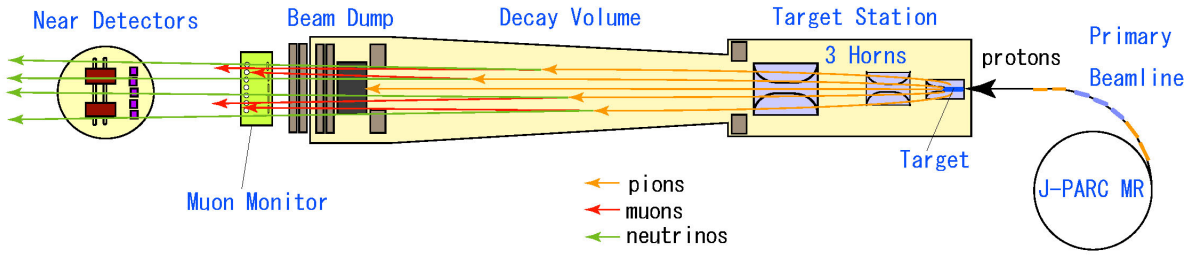


Figure 2.1 The schematic view of the T2K beamline.

The probability that  $\nu_\mu$  will oscillate to  $\nu_e$  is (we use the 2-flavor oscillation probability for simplicity):

$$P(\nu_\mu \rightarrow \nu_e) = \sin^2 2\theta_{23} \sin^2 \left( \frac{\Delta m_{32}^2 L}{4E} \right) \quad (2.1)$$

Therefore, long-baseline experiments measure precisely  $\Delta m_{32}^2$  and  $\theta_{23}$ . The oscillation probability depends on the baseline  $L$  and neutrino energy  $E$ , so the experimental design (neutrino flux energy and baseline) is optimized to detect neutrinos at the maximum oscillation probability.

Neutrino long-baseline experiments are also sensitive to the CP-violation. CP-asymmetry can be calculated as follows:

$$A_{CP} = \frac{P_{\nu_\mu \rightarrow \nu_e} - P_{\bar{\nu}_\mu \rightarrow \bar{\nu}_e}}{P_{\nu_\mu \rightarrow \nu_e} + P_{\bar{\nu}_\mu \rightarrow \bar{\nu}_e}} \propto \sin(\delta_{CP}) \quad (2.2)$$

and therefore needs to be measured in experiments with both neutrino and antineutrino beam operation modes. Long baseline experiments are also sensitive to  $\theta_{13}$  (with less precision than reactor experiments) and to the sign of  $\Delta m_{32}^2$  (i.e., mass ordering, MO) through the measurement of matter effects. Matter effects stem from the charged-current interaction with Earth medium and differ for neutrinos and antineutrinos. They depend on the sign of the  $\Delta m_{32}^2$ , allowing for Mass Ordering (MO) studies. The longer the baseline of the experiment, the more measurements are affected by the matter effects and, therefore, the largest is the sensitivity to MO [5].

The story of accelerator neutrino experiments started from K2K [6]. The neutrino beam was created by the 12 GeV proton accelerator in KEK, Tsukuba (Japan). Neutrinos were registered in the far detector Super-Kamiokande located 250 km away. It was the first experiment that had the neutrino source under control. Before, scientists relied on neutrinos from Sun or other cosmic sources. The oscillation parameters measured by K2K were in agreement with the Super-Kamiokande measurements. T2K—the successor of K2K—started data taking in 2010. The detailed structure of the T2K detector will be described in the next section. T2K uses, again, Super-Kamiokande as far detector. T2K discovered in 2013 the appearance of electron neutrinos in a muon neutrino flux (demonstrating the non-zero value of the  $\theta_{13}$  angle) [7]. T2K also published in 2020 on Nature cover the first  $3\sigma$  limits on the degree of CPV, showing first hints for maximal CPV [8].

Another long baseline neutrino experiment, OPERA [9], took neutrino data from 2008 to 2012. Its goal was the study of the  $\nu_\mu \rightarrow \nu_\tau$  oscillations. The baseline from the neutrino source at CERN to the detector in the Gran Sasso laboratory (Italy) was 732 km. Thanks to the nuclear emulsions used in the detector, OPERA had an outstanding spatial resolution of  $\sim 1 \mu\text{m}$  that was essential for the  $\tau$ -lepton detection. OPERA discovered  $\nu_\mu \rightarrow \nu_\tau$  oscillations with the  $6.1\sigma$  significance [10].

Another facility to study the properties of neutrino oscillations is at Fermilab, USA. The first accelerator experiment at Fermilab was MINOS [11], working from 2005 to 2016. The far detector was located 735 km away. The beam energy was 3 GeV, which was later upgraded to 7 GeV (MINOS+). The far detector also allowed the studies with atmospheric neutrinos.

NOvA [12] has continued the MINOS program starting the data-taking in 2014. The far detector consists of PVC cells filled with liquid scintillator, allowing for both muon and electron neutrinos detection. Thanks to the long baseline (810 km, peak neutrino energy is 1.8 GeV), NOvA has sensitivity to mass ordering at the expense of a degraded sensitivity to CPV, due to degeneracy between the two effects on neutrino oscillation observables.

The studies of neutrino oscillations with accelerator-produced neutrinos will continue with the future programs of Hyper-Kamiokande and DUNE that will be discussed in detail in section 2.4. Fig. 2.2 summarises the history of the long baseline neutrino experiments.

The future measurements at long-baseline neutrino oscillation experiments demand detailed control of the systematic uncertainties due to imperfect knowledge of neutrino flux and neutrino interaction cross section. The strategy used in current experiments (T2K and NOvA) is to use a Near Detector complex located a few hundred meters from the neutrino source to reduce uncertainties on the neutrino flux and neutrino cross section. NOvA utilizes a near detector composed of the same material as the far detector, while T2K uses various target materials for the near and far detectors.

In the combination of near and far detector measurement for the extraction of neutrino oscillations, there are two dominant challenges: the neutrino energy flux differs before and

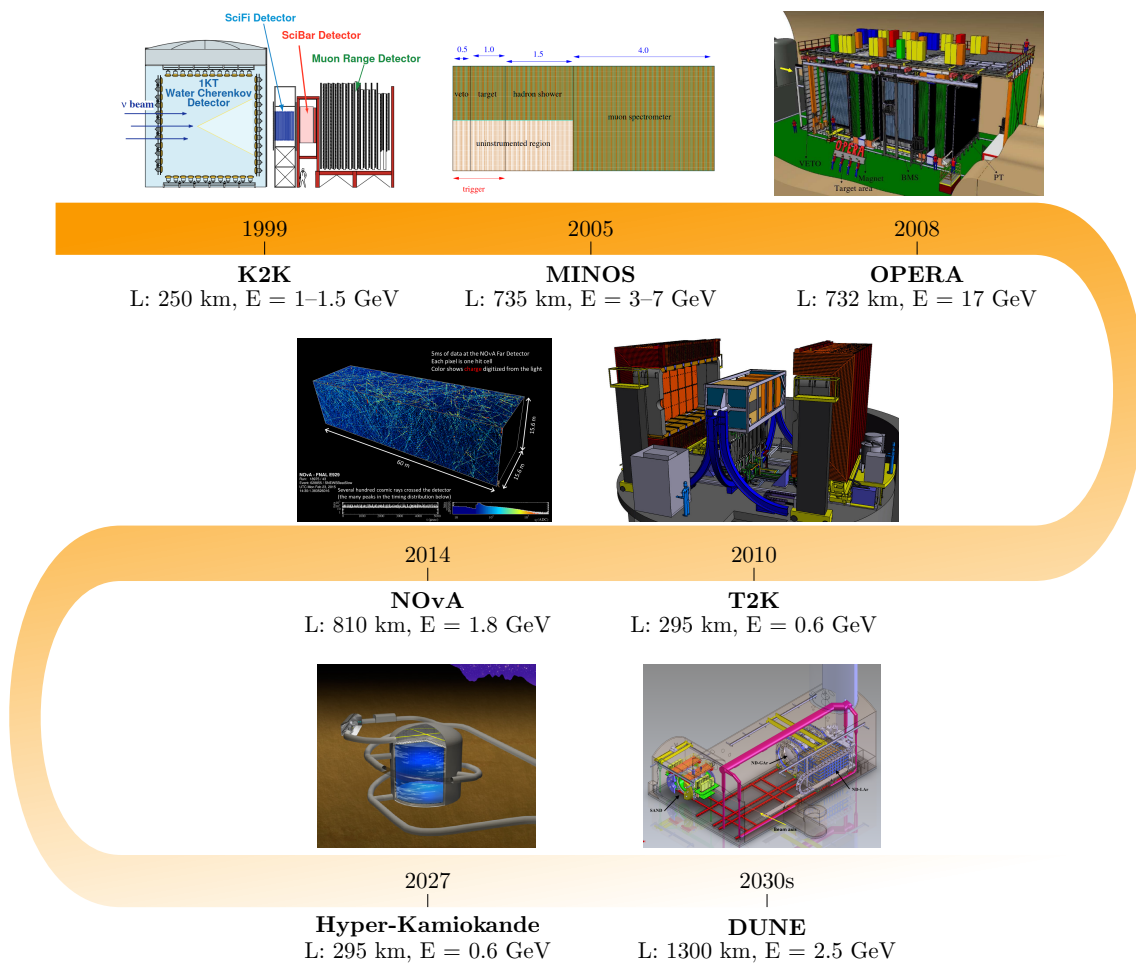


Figure 2.2 Timeline of the long-baseline neutrino experiments. The baseline  $L$  and the peak neutrino energy  $E$  are indicated. For all the experiments the schematic views of the near detectors are shown, but for the Hyper-Kamiokande detector, the far detectors scheme is used since the near detector will be an upgraded near detector facility used by T2K. The figures were adapted from [13–19].

after oscillation, and the neutrino interaction cross section measured by the near detector is convoluted with the neutrino flux, while these variables must be extracted separately. For this reason, experiments rely on nuclear models and external neutrino flux and cross section measurements.

The hadron production cross section from the interaction of the initial protons with the target is the main uncertainty for the neutrino flux prediction. In T2K, it is constrained using data from the NA61/SHINE experiment [20] that measures the multiplicity and kinematics of the produced hadrons using the T2K replica target. There are also promising projects dedicated to novel neutrino beam production where the composition and neutrino energy spectrum are precisely known. ENUBET (Enhanced NeUtrino BEams from kaon Tagging) [21] proposes to tag the electron or positron produced in kaon decay (for example, via the fol-

lowing reaction:  $K^+ \rightarrow \pi^0 e^+ \nu_e$ ) to create a tagged electron-neutrino beam. Using the decay kinematics to estimate the  $\bar{\nu}_e$  energy on the event-by-event basis will lower the uncertainties associated with the neutrino flux and flavor down to  $\sim 1\%$ . Another idea is to create a facility to store  $\mu^\pm$  beams (The Neutrinos from Stored Muons, nuSTORM facility [22]) that will generate neutrino beams with energies from  $\sim 300$  MeV to 5.5 GeV. Such a neutrino energy spectrum corresponds to the region of interest of the DUNE and Hyper-Kamiokande experiments. Since in nuSTORM, neutrinos are produced from muon decays that are well understood (unlike pion decay where the energy and angle of pions depend on nuclear effects of proton scattering on a target), and the muon energy in the storage ring is well controlled, the facility will allow determining the neutrino flux and provide accurate  $\nu_\mu/\bar{\nu}_\mu A$  scattering cross section measurements with the percent-level precision.

At the far detector, the neutrino rate depends on the neutrino flux, the neutrino oscillation probability, the interaction cross section, and the detector acceptance, as shown in Fig. 2.3. Most of these variables depend on the true neutrino energy which is not known event-by-event. Sophisticated neutrino cross section models are needed to simulate neutrino-nucleus interactions to extrapolate the cross section measurements from the near detectors to the oscillated flux at the far detector. Cross section models used in T2K rely on dedicated measurement with the near detector but also on external data, coming, for example, from the Mini Booster Neutrino Experiment (MiniBooNE) [23], and the Main Injector Experiment for  $\nu$ -A (MINERvA) [24]. MINERvA performs high-precision measurements of neutrino interaction on different nuclei in support to the neutrino oscillation experiments.

$$\begin{array}{c}
 \nu \text{ rate} \\
 \overbrace{R_{FD}^{\nu'}(E_\nu)} = \underbrace{\Phi^\nu(E_\nu)}_{\nu \text{ flux}} \otimes \overbrace{P_{osc}^{\nu \rightarrow \nu'}(E_\nu)}^{\text{oscillation probability}} \otimes \underbrace{\sigma^{\nu'}(E_\nu)}_{\nu \text{ cross-section}} \otimes \overbrace{\varepsilon}^{\text{detector acceptance}}
 \end{array}$$

Figure 2.3 Factors that contribute to the neutrino rate calculation at the far detector. Most of them depend on the true neutrino energy.

A new approach has been developed for future detectors to better control neutrino flux and cross-section: a movable detector along the off-axis angle. The Intermediate Water Cherenkov Detector (IWCD) [25] is a intermediate detector proposed within the Hyper-Kamiokande physics program. DUNE near detector complex also contains a DUNE Precision Reaction-Independent Spectrum Measurement (DUNE-PRISM) ND [19] that will make measurements at various off-axis positions. The neutrino energy varies with an off-axis angle, so performing neutrino measurements at different off-axis angles allows to measure the flux and the cross-section as a function of energy. This method provides another way to know the neutrino energy dependence of flux and cross section, without directly relying on nuclear physics.

In order to measure precisely the neutrino oscillated spectrum at the far detector and to carefully constrain the flux and cross-section as a function of energy at the near detectors, a precise neutrino energy reconstruction is needed. The neutrino energy is not observable and can be evaluated using the final state particles produced in the neutrino interaction. In order to improve the neutrino energy reconstruction, better neutrino interaction modeling is needed since we will use models to correct for invisible particles in the detector and the energy they carry out. Along with the modeling improvement, new generation detectors are also needed in order to improve the precision of the neutrino energy reconstruction.

## 2.2 The T2K experiment

The T2K experiment located in Japan is a long-baseline neutrino oscillation experiment that aims to search for CP violation in the lepton sector [26] and measure the neutrino oscillation parameters [27]. It also has a broad spectrum of exotic analyses, for example search for the light sterile neutrinos at the far detector [28] and search for the heavy neutrinos with the ND280 near detector [29]. The schematic view of the T2K experiment is presented on Fig. 2.4.

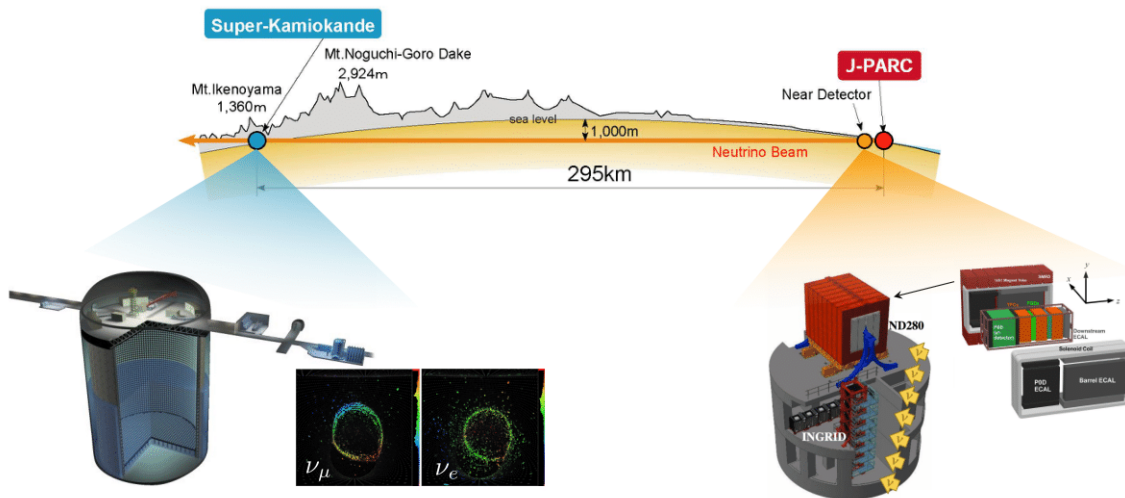


Figure 2.4 The schematic view of the T2K experiment, including its far detector and the near detector complex. Figures are adapted from [30–32].

The neutrino beam is produced at the Japan Proton Accelerator Research Complex (J-PARC) [33] in Tokai, Ibaraki prefecture. J-PARC produces a proton beam, which is shot to a graphite target to produce pions and kaons that decay into neutrinos and antineutrinos. The neutrino and antineutrino flux is chosen by selecting the magnetic horn's current (forward or reverse horn current; FHC or RHC). T2K uses a water Cherenkov detector Super-

Kamiokande [34] as a far detector 295 km from the neutrino source. The Far Detector (FD) and some detectors of the near detector complex are placed off the neutrino beam axis. Such configuration decreases slightly the neutrino rate but narrows down the neutrino energy spectrum. Fig. 2.5 shows the  $\nu_\mu$  survival probability and the neutrino flux on-axis and at different off-axis angles. The T2K off-axis angle ( $2.5^\circ$ ) is such that the center value of the neutrino flux corresponds to the maximum  $\nu_\mu$  disappearance probability. To characterize the neutrino flux and the neutrino interactions, T2K utilizes the near-detector facility located at 280 meters from the neutrino flux production target, which consists of on-axis detectors INGRID (Interactive Neutrino GRID) [36] and MUMON [37] and two off-axis detectors WAGASCI-BabyMIND [38] and ND280. INGRID and MUMON are used to precisely measure the neutrino flux direction and position. WAGASCI has an enriched water target (80% of water and 20% CH) [39] and it allows for neutrino cross section measurements on water target (same target as Super-Kamiokande far detector) at a different off-axis angle. The off-axis detector ND280 is designed to measure the neutrino flux and the neutrino-nucleus cross sections. As WAGASCI, ND280 is also equipped with the water target module and performs measurements at the same off-axis angle as the far detector.

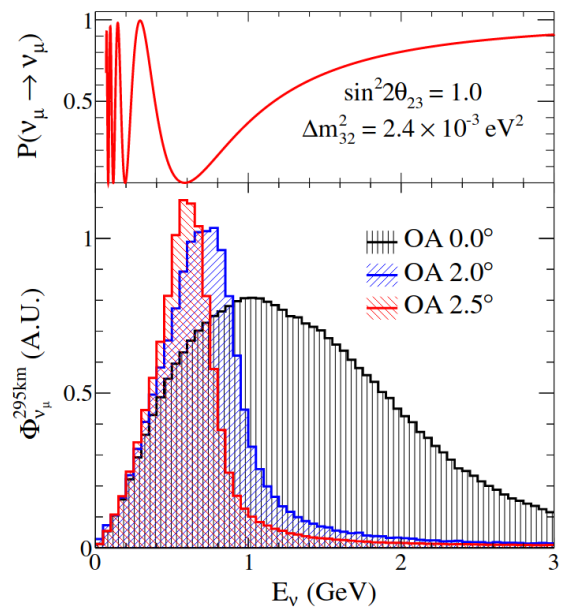


Figure 2.5 Muon neutrino survival probability and the neutrino fluxes at different off-axis angles. The figure is taken from [35].

### 2.2.1 The Far Detector

The Super-Kamiokande (Super-K) experiment is situated in the Mozumi Mine 1000 m underground in Kamioka, Japan. It has a rich scientific program, including the search for the proton decay (see for example [40, 41]), measurement of oscillations with atmospheric neutrinos [42, 43], supernova neutrinos search [44, 45], solar neutrino measurements [46], and the role of far detector for T2K.

The detailed description of Super-K can be found in Ref. [48]. Super-K is a cylinder-shaped reservoir with a height of 41.4 m and a diameter of 39.3 m filled with 50 thousand tons of highly purified water and around 13000 photomultiplier tubes (PMTs). The Cherenkov light produced by charged particles traversing the sensitive detector volume is collected by the

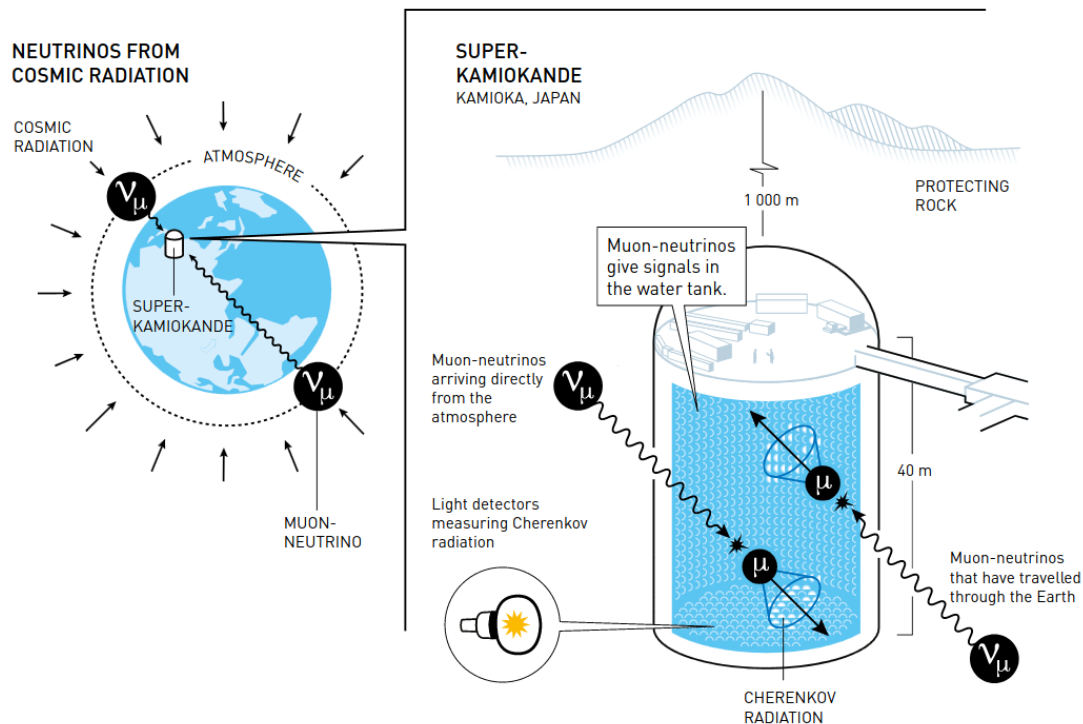


Figure 2.6 Schematic overview of the Super-Kamiokande experiment. The picture is taken from [47]

PMTs and is used for event reconstruction. The fuzziness of Cherenkov rings allows for the determination of muons from electrons and positrons, which gives information about the interacted neutrino. Fig. 2.7 shows examples of muon and electron-like events.

### 2.2.2 The Near Detector

The ND280 detector's primary goals are the measurement of the  $\nu_\mu$  beam, estimation of the  $\nu_e$  content in the  $\nu_\mu$  beam [49] and the precise measurement of the various neutrino-nucleus interactions (see for example [50]). The scheme of the ND280 detector is presented in Fig. 2.8. It consists of a few sub-detectors: the  $\pi^0$  detector (PØD) and three Time Projection Chambers (TPC) that alternate with the two Fine Grained Detectors (FGD). The electromagnetic calorimeters PØD ECal, Barrel ECal, and a 0.2 T magnet surround the PØD, TPCs, and FGDs. The ECal consists of alternating layers of lead and a scintillator and is read out with multi-pixel photon counters (MPPCs). ECal enables precise measurement of neutral particles and containment of electron/positron and gamma showers. It can also be used to measure the neutrino interaction cross section in lead [51]. The air cavities of the UA1 magnet are equipped with the 440 plates of the side muon range detector (SMRD) [52]. SMRD is designed to measure the energy of muons produced in neutrino interactions, identify neutrino beam

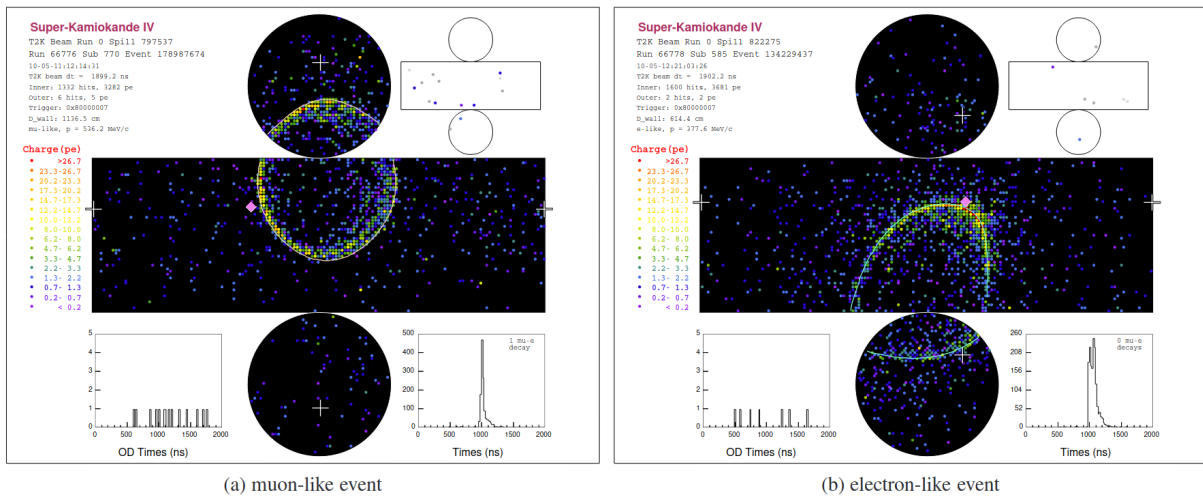


Figure 2.7 Example of reconstructed T2K events in Super-Kamiokande for (a) a muon-like ring and (b) an electron-like ring. The figures show the projection of the cylindrical detector onto a plane. Each point is a PMT, and the color corresponds to the amount of charge. Reconstructed light cone is depicted as a white line. The picture is taken from [32].

interactions background in the magnet yoke and the experimental hall walls, and provide a cosmic trigger signal for ND280 detector calibration.

The PØD consists of scintillating bars alternated with either water target or brass or lead foils. It aims to measure the neutral current process with  $\pi^0$  production. The two fine-grained detectors (FGD1 and FGD2) [53] act as active targets for the neutrino interactions and serve for the tracking of charged particles. They consist of polystyrene scintillator bars oriented perpendicular to the beam in either the x or y direction. Each bar has a Wave-Length Shifting (WLS) fiber in the center and is read by MPPCs and associated electronics. The FGD2 is also equipped with six water target modules.

TPCs [54] are used to provide precise tracking of the charged particles produced by neutrino interactions in FGD and crossing the TPCs, and to distinguish different kinds of charged particles by ionization. The TPCs consist of an inner box filled with argon-based gas (Ar–CF<sub>4</sub>–IC<sub>4</sub>H<sub>10</sub> in ratios 95%, 3% and 2% respectively) and an outer box filled with CO<sub>2</sub>. The inner box is subdivided by the cathode located in the middle and supports 12 MicroMegas modules parallel to the cathode plane at each end of the box. The bulk MicroMegas detectors are used for charge amplification and read-out. In total, 72 MicroMegas detectors are used in the three TPCs. The cathode provides a highly uniform electric field aligned with the magnetic field of the UA1 magnet.

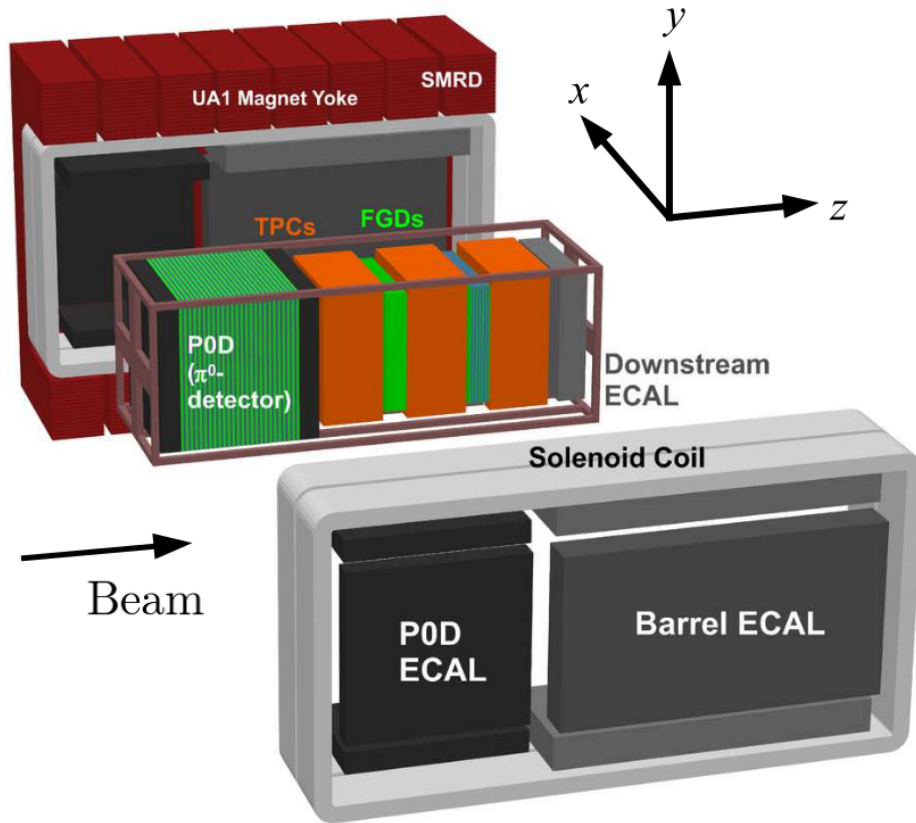


Figure 2.8 The schematic view of the T2K near detector ND280. The picture is taken from [32].

Currently in the T2K oscillation analysis, the neutrino energy is reconstructed relying solely on the muon kinematics:

$$E_{QE} = \frac{m_p^2 - m_\mu^2 - (m_n - E_B)^2 + 2E_\mu(m_n - E_B)}{2(m_n - E_B - E_\mu + p_\mu^z)}, \quad (2.3)$$

where  $m_{p/\mu/n}$  is the mass of a proton/muon/neutron;  $E_\mu$  and  $p_\mu^z$  is the outgoing muon energy and momentum in projected along the direction of the incoming neutrino; and  $E_B$  is the binding energy of the struck nucleon (which is related to, but not exactly, the removal energy and is usually taken to be  $\sim 25$  MeV for carbon).

This approximated formula works reasonably well for quasi-elastic interactions (CCQE), which are by far the largest fraction of neutrino interactions at T2K energy (as shown in Sec. 3.1). Moreover, this is the only possible strategy at the far detector, given the high-momentum threshold of Cherenkov light for protons and the fact that neutrons are undetectable. On the other hand, at the near detector, another method could be pursued, which

also uses the information about the leading outgoing nucleon:

$$E_{vis} = E_{\mu} + T_N, \quad (2.4)$$

where  $E_{vis}$  is the total visible energy of all outgoing particles,  $T_N$  is the kinetic energy of the outgoing proton (neutron) in neutrino (anti-neutrino) interactions, and  $E_{\mu}$  is the total energy of the outgoing muon. Fig. 2.9 presents the neutrino energy resolution calculated using the two approaches described above.  $E_{vis}$  certainly provides a better resolution.

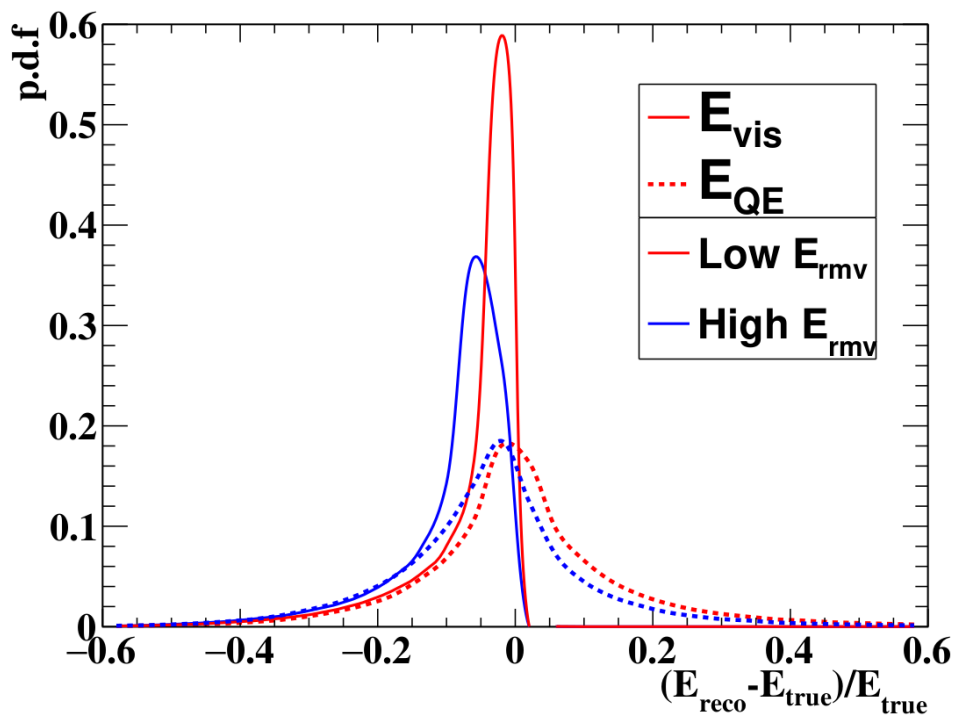


Figure 2.9 The neutrino energy reconstruction resolution and bias calculated for  $E_{vis}$  and  $E_{QE}$  for  $\pm 10$  MeV shifts to the nominal removal energy distribution (denoted by the red and blue colors respectively). The calculation is done for the CCQE events. The picture and the description are adapted from [55].

The current near detector has not been designed to detect neutrons and could detect protons only above a relatively large momentum threshold (300–400 MeV). Moreover, ND280 has been designed to measure mostly forward going particles (considering the highly boosted nature of neutrino interactions from the neutrino flux). On the other hand, the far detector has  $4\pi$  acceptance, covering also less frequent interactions producing high-angle or backward-going muons. The upgrade of the ND280 detector will address these limitations: it will improve the angular acceptance for large angle and backward-going tracks and the acceptance for low momentum hadrons (protons, pions), it will also enable neutron detection and energy reconstruction for the first time in neutrino interactions [16]. All these improvements will

allow to use the approach shown in Fig. 2.9 with high precision, and thus will provide much better neutrino energy reconstruction.

## 2.3 ND280 upgrade for T2K

The schematic view of the ND280 upgrade is shown in Fig. 2.10. The PØD will be substituted by the High-Angle TPCs (HA-TPC) sandwiched with the Super Fine Grained Detector (SuperFGD). The new tracking system will be surrounded by 6 Time-of-Flight (TOF) detectors.

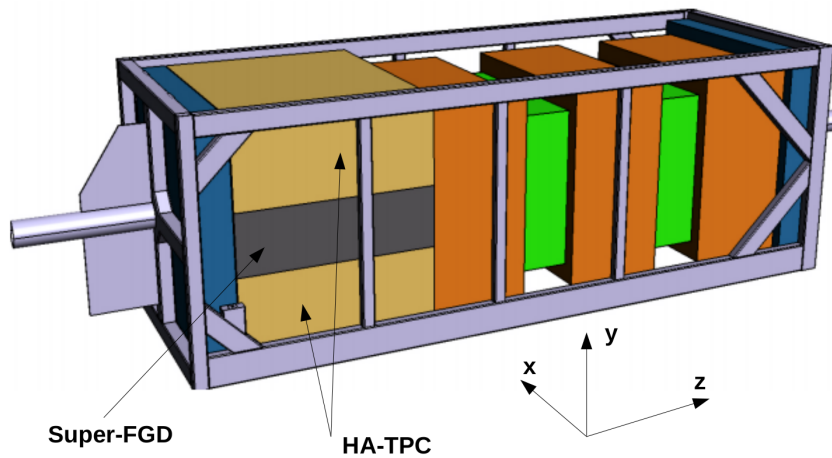


Figure 2.10 The schematic view of the T2K ND280 upgrade detector. The picture is taken from [16].

### 2.3.1 The SuperFGD detector

The SuperFGD detector is a fine-grained fully-active plastic scintillator detector that is designed to provide a target for neutrino interactions, have acceptance for muons and electrons at large scattering angles, and reconstruct and identify short tracks around the vertex. Such a detector also enables the reconstruction of neutron kinetic energy by measuring the time-of-flight between the neutrino interaction vertex and the first neutron secondary interaction. Its schematic view is presented in Fig. 2.11.

SuperFGD consists of the  $192 \times 192 \times 56$  scintillator cubes with size of  $1 \times 1 \times 1 \text{ cm}^3$ . Each cube contains three holes where WLS fibers are placed. Each fiber is read with a Multi-Pixel Photon Counters placed on the detector's upstream, top, left, and right sides. To equalize the distribution of readout channels in the  $y$ - $z$  plane, half of MPPCs are placed on each of the left and right sides.

SuperFGD will provide significantly more information on the neutrino interaction than current FGDs since it will provide projections of charged particle trajectories onto three planes without inactive regions.

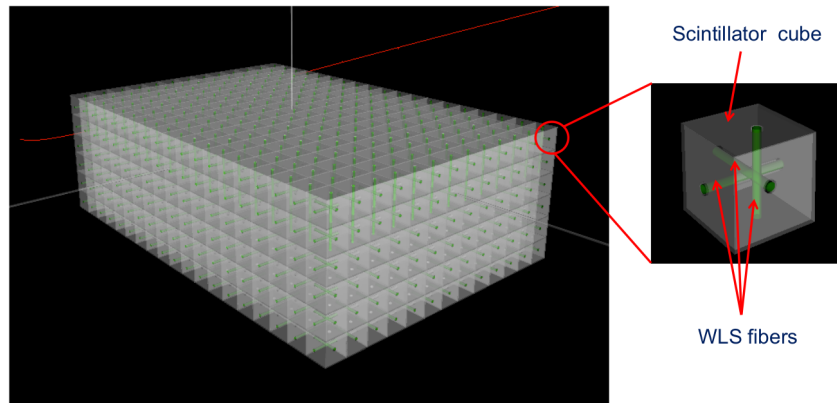


Figure 2.11 The schematic view of the SuperFGD structure. The picture is taken from [16].

### 2.3.2 HA-TPC

The current ND280 TPCs fulfilled their requirements and have been particularly useful for 3D track reconstruction,  $dE/dx$  reconstruction, and charge and momentum measurements. These features will be preserved in the new High-Angle TPCs. The HA-TPC design is based on the existing TPCs with one important technological difference: the "resistive bulk" MicroMegs will be used that introduces charge spread on multiple channels of the readout plane and therefore allows for the use of lower density readout pads and improves the spatial resolution. HA-TPC will be placed parallel to the neutrino beam and will be able to track particles produced in neutrino interactions in the SuperFGD and going in the transverse direction.

Fig. 2.12 shows the schematic view of the HA-TPC. It consists of a box filled with gas (composition of Ar,  $CF_4$  and  $IC_4H_{10}$  in ratios 95%, 3% and 2% respectively) that also serves as a Field Cage to provide a highly uniform electrostatic field, a high-voltage (HV) cathode located in the middle of the box, and two module frames at each end of the box that holds the MicroMegs readout modules and seal the TPC volume.

The Module Frame carries eight MicroMegs charge readout modules. The resistive MicroMegs (Fig. 2.13) signal amplification structure spreads the charge around a few pads, giving better spatial resolution: additional information on the signal from these pads allows for more precise track reconstruction. This technology is called the "Encapsulated Resistive Anode Micromegas" (ERAM) detector [56]. Each ERAM module consists of the Micromegas module, two Front-End cards (FEC), two FEC cooling plates, one Front-End Module (FEM), and the FEM cooling plate connected to the water cooling piping.

The HA-TPC prototype has been exposed to CERN and DESY test-beams [56, 57] to measure spatial and  $dE/dx$  resolution that were found to perfectly fulfill the HA-TPCs requirements for the T2K upgrade.

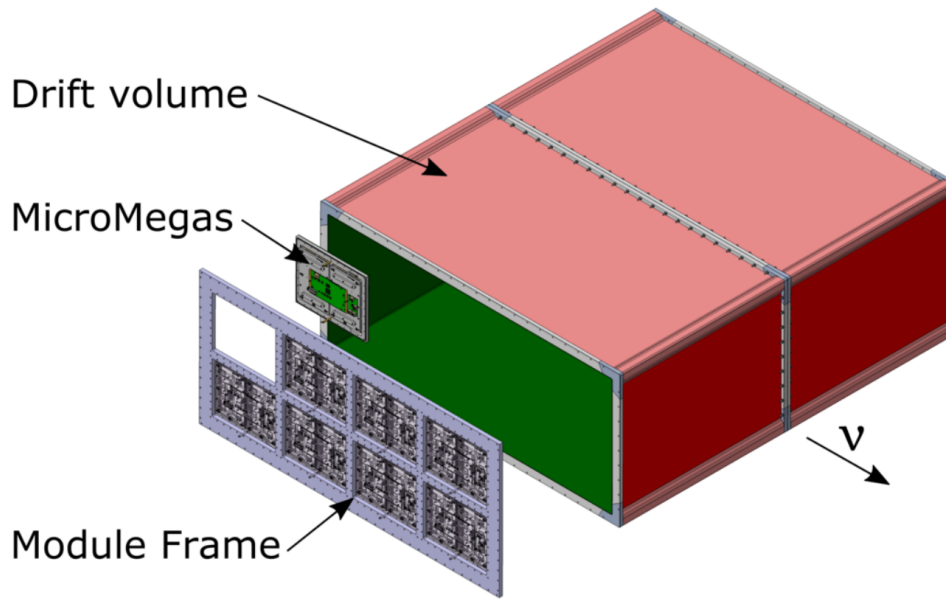


Figure 2.12 The schematic view of the HA-TPC. The picture is taken from [16].

## 2.4 Future experiments

Few projects are designed to push the boundaries of the current neutrino measurements even further. Hyper-Kamiokande (Hyper-K) is the successor of the T2K and Super-Kamiokande experiments with significantly improved sensitivity. The two most critical improvements are the upgraded neutrino beam power (that is being enhanced from 500kW to 1MW in T2K and then ultimately to 1.2MW, the neutrino energy flux will remain the same and centered at 0.6 GeV) and the fiducial volume that will be eight times larger than the one of Super-Kamiokande. Intermediate Water Cherenkov Detector (IWCD) is a part of the Hyper-Kamiokande long-baseline neutrino physics program. It is a small-scale water Cherenkov detector placed 1 km from the J-PARC and will serve as an intermediate detector of Hyper-Kamiokande. The details about Hyper-K can be found in [18]. Hyper-Kamiokande aims to discover CP-violation and precisely measure the neutrino oscillation parameters (including  $\delta_{CP}$ ). Another critical point in the Hyper-K program is the study of the atmospheric neutrino flux that is essential for the neutrino mass ordering measurements. Hyper-K will also continue the study of the solar neutrino (for example, day-night flux measurements, as performed by the Super-Kamiokande experiment that indicated its asymmetry with  $3\sigma$  [58]). Part of the Hyper-Kamiokande program is dedicated to neutrino astrophysics and geophysics. Hyper-Kamiokande design will result in an increased sensitivity to the supernova burst neutrinos and to neutrinos from diffuse supernova background. Beyond neutrino physics, Hyper-K will continue the search for proton decay. An enhanced beam and a large fiducial volume will increase the sensitivity of Hyper-K to exotic physics (for instance, dark matter search, sterile and heavy neutrinos).

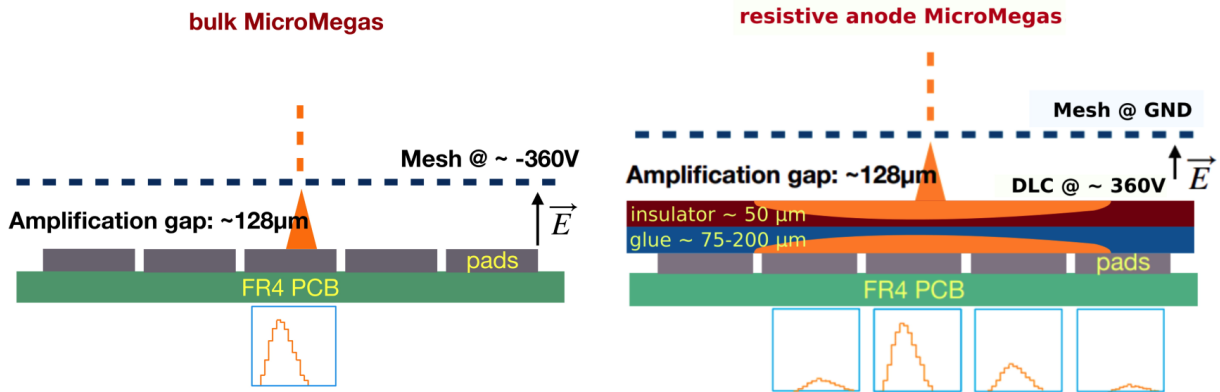


Figure 2.13 The schematic view of the bulk MicroMegas (left) used in current TPCs and the resistive MicroMegas (right). The picture is taken from [56].

Super-Kamiokande is performing an SK-Gd project, where in the Super-K water is added 0.2% gadolinium sulfate ( $\text{Gd}_2(\text{SO}_4)_3$ ) to enhance the neutron detection efficiency and detect an additional signal from the neutron gadolinium capture [59]. Such detector improvement is essential for the supernova relic neutrinos (SRN) search [60]. If proved successful, this practice can also be used later for the Hyper-Kamiokande detector.

The Deep Underground Neutrino Experiment (DUNE) is a future long baseline neutrino experiment on a new neutrino beam produced at Fermi National Accelerator Laboratory in Batavia, Illinois. The neutrino flux is centered around 2.5 GeV. DUNE will utilize a wide-band beam covering two oscillation maxima. It will have a near detector close to the beam target and a far detector 1300 km downstream, more than a kilometer underground, at the Sanford Underground Research Laboratory in Lead, South Dakota. The Liquid Argon Time Projection Chambers technology will be used, which will allow to extract the precise information about the particles produced in the final state and, hence, allow for unprecedented neutrino energy reconstruction. The DUNE research proposal includes reaching more than  $3\sigma$  sensitivity for the CP violation, determining the neutrino mass ordering at  $5\sigma$ , measuring the neutrino oscillation parameters, in particular,  $\theta_{23}$  and  $\Delta m_{32}^2$ , searching for the proton decay, and detecting and measuring the  $\nu_e$  flux from a core-collapse supernova. The complete information about DUNE physics can be found in [61]

## References

- [1] M. Schwartz. “Feasibility of Using High-Energy Neutrinos to Study the Weak Interactions”. In: *Phys. Rev. Lett.* 4 (6 1960), pp. 306–307.
- [2] B. Pontecorvo. “Electron and Muon Neutrinos”. In: *Zh. Eksp. Teor. Fiz.* 37 (1959), pp. 1751–1757.
- [3] G. Danby et al. “Observation of High-Energy Neutrino Reactions and the Existence of Two Kinds of Neutrinos”. In: *Phys. Rev. Lett.* 9 (1 1962), pp. 36–44.
- [4] Luke Southwell. *Measuring the electron anti-neutrino beam component in the T2K near detector ND280*. 2015.
- [5] Sara Bolognesi. “Neutrino Physics with Particle Beams”. In: *PoS EPS-HEP2021* (2022), p. 042.
- [6] M. H. Ahn et al. “Measurement of neutrino oscillation by the K2K experiment”. In: *Physical Review D* 74.7 (2006).
- [7] K. Abe et al. “Observation of Electron Neutrino Appearance in a Muon Neutrino Beam”. In: *Physical Review Letters* 112.6 (2014).
- [8] K. Abe et al. “Constraint on the matter–antimatter symmetry-violating phase in neutrino oscillations”. In: *Nature* 580.7803 (2020), pp. 339–344.
- [9] M. Guler et al. “OPERA: An appearance experiment to search for  $\nu_\mu \leftrightarrow \nu_\tau$  oscillations in the CNGS beam. Experimental proposal”. In: (July 2000).
- [10] N. Agafonova et al. “OPERA tau neutrino charged current interactions”. In: *Sci. Data* 8.1 (2021), p. 218.
- [11] E. Ables et al. “P-875: A Long baseline neutrino oscillation experiment at Fermilab”. In: (Feb. 1995).
- [12] D. S. Ayres et al. “NOvA: Proposal to Build a 30 Kiloton Off-Axis Detector to Study  $\nu_\mu \rightarrow \nu_e$  Oscillations in the NuMI Beamline”. In: (Mar. 2004). arXiv: hep-ex/0503053.
- [13] M. H. Ahn et al. “Measurement of neutrino oscillation by the K2K experiment”. In: *Phys. Rev. D* 74 (7 2006), p. 072003.
- [14] I. Ambats et al. “The MINOS Detectors Technical Design Report”. In: (Oct. 1998).
- [15] R. Acquafredda et al. “The OPERA experiment in the CERN to Gran Sasso neutrino beam”. In: *JINST* 4 (2009), P04018.
- [16] K. Abe et al. “T2K ND280 Upgrade - Technical Design Report”. In: (Jan. 2019). arXiv: 1901.03750 [physics.ins-det].

- [17] *Finding Neutrinos in NOvA's Event Display*. <https://nusoft.fnal.gov/nova/public/neutrinos.html>.
- [18] Hyper-Kamiokande Proto-Collaboration: K. Abe et al. *Hyper-Kamiokande Design Report*. 2018.
- [19] A. Abed Abud et al. *Deep Underground Neutrino Experiment (DUNE) Near Detector Conceptual Design Report*. 2021.
- [20] N. Abgrall et al. “Measurements of  $\pi^\pm$ ,  $K^\pm$ ,  $K_S^0$ ,  $\Lambda$  and proton production in proton–carbon interactions at 31 GeV/c with the NA61/SHINE spectrometer at the CERN SPS”. In: *The European Physical Journal C* 76.2 (2016).
- [21] A. Longhin and F. Terranova. *Enhanced Neutrino BEams from kaon Tagging (ENUBET)*. 2022.
- [22] L. Alvarez Ruso et al. *Neutrinos from Stored Muons (nuSTORM)*. 2022.
- [23] A. A. Aguilar-Arevalo et al. “First measurement of the muon neutrino charged current quasielastic double differential cross section”. In: *Phys. Rev. D* 81 (9 2010), p. 092005.
- [24] G. A. Fiorentini et al. “Measurement of Muon Neutrino Quasielastic Scattering on a Hydrocarbon Target at  $E_\nu \sim 3.5$  GeV”. In: *Phys. Rev. Lett.* 111 (2 2013), p. 022502.
- [25] Tailin Zhu. “Investigating the Impact of the Intermediate Water Cherenkov Detector on the Hyper-Kamiokande Neutrino Oscillation Measurements”. In: *30th International Conference on Neutrino Physics and Astrophysics*.
- [26] K. Abe et al. “Constraint on the matter–antimatter symmetry-violating phase in neutrino oscillations”. In: *Nature* 580.7803 (2020). [Erratum: *Nature* 583, E16 (2020)], pp. 339–344. arXiv: 1910.03887 [hep-ex].
- [27] K. Abe et al. “Improved constraints on neutrino mixing from the T2K experiment with  $3.13 \times 10^{21}$  protons on target”. In: *Phys. Rev. D* 103.11 (2021), p. 112008. arXiv: 2101.03779 [hep-ex].
- [28] K. Abe et al. “Search for light sterile neutrinos with the T2K far detector Super-Kamiokande at a baseline of 295 km”. In: *Phys. Rev. D* 99.7 (2019), p. 071103. arXiv: 1902.06529 [hep-ex].
- [29] K. Abe et al. “Search for heavy neutrinos with the T2K near detector ND280”. In: *Physical Review D* 100.5 (2019).
- [30] A. Bernstein et al. *Report on the Depth Requirements for a Massive Detector at Homestake*. 2009.
- [31] T. Kajita, Edward Kearns, and Mikio Shiozawa. “Establishing Atmospheric Neutrino Oscillations with Super-Kamiokande”. In: *Nuclear Physics B* 908 (Apr. 2016).

- [32] K. Abe et al. “The T2K Experiment”. In: *Nucl. Instrum. Meth. A* 659 (2011), pp. 106–135. arXiv: 1106.1238 [physics.ins-det].
- [33] Shinya Sawada. “J-PARC Facility”. In: *Nuclear Physics A* 834.1 (2010). The 10th International Conference on Nucleus-Nucleus Collisions (NN2009), pp. 701c–706c.
- [34] Y. Fukuda et al. “The Super-Kamiokande detector”. In: *Nucl. Instrum. Meth. A* 501 (2003). Ed. by V. A. Ilyin, V. V. Korenkov, and D. Perret-Gallix, pp. 418–462.
- [35] K. Abe et al. “T2K neutrino flux prediction”. In: *Physical Review D* 87.1 (2013).
- [36] K. Abe et al. “Measurements of the T2K neutrino beam properties using the INGRID on-axis near detector”. In: *Nuclear Instruments and Methods in Physics Research Section A: Accelerators, Spectrometers, Detectors and Associated Equipment* 694 (2012), pp. 211–223.
- [37] K. Suzuki et al. “Measurement of the muon beam direction and muon flux for the T2K neutrino experiment”. In: *PTEP* 2015.5 (2015), p. 053C01. arXiv: 1412.0194 [physics.ins-det].
- [38] M. Antonova et al. “Baby MIND: A Magnetised Spectrometer for the WAGASCI Experiment”. In: *Prospects in Neutrino Physics*. Apr. 2017. arXiv: 1704.08079 [physics.ins-det].
- [39] T. Koga et al. “Water/CH Neutrino Cross Section Measurement at J-PARC (WAGASCI Experiment)”. In: *Proceedings of the 2nd International Symposium on Science at J-PARC — Unlocking the Mysteries of Life, Matter and the Universe —*. eprint: <https://journals.jps.jp/doi/pdf/10.7566/JPSCP8.023003>.
- [40] M. Tanaka et al. “Search for proton decay into three charged leptons in 0.37 megaton-years exposure of the Super-Kamiokande”. In: *Phys. Rev. D* 101 (5 2020), p. 052011.
- [41] A. Takenaka et al. “Search for proton decay via  $p \rightarrow e^+ \pi^0$  and  $p \rightarrow \mu^+ \pi^0$  with an enlarged fiducial volume in Super-Kamiokande I-IV”. In: *Physical Review D* 102.11 (2020).
- [42] K. Abe et al. “Evidence for the Appearance of Atmospheric Tau Neutrinos in Super-Kamiokande”. In: *Phys. Rev. Lett.* 110 (18 2013), p. 181802.
- [43] K. Abe et al. “Atmospheric neutrino oscillation analysis with external constraints in Super-Kamiokande I-IV”. In: *Phys. Rev. D* 97 (7 2018), p. 072001.
- [44] H. Zhang et al. “Supernova Relic Neutrino search with neutron tagging at Super-Kamiokande-IV”. In: *Astroparticle Physics* 60 (2015), pp. 41–46.
- [45] K. Abe et al. In: *Astroparticle Physics* 81 (2016), pp. 39–48.
- [46] K. Abe et al. “Solar neutrino measurements in Super-Kamiokande-IV”. In: *Phys. Rev. D* 94 (5 2016), p. 052010.
- [47] *The Nobel Prize*. <https://www.nobelprize.org/prizes/physics/2015/popular-information/>.

- [48] S. Fukuda et al. “The Super-Kamiokande detector”. In: *Nuclear Instruments and Methods in Physics Research Section A: Accelerators, Spectrometers, Detectors and Associated Equipment* 501.2 (2003), pp. 418–462.
- [49] K. Abe et al. “Measurement of the intrinsic electron neutrino component in the T2K neutrino beam with the ND280 detector”. In: *Phys. Rev. D* 89 (2014), p. 092003. arXiv: 1403.2552 [hep-ex].
- [50] K. Abe et al. “Measurement of the  $\nu_\mu$  charged-current quasielastic cross section on carbon with the ND280 detector at T2K”. In: *Phys. Rev. D* 92.11 (2015), p. 112003. arXiv: 1411.6264 [hep-ex].
- [51] D Allan et al. “The electromagnetic calorimeter for the T2K near detector ND280”. In: *Journal of Instrumentation* 8.10 (2013), P10019–P10019.
- [52] S. Aoki and other. “The T2K Side Muon Range Detector (SMRD)”. In: *Nuclear Instruments and Methods in Physics Research Section A: Accelerators, Spectrometers, Detectors and Associated Equipment* 698 (2013), pp. 135–146.
- [53] P.-A. Amaudruz et al. “The T2K fine-grained detectors”. In: *Nuclear Instruments and Methods in Physics Research Section A: Accelerators, Spectrometers, Detectors and Associated Equipment* 696 (2012), pp. 1–31.
- [54] T2K ND280 TPC Collaboration. *Time Projection Chambers for the T2K Near Detectors*. 2010.
- [55] S. Dolan et al. “Sensitivity of the upgraded T2K Near Detector to constrain neutrino and antineutrino interactions with no mesons in the final state by exploiting nucleon-lepton correlations”. In: *Phys. Rev. D* 105 (3 2022), p. 032010.
- [56] D. Attié et al. “Characterization of resistive Micromegas detectors for the upgrade of the T2K Near Detector Time Projection Chambers”. In: *Nucl. Instrum. Meth. A* 1025 (2022), p. 166109. arXiv: 2106.12634 [physics.ins-det].
- [57] D. Attié et al. “Analysis of test beam data taken with a prototype of TPC with resistive Micromegas for the T2K Near Detector upgrade”. In: (Dec. 2022). arXiv: 2212.06541 [physics.ins-det].
- [58] A. Renshaw et al. “First Indication of Terrestrial Matter Effects on Solar Neutrino Oscillation”. In: *Phys. Rev. Lett.* 112 (9 2014), p. 091805.
- [59] John F. Beacom and Mark R. Vagins. “GADZOOKS! Antineutrino Spectroscopy with Large Water Čerenkov Detectors”. In: *Physical Review Letters* 93.17 (2004).
- [60] C. Simpson et al. “Sensitivity of Super-Kamiokande with Gadolinium to Low Energy Anti-neutrinos from Pre-supernova Emission”. In: *Astrophys. J.* 885 (2019), p. 133. arXiv: 1908.07551 [astro-ph.HE].

- [61] B. Abi et al. *Deep Underground Neutrino Experiment (DUNE), Far Detector Technical Design Report, Volume II: DUNE Physics*. 2020.

# 3

## Neutrino-nucleus interactions

In this chapter, we discuss the characteristics of the different neutrino interaction modes (primarily the CCQE reaction) and the nuclear effects to be considered. Many neutrino interaction models utilize the *plane-wave impulse approximation* (PWIA) approach assuming no impact of the nuclear potential on the states describing all the final state particles (hadrons and leptons), which are therefore characterized by the *plane waves*. At the same time, there are models that consider distorted waves for outgoing particles, for example, models that utilize the mean-field approximation (MFA) that can be found in Refs. [1–4]. PWIA allows for *factorization* of the lepton-nucleus cross section, meaning that the cross section is modeled as a convolution of the cross section of the interaction on the single nucleon and a nuclear model describing the dynamics of these target nucleons. In this case, the further reinteractions of the outgoing hadrons in the nuclear medium are simulated separately. The simulation procedure of the neutrino-nucleus interactions is shown in Fig. 3.1. We will discuss the neutrino primary vertex modeling on the free nucleon in Section 3.1 and models to simulate the initial and final state interactions in Sections 3.2 and 3.3. We also present an overview of the currently used neutrino Monte-Carlo event generators in Section 3.4.

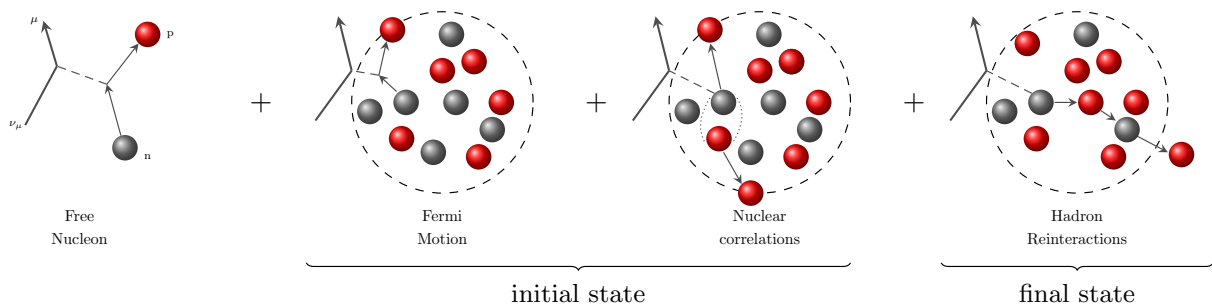


Figure 3.1 The factorization scheme of the neutrino-nucleus interaction modeling.

### 3.1 Neutrino primary vertex

In this section, we discuss the neutrino-nucleus interaction modes. Neutrino interactions are described within the electroweak theory of the Standard Model. As they are electrically neutral, their interactions are mediated via the  $W^\pm$  and  $Z$ -bosons.  $W^\pm$ -bosons are involved in the electric charge exchange, and therefore processes mediated by the  $W$ -bosons are called *charged current* (CC). In the reactions mediated by the  $Z$ -bosons, the nature of interacting particles does not change. These processes are called *neutral current* (NC). The examples of the CC and NC neutrino (quasi-)elastic interactions are shown in Fig. 3.2.

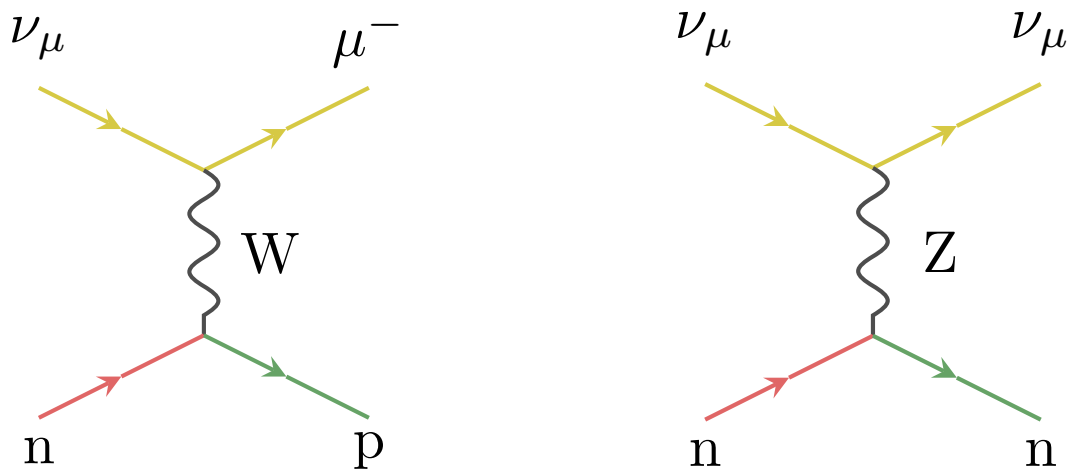


Figure 3.2 Examples of the neutrino quasi-elastic CC (left) and elastic NC (right) neutrino interactions.

Since neutrino detection is mostly performed via the charged lepton outgoing from the neutrino vertex, we will focus on the CC interactions. In the region of interest of the accelerator neutrino experiments, the essential reactions are quasi-elastic scattering, resonance production, coherent pion production, and deep inelastic scattering. Fig. 3.3 shows the total neutrino cross section in the energy region of interest. It also presents the fundamental neutrino interaction modes and some experimental data taken before 2012. These experiments include the measurements done with various targets (from deuterium to aluminum), including complex targets such as  $CF_3Br$  and probing different neutrino energy regions allowing us to see contributions from various neutrino interaction channels. More recent modern measurements, such as T2K and MINERvA, which do not measure cross section as a function of neutrino energy to avoid model-dependency, are missing.

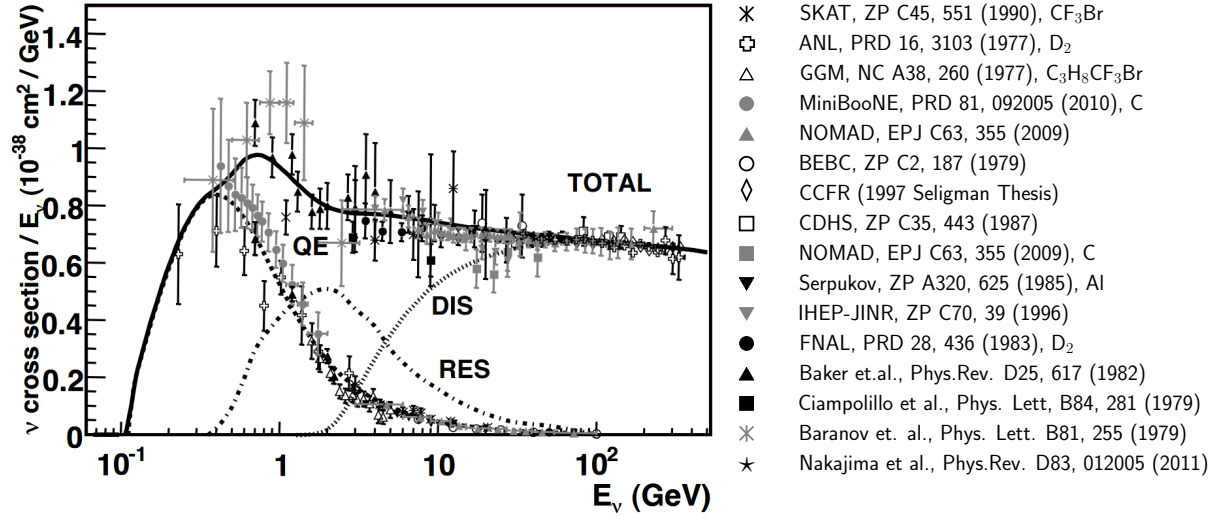


Figure 3.3 Total neutrino and antineutrino per nucleon CC cross sections divided by neutrino energy and plotted as a function of neutrino energy. Contributions of different channels are shown: quasi-elastic (dashed line), resonance (dash-dotted line) production, and deep inelastic scattering (dotted line). The experimental data coming from different measurements are also added. The figure is adapted from [5].

### Charge current quasi-elastic scattering (CCQE)

The CCQE interaction is a dominant neutrino reaction at the incident neutrino energies below  $\sim 1.5$  GeV. This reaction is the leading channel of the T2K experiment, and in the scope of this thesis, we will focus on this interaction. As Fig. 3.2 shows, in such a reaction, the nucleon with the isospin opposite to the one on which neutrino interacted and the lepton are produced:



Being the simplest neutrino interaction mode, CCQE is the most studied reaction (as can also be concluded from the available experimental measurements of the CCQE interactions shown in Fig. 3.3). The CCQE cross section is usually parametrized using the Llewellyn-Smith model [6], which gives the differential cross section dependence on the square of the four-momentum transfer:

$$\frac{d\sigma^{\nu/\bar{\nu}}}{d|q^2|} = \frac{M^2 G^2 (f^{CC/NC})^2}{8\pi E_\nu^2} \left[ A(q^2) \mp B(q^2) \frac{(s-u)}{M^2} + \frac{C(q^2)(s-u)^2}{M^4} \right]. \quad (3.2)$$

In this parametrization, the  $\mp$  corresponds to the neutrino and antineutrino reactions respectively,  $M$  is an average nucleon mass,  $G$  is the Fermi constant,  $f^{CC} = \cos\theta_C$ , where  $\theta_C$  is a Cabibbo angle,  $f^{NC} = 1$ ,  $s$  and  $u$  are the Mandelstam variables, and  $A$ ,  $B$ , and  $C$  are the functions of the four-momentum transfer  $q^2$  expressed by the nucleon form factors. We will

describe the ingredients of this formula and the recipe for its implementation to the MC generators in Section 4.4 while discussing the possibility of implementing neutrino reaction in INCL.

### Multinucleon knock-out

$np-nh$  reaction, where neutrino knocks out  $n$  particles leaving  $n$  holes in the nucleus, is an important reaction, significantly contributing to the region between the CCQE and the  $\Delta$ -resonance production (the so-called "dip region"). The example of the 2p-2h interaction is shown in Fig. 3.4. Due to FSI, it is difficult to distinguish CCQE events, single pion production, and  $np-nh$  events in the detector. Therefore, it is crucial to have a reliable model implemented in neutrino event generators to properly estimate the  $np-nh$  contribution in the detector. Current MC generators utilize a few models describing  $np-nh$  [7–11].

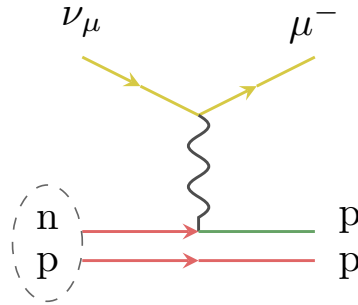


Figure 3.4 Example of the multinucleon knock-out production.

### Resonance production (RES)

If the center-of-mass energy is sufficient (more than the mass of the  $\Delta$  resonances (1232 MeV)), the  $\Delta$ -resonances can be produced in the neutrino-nucleus reaction. The example of the interaction resulting in  $\Delta$ -resonance production is shown in Fig. 3.5. It is a dominant neutrino interaction mode for the neutrino energies of the order of a few GeV and is essential for the NOvA and the future DUNE experiment, which operate at higher neutrino energies than T2K.

There are four Charged Current interactions:

$$\begin{aligned}
 \nu + p &\rightarrow l^- + \Delta^{++} \\
 \nu + n &\rightarrow l^- + \Delta^+ \\
 \bar{\nu} + p &\rightarrow l^+ + \Delta^0 \\
 \bar{\nu} + n &\rightarrow l^+ + \Delta^-
 \end{aligned}
 \tag{3.3}$$

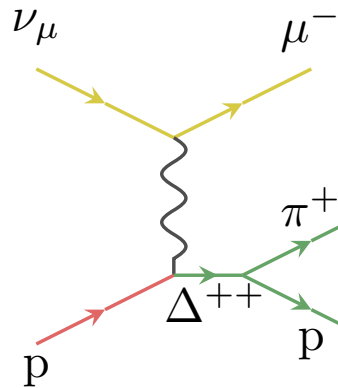


Figure 3.5 Example of the neutrino resonance production.

with the subsequent  $\Delta$ -resonance decay that produces pions:

$$\begin{aligned}
 \Delta^{++} &\rightarrow p + \pi^+ \\
 \Delta^+ &\rightarrow p + \pi^0 \text{ or } n + \pi^+ \\
 \Delta^0 &\rightarrow p + \pi^- \text{ or } n + \pi^0 \\
 \Delta^- &\rightarrow n + \pi^-
 \end{aligned}
 \tag{3.4}$$

The reactions described above lead to various final states with one nucleon and one pion, and the relative amplitudes can be calculated utilizing the Clebsh-Gordan coefficients [12]. The resonance production cross section is usually described with the Rein-Seghal model [13] that covers the single-pion production in the resonant region up to 2 GeV. It contains interfering resonances below 2 GeV and a simple non-interfering *non-resonant background* (contribution to the  $\Delta$ -resonance region coming from non-resonant processes).

### Deep inelastic scattering (DIS)

At high enough neutrino energies, neutrinos interact with the internal constituents of the nucleons, quarks and gluons (as depicted in Fig. 3.6). This reaction, known as deep inelastic scattering, is the dominant neutrino interaction channel for neutrino energies higher than 5 GeV. DIS is typically modeled using the quark-parton model [14], which describes the neutrino scattering on quarks and gluons.

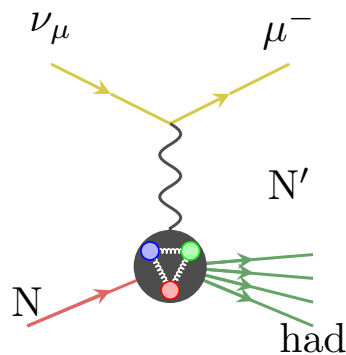
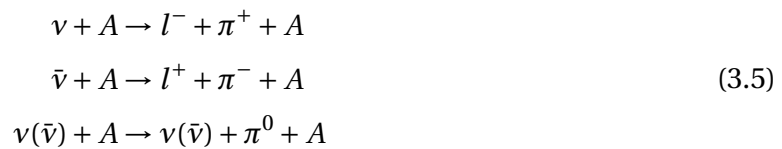


Figure 3.6 Example of the neutrino deep inelastic scattering.

### Coherent pion production (COH)

Neutrinos are also able to interact with the whole nucleus:



An example of such interaction is shown in Fig. 3.7. COH is typically described with the

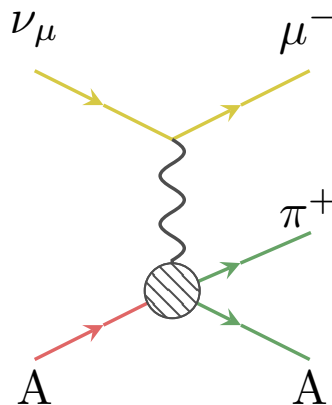


Figure 3.7 Example of the coherent pion production.

Rein-Sehgal model (not the same Rein-Segnal model that is used for the RES modeling) [15]. The total cross section for the charged current coherent pion production process simulated with NuWro and compared to various data [16–23] is shown in Fig. 3.8.

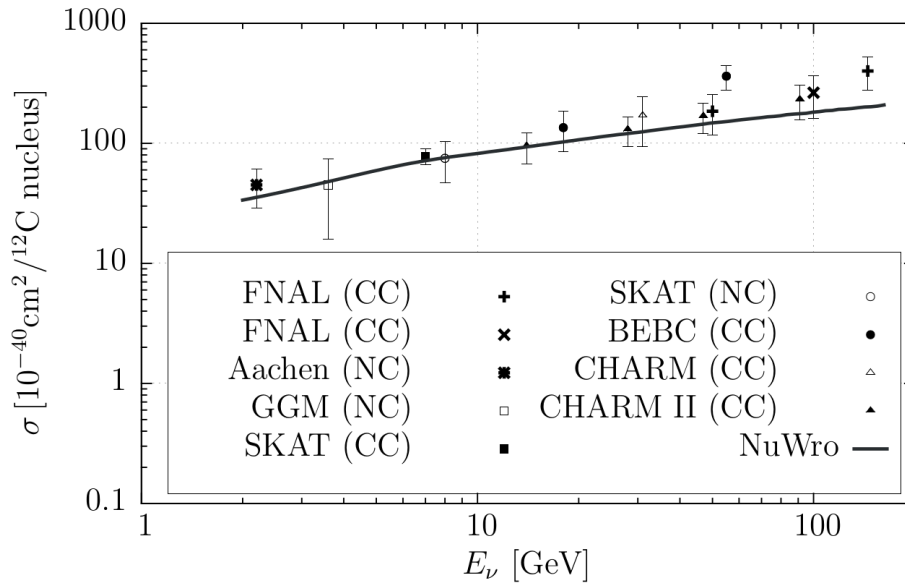


Figure 3.8 Total cross section for charged current coherent pion production. Data are scaled to  $^{12}\text{C}$  assuming the  $A^{1/3}$  dependence. NC data are multiplied by factor 2 assuming  $\sigma_{COH}^{CC} = 2\sigma_{COH}^{NC}$ . The figure is taken from Ref. [24].

## 3.2 Initial state models

The neutrino interaction modes described above are considered for the neutrino interaction on a single nucleon. In order to accurately simulate the neutrino interaction with the target nuclei of modern experiments (e.g., carbon, oxygen, or argon), we also need to consider the in-medium effects. These effects can modify the interaction cross section. For example, *short-range correlations* (SRC) add momentum to the outgoing nucleon compared to the Fermi motion, and the Pauli principle can block some transitions. Different nuclear models are able to precisely calculate the initial momentum of the interacting nucleon and give a realistic description of the nuclear medium. These models are referred to as "Initial state models" in the following. The models describing complex hadronic reinteractions in the nucleus after the primary neutrino interactions are called the Final State Models. In this section, we will cover some commonly used nuclear models.

### Relativistic Fermi Gas (RFG)

The Fermi gas model is the simplest model used to calculate the density of states in the nucleus. In the Fermi gas model, nucleons are considered independent particles occupying available energy states confined in a constant square potential, as shown in Fig. 3.9.

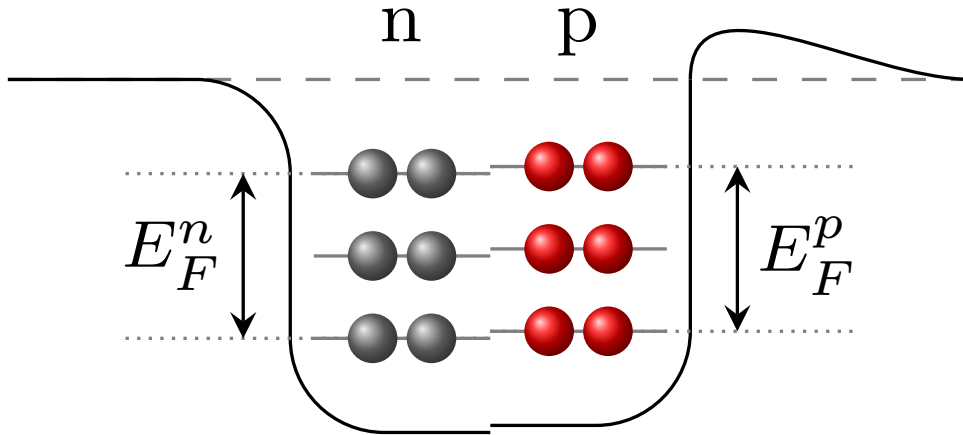


Figure 3.9 Nuclear potential wells for protons and neutrons.  $E_F^p$  and  $E_F^n$  are the Fermi energies of protons and neutrons,  $E_B$  is a binding energy. The inspiration for the figure is taken from [24].

Considering all particles are confined in an infinite three-dimensional well, we can calculate the density of states:

$$\rho(E) = \frac{dN(E)}{dE} = D \frac{V}{2\pi^2 \hbar^3} \sqrt{2m^3 E}, \quad (3.6)$$

where  $N(E)$  is the number of particle states with kinetic energy less than  $E$ ,  $V$  is the nuclear volume,  $m$  is the nucleon's mass, and  $D = 4$  is the spin-isospin degeneracy. Particles must obey the Pauli exclusion principle; therefore, there can be only one particle in each state. These states are filled up to the maximal momentum that is called *Fermi momentum* ( $p_F$ ), which can be derived from

$$A = \int_0^{p_F} dN, \quad (3.7)$$

where  $A$  is the total number of nucleons. Expressing  $dN$  as a function of momentum:

$$dN = \frac{4\pi p^2 dp}{(2\pi \hbar)^3} V, \quad (3.8)$$

we get

$$p_F = (3\pi^2)^{1/3} \hbar \left( \frac{A}{2V} \right)^{1/3}. \quad (3.9)$$

Finally, taking into account the volume of the nucleus ( $V = \frac{4}{3}\pi r_0^3 A$ , where  $r_0$  can be derived from the relation between  $A$  and the radius of the nucleus:  $R = r_0 A^{1/3}$ ), we get:

$$p_F = \left( \frac{9\pi}{8} \right)^{1/3} \frac{\hbar}{r_0}. \quad (3.10)$$

We can take another step further, taking into account nuclei with different number of protons and neutrons. Then we get the different Fermi momentum for protons and neutrons:

$$p_F^p = \left( \frac{9\pi Z}{4A} \right)^{1/3} \frac{\hbar}{r_0}, \quad p_F^n = \left( \frac{9\pi(A-Z)}{4A} \right)^{1/3} \frac{\hbar}{r_0}. \quad (3.11)$$

Relativistic Fermi gas model with different Fermi momenta for protons and neutrons is called an *asymmetric relativistic Fermi gas* (ARFG) [25].

The pure RFG model does not include a description of any explicit nucleon-nucleon interactions and sophisticated correlations. In the RFG models implemented in neutrino event generators, the confining potential is added by generating the binding energy  $E_B$ , which comes from the mutual interactions of nucleons.

### Local Fermi Gas (LFG)

In the previously described approach, the nucleus was considered an ideal sphere, and binding energy and Fermi momentum were constant for the whole nucleus. This is why the RFG model is also called a global Fermi gas model.

Another way to describe the nucleus is to use the *local density approximation* (LDA) [26, 27]. In LDA, the neutron and proton Fermi momenta are given in terms of the nuclear density  $\rho(r)$ , obtained from the electron scattering data [28]. Therefore, the Fermi momentum can be calculated as:

$$p_F^p = \hbar \left( 3\pi^2 \rho(r) \frac{Z}{A} \right)^{1/3}, \quad p_F^n = \hbar \left( 3\pi^2 \rho(r) \frac{A-Z}{A} \right)^{1/3}. \quad (3.12)$$

The Fermi gas model that utilizes the local density approximation is called *local Fermi gas* model (LFG).

### SuSA and SuSAv2

The nuclear models must be relativistic or contain relativistic corrections in the GeV energy region. As an example of a relativistic model, we would like to mention the *Super Scaling Approach* (SuSA) model [29]. Scaling is described, for instance, in Ref. [30]. Scaling occurs in the limit of high-momentum transfers when some specific function depends only on a single variable called scaling variable  $\psi$ , a function of momentum transfer  $q$  and energy transfer  $\omega$ . As a result, in the high  $q$  region, the function depends not on  $q$  and  $\omega$  separately but on  $\psi$ . The ratio of lepton-nucleus cross section to lepton-nucleon cross section function  $f(q, \omega) \xrightarrow{q \rightarrow \infty} f(\psi)$  is called the scaling function. There are two types of scaling: the one described above and the one occurring when the scaling function is independent of the nuclear mass number. If co-occurring, this phenomenon is called *superscaling*.

The simplest relativistic model is the RFG model described above. It also satisfies the mentioned above scaling conditions. The RFG cross sections can be used to construct the

scaling functions. The idea behind the SuSA model is to replace the RFG superscaling function, which does not describe the electron scattering data well, with the phenomenological one [29]. SuSA utilizes the hypothesis that the neutrino cross section scales similarly to the electron-scattering cross section.

The SuSAv2 model [30, 31] is an extension of the SuSA model that incorporates the *relativistic mean field* (RMF) model formalism [32]. RMF describes the nucleus as a system of the Dirac nucleons interacting via meson mean fields. This model provides a self-consistent relativistic description of nuclei and nuclear dynamics.

Although the SuSA is an efficient and powerful way of parametrizing the lepton-nucleus inclusive cross section, it is unsuitable for exclusive studies, which become increasingly crucial for modern and future neutrino experiments.

### Shell model

Many modern nuclear calculations are based on the shell model, so we find it important to briefly describe it here. Contrary to the described above Fermi gas models, where nucleons do not interact and follow only basic quantum mechanical principles, the shell model approach describes the nucleon interaction with a mean-field potential. Here we explicitly solve the dynamics of nucleons in the average nuclear potential.

The nucleus at low excitation energy can be described at the non-relativistic level. The nucleus is an  $A$ -body problem, but the mean free path of nucleons in the nuclear medium is still very large so nucleon-nucleon interactions can be treated as interactions of the independent nucleons with the mean-field (MF). In order to obtain the realistic MF potential, we need to solve the Shrödinger equation:

$$[T + U(r)] \phi_a(\vec{r}) = \epsilon_a \phi_a(\vec{r}), \quad (3.13)$$

where  $T$  is the kinetic energy operator,  $U(r)$  is the average field operator created by all the nucleons, and  $\phi_a$  is the solution of the Shrödinger equation with energy  $\epsilon_a$  for the  $a$  nucleon configuration. Hamiltonian for  $A$  nucleons can be written as

$$H_0 = \sum_{i=1}^A (T_i + U_i(\vec{r}_i)). \quad (3.14)$$

The eigenfunctions of  $H_0$  are

$$\psi_{a_1, a_2, \dots, a_A}(\vec{r}_1, \vec{r}_2, \dots, \vec{r}_A) = \prod_{i=1}^A \phi_{a_i}(\vec{r}_i) \quad (3.15)$$

The eigenfunctions 3.15 should fulfill the Pauli exclusion principle, so we rewrite in the Slater determinant form

$$\Phi_{a_1, \dots, a_A}(\vec{r}_1, \dots, \vec{r}_A) = \frac{1}{\sqrt{A!}} \begin{vmatrix} \phi_{a_1}(\vec{r}_1) & \dots & \phi_{a_1}(\vec{r}_A) \\ \vdots & \ddots & \vdots \\ \phi_{a_A}(\vec{r}_1) & \dots & \phi_{a_A}(\vec{r}_A) \end{vmatrix}. \quad (3.16)$$

The average field with the potential  $U_i(\vec{r})$  is not explicitly given, and we need to start with the A-nucleon Hamiltonian

$$H = \sum_{i=1}^A T_i + \frac{1}{2} \sum_{i,j=1}^A V_{ij}, \quad (3.17)$$

that describes only the two-nucleon interaction. Now we can include the potential  $U(r)$  again:

$$H = \sum_{i=1}^A (T_i + U(\vec{r}_i)) + \left( \frac{1}{2} \sum_{i,j=1}^A V_{ij} - \sum_{i=1}^A (U(\vec{r}_i)) \right) = H_0 + H_{res}, \quad (3.18)$$

where  $H_0$  describes the motion of independent A nucleons in the same average field and  $H_{res}$  describes residual nucleon-nucleon interactions remaining outside the average field. The smaller  $H_{res}$  is, the better an assumption of an average independent field.  $U(\vec{r}_i)$  can be derived starting from known  $V_{ij}$  and Slater determinant using the Hartree-Fock method.

Solving the Schrödinger equation with the known potential (that can be found, for example, in Ref. [33]) will give the discrete energy eigenvalues. The shell model picture is shown in Fig. 3.10.

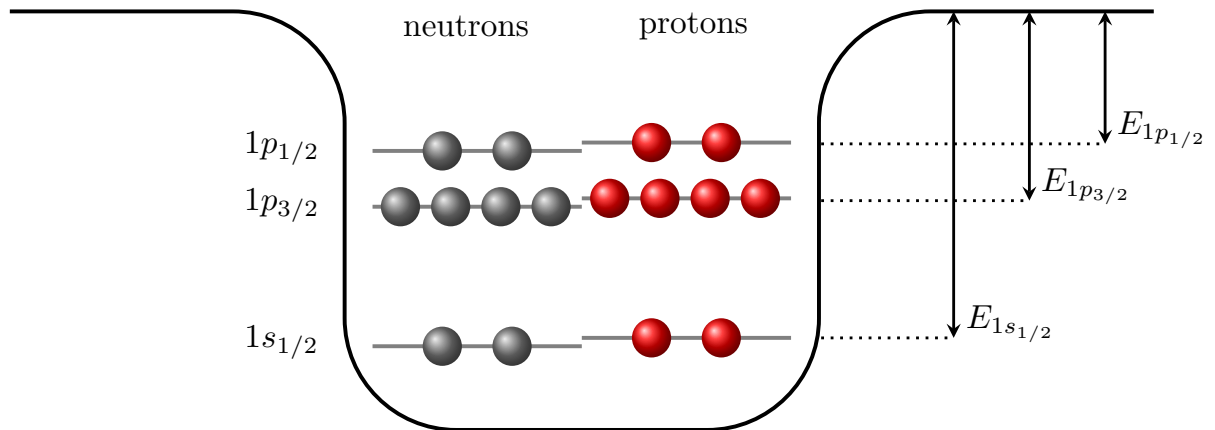


Figure 3.10 A shell model picture used to describe the nucleus,  $^{16}\text{O}$  example.  $E_{1s_{1/2}}$ ,  $E_{1p_{3/2}}$ , and  $E_{1p_{1/2}}$  are the binding energies of shells  $1s_{1/2}$ ,  $1p_{3/2}$ , and  $1p_{1/2}$ , respectively.

### Spectral function

Spectral function is a general name for initial state models (including those previously discussed). In neutrino physics, by spectral function is often meant the spectral function of Omar Benhar et.al. [34]. In this thesis, we will also refer to that model as the *Spectral Function* (SF).

Fermi gas-based models, despite their simplicity, adequately describe different experimental data and are widely used in various analyses. However, Fermi gas models treat nucleons as non-interacting fermions, while the electron scattering data indicates that nucleon-nucleon interactions alter the initial state nucleon momenta distribution inside the nucleus [35, 36]. Additionally, nucleon-nucleon interactions lead to pairs of strongly repulsive nucleons, known as *short-range correlations* (SRC). From the recent scattering experiments [37–45] it is known that SRC account for 20—25% of all nucleons. Contrary to RFG, the Spectral Function, based on the shell model, includes SRC characterization and therefore incorporates all the above-stated effects and provides a more realistic description of nuclei. The hole spectral function typically consists of the mean field and correlation parts:

$$P(\vec{p}, E) = P_{MF}(\vec{p}, E) + P_{corr}(\vec{p}, E), \quad (3.19)$$

where  $\vec{p}$  and  $E$  are the momentum and energy of the hole state left after the proton emission. To obtain the spectral function for nuclei with  $A = 3$  and  $A = 4$ , the non-relativistic nuclear many-body theory (NMBT) is employed. Heavier nuclei are modeled using the local density approximation that utilizes the experimental data from the nucleon knock-out measurements combined with the theoretical calculations [34].

According to Ref. [46], the mean-field part of the spectral function can be parametrized as:

$$P_{MF}(\vec{p}, E) = \sum_n Z_n |\phi_n(\vec{p})|^2 F_n(E - E_n), \quad (3.20)$$

where momentum-space wave functions  $\phi_n$ , associated with the single particle shell model state  $n$ , are summed over all the occupied states from the Fermi sea. The width of the states  $n$  is described by the function  $F_n(E - E_n)$ . The normalization of the  $n$ th state is provided by the spectroscopic factor  $Z_n$ . Spectroscopic factors  $Z_n$  are constrained by normalization:

$$\int d^3p dE P(\vec{p}, E) = 1. \quad (3.21)$$

In the case of absence of SRC, equation 3.20 would entirely describe spectral function, and  $F_n(E - E_n) \equiv \delta(E - E_n)$ ,  $Z_n \equiv 1$ .

The estimation of the correlated part of the spectral function can be done using the local density approximation[34]:

$$P_{corr} = \int d^3r \rho_A(\vec{r}) P_{corr}^{NM}(\vec{p}, E; \rho = \rho_A(\vec{r})), \quad (3.22)$$

where  $\rho_A(\vec{r})$  is the local density distribution, and  $P_{corr}^{NM}(\vec{p}, E; \rho)$  is the correlation component of the spectral function of uniform nuclear matter at density  $\rho$ .

The example of the spectral function  $P(\vec{p}, E)$  for oxygen  $^{16}\text{O}$  isotope is shown in Fig. 3.11.

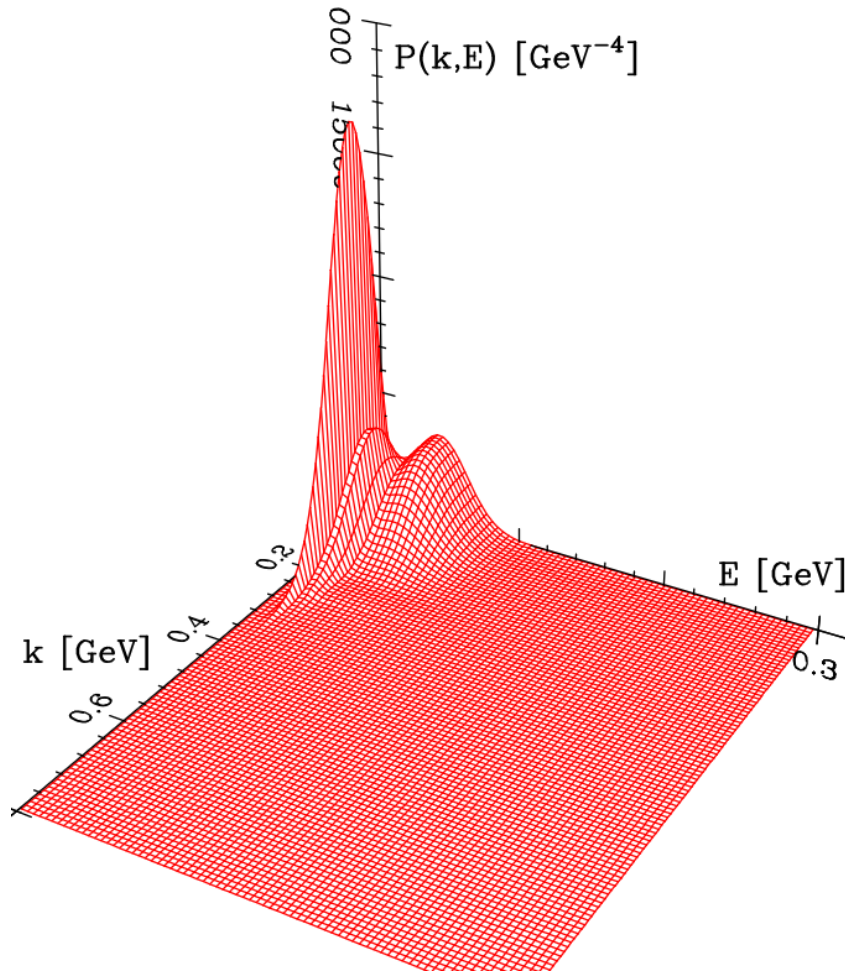


Figure 3.11 Three-dimensional plot of the oxygen spectral function. Here  $k$  is the nucleon momentum. The figure is adapted from [46].

Figure 3.12 concludes the description of different nuclear models representing momenta distributions simulated by various models. In the scope of this thesis, we will mainly utilize the Spectral Function implemented in NuWro. RFG has a strict nonphysical cut at the Fermi momentum. The LFG model's prediction is closer to the one of the spectral function. Spectral function contains the SRC pairs that can have momentum higher than the Fermi momentum, extending the momentum distribution of the initial nucleons to the higher region.

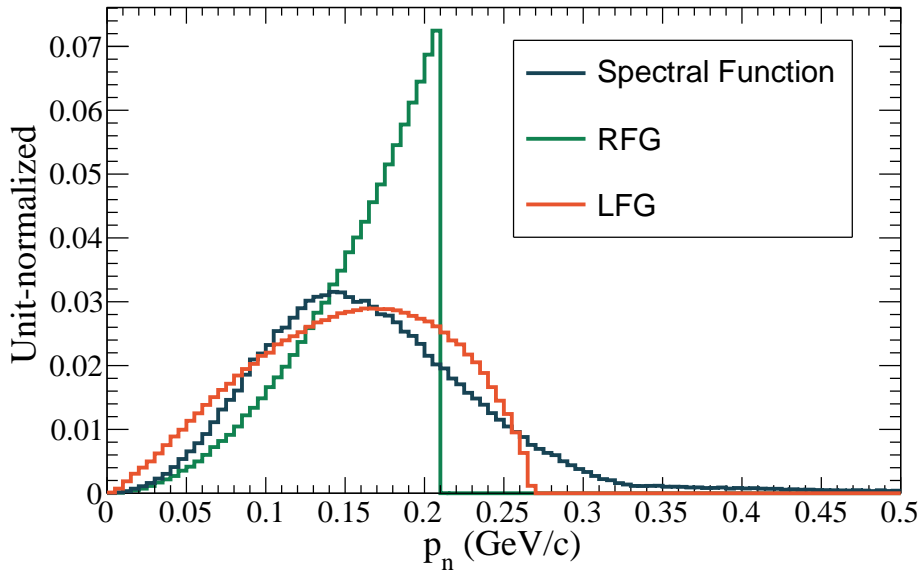


Figure 3.12 The initial nucleon momentum distribution within a Carbon nucleus simulated using the Spectral function, Local Fermi Gas (LFG), and Relativistic Fermi Gas (RFG) implemented in NuWro. The geometrical factor  $p_n^2$  is implied.

There are also other more sophisticated models (some of them can be found, for example, in Refs. [47–49]), but to our knowledge, they are not available within the neutrino MC generators framework.

### 3.3 Final state interactions

Hadrons produced in the neutrino interaction must leave the nucleus to be further detected in the experiment. Before escaping, they might re-interact with the nuclear medium leading to potential absorption, energy change of these nucleons, or production of other particles. These reinteractions are known as *final state interactions* (FSI). Modeling final-state interactions is a challenging many-body problem that bears a tension between numerical efficiency and the accuracy of nuclear calculations.

FSI are commonly described by the semi-classical *cascade models*. A visualization of FSI in a cascade model is shown in Fig. 3.13. One possible way to simulate FSI is to utilize the *space-like approach*, where mean free paths are attributed to the particles propagated in straight lines with steps of  $x$  through a continuous medium. Such Monte Carlo sampling uses the standard non-interaction probability formula

$$P(x) = \exp(-x/\lambda), \quad (3.23)$$

where  $\lambda = (\rho\sigma)^{-1}$  is the mean free path calculated locally, expressed in nuclear density  $\rho$  and an effective interaction cross section  $\sigma$ . The difficulty is that the nuclear density  $\rho$  is not constant and changes with the particle propagation. In the MC event generators, this problem is solved numerically.  $\rho$  and  $\lambda$  are calculated for some simulation step  $\Delta x$ . For these values, the propagation of the particle  $x$  is sampled from the equation 3.23. If  $x < \Delta x$ , a particle is propagated along the straight line for the distance  $x$ , and the interaction is simulated. Otherwise, the particle is moved for the distance  $\Delta x$ . At this point, the new step of the simulation starts, and the values of  $\rho$  and  $\lambda$  are reevaluated again. The value of  $\Delta x$  is phenomenological and, for most of the generators, is set to  $\Delta x = 0.2$  fm. This procedure continues until the particle has left the nucleus. This approach is utilized, for example, in GENIE [50], NEUT [51], and NuWro [52] neutrino event generators.

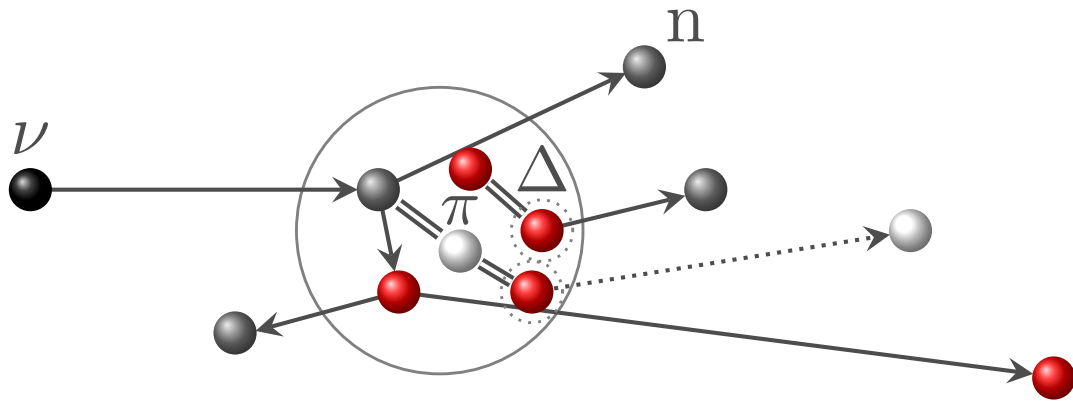


Figure 3.13 Schematic view of a nuclear cascade induced by an incident neutrino.

Another approach is called the *time-like* cascade that considers all the nucleons inside the nucleus with associated position and momentum. All of the particles are propagated until the two of them are close enough to interact. This approach is used in the INCL model that will be described in Chapter 4.

### 3.4 Neutrino MC generators

In this section, we describe the most commonly used MC generators in neutrino physics: GENIE, NEUT, and NuWro. In the scope of this thesis, out of all these MC generators, we will use NuWro, and, therefore, we will describe it in more detail.

#### NuWro

Since 2005, the theoretical group of the University of Wrocław has developed NuWro as a comprehensive Monte Carlo lepton-nucleus event generator [52], optimizing it for use in

accelerator-based neutrino oscillation experiments, i.e., the few-GeV energy region. Depending on the energy transferred from the interacting leptonic probe to the hadronic system, NuWro provides quasielastic [53], hyperon production [54], single-pion production and more inelastic channels (DIS) [55] for scattering off free nucleons. After including composite nuclear targets, additional channels such as two-body processes [56], coherent pion production [57], and neutrino scattering off atomic electrons [58] are included. The framework utilizes various nuclear models to provide predictions for the dynamics of target nucleons (e.g., global or local Fermi gas, spectral functions [34, 59], or a momentum-dependent nuclear potential [53]). Finally, FSI are simulated by an intranuclear cascade which propagates the outgoing nucleons [60] and produced pions [61] through the residual nucleus. In the context of this work, the technical aspects of modeling quasi-elastic neutrino-nucleus scattering and the subsequent FSI are emphasized. More details on the used NuWro version (19.02.2) can be found in Refs. [60, 62].

In the quasi-elastic interaction channel, PWIA and factorization are used, as described above. The process of knock-out on a single off-shell nucleon is convoluted with a particle-hole spectral function which represents the probability of leaving the residual system with specific excitation energy and recoil. The approach relies on the calculation by *O. Benhar et al.* [34] that takes into account the electron scattering input to the single-particle wave functions and adding the correlated part evaluated within the local density approximation. Additionally, in this model, the prescription by *A. Ankowski et al.* [63] is applied to go beyond the factorized picture and account for the effects of distorting the final nucleon wave function by an optical potential. It is defined on the level of the inclusive cross section and makes certain assumptions about the hadronic part of the interaction and modifies the energy conservation to include the effects of the outgoing nucleon being in a potential. For the inclusive electron scattering, it mimics the difference between PWIA and DWIA models. In NuWro, it was extrapolated to the exclusive channels but creates some unwanted behavior. In this thesis, this feature is referred to as the *spectral function FSI* (SF FSI) and is disabled unless stated otherwise. Alternatively, the RFG and LFG models described above can be used. Finally, the primary interaction vertex is constrained by the conserved vector current (CVC) and partially conserved axial current (PCAC) hypotheses. The vector form factors are provided by the BBBA05 parametrization [64], while the axial form factor has a dipole shape with  $g_A = 1.267$  and the axial mass parameter  $M_A = 1.03 \text{ GeV}/c^2$ , according to the discussion in Ref. [65].

NuWro FSI simulation is based on seminal papers by *N. Metropolis et al.* [66, 67], which describe an algorithm of the space-like cascade model, and applied up-to-date physics ingredients. The maximal step of the particle propagation, needed for the particle propagation sampling as described in Section 3.3, is set to  $\Delta x = 0.2 \text{ fm}$ , which is sufficient to grasp the structure of commonly used density profiles. By default, the nucleons constituting the nuclear

medium originate from the LFG model and, therefore, meet its Pauli blocking rules (applied on an event-by-event basis). The cascade terminates when all the moving hadrons leave the nucleus or do not have enough kinetic energy and are stuck in the nuclear potential (with the separation energy of 7 MeV). The remnant nucleus is in an excited state, and its de-excitation is not modeled.

The main ingredients of the nucleon part of the NuWro cascade lie in nucleon-nucleon interaction cross sections, which replicate the PDG dataset [68], the fraction of single-pion production adjusted to follow the fits of Ref. [69], and the center-of-momentum frame angular distributions of Ref. [70]. Additionally, the cross sections are modified with in-medium corrections [71, 72] and two-nucleon correlation effects [60]. Finally, the pion-nucleon interaction dynamics is taken from the model of *L.L. Salcedo et al.* [73]. This aspect, together with the formation zone effect for the inelastic scattering channels, has been presented and compared to data in Ref. [61]. In Ref. [60], the nucleon part of the NuWro cascade has been extensively tested, aiming to reproduce the nuclear transparency in exclusive  $(e, e' p)$  scattering experiments.

## GENIE

GENIE (**Generates Events for Neutrino Interaction Experiments**) [50, 74] is a neutrino event generator which inherits the experience learned from the NEUGEN package [75]. Nuclei are simulated using the RFG nuclear model with Bodek and Ritchie modification to incorporate an effective description of the short-range correlations [76]. Quasi-elastic neutrino interactions are simulated with the implementation of the Llewellyn-Smith model [6]. The vector form factors are related to the electromagnetic form factors through CVC. Electromagnetic form factors are known from the electron elastic scattering experiments and are available in various parametrizations, with BBBA2005 [64] being a default option. The pseudo-scalar form factor is constrained using the PCAC hypothesis [6], and the axial form factor is assumed to have a dipole form with an axial mass parameter  $M_A = 0.99 \text{ GeV}/c^2$  [77].

The resonance production for the neutral and charged currents is described with the Rein-Sehgal model [13]. GENIE includes 16 unambiguous resonances listed in PDG baryon tables [78]. The interference between neighboring resonances is neglected. Coherent pion production is modeled according to the Rein-Sehgal model [15]. Deep (and not-so-deep) inelastic scattering is calculated with an effective leading order model using the modifications by Bodek and Yang [79]. Hadronization is done with the AGKY model [80] for low invariant masses with a smooth transition to PYTHIA-6 [81] for high invariant masses. Final state interactions are handled with the INTRANUKE subpackage tuned to hadron-nucleus data [82]. There are two types of FSI modeling in GENIE. The first one—hA—is data-driven. It utilizes the total cross-section for each possible nuclear process for pions and nucleons as a function of energy and does not calculate the cascade of hadronic interactions as the complete INC

models. It focuses on iron since its first application was for the MINOS experiment. Cross sections for other targets are obtained by scaling the iron cross section by  $A^{2/3}$ . Another model—hN—is more similar to the cascades implemented in NuWro and NEUT. Being a full INCL model, the hM model can calculate reactions on all types of nuclei. More information about these two FSI models can be found in Ref. [83]. The latest GENIE release also features implementation of the INCL and Bertini cascades [84].

### NEUT

NEUT [51] was initially developed for the Kamiokande experiment and has also been used by SuperKamiokande, K2K, T2K, and SciBoone, among others. The set of the cross section models is similar to the one in NuWro and GENIE: the Llewellyn-Smith formalism for quasi-elastic scattering, the Rein-Sehgal models for RES and COH, and the Bodek-Young model for DIS. For the QEL simulation, RFG, LFG, and spectral function nuclear models are available. Hadronization is performed using PYTHIA routines. The transport of particles through the nuclear matter is realized through the custom intra-nuclear cascade (INC) model. As in NuWro, the maximal step of the particle propagation is fixed at 0.2 fm.

### GiBUU

The Giessen Boltzmann-Uehling-Uhlenbeck (GiBUU) model [85, 86] features a wide class of interaction, including photon-, electron- and neutrino-induced reactions. The BUU equation describes the space-time evolution of a many-body system in the presence of potentials and a collision term. It is used as the basis for transport models which describe scattering over a broad range of incident energies. The objective of GiBUU is to use a self-consistent microscopic model with the same physics input to represent a wide variety of external data. This technique ensures consistency of the nuclear effects in the initial (Pauli blocking, Fermi motion, etc.) and final states. GiBUU uses an effective nucleon-nucleon interaction to be as much as possible independent of the experimental data set. The particle momenta are distributed according to a local Thomas-Fermi (LTF) approximation

$$f_{n,p}(\mathbf{r}, \mathbf{p}) = \theta [p_{F,n,p}(\mathbf{r}) - |\mathbf{p}|], \quad (3.24)$$

where  $\theta(x)$  is a Heaviside function and  $p_{F,n,p}$  is the Fermi momentum, which distribution is given by an isotropic Fermi sphere at each point in space with the radius in momentum space determined by the local Fermi momentum,

$$p_{F,n,p} = [3\pi^2 \rho_{n,p}(\mathbf{r})]^{1/3} \quad (3.25)$$

This ground state is applied to *all* types of the interactions, such as QE-scattering, pion production, and DIS. The QE interactions simulation is described in Ref. [87]. As in other generators, the vector form factors are related to the electromagnetic form factors via CVC, and BBA2003 parametrization is used [88]. Refs. [89] and [90] provide details of the pion production in GiBUU.  $\Delta$  resonance is modeled according to Ref. [91] that proceeds through nucleon resonances with invariant masses less than 2 GeV. DIS is simulated with PYTHIA. One can find more information about the neutrino interactions simulation in GiBUU in Ref. [92].

GiBUU does not use the standard INC models as the other neutrino MC generators described above. It employs a semi-classical transport model that describes the space-time evolution of a many-body system.

## References

- [1] J. M. Udías et al. “Relativistic mean field approximation to the analysis of  $^{16}\text{O}(e, e'p)^{15}\text{N}$  data at  $Q^2 \leq 0.4(\text{GeV}/c)^2$ ”. In: *Physical Review C* 64.2 (2001).
- [2] R. González-Jiménez et al. “Neutral current (anti)neutrino scattering: Relativistic mean field and superscaling predictions”. In: *Physics Letters B* 718.4-5 (2013), pp. 1471–1474.
- [3] R. González-Jiménez et al. “Constraints in modeling the quasielastic response in inclusive lepton-nucleus scattering”. In: *Phys. Rev. C* 101 (1 2020), p. 015503.
- [4] V. Pandey et al. “Low-energy excitations and quasielastic contribution to electron-nucleus and neutrino-nucleus scattering in the continuum random-phase approximation”. In: *Physical Review C* 92.2 (2015).
- [5] J. A. Formaggio and G. P. Zeller. “From eV to EeV: Neutrino cross sections across energy scales”. In: *Reviews of Modern Physics* 84.3 (2012), pp. 1307–1341.
- [6] C.H. Llewellyn Smith. “Neutrino reactions at accelerator energies”. In: *Physics Reports* 3.5 (1972), pp. 261–379.
- [7] J. Nieves, I. Ruiz Simo, and M. J. Vicente Vacas. “Inclusive charged-current neutrino-nucleus reactions”. In: *Phys. Rev. C* 83 (4 2011), p. 045501.
- [8] Jan T. Sobczyk. *Modelling nuclear effects in neutrino interactions in 1 GeV region*. 2003. arXiv: nucl-th/0307047 [nucl-th].
- [9] M. Martini et al. “Unified approach for nucleon knock-out and coherent and incoherent pion production in neutrino interactions with nuclei”. In: *Phys. Rev. C* 80 (6 2009), p. 065501.
- [10] A. Bodek, H. S. Budd, and M. E. Christy. “Neutrino quasielastic scattering on nuclear targets”. In: *The European Physical Journal C* 71.9 (2011), p. 1726.
- [11] S. Dolan, G. D. Megias, and S. Bolognesi. “Implementation of the SuSv2-meson exchange current 1p1h and 2p2h models in GENIE and analysis of nuclear effects in T2K measurements”. In: *Phys. Rev. D* 101 (3 2020), p. 033003.
- [12] G.L. Fogli and G. Nardulli. “A new approach to the charged current induced weak one-pion production”. In: *Nuclear Physics B* 160.1 (1979), pp. 116–150.
- [13] Dieter Rein and Lalit M Sehgal. “Neutrino-excitation of baryon resonances and single pion production”. In: *Annals of Physics* 133.1 (1981), pp. 79–153.
- [14] Richard P. Feynman. “Very High-Energy Collisions of Hadrons”. In: *Phys. Rev. Lett.* 23 (24 1969), pp. 1415–1417.

- [15] Dieter Rein and Lalit M. Sehgal. “Coherent  $\pi^0$  production in neutrino reactions”. In: *Nuclear Physics B* 223.1 (1983), pp. 29–44.
- [16] M Aderholz et al. “Coherent production of  $\pi^+$  and  $\pi^-$  mesons by charged-current interactions of neutrinos and antineutrinos on neon nuclei at the Fermilab Tevatron”. In: *Phys Rev Lett* 63.21 (Nov. 1989), pp. 2349–2352.
- [17] S. Willocq et al. “Coherent production of single pions and  $\rho$  mesons in charged-current interactions of neutrinos and antineutrinos on neon nuclei at the Fermilab Tevatron”. In: *Phys. Rev. D* 47 (7 1993), pp. 2661–2674.
- [18] H. Faissner et al. “Observation of Neutrino and Anti-neutrino Induced Coherent Neutral Pion Production Off  $^{27}\text{Al}$ ”. In: *Phys. Lett. B* 125 (1983), pp. 230–236.
- [19] Engin Isiksal, Dieter Rein, and Jorge G. Morfin. “Evidence for Neutrino- and Antineutrino-Induced Coherent  $\pi^0$  Production”. In: *Phys. Rev. Lett.* 52 (13 1984), pp. 1096–1099.
- [20] H.-J. Grabosch et al. “Coherent pion production in neutrino and antineutrino interactions on nuclei of heavy freon molecules”. In: *Zeitschrift für Physik C Particles and Fields* 31.2 (1986), pp. 203–211.
- [21] P. Marage et al. “Coherent Production of  $\pi^+$  Mesons in Neutrino - Neon Interactions”. In: *Z. Phys. C* 43 (1989), pp. 523–526.
- [22] F. Bergsma et al. “Measurement of the Cross-section of Coherent  $\pi^0$  Production by Muon Neutrino and Anti-neutrino Neutral Current Interactions on Nuclei”. In: *Phys. Lett. B* 157 (1985), pp. 469–474.
- [23] P. Vilain et al. “Coherent single charged pion production by neutrinos”. In: *Phys. Lett. B* 313 (1993), pp. 267–275.
- [24] Tomasz Golan. “Modeling nuclear effects in NuWro Monte Carlo neutrino event generator”. PhD thesis. University of Wroclaw, 2014.
- [25] M. B. Barbaro et al. “Asymmetric relativistic Fermi gas model for quasielastic lepton-nucleus scattering”. In: *Phys. Rev. C* 98 (3 2018), p. 035501.
- [26] S. K. Singh and E. Oset. “Inclusive quasielastic neutrino reactions in  $^{12}\text{C}$  and  $^{16}\text{O}$  at intermediate energies”. In: *Phys. Rev. C* 48 (3 1993), pp. 1246–1258.
- [27] T. S. Kosmas and E. Oset. “Charged current neutrino-nucleus reaction cross sections at intermediate energies”. In: *Phys. Rev. C* 53 (3 1996), pp. 1409–1415.
- [28] H. De Vries, C. W. De Jager, and C. De Vries. “Nuclear charge and magnetization density distribution parameters from elastic electron scattering”. In: *Atom. Data Nucl. Data Tabl.* 36 (1987), pp. 495–536.

- [29] Maria B. Barbaro, Arturo De Pace, and Luisa Fiume. “The SuSA Model for Neutrino Oscillation Experiments: From Quasielastic Scattering to the Resonance Region”. In: *Universe* 7.5 (2021), p. 140. arXiv: 2104.10472 [hep-ph].
- [30] R. González-Jiménez et al. “Extensions of superscaling from relativistic mean field theory: The SuSAv2 model”. In: *Phys. Rev. C* 90 (3 2014), p. 035501.
- [31] R. González-Jiménez et al. “Extensions of Superscaling from Relativistic Mean Field Theory: the SuSAv2 Model”. In: *Phys. Rev. C* 90.3 (2014), p. 035501. arXiv: 1407.8346 [nucl-th].
- [32] P G Reinhard. “The relativistic mean-field description of nuclei and nuclear dynamics”. In: *Reports on Progress in Physics* 52.4 (1989), p. 439.
- [33] Kris L. G. Heyde. *Nuclear Structure, (Springer Berlin, Heidelberg, 1990)*.
- [34] O. Benhar et al. “Spectral function of finite nuclei and scattering of GeV electrons”. In: *Nuclear Physics A* 579.3 (1994), pp. 493–517.
- [35] P K A de Witt Huberts. “Proton spectral functions and momentum distributions in nuclei from high-resolution (e,e’p) experiments”. In: *Journal of Physics G: Nuclear and Particle Physics* 16.4 (1990), p. 507.
- [36] D. Rohe et al. “Correlated strength in nuclear spectral function”. In: *Phys. Rev. Lett.* 93 (2004), p. 182501. arXiv: nucl-ex/0405028.
- [37] L.L. Frankfurt et al. “Evidence for short-range correlations from high Q<sup>2</sup> (e,e’) reactions”. In: *Physical Review C* 48.5 (1993). Cited by: 157, 2451 – 2461.
- [38] K. Sh. Egiyan et al. “Observation of nuclear scaling in the  $A(e, e')$  reaction at  $x_B g t; 1$ ”. In: *Phys. Rev. C* 68 (1 2003), p. 014313.
- [39] N. Fomin et al. “New Measurements of High-Momentum Nucleons and Short-Range Structures in Nuclei”. In: *Phys. Rev. Lett.* 108 (9 2012), p. 092502.
- [40] K. S. Egiyan et al. “Measurement of Two- and Three-Nucleon Short-Range Correlation Probabilities in Nuclei”. In: *Phys. Rev. Lett.* 96 (8 2006), p. 082501.
- [41] A. Tang et al. “ $n-p$  Short-Range Correlations from  $(p, 2p + n)$  Measurements”. In: *Phys. Rev. Lett.* 90 (4 2003), p. 042301.
- [42] E. Piassetzky et al. “Evidence for Strong Dominance of Proton-Neutron Correlations in Nuclei”. In: *Phys. Rev. Lett.* 97 (16 2006), p. 162504.
- [43] R. Subedi et al. “Probing Cold Dense Nuclear Matter”. In: *Science* 320.5882 (2008), pp. 1476–1478. eprint: <https://www.science.org/doi/pdf/10.1126/science.1156675>.
- [44] I. Korover et al. “Probing the Repulsive Core of the Nucleon-Nucleon Interaction via the  ${}^4\text{He}(e, e' pN)$  Triple-Coincidence Reaction”. In: *Phys. Rev. Lett.* 113 (2 2014), p. 022501.

- [45] O. Hen et al. “Momentum sharing in imbalanced Fermi systems”. In: *Science* 346.6209 (2014), pp. 614–617. eprint: <https://www.science.org/doi/pdf/10.1126/science.1256785>.
- [46] Omar Benhar et al. “Electron- and neutrino-nucleus scattering in the impulse approximation regime”. In: *Phys. Rev. D* 72 (5 2005), p. 053005.
- [47] C. Maieron et al. “Nuclear model effects in charged-current neutrino-nucleus quasielastic scattering”. In: *Phys. Rev. C* 68 (4 2003), p. 048501.
- [48] Andrea Meucci, Carlotta Giusti, and Franco Davide Pacati. “Relativistic Green's function approach to charged-current neutrino–nucleus quasielastic scattering”. In: *Nuclear Physics A* 739.3-4 (2004), pp. 277–290.
- [49] V. Pandey et al. “Low-energy excitations and quasielastic contribution to electron-nucleus and neutrino-nucleus scattering in the continuum random-phase approximation”. In: *Phys. Rev. C* 92 (2 2015), p. 024606.
- [50] *GENIE*. <https://hep.ph.liv.ac.uk/~costasa/genie/index.html>.
- [51] Yoshinari Hayato and Luke Pickering. “The NEUT neutrino interaction simulation program library”. In: *The European Physical Journal Special Topics* 230.24 (2021), pp. 4469–4481.
- [52] *NuWro official repository*. <https://github.com/NuWro/nuwro>.
- [53] C. Juszczak, J. A. Nowak, and J. T. Sobczyk. “Spectrum of recoil nucleons in quasi-elastic neutrino nucleus interactions”. In: *Eur. Phys. J. C* 39 (2005), pp. 195–200.
- [54] Christopher Thorpe et al. “Second class currents, axial mass, and nuclear effects in hyperon production”. In: *Phys. Rev. C* 104.3 (2021), p. 035502. arXiv: 2010.12361 [hep-ph].
- [55] Cezary Juszczak, Jaroslaw A. Nowak, and Jan T. Sobczyk. “Simulations from a new neutrino event generator”. In: *Nucl. Phys. B Proc. Suppl.* 159 (2006). Ed. by F. Cavanna, J.G. Morfin, and T. Nakaya, pp. 211–216. arXiv: hep-ph/0512365.
- [56] Tomasz Bonus et al. “Data-based two-body current contribution to the neutrino-nucleus cross section”. In: *Phys. Rev. C* 102.1 (2020), p. 015502. arXiv: 2003.00088 [hep-ex].
- [57] Ch. Berger and L. M. Sehgal. “PCAC and coherent pion production by low energy neutrinos”. In: *Phys. Rev. D* 79 (2009), p. 053003. arXiv: 0812.2653 [hep-ph].
- [58] Dmitry Zhuridov et al. “Monte Carlo event generation of neutrino–electron scattering”. In: *J. Phys. G* 48.5 (2021), p. 055002. arXiv: 2007.14426 [hep-ph].
- [59] Artur M. Ankowski and Jan T. Sobczyk. “Construction of spectral functions for medium-mass nuclei”. In: *Phys. Rev. C* 77 (2008), p. 044311. arXiv: 0711.2031 [nucl-th].

- [60] Kajetan Niewczas and Jan T. Sobczyk. “Nuclear Transparency in Monte Carlo Neutrino Event Generators”. In: *Phys. Rev. C* 100.1 (2019), p. 015505. arXiv: 1902.05618 [hep-ex].
- [61] Tomasz Golan, Cezary Juszczak, and Jan T. Sobczyk. “Final State Interactions Effects in Neutrino-Nucleus Interactions”. In: *Phys. Rev. C* 86 (2012), p. 015505. arXiv: 1202.4197 [nucl-th].
- [62] K. Niewczas et al. “Angular distributions in Monte Carlo event generation of weak single-pion production”. In: *Phys. Rev. D* 103.5 (2021), p. 053003. arXiv: 2011.05269 [hep-ph].
- [63] Artur M. Ankowski, Omar Benhar, and Makoto Sakuda. “Improving the accuracy of neutrino energy reconstruction in charged-current quasielastic scattering off nuclear targets”. In: *Phys. Rev. D* 91.3 (2015), p. 033005. arXiv: 1404.5687 [nucl-th].
- [64] R. Bradford et al. “A New parameterization of the nucleon elastic form-factors”. In: *Nucl. Phys. B Proc. Suppl.* 159 (2006). Ed. by F. Cavanna, J. G. Morfin, and T. Nakaya, pp. 127–132. arXiv: hep-ex/0602017.
- [65] G. D. Megias et al. “New evaluation of the axial nucleon form factor from electron- and neutrino-scattering data and impact on neutrino-nucleus cross sections”. In: *Phys. Rev. C* 101.2 (2020), p. 025501. arXiv: 1910.13263 [hep-ph].
- [66] N. Metropolis et al. “Monte Carlo Calculations on Intranuclear Cascades. I. Low-Energy Studies”. In: *Phys. Rev.* 110.1 (1958), p. 185.
- [67] N. Metropolis et al. “Monte Carlo Calculations on Intranuclear Cascades. 2. High-Energy Studies and Pion Processes”. In: *Phys. Rev.* 110 (1958), pp. 204–219.
- [68] C. Patrignani et al. “Review of Particle Physics”. In: *Chin. Phys. C* 40.10 (2016), p. 100001.
- [69] J. Bystricky et al. “Energy dependence of nucleon-nucleon inelastic total cross-sections”. In: *J. Phys. France* 48.11 (1987), pp. 1901–1924.
- [70] J. Cugnon, D. L’Hôte, and J. Vandermeulen. “Simple parametrization of cross-sections for nuclear transport studies up to the GeV range”. In: *Nuclear Instruments and Methods in Physics Research Section B: Beam Interactions with Materials and Atoms* 111.3 (1996), pp. 215–220.
- [71] V. R. Pandharipande and Steven C. Pieper. “Nuclear transparency to intermediate-energy nucleons from (e,e’p) reactions”. In: *Phys. Rev. C* 45 (2 1992), pp. 791–798.
- [72] Dietrich Klakow, Gerd Welke, and Wolfgang Bauer. “Nuclear flow excitation function”. In: *Phys. Rev. C* 48 (1993), pp. 1982–1987. arXiv: nucl-th/9304008.
- [73] L. L. Salcedo et al. “Computer Simulation of Inclusive Pion Nuclear Reactions”. In: *Nucl. Phys. A* 484 (1988), pp. 557–592.

- [74] C. Andreopoulos et al. “The GENIE neutrino Monte Carlo generator”. In: *Nuclear Instruments and Methods in Physics Research Section A: Accelerators, Spectrometers, Detectors and Associated Equipment* 614.1 (2010), pp. 87–104.
- [75] H. Gallagher. “The NEUGEN neutrino event generator”. In: *Nucl. Phys. B Proc. Suppl.* 112 (2002). Ed. by J. G. Morfin, M. Sakuda, and Y. Suzuki, pp. 188–194.
- [76] A. Bodek and J. L. Ritchie. “Further studies of Fermi-motion effects in lepton scattering from nuclear targets”. In: *Phys. Rev. D* 24 (5 1981), pp. 1400–1402.
- [77] Costas Andreopoulos et al. *The GENIE Neutrino Monte Carlo Generator: Physics and User Manual*. 2015. arXiv: 1510.05494 [hep-ph].
- [78] R. L. Workman et al. “Review of Particle Physics”. In: *PTEP* 2022 (2022), p. 083C01.
- [79] A Bodek and U K Yang. “Higher twist,  $\eta_W$  scaling, and effective LO PDFs for lepton scattering in the few GeV region”. In: *Journal of Physics G: Nuclear and Particle Physics* 29.8 (2003), p. 1899.
- [80] T. Yang et al. “A hadronization model for the MINOS experiment”. In: *AIP Conf. Proc.* 967.1 (2007). Ed. by Geralyn P. Zeller, Jorge G. Morfin, and Flavio Cavanna, pp. 269–275.
- [81] Torbjörn Sjöstrand, Stephen Mrenna, and Peter Skands. “PYTHIA 6.4 physics and manual”. In: *Journal of High Energy Physics* 2006.05 (2006), pp. 026–026.
- [82] Steven Dytman. “Neutrino event generators”. In: *AIP Conf. Proc.* 896.1 (2007). Ed. by M. Albrow and R. Raja, pp. 178–184.
- [83] Steven Dytman. “Final state interactions in neutrino-nucleus experiments”. In: *Acta Phys. Polon. B* 40 (2009). Ed. by Arthur Ankowski and Jan Sobczyk, pp. 2445–2460.
- [84] Luis Alvarez-Ruso et al. “Recent highlights from GENIE v3”. In: *Eur. Phys. J. ST* 230.24 (2021), pp. 4449–4467. arXiv: 2106.09381 [hep-ph].
- [85] *GiBUU*. <https://gibuu.hepforge.org>.
- [86] O. Buss et al. “Transport-theoretical Description of Nuclear Reactions”. In: *Phys. Rept.* 512 (2012), pp. 1–124. arXiv: 1106.1344 [hep-ph].
- [87] T. Leitner, L. Alvarez-Ruso, and U. Mosel. “Charged current neutrino-nucleus interactions at intermediate energies”. In: *Phys. Rev. C* 73 (6 2006), p. 065502.
- [88] H. Budd, A. Bodek, and J. Arrington. *Modeling Quasi-elastic Form Factors for Electron and Neutrino Scattering*. 2003. arXiv: hep-ex/0308005 [hep-ex].
- [89] O. Lalakulich and U. Mosel. “Pion production in the MiniBooNE experiment”. In: *Phys. Rev. C* 87 (1 2013), p. 014602.
- [90] O. Lalakulich et al. “One pion production in neutrino reactions: Including nonresonant background”. In: *Phys. Rev. D* 82 (9 2010), p. 093001.

- 
- [91] E. Hernández, J. Nieves, and M. J. Vicente Vacas. “Single  $\pi$  production in neutrino-nucleus scattering”. In: *Phys. Rev. D* 87 (11 2013), p. 113009.
- [92] K. Gallmeister, U. Mosel, and J. Weil. “Neutrino-induced reactions on nuclei”. In: *Physical Review C* 94.3 (2016).

# 4

## Liège Intranuclear Cascade code

This chapter is devoted to a general presentation of the intranuclear cascade code, its ingredients, and its coupling with other codes and distributions. At the end of this chapter, we also present work started in this thesis and ongoing to implement charge current quasi-elastic reaction in the code. Section 4.1 details the ingredients of the code, while section 4.2 describes the coupling of INCL to the de-excitation codes. Section 4.3 lists other softwares within which INCL is distributed. Section 4.4 presents the current status and a plan for future developments toward the neutrino vertex implementation in INCL.

### 4.1 The INCL code

The Liège Intranuclear Cascade Model (INCL) is a code originally developed by Joseph Cugnon to simulate nuclear reactions induced by hadrons and light nuclei in the few tens of MeV to few GeV range. The lower bound of the range is imposed by the assumption that nucleons can be treated as point-like, classical, and free particles immersed in a mean field. Below a few tens of MeV, such an assumption is no longer valid. INCL must be coupled to codes that can treat the de-excitation or the break-up of the nucleus after the thermal equilibrium is reached. INCL cascade is usually coupled to the de-excitation code ABLA [1]. However, it can also be combined with the SMM [2, 3] or GEMINI++ [4, 5] de-excitation codes. Above a few GeV, the number of inelastic channels increases, and the upper bound is defined by the number of inelastic channels implemented in INCL (say which channels are treated). The code has been recently extended toward high energies ( $\approx 20$  GeV), including new interaction processes such as multipion production [6, 7], production of  $\eta$  and  $\omega$  mesons [8], and strange particles like kaons and hyperons [9–11]. INCL relies on as few free parameters as possible. As the output of the simulation, INCL predicts numerous pertinent variables, for example, total

reaction cross section, double differential cross section, particle multiplicity, recoil energy spectra, and more.

INCL solves numerically the Boltzmann equation for the transport of particles in the previously defined range. It uses the Monte-Carlo technique to propagate and follow the successive collisions of the nucleons. This method offers the advantage of treating all the nucleons dynamically, preserving their correlations. Despite the stochastic nature of the method, the computing time stays sufficiently reasonable to be implemented into more extensive transport codes as Geant4 [12–14] or MCNP [15] (an advantage compare to BUU). Within Geant4, INCL features diverse applications, including utilization for Accelerator-Driven Systems (ADS), spallation targets, radioprotection close to high-energy accelerators, radioprotection in space, proton or carbon therapy, and production of beams of exotic nuclei.

INCL features a notable agreement with an exhaustive list of experimental data [16, 17]. In Fig. 4.1, we present the benchmark to proton data that is particularly relevant to the scope of this thesis. The figure also shows the comparison with the NuWro simulation to the same data set.

The original INCL code was written in Fortran at the beginning of the 80s and was re-designed and rewritten in C++ in 2012. In this thesis, the C++ release version 6.25 is used.

### 4.1.1 Model ingredients

The INCL simulation starts when a projectile triggers a cascade of binary collisions inside the target nucleus that is generated according to the implemented nuclear model. In the following, we will detail the different ingredients of the simulation and the sequence of a cascade.

#### Projectile

The currently available projectiles are baryons (nucleons,  $\Lambda$ ,  $\Sigma$ ), mesons (pions and kaons) or light nuclei ( $A \leq 18$ ). At the beginning, the incident projectile is located with its own impact parameter on the surface of the working sphere. A *working sphere*, where all events take place, is defined as a sum of the  $R_{max}$  and an interaction distance  $d_{int}$ , where  $R_{max}$  is:

$$R_{max} = \begin{cases} R_0 + 8a & \text{for } A > 19 \\ 5.5 + 0.3(A - 6) / 12 & \text{for } 6 \leq A \leq 19 \\ R_0 + 4.5 & \text{for } 2 \leq A < 6 \end{cases} \quad (4.1)$$

where  $R_0$  [fm] and  $a$  [fm] are the radius and diffuseness of the target nucleus density, respectively. For example for carbon,  $R_{max} = 5.7$  fm. The interaction distance is defined as:

$$d_{int} = \sqrt{\sigma_{max} / 10\pi}, \quad (4.2)$$

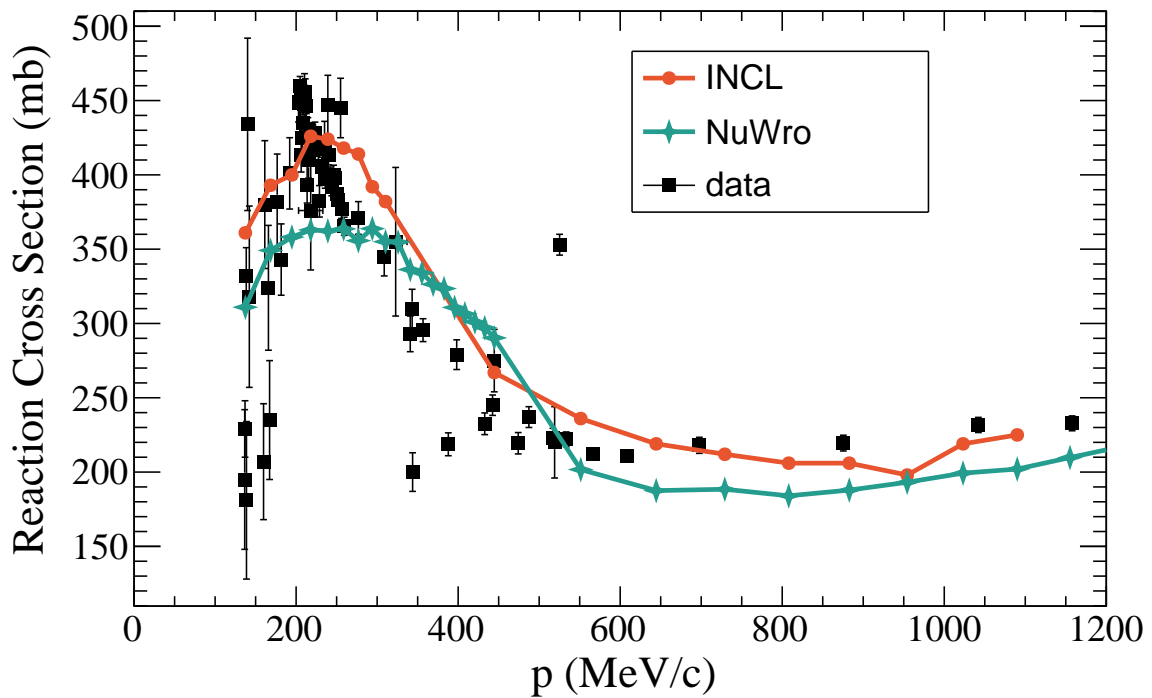


Figure 4.1 Proton induced reaction cross section on  $^{12}\text{C}$  as a function of the proton momentum calculated with INCL and NuWro models: comparison of the INCL and NuWro models to available experimental data [18–36]. Results of the NuWro 19.02.2 simulation were taken from Ref. [37].

where  $\sigma_{max}$  is maximal total reaction cross section. The impact parameter is randomly determined in a circle of radius  $R_{max}$  centered on the incident direction passing by the center of the target, as shown in Fig. 4.2. Suppose the trajectory of the projectile, defined by a randomly chosen asymptotic impact parameter and modified by the classical Coulomb field of the target, intersects the working sphere. In that case, the projectile enters the nucleus and can interact with the nucleons or not (a *transparent* event).

### Target nucleus modeling

The INCL nuclear model is essentially classical, with some additional ingredients to mimic quantum effects. Each nucleon in the nucleus has its position and momentum and moves freely in a square potential well. The radius of the potential well depends on the nucleon's kinetic energy. Nucleon momenta are distributed uniformly in the Fermi sphere (sphere with the radius of the Fermi momentum representing allowed bound nucleon momenta). The

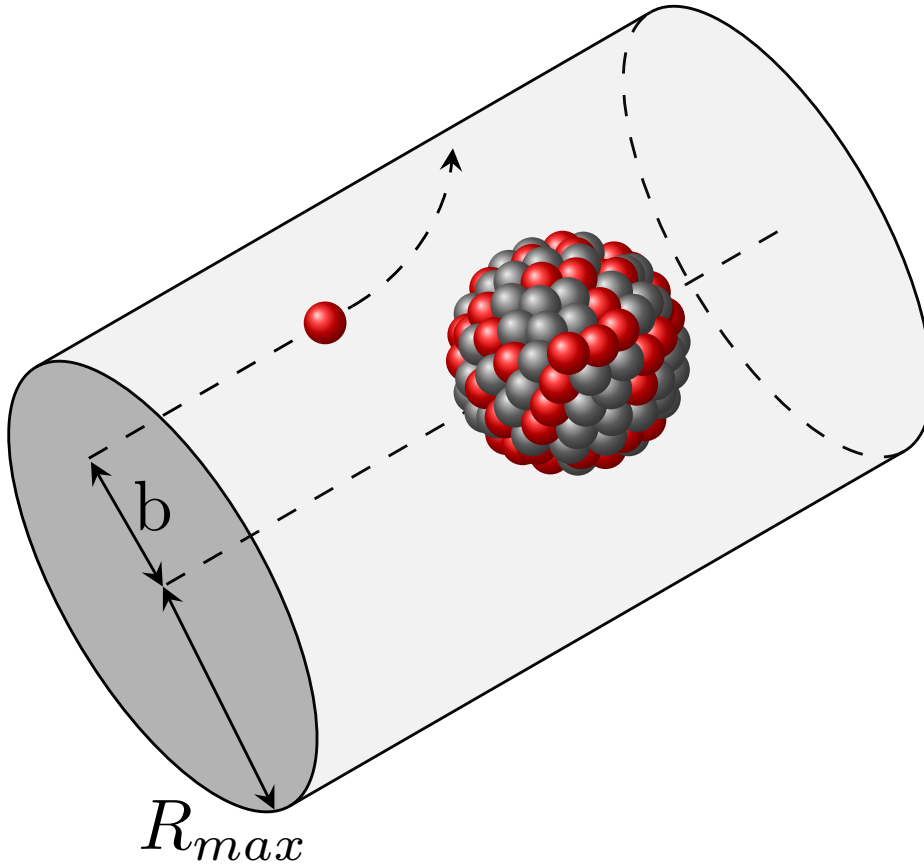


Figure 4.2 The scheme of the impact parameter  $b$  definition. Deflection because of the classical Coulomb field is also shown.

target density profile depends on its mass number:

$$\rho(r) = \begin{cases} \rho_0 \frac{1}{1 + \exp\left(\frac{r-R_0}{a}\right)} & \text{for } A > 19 \\ \rho_0 \frac{(1 + \alpha(r/a)^2)}{\exp((r/a)^2)} & \text{for } 6 < A \leq 19 \\ \rho_0 \frac{1}{\exp((r/a)^2)} & \text{for } A \leq 6, \end{cases} \quad (4.3)$$

where the density  $\rho_0$  is such that the distribution is normalized to the target mass number  $A_T$ . These parameterizations are known as the Woods-Saxon, modified-harmonic-oscillator (MHO), and Gaussian density distributions, respectively, from top to bottom in Eq. 4.3. The parameters of the Woods-Saxon distribution are taken from electron scattering measurements and parametrized according to Ref. [38]. The general shape of the density profile is shown on Fig. 4.3. The rest of the parameterizations are taken from Ref. [39]. In the former *classical* picture, for a given momentum, the particle is allowed to move in a sphere with the maximum radius fixed by the momentum, so its position is sampled in this sphere, as shown in Fig. 4.3.

The nucleon momentum is generated according to a Fermi sphere distribution with a maximal allowed Fermi momentum  $p_F$ . These  $r - p$  correlations make it impossible to generate the  $r$  and  $p$  distributions independently.

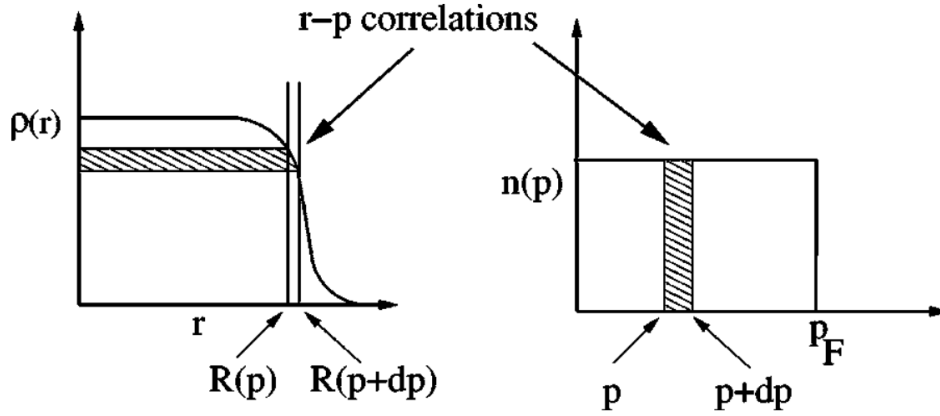


Figure 4.3 Illustration of the correlation between the spatial and momentum distributions implied by the phase space distribution from Eq. 4.3. Particles with momentum between  $p$  and  $p + dp$  can reach a maximum radial distance between  $R(p)$  and  $R(p + dp)$ . Figure and the caption are adapted from [38].

This picture has been refined to consider the quantum properties of the wave functions. Based on the *Hartree-Fock-Bogoliubov formalism* (HFB), the correlation is still valid but less strict, i.e., the nucleon has a non-zero probability for going beyond the maximum radius. The HFB calculations were performed with the HFBRAD code [40]. The HFBRAD calculated proton and neutron densities were fitted according to the Eq. 4.3 to be used as an INCL input thanks to the *fuzziness* parameter (that is defined as inverse of the correlation strength). This procedure is explained in detail in Ref. [41].

Returning to the Fermi momentum calculation, a few options are available. The default version is the constant Fermi momentum that equals  $1.37\hbar = 270 \text{ MeV}/c$ . Another option assumes the mass dependence of the Fermi momentum [42]:

$$\begin{aligned}
 p_F(A) &= \alpha - \beta \exp(-\gamma A), \\
 \alpha &= 259.416 \text{ MeV}/c, \\
 \beta &= 152.824 \text{ MeV}/c, \\
 \gamma &= 9.5157 \times 10^{-2}.
 \end{aligned}
 \tag{4.4}$$

This formula is a fit to the direct measurements by quasi-elastic electron scattering [43]. In the scope of this thesis, we use the mass-dependent Fermi momentum.

### Propagation of the particles: the cascade

The cascade reaction can be described as an avalanche of independent binary collisions. During the cascade, particles propagate inside the nucleus according to relativistic kinematics following straight trajectories. Particles are divided into *participants*—projectiles or particles that have undergone collisions with a projectile particle or another participant—and *spectators*—target particles that did not participate in any collision. In the beginning, there is only one participant: the projectile. As the projectile propagates through the target medium, the spectator particles of the target collide with the projectile and get promoted to participants. There is no interaction between the spectator nucleons of the target in order to prevent nuclear boiling. A participant nucleon can become a spectator again (*back-to-spectator* option) if its energy decreases below a threshold which is the sum of Fermi energy emission threshold, and Coulomb barrier (for protons) [44].

INCL, in advance, generates a chronological table of events based on the straight trajectories and relativistic kinematics for the possible *avatars*—types of events in INCL. Three types of avatars inside the cascade can happen: collisions, reflections or transmissions at the surface, and decay. INCL follows the **time-like approach**, meaning that all the particles are propagated until they meet one of the interaction conditions:

- two particles reach the minimal distance to interact,
- a particle hits the border of the potential well, then it deflects back or leaves the nucleus,
- a particle decays (e.g. a  $\Delta$  resonance or  $\omega$  meson).

The fate with the shortest time is chosen. If the collision is blocked, particles propagate until the next time. In case of a successful reaction, the table is updated to consider the new trajectories of the outgoing particles.

### Nuclear clusters emission

Concerning a participant nucleon at the surface, it can be reflected or emitted. It leaves the nucleus if its energy is higher than Fermi energy plus the value of its separation energy taken from mass tables based on experimental data [45] and plus Coulomb barrier for the charged particles. A notable feature of INCL is that an outgoing nucleon can become a leading nucleon for the nuclear cluster formation, assuming that the involved nucleons are located sufficiently near each other in the phase space. This feature is extensively described in Ref. [44].

Fig. 4.4 shows all the possible clusters considered up to  $A_{cl}^{max} = 12$ . For computational reasons, the default maximal cluster mass is  $A_{cl}^{max} = 8$ . If several clusters are formed, the least excited one is produced.

The cluster is emitted if all the following conditions are satisfied:

8				2p				<sup>16</sup> O	<sup>17</sup> O
7			p	p	11 ms		<sup>14</sup> N	<sup>15</sup> N	
6		2p	0.13 s	19 s	0.33 h	<sup>12</sup> C	<sup>13</sup> C		
5	2p	p	0.77 s	p	<sup>10</sup> B	<sup>11</sup> B	20 ms		
4		2p	53 d	α	<sup>9</sup> Be	1.6 10 <sup>6</sup> yr	13.8 s	24 ms	
3	p	p	<sup>6</sup> Li	<sup>7</sup> Li	0.84 s	0.18 s	n	8.5 ms	n
2	<sup>3</sup> He	<sup>4</sup> He	n	0.8 s	n	0.12 s	n	2n	
1	<sup>2</sup> H	12.3 yr	n	2n	n	2n			
<b>Z/N</b>	1	2	3	4	5	6	7	8	9

Figure 4.4 The considered clusters for the maximal allowed mass number  $A_{cl}^{max} = 12$  are identified by their charge  $Z$  (vertical ordering), and neutron  $N$  (horizontal ordering) numbers and are displayed inside the perimeter delineated by the heavy line. Stable clusters are depicted inside the yellow cells. Time-displaying cells represent clusters with a lifetime larger than 1 ms, which are considered to be detectable. Other cells (in blue) correspond to clusters with a lifetime smaller than 1 ms and are forced to decay. The picture and description are adapted from [44].

- the cluster has enough energy to leave the nucleus:

$$T_{cl} = \sum (T_i - V_i) - B_{cl} > 0, \quad (4.5)$$

where  $T_i$ 's are the kinetic energies of the nucleons,  $V_i$ 's are the depth of their potential wells and  $B_{cl}$  is a binding energy of a nuclear cluster;

- the cluster has to be able to penetrate the Coulomb barrier;
- if the nuclear cluster is emitted to tangentially, it might stay for too long in the vicinity of the nucleus and could be dissolved. Therefore we demand that the angle between the cluster's three-momentum and the radial outward direction passing by the center of mass of the potential cluster should fulfill the condition:  $\cos(\theta) > 0.7$ .

If all the conditions are met, the cluster is emitted in the direction of its total three-momentum with the kinetic energy  $T_{cl} = \sum (T_i - V_i) - B_{cl}$ , where the  $T_i$  are the kinetic energies of the nucleons,  $V_i$  are the depths of their potential wells, and  $B_{cl}$  is the binding energy of the cluster. Otherwise, only the leading nucleon is emitted.

### Pauli blocking

About quantum effects, in addition to those embedded in the elementary cross-sections used and the one previously quoted with the refined position-momentum correlation related to the quantum behavior of the wave function, the Pauli-blocking is considered and checked. There are several Pauli blocking models implemented in INCL. The *strict* Pauli blocking forbids the

interaction if the projectile momentum is below the Fermi momentum. The *statistical* Pauli blocking model considers only nearby nucleons in a phase-space volume and calculates the occupation probability. If the two nucleons  $i$  and  $j$  at positions  $r_{i(j)}$  undergo an interaction that leads to the final state with momenta  $p_{i(j)}$ , the phase-space occupation probabilities  $f_i$  are evaluated by counting nearby nucleons in a small phase space volume that is centered on the point  $(r_{i(j)}, p_{i(j)})$ :

$$f_i = \frac{1}{2} \frac{(2\pi\hbar)^3}{\frac{4\pi}{3} r_{PB}^3 \frac{4\pi}{3} p_{PB}^3} \sum_{k \neq i} \theta(r_{PB} - |\vec{r}_k - \vec{r}_i|) \theta(p_{PB} - |\vec{p}_k - \vec{p}_i|), \quad (4.6)$$

where  $\theta(x)$  is the Heaviside function, and the sum is limited to particles  $k$  with the same isospin component as particle  $i(j)$ . The factor 1/2 is introduced since spin components are ignored. Whether the collision between  $i$  and  $j$  is allowed depends on comparing the random number with the product  $(1 - f_i)(1 - f_j)$ .  $r_{PB}$  and  $p_{PB}$  depend on the nucleus, but are constrained by the fixed phase-space volume. Pauli blocking is not applied to  $\Delta$  resonances because their density is always very small. However, it is enforced for nucleons resulting from  $\Delta$  decays.

Statistical Pauli blocking and the fluctuations of the randomly-generated phase space occupation in the initial state (*Fermi sea*) might lead to non-physical results (for example, negative excitation energy). Non-uniformity of the Fermi sea might allow the interaction that would be strictly forbidden in the perfect picture. An additional procedure is applied to avoid non-physical results: the energy in the Fermi sphere is evaluated (kinetic energy of particles with  $p < p_F$ ), and collisions are not allowed if this energy is smaller than the Fermi-gas minimum energy. This procedure is referred to as the *Coherent Dynamical Pauli Principle* (CDPP) [38].

Non-uniform Fermi sea might allow for strictly forbidden interactions. However, it also allows accounting for surface effects and for effects of the depletion of the Fermi sea as the cascade process evolves. The compromising solution is to apply the strict Pauli blocking for the first collision and the statistical one for the subsequent ones [44, 46].

### End of the cascade

The cascade lasts until one of these conditions is satisfied:

- there are no more participants,
- the mass number of the target is less than 4,
- the projectile leaves without any interaction (transparent event),
- the stopping time determined by the model is reached.

The stopping time of the cascade depends on the target mass number  $A_T$  and is defined as:

$$t_{stop} = 29.8 (A_T)^{0.16} [fm/c], \quad (4.7)$$

for hadrons and for mesons it is:

$$t_{stop} = 30.18 (A_T)^{0.17} [fm/c]. \quad (4.8)$$

At the end of the cascade process, all the resonances and short-lived clusters with a lifetime of less than 1 ms (e.g.,  ${}^5\text{Li}$ ) are forced to decay. Before providing the information about the remnant to the further de-excitation routine, INCL checks the conservation of baryon number, charge, energy, momentum, and angular momentum.

### 4.1.2 Elementary collisions in INCL

In this section, we will cover the handling of collisions in INCL. The outgoing channel is chosen using the Monte Carlo method, comparing a random number and the elementary cross sections of the available channels.

#### Baryon-baryon collisions

The Binary Collision Avatar class manages the baryon-baryon collisions. The possible collisions are:

$$\begin{aligned} NN &\rightarrow NN \\ NN &\leftrightarrow N\Delta \\ N\Delta &\rightarrow N\Delta \\ \Delta\Delta &\rightarrow \Delta\Delta, \end{aligned} \quad (4.9)$$

where  $N$  is a nucleon and  $\Delta$  is a resonance  $\Delta_{1232}$ . The reaction  $N\Delta \rightarrow \Delta\Delta$  is neglected. In order to choose the elastic or inelastic channel, the random number comprised between 0 and 1 is compared to  $\sigma_{el}/\sigma_{tot}$ . If the  $\sigma_{el}/\sigma_{tot}$  is larger than this random number, the elastic channel will be simulated. Otherwise, the inelastic channel will be chosen. Fig. 4.5 presents the total, elastic, and inelastic nucleon-nucleon cross sections implemented in INCL. The polar scattering angle in the center-of-mass (CMS) system is drawn randomly according to a law parameterized on the experimental angular distributions. The azimuthal angle is randomly generated.

In the case of the elastic collision, the differential cross section is used to generate the final state of the system in the CMS frame. Refs.[47] and [38] contain a detailed description of the baryon-baryon collisions and the cross section parametrization. Here we will discuss only the proton-proton collision case. The differential elastic  $p-p$  cross section is well parametrized

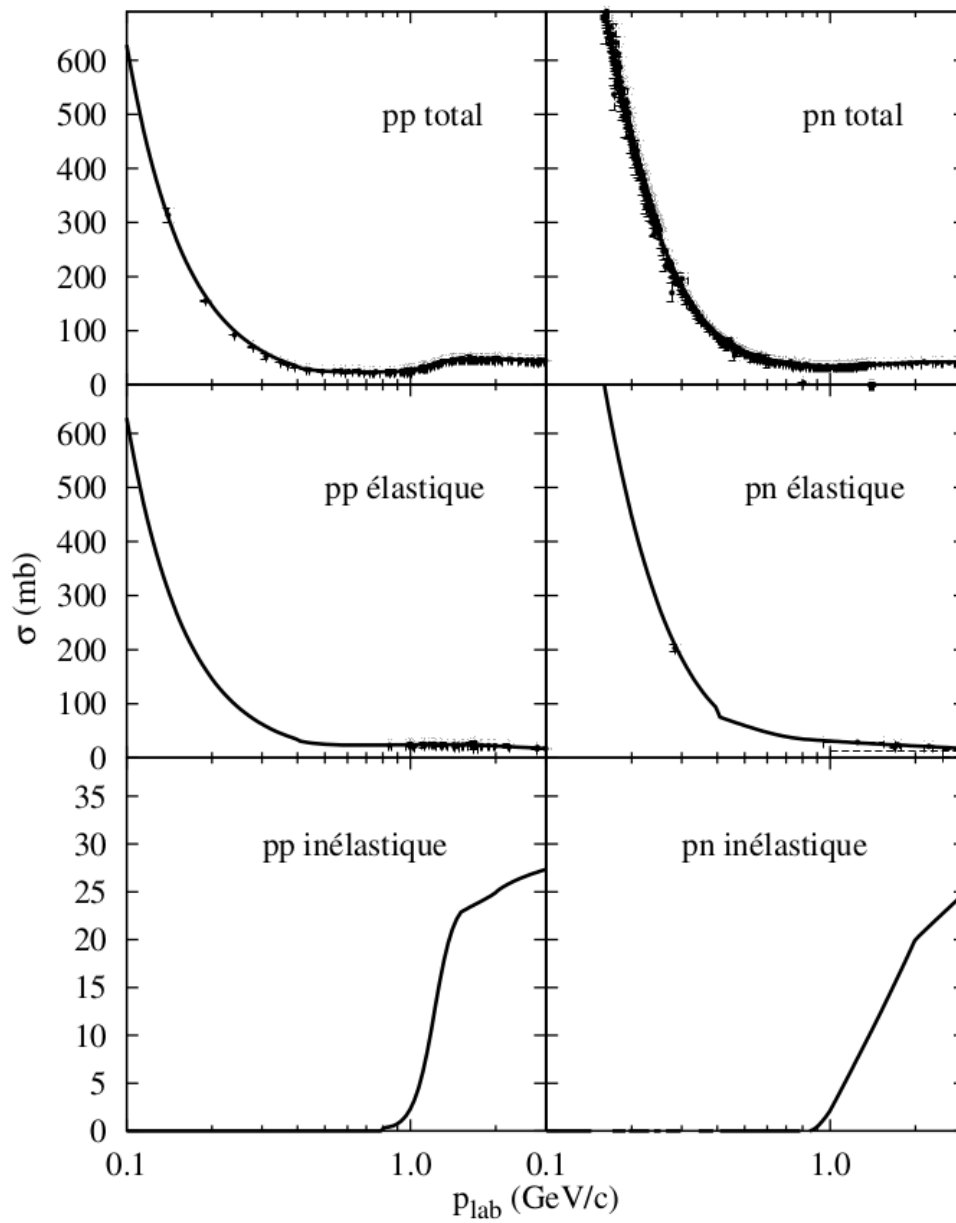


Figure 4.5 Elementary nucleon-nucleon cross sections. The lines represent the parametrization used in INCL [38, 47]. Experimental data are taken from Ref. [48]. The plot and the description are adapted from [49].

by:

$$\frac{d\sigma}{dt} \propto e^{B_{pp}t}, \quad (4.10)$$

where  $t$  is the Mandelstam variable and  $B_{pp}$  is the function the incident lab momentum  $p_{lab}$  in GeV/c:

$$\begin{aligned} B_{pp} &= \frac{5.5p_{lab}^8}{7.7 + p_{lab}^8}, & p_{lab} < 2, \\ &= 5.334 + 0.67(p_{lab} - 2), & 2 < p_{lab}. \end{aligned} \quad (4.11)$$

Equation 4.10 is sufficient to generate the final state in the proton-proton center-of-mass since the protons are emitted back-to-back.

### $\Delta$ production and decay

The inelastic cross section is calculated as the difference between the total and the elastic cross sections.  $\Delta$  resonance is created with the lifetime randomly assigned according to the following exponential law:

$$\rho(\tau) = \exp\left(\frac{-q^3}{q^3 + 180^3} \frac{\Gamma}{\hbar} \tau\right), \quad (4.12)$$

where  $\Gamma$  is the characteristic width of the  $\Delta$  resonance ( $\Gamma \sim 115$  MeV) and  $q$  (in MeV/c) is given by

$$q^2 = \frac{[m_{\Delta}^2 - (m_N - m_{\pi})^2][m_{\Delta}^2 - (m_N + m_{\pi})^2]}{4m_{\Delta}^2} \quad (4.13)$$

The mass  $m_{\Delta}^2$  is chosen randomly according to the distribution:

$$f(m_{\Delta}) = F_N \frac{q^3}{q^3 + q_0^3} \frac{1}{1 + 4\left(\frac{m_{\Delta} - m_{\Delta}^0}{\Gamma_0}\right)}, \quad (4.14)$$

where  $F_N$  is the normalization constant, and the parameters are  $q_0 = 0.18$  GeV,  $m_{\Delta}^0 = 1.215$  GeV, and  $\Gamma_0 = 0.13$  GeV.

$\Delta$  decays at the end of its assigned lifetime in a pion and a nucleon  $\Delta \rightarrow \pi N$ . The decay of  $\Delta$  is anisotropic, and the chosen angular distribution for the produced pions is given in the  $\Delta$  CMS reference frame by [50]:

$$\frac{d\sigma}{d\Omega} = 1 + 3\lambda \cos^2\theta_{\pi}, \quad (4.15)$$

where  $\theta_{\pi}$  is the angle between the directions of pion and  $\Delta$  in the rest frame of latter and  $\lambda$  is the helicity of the  $\Delta$  resonance. For example, in  $N - N$  collision, the helicity is given by  $\cos^2\theta$ , where  $\theta$  is a polar angle in the CMS frame, at which  $\Delta$  was produced.

### $\pi$ -nucleon collisions

Collisions between pions and between a pion and a  $\Delta$  are neglected, and pions, feeling, by hypothesis, no potential, cannot be reflected at the nuclear surface. Inelastic  $\pi N$  scattering is also omitted for convenience [51].

Fig. 4.6 represents the experimental  $\pi^+ p$  and  $\pi^- p$  total cross sections. Like the baryon-baryon cross sections, the pion-nucleon cross sections have been parameterized from experimental data. Only the  $\pi^+ p \rightarrow \Delta^{++}$  cross section is implemented, and the other cross sections are determined by isobaric symmetry.

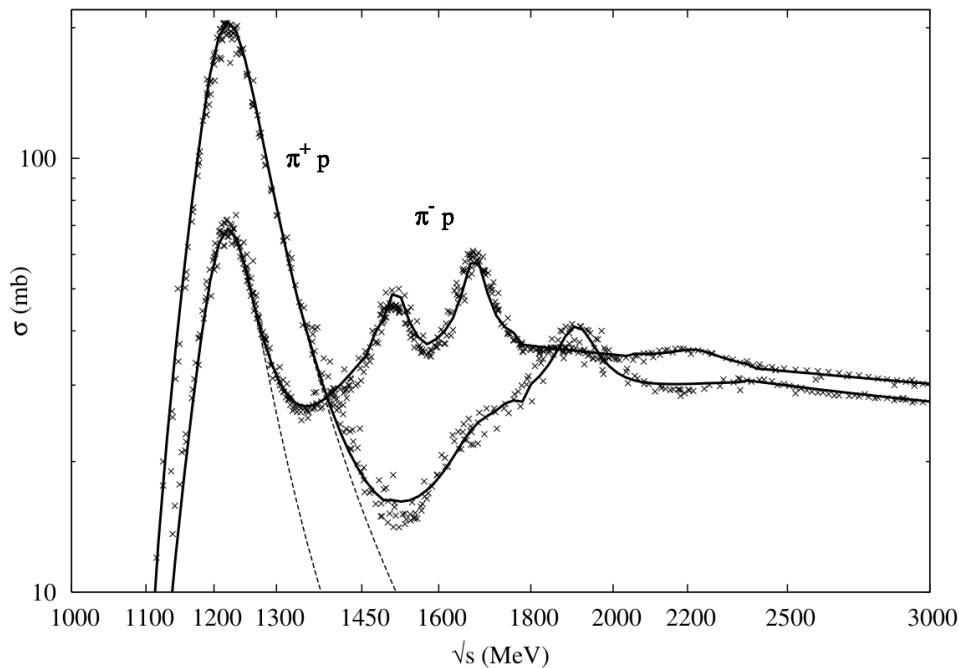


Figure 4.6 Parametrization for the  $\pi^+ p$  and  $\pi^- p$  total cross sections. The crosses represent experimental data coming from Particle Data Group [52]. Continuous lines and dotted lines stand for the total reaction cross section and the  $\Delta$  recombination cross section used in INCL. The plot and the description are adapted from [49].

### Multipion production $NN \rightarrow NNn\pi$

The multipion production is extensively described in Ref. [53]. All the cross sections  $\sigma_T(NN \rightarrow NNn\pi)$  for producing  $n$  pions in the N-N collision are constructed for the given isospin state  $T$  from the adjusted parametrizations of experimentally known cross sections for specific final states. Cross sections are constructed explicitly until  $n = 3$ . The test of the total cross section is considered to correspond to the  $n = 4$  case.

Table 4.1 List of considered reactions involving strangeness based on experimental data.

$NN \rightarrow N\Lambda K$	$\pi N \rightarrow \Lambda K$	$N\bar{K} \rightarrow N\bar{K}$	$NK \rightarrow NK$
$\rightarrow N\Sigma K$	$\rightarrow \Sigma K$	$\rightarrow \Lambda\pi$	$\rightarrow NK\pi$
$\rightarrow N\Lambda K\pi$	$\rightarrow \Lambda K\pi$	$\rightarrow \Sigma\pi$	$\rightarrow NK\pi\pi$
$\rightarrow N\Sigma K\pi$	$\rightarrow \Sigma K\pi$	$\rightarrow N\bar{K}\pi$	$N\Lambda \rightarrow N\Lambda$
$\rightarrow N\Lambda K\pi\pi$	$\rightarrow \Lambda K\pi\pi$	$\rightarrow \Lambda\pi\pi$	$\rightarrow N\Sigma$
$\rightarrow N\Sigma K\pi\pi$	$\rightarrow \Lambda\pi\pi$	$\rightarrow \Sigma\pi\pi$	$N\Sigma \rightarrow N\Lambda$
$\rightarrow NNK\bar{K}$	$\rightarrow NK\bar{K}$	$\rightarrow N\bar{K}\pi\pi$	$\rightarrow N\Sigma$

Table 4.2 List of the reactions involving strangeness and requiring information that has been taken exclusively from models. The X stands for all possible reactions, excluding the reaction summarised in Table 4.1.

$\Delta N \rightarrow N\Lambda K$	$NN \rightarrow K + X$
$\rightarrow N\Sigma K$	
$\rightarrow \Delta\Lambda K$	$\pi N \rightarrow K + X$
$\rightarrow \Delta\Sigma K$	
$\rightarrow NNK\bar{K}$	

### Reactions involving strange particles

The kaons ( $K^0$  and  $K^+$ ), antikaons ( $\bar{K}^0$  and  $K^-$ ), the  $\Sigma$ 's ( $\Sigma^-$ ,  $\Sigma^0$ , and  $\Sigma^+$ ) and the  $\Lambda$  can be produced in INCL [54]. The heavier strange particles have lower production rates and therefore are not modeled. Table 4.1 summarized the implemented reactions based on the experimental data. Reactions mentioned in table 4.2 are also considered, though there is limited experimental data, and the cross sections are coming from models.

At the end of the cascade, the hyperremnant (remnant with at least one hyperon inside) might be produced with at least one strange particle inside the target nucleus. In INCL, the trapped kaons are ejected at the end of the cascade, and their kinematics is corrected according to their potential. The  $\Sigma$ 's and antikaons are absorbed, and the excess energy is converted into the excitation energy. At that stage, the hyperremnant contains only protons, neutrons, and  $\Lambda$ 's and is handled by the de-excitation code ABLA [55].

## 4.2 Coupling to the de-excitation models

After the intranuclear-cascade stage, the nucleus still has the excitation energy that needs to be released. This excited nucleus, called the *cascade remnant*, usually relaxes by particle emission (photons, nucleons, light nuclei), fission, or other mechanisms (e.g., multifragmentation). Therefore, coupling a de-excitation code is mandatory to describe the full reaction correctly. Currently, INCL has an interface to be used with GEMINI [4, 5], SMM [2, 3], and ABLA [1]. Regardless of the choice of the de-excitation model, INCL, by default, applies the Fermi

breakup model for the light remnants ( $A \leq 16$ ). In order to use the other de-excitation models for the light nuclei, the Fermi breakup model has to be explicitly disabled. Since the ABLA code proved to be accurate for the light nuclei [56], which is relevant in the scope of this thesis, we will focus on describing it in more detail.

### 4.2.1 The de-excitation code ABLA

The ablation model ABLA [55] describes the de-excitation of an excited nuclear system through the emission of  $\gamma$ -rays, neutrons, light-charged particles, and intermediate-mass fragments, or fission in case of hot and heavy remnants. Fig. 4.7 shows the ABLA de-excitation diagram with the choice between the different processes. In the following, we describe the predominant features of each decay process.

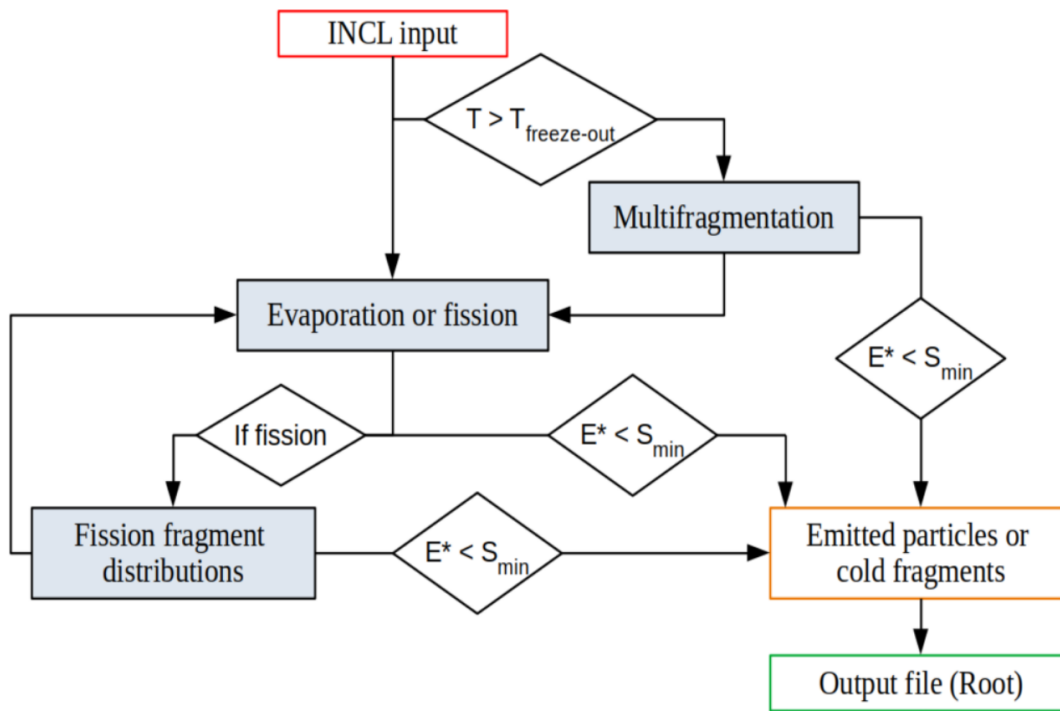


Figure 4.7 ABLA diagram of de-excitation processes, where  $E^*$  and  $T$  represent the excitation energy and temperature of the nuclear system, respectively,  $S_{min}$  is the minimum particle separation energy, and  $T_{freeze-out} = \max \left[ 5.5, 9.33e^{(-2.82 \times 10^{-3} A_{rem})} \right]$  is the freeze-out temperature;  $A_{rem}$  is the mass number of the remnant. The picture and description are adapted from [55].

**Multifragmentation:** the multifragmentation stage begins with a hot nuclear system (*spectator* or *residue*), left after the initial collision stage. If the residue's excitation energy per nucleon is high enough [57], the system will undergo multifragmentation decay; otherwise,

the excited remnant will de-excite directly via the subsequent evaporation and/or fission. If the temperature threshold is overcome:

$$T_{freeze-out} = \max \left[ 5.5, 9.33 e^{(-2.82 \times 10^{-3} A_{rem})} \right], \quad (4.16)$$

where  $A_{rem}$  is the mass number of the remnant, the remnant breaks into the set of nucleons and fragments, whose mass is sampled from the empirical law:

$$\frac{d\sigma}{dA} = A^{-\tau(E^*/A)}, \quad (4.17)$$

where the slope depends on the remnant's mass number and excitation energy and is parameterized according to Ref. [58]. Each breakup residue with  $A > 4$  will then be subject to particle evaporation or, if appropriate, fission. What is observed in the detector after this process are cold fragments, also known as *intermediate-mass fragments* (IMFs).

**Particle evaporation:** the particle emission probabilities are calculated according to the Weisskopf-Ewing formalism [59] to compute the decay width  $\Gamma_\nu$  of a specific initial nucleus by emission of a particle  $\nu$ . The kinetic-energy spectra of the emitted particles are directly calculated from the inverse cross sections. Particle emission channels massively dominate over the  $\gamma$  emission, so many de-excitation models do not include the  $\gamma$ -ray emission at all. However, at the end of the de-excitation stage,  $\gamma$  emission can become competitive to particle decay. The  $\gamma$  radiation rate can be parameterized as:

$$\Gamma_\gamma(T) = 0.624 \times 10^{-9} A^{1.6} T^5, \quad (4.18)$$

where  $A$  is the mass number of the initial nucleus and  $T$  is the nuclear-temperature parameter [60]. The discrete  $\gamma$ -ray emission from the lower-lying nuclear levels is omitted in ABLA since this requires specific nuclear structure databases [61].

**Fission:** this process plays a leading role in the decay of heavy nuclei. A competition between fission and other decay channels is calculated at each de-excitation stage. The kinetic energies of the fission fragments are calculated according to Ref. [62]. In the end, fission is followed by the de-excitation until the residual excitation energies of the fission fragments are significantly lower than the lowest particle-emission threshold.

### 4.3 INCL distribution within other softwares

The INCL model is available within the latest Geant4 packages (starting from version 9.5) within QGSP\_INCLXX, QGSP\_INCLXX\_HP, FTFP\_INCLXX, and FTFP\_INCLXX\_HP physics

lists that use the Quark-Gluon String model (QGS) and the Fritiof model (FTF) at high energy and NeutronHP model if the HP option is selected for neutron interactions at low energy. INCL model is also directly accessible through its interface (G4INCLXXInterface). The model covers the 1 MeV—20 GeV energy range and any target nucleus starting from  $^2\text{H}$ . Fig. 4.8 shows the map of models for the INCLXX-based physics lists. The ABLA++ model can be used for the further de-excitation stage.

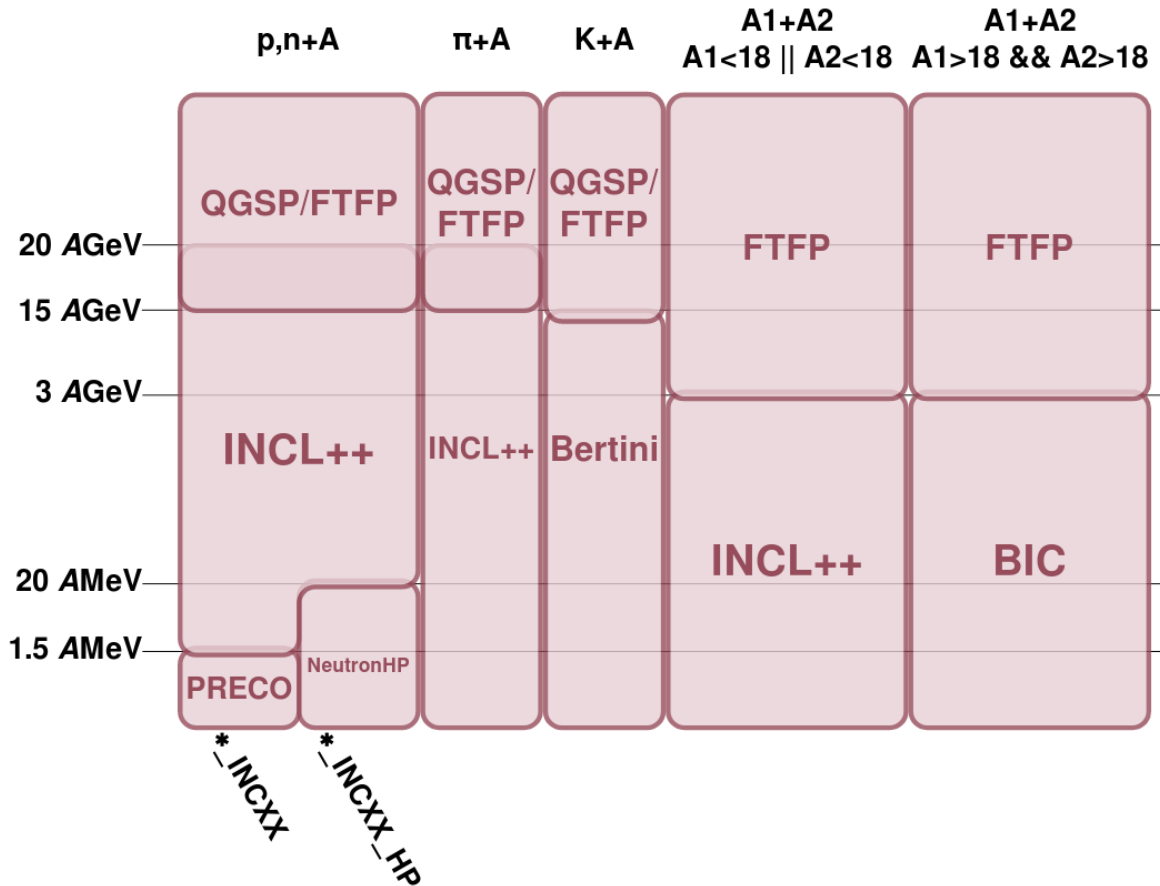


Figure 4.8 Model map for the INCL-based physics lists. The first two columns represent nucleon- and pion-induced reactions. The fourth column represents nucleus-nucleus reactions where at least one of the partners is below  $A=18$ . The fifth column represents other nucleus-nucleus reactions. The picture is adapted from [63].

INCL is available in Monte Carlo N-Particle (MCNP) [15] which is a particle transport software developed at Los Alamos National Laboratory. The public release of MCNPX2.7.0 contains the INCL4.2 version; INCL4.6/ABLA07 was implemented in a private version [64]. PHITS (Particle and Heavy Ion Transport code System) [65]—a general purpose Monte Carlo particle transport simulation code developed in Japan—employs the last Fortran version of INCL for simulating the dynamic stage of hadron-induced nuclear reactions in the intermediate energy region. INCL is implemented not only by software propagating particles through

matter but also by one of the neutrino MC generators—GENIE. It is available in the latest GENIE release [66].

## 4.4 CCQE implementation in INCL

Currently, INCL does not support leptons as projectiles. We make a step forward towards lepton implementation by preparing a quasi-elastic neutrino/antineutrino vertex (both the charged current and neutral current). As mentioned in Chapter 3, for the neutrino scattering off the free nucleon target cross section calculation the Llewellyn-Smith formula [67] is employed. It describes both neutral and charged currents for neutrinos and antineutrinos:

$$\frac{d\sigma^{v/\bar{v}}}{d|q^2|} = \frac{M^2 G^2 (f^{CC/NC})^2}{8\pi E_\nu^2} \left[ A(q^2) \mp B(q^2) \frac{(s-u)}{M^2} + \frac{C(q^2)(s-u)^2}{M^4} \right], \quad (4.19)$$

where  $M = \frac{M_p + M_n}{2}$  is an average nucleon mass,  $G$ —Fermi constant,  $f^{CC} = \cos(\theta_C)$ , where  $\theta_C$  is a Cabibbo angle,  $f^{NC} = 1$ ,  $q^2 = -Q^2$ —four-momentum transfer,  $s - u = 4ME_\nu + q^2 - m^2$ —Mandelstam variables. The A, B, and C coefficients are defined as follows:

$$\begin{aligned} A &= \frac{1}{4} \left( \frac{m^2}{M^2} - z \right) \left[ (4-z)(G_A)^2 - (4+z)(F_1^V)^2 - z(F_2^V)^2 \left( 1 + \frac{1}{4}z \right) \right. \\ &\quad \left. - 4F_1^V F_2^V z - \frac{m^2}{M^2} \left( (F_1^V + F_2^V)^2 + (G_A + 2F_p)^2 + (z-4)(F_p)^2 \right) \right] \\ B &= -zG_A(F_1^V + F_2^V) \\ C &= \frac{1}{4} \left[ (G_A)^2 + (F_1^V)^2 - z \left( \frac{F_2^V}{2} \right)^2 \right], \end{aligned} \quad (4.20)$$

where  $z = \frac{q^2}{M^2}$ ,  $m$  is a mass of a charged lepton or a neutrino for CC or NC scattering,  $F_{1,2}^V$  and  $G_A$  are vector and axial form-factors,  $F_p$  is a pseudoscalar axial form factor. We follow Ref. [68] for the  $F_{1,2}^V$ ,  $G_A$  and  $F_p$  definitions:

$$\begin{aligned} (F_{1,2}^V)^{CC} &= F_{1,2}^p - F_{1,2}^n \\ (F_{1,2}^V)^{NCp/n} &= \pm \frac{1}{2} \left[ F_{1,2}^p - F_{1,2}^n \right] - 2 \sin^2 \theta_W F_{1,2}^{p/n} - \frac{1}{2} F_{1,2}^s, \end{aligned} \quad (4.21)$$

where  $\theta_W$  is the Weinberg angle. Vector form factors are defined as:

$$\begin{aligned} F_1^{V,p/n} &= \left( 1 - \frac{1}{4}y \right)^{-1} \left[ G_E^{p/n} - \frac{1}{4}yG_M^{p/n} \right] \\ F_2^{V,p/n} &= \left( 1 - \frac{1}{4}y \right)^{-1} \left[ G_M^{p/n} - G_E^{p/n} \right], \end{aligned} \quad (4.22)$$

where  $(G_E)$  and  $(G_M)$  are electric and magnetic form factors. Following the example of the NuWro code, we use the BBBA05 parametrization [69]. The axial form factors are:

$$\begin{aligned} G_A^{CC} &= g_A (1 + Q^2/M_A^2)^{-2} \\ G_A^{NC,p/n} &= \frac{1}{2} (1 + Q^2/M_A^2)^{-2} (\pm g_A - g_A^s) \\ F_{1,2}^s &= F_{1,2}^s(0) (1 + Q^2/4M^2)^{-1} (1 + Q^2/M_V^2)^{-2}, \end{aligned} \quad (4.23)$$

where  $g_A = 1.2670 \pm 0.0035$  [52], and  $M_V = 0.84$  GeV [70],  $M_A = 1.03$  GeV is the axial mass, and  $g_A^s$  is the contribution of quark-antiquark pairs to the nucleon's spin. In our case,  $g_A^s = 0$ . The pseudoscalar axial form factor can be written in terms of the axial form factor:

$$F_P = \frac{4M^2}{m_\pi^2 + Q^2} G_A^{CC} \quad (4.24)$$

The above cross section formula was implemented in a standalone CCQE code that will later become a part of INCL. To ensure the correct implementation, we have compared the calculations with the Llewellyn-Smith formula implemented in NuWro and our standalone implementation, which is shown in Fig. 4.9. The results are identical for both cases, ensuring our implementation is correct. In the following, we discuss the further steps to finalize the CCQE implementation in INCL.

In this reaction, the four-momentum transfer is:

$$q^2 = (k - k')^2 = (p' - p)^2, \quad (4.25)$$

where  $k, k', p, p'$  are the four-momenta of the initial and final leptons and the initial and final nucleons.  $k$  and  $p$  are known since these are the four-momenta of the neutrino and the initial lepton. The general idea of the CCQE simulation is to generate  $k'$  and  $p'$  having  $k$  and  $p$ ; calculate  $q^2$  and  $(s - u)$  based on the generated kinematics; calculate the cross section and obtain the total cross section using the Monte-Carlo method:

$$\sigma_{total} \sim \frac{1}{N} \sum_{i=1}^N \sigma(q_i^2), \quad (4.26)$$

where  $N$  is the number of simulated events and  $q_i^2$  is a four-momentum transfer in the event number  $i$ .

To generate the kinematics of the outgoing particles, we need to move to the CMS (fig. 4.10). The Mandelstam variable  $s$  is invariant under Lorentz transformation:

$$s = (k + p)^2 = (E + E_p)^2 - (\vec{k} + \vec{p})^2 = (E^* + E_p^*)^2 \quad (4.27)$$

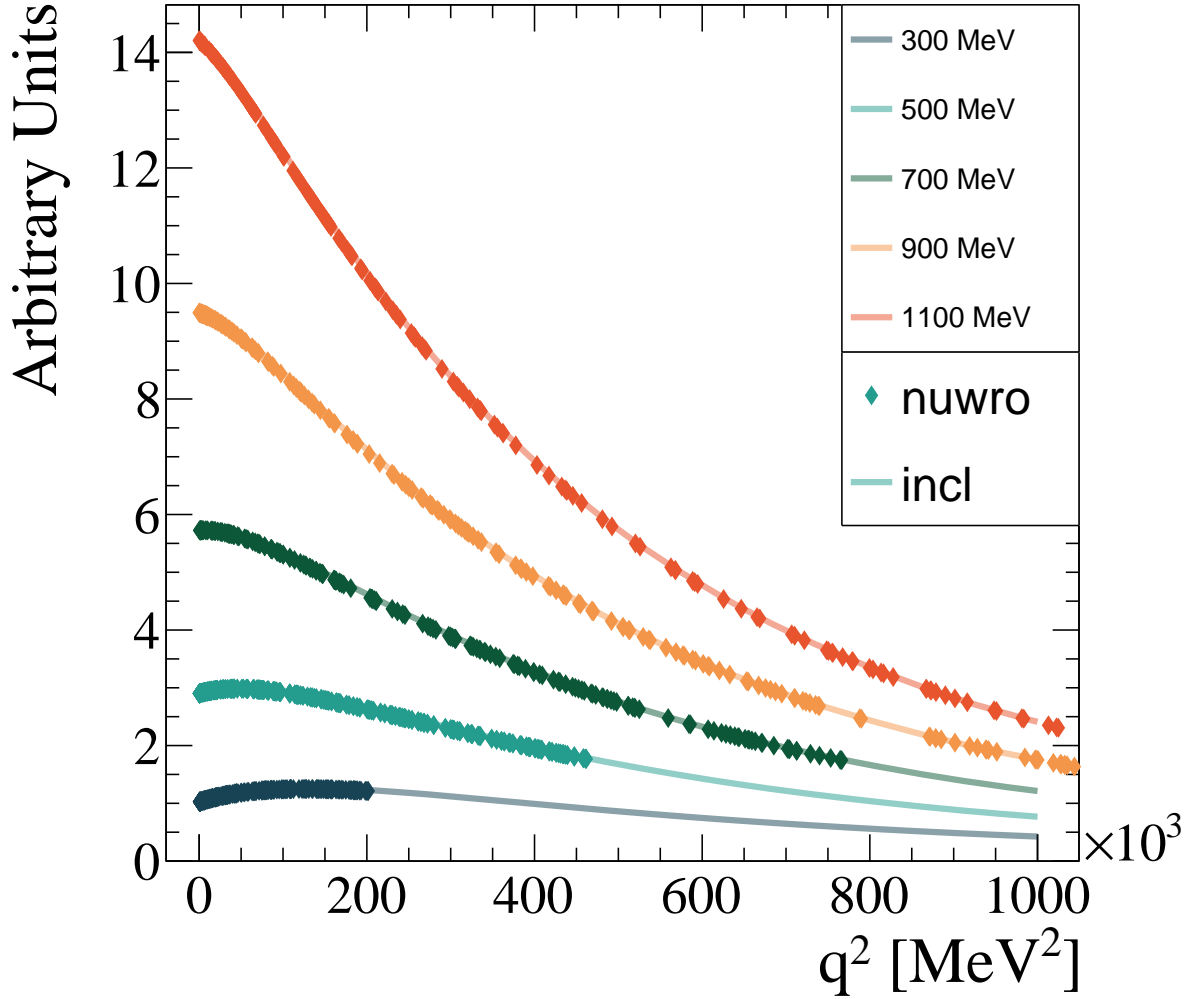


Figure 4.9  $\left[ A(q^2) \mp B(q^2) \frac{(s-u)}{M^2} + \frac{C(q^2)(s-u)^2}{M^4} \right]$  simulated with NuWro and standalone CCQE code for different neutrino energies. The standalone CCQE code does not have the energy transfer constraints implemented yet. It, therefore, is extended to the nonphysical  $q^2$  region.

Thus, the  $\sqrt{s}$  in CMS is:

$$\sqrt{s} = E^* + E_p^* = \sqrt{p^{*2} + m^2} + \sqrt{p^{*2} + M^2} \quad (4.28)$$

Using equation 4.28 we can calculate  $p^*$ :

$$p^* = \sqrt{E^{*2} - m^2} = \frac{[s - (m - M)^2][s - (m + M)^2]}{2\sqrt{s}} \quad (4.29)$$

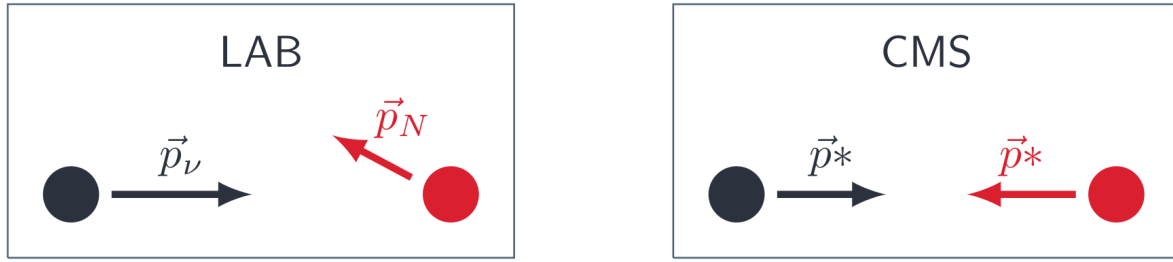


Figure 4.10 The transition scheme from the laboratory frame to CMS for the final state kinematics generation. The picture is adapted from [71].

For simplicity, we use the spherical coordinate system to generate the momentum direction in CMS:

$$\vec{p}^* = p^* (\sin\theta \cos\phi, \sin\theta \sin\phi, \cos\theta), \quad (4.30)$$

where  $\phi$  and  $\theta$  are generated randomly:

$$\begin{aligned} \phi &= 2\pi \cdot \text{Rand}[0, 1] \\ \theta &= 2 \cdot \text{Rand}[0, 1] - 1, \end{aligned} \quad (4.31)$$

where  $\text{Rand}[0, 1]$  is a random number between 0 and 1.

To obtain the results in the laboratory frame, we must apply the Lorentz boost in direction  $\hat{n} = \vec{v}/v$ , where  $\vec{v}$  is:

$$\vec{v} = \frac{\vec{p}_\nu + \vec{p}_N}{E_\nu + E_N} \quad (4.32)$$

We must implement the accept-reject method to get the final cross section and the energy transfer distribution. Since the given cross section formula is complex, it is impossible to integrate it analytically, and we will need to employ numerical methods. The two options are creating splines that will approximate the initial function (as done, for example, in GENIE) or using the Monte-Carlo method of throwing so-called test events to numerically find the maximum of the function (as done in NuWro). Once the energy transfer is known, one can sample the rest of the kinematics in the rest frame and then translate the result to the laboratory frame. This framework can be adjusted later to suit the simulation of electron scattering.

For neutrino studies, simulating the particular experimental neutrino flux is often essential. Currently, INCL supports only the simulation of mono-energetic projectiles. The possibility of generating the projectile energy according to the given distribution must be implemented. We leave the continuation of this work for the future.

## References

- [1] *Proceedings of Joint ICTP-IAEA Advanced Workshop on Model Codes for Spallation Reactions (ICTP Trieste, Italy, 4-8 February 2008)*. 2008, pp. 181–221.
- [2] A. S. Botvina et al. “Multifragmentation of spectators in relativistic heavy ion reactions”. In: *Nucl. Phys. A* 584 (1995), pp. 737–756.
- [3] J. P. Bondorf et al. “Statistical multifragmentation of nuclei”. In: *Phys. Rept.* 257 (1995), pp. 133–221.
- [4] Davide Mancusi, Robert J. Charity, and Joseph Cugnon. “Unified description of fission in fusion and spallation reactions”. In: *Phys. Rev. C* 82 (2010), p. 044610. arXiv: 1007.0963 [nucl-th].
- [5] R. J. Charity et al. “Systematics of complex fragment emission in niobium-induced reactions”. In: *Nucl. Phys. A* 483 (1988), pp. 371–405.
- [6] S. Pedoux et al. “Extension of INCL4 between 2 and 15GeV”. In: *Advances in Space Research* 44.8 (2009). Life Sciences in Space, pp. 926–933.
- [7] Davide Mancusi et al. “On the role of secondary pions in spallation targets”. In: *Eur. Phys. J. A* 53.5 (2017), p. 80. arXiv: 1603.05453 [nucl-th].
- [8] J. C. David et al. “ $\eta$  and  $\omega$  mesons as new degrees of freedom in the intranuclear cascade model INCL”. In: *Eur. Phys. J. Plus* 133.7 (2018), p. 253. arXiv: 1802.04731 [nucl-ex].
- [9] J. Hirtz et al. “Parametrization of cross sections for elementary hadronic collisions involving strange particles”. In: *Eur. Phys. J. Plus* 133.10 (2018), p. 436. arXiv: 1805.01655 [nucl-th].
- [10] J. L. Rodríguez-Sánchez et al. “Constraining the  $\Lambda$ -nucleus potential within the Liège intranuclear cascade model”. In: *Phys. Rev. C* 98 (2 2018), p. 021602.
- [11] J. Hirtz et al. “Strangeness production in the new version of the Liège intranuclear cascade model”. In: *Phys. Rev. C* 101 (1 2020), p. 014608.
- [12] S. Agostinelli et al. “Geant4—a simulation toolkit”. In: *Nuclear Instruments and Methods in Physics Research Section A: Accelerators, Spectrometers, Detectors and Associated Equipment* 506.3 (2003), pp. 250–303.
- [13] J. Allison et al. “Geant4 developments and applications”. In: *IEEE Transactions on Nuclear Science* 53.1 (2006), pp. 270–278.
- [14] J. Allison et al. “Recent developments in Geant4”. In: *Nuclear Instruments and Methods in Physics Research Section A: Accelerators, Spectrometers, Detectors and Associated Equipment* 835 (2016), pp. 186–225.

- [15] *The MPCNP code*. <https://mcnp.lanl.gov/index.html>.
- [16] J. C. David. “Spallation reactions: A successful interplay between modeling and applications”. In: *The European Physical Journal A* 51.6 (2015).
- [17] S. Leray et al. “Results from the IAEA Benchmark of Spallation Models”. In: *J. Korean Phy. Soc.* 59.2 (2011), pp. 791–796.
- [18] A. Auce et al. “Reaction cross sections for protons on  $^{12}\text{C}$ ,  $^{40}\text{Ca}$ ,  $^{90}\text{Zr}$ , and  $^{208}\text{Pb}$  at energies between 80 and 180 MeV”. In: *Phys. Rev. C* 71 (6 2005), p. 064606.
- [19] A. Ingemarsson et al. “Reaction cross sections for 65 MeV protons on targets from  $^9\text{Be}$  to  $^{208}\text{Pb}$ ”. In: *Nucl. Phys. A* 653 (1999), pp. 341–354.
- [20] M. Trzaska et al. “Excitation of the Delta (1232) resonance in proton - nucleus collisions”. In: *Z. Phys. A* 340 (1991), pp. 325–331.
- [21] I. Slaus et al. “Structure in the energy dependence of the proton total reaction cross section for C and Si in the energy region 20-40 MeV”. In: *Phys. Rev. C* 12 (1975), pp. 1093–1095.
- [22] J. J. H. Menet et al. “Total Reaction Cross-Section Measurements With 60-MeV Protons”. In: *Phys. Rev. Lett.* 22 (21 1969), pp. 1128–1131.
- [23] J. J. H. Menet et al. “Total-Reaction-Cross-Section Measurements for 30-60-MeV Protons and the Imaginary Optical Potential”. In: *Phys. Rev. C* 4 (4 1971), pp. 1114–1129.
- [24] Robert E. Pollock and G. Schrank. “Proton Total Reaction Cross Sections at 16.4 MeV”. In: *Phys. Rev.* 140 (3B 1965), B575–B585.
- [25] Bruce D. Wilkins and George Igo. “10-MeV Proton Reaction Cross Sections for Several Elements”. In: *Phys. Rev.* 129 (5 1963), pp. 2198–2206.
- [26] Verena Meyer, R. M. Eisberg, and R. F. Carlson. “Total Reaction Cross Sections of Several Nuclei for 61-MeV Protons”. In: *Phys. Rev.* 117 (5 1960), pp. 1334–1336.
- [27] T.J. Gooding. “Proton total reaction cross sections at 34 MeV”. In: *Nuclear Physics* 12.3 (1959), pp. 241–248.
- [28] Edward J. Burge. “The total proton reaction cross section of carbon from 10—68 MeV by a new method”. In: *Nuclear Physics* 13.4 (1959), pp. 511–515.
- [29] J. M. Cassels and J.D. Lawson. In: *Proceedings of the Physical Society* 67 (1954), p. 125.
- [30] P.U. Renberg et al. “Reaction cross sections for protons in the energy range 220–570 MeV”. In: *Nuclear Physics A* 183.1 (1972), pp. 81–104.
- [31] J. F. Dicello and G. Igo. “Proton Total Reaction Cross Sections in the 10-20-MeV Range: Calcium-40 and Carbon-12”. In: *Phys. Rev. C* 2 (2 1970), pp. 488–499.

- [32] P. Kirkby and W. T. Link. “FARADAY-CUP MEASUREMENT OF PROTON TOTAL REACTION CROSS SECTIONS AT 100MeV”. In: *Canadian Journal of Physics* 44.8 (1966), pp. 1847–1862. eprint: <https://doi.org/10.1139/p66-155>.
- [33] Motoji Q. Makino, Charles N. Waddell, and Robert M. Eisberg. “Total reaction cross sections for 29 MeV protons”. In: *Nuclear Physics* 50 (1964), pp. 145–156.
- [34] A.E. Taylor and E. Wood. “Proton scattering from light elements at 142 MeV”. In: *Nuclear Physics* 25 (1961), pp. 642–655.
- [35] R. Goloskie and K. Strauch. “Measurement of proton inelastic cross sections between 77 MeV and 133 MeV”. In: *Nuclear Physics* 29 (1962), pp. 474–485.
- [36] J. Jaros et al. “Nucleus-nucleus total cross sections for light nuclei at 1.55 and 2.89 GeV/c per nucleon”. In: *Phys. Rev. C* 18 (5 1978), pp. 2273–2292.
- [37] S. Dytman et al. “Comparison of validation methods of simulations for final state interactions in hadron production experiments”. In: *Phys. Rev. D* 104 (5 2021), p. 053006.
- [38] A. Boudard et al. “Intranuclear cascade model for a comprehensive description of spallation reaction data”. In: *Phys. Rev. C* 66 (4 2002), p. 044615.
- [39] H. De Vries, C.W. De Jager, and C. De Vries. “Nuclear charge-density-distribution parameters from elastic electron scattering”. In: *Atomic Data and Nuclear Data Tables* 36.3 (1987), pp. 495–536.
- [40] K. Bennaceur and J. Dobaczewski. “Coordinate-space solution of the Skyrme–Hartree–Fock–Bogolyubov equations within spherical symmetry. The program HFBRAD (v1.00)”. In: *Computer Physics Communications* 168.2 (2005), pp. 96–122.
- [41] Jose Luis Rodríguez-Sánchez et al. “Improvement of one-nucleon removal and total reaction cross sections in the Liège intranuclear-cascade model using Hartree-Fock-Bogoliubov calculations”. In: *Phys. Rev. C* 96.5 (2017), p. 054602.
- [42] Davide Mancusi et al. “Extension of the Liège intranuclear-cascade model to reactions induced by light nuclei”. In: *Phys. Rev. C* 90.5 (2014), p. 054602. arXiv: 1407.7755 [nucl-th].
- [43] E. J. Moniz et al. “Nuclear Fermi Momenta from Quasielastic Electron Scattering”. In: *Phys. Rev. Lett.* 26 (8 1971), pp. 445–448.
- [44] Alain Boudard et al. “New potentialities of the Liège intranuclear cascade model for reactions induced by nucleons and light charged particles”. In: *Phys. Rev. C* 87.1 (2013), p. 014606. arXiv: 1210.3498 [nucl-th].
- [45] *Nuclear wallet cards*. [https://www.nndc.bnl.gov/nudat3/indx\\_sigma.jsp](https://www.nndc.bnl.gov/nudat3/indx_sigma.jsp).

- [46] J. Cugnon and P. Henrotte. “The low-energy limit of validity of the intranuclear cascade model”. In: *Eur. Phys. J. A* 16 (2003), pp. 393–407.
- [47] J. Cugnon, D. L’Hôte, and J. Vandermeulen. “Simple parametrization of cross-sections for nuclear transport studies up to the GeV range”. In: *Nuclear Instruments and Methods in Physics Research Section B: Beam Interactions with Materials and Atoms* 111.3 (1996), pp. 215–220.
- [48] Joseph Cugnon and Pascal Henrotte. “The low-energy limit of validity of the intranuclear cascade model”. English. In: *European Physical Journal. A, Hadrons and Nuclei* 16.3 (March 2003).
- [49] Sophie Pedoux. “Extension of the Liège Intranuclear Cascade Model to the 2-15 GeV Incident Energy Range”. PhD thesis. Liege U., 2011.
- [50] J. Cugnon et al. “New constraints on the  $\Delta$  production cross section”. In: *Phys. Rev. C* 56 (5 1997), pp. 2431–2439.
- [51] J. Cugnon, C. Volant, and S. Vuillier. “Improved intranuclear cascade model for nucleon-nucleus interactions”. In: *Nuclear Physics A* 620.4 (1997), pp. 475–509.
- [52] R. L. Workman et al. “Review of Particle Physics”. In: *PTEP* 2022 (2022), p. 083C01.
- [53] Sophie Pedoux and Joseph Cugnon. “Extension of the Liege intranuclear cascade model at incident energies between 2-GeV and 12-GeV. Aspects of pion production”. In: *Nucl. Phys. A* 866 (2011), pp. 16–36.
- [54] J. Hirtz et al. “Strangeness production in the new version of the Liège intranuclear cascade model”. In: *Phys. Rev. C* 101.1 (2020), p. 014608. arXiv: 1909.02246 [nucl-th].
- [55] J. L. Rodríguez-Sánchez et al. “Hypernuclei formation in spallation reactions by coupling the Liège intranuclear cascade model to the deexcitation code ABLA”. In: *Phys. Rev. C* 105 (1 2022), p. 014623.
- [56] Benjamin Braunn et al. “Assessment of nuclear-reaction codes for proton-induced reactions on light nuclei below 250 MeV”. In: *The European Physical Journal Plus* 130.7 (2015), p. 153.
- [57] K.-H. Schmidt et al. “Production of neutron-rich heavy residues and the freeze-out temperature in the fragmentation of relativistic  $^{238}\text{U}$  projectiles determined by the isospin thermometer”. In: *Nuclear Physics A* 710.1 (2002), pp. 157–179.
- [58] A. S. Botvina et al. “Modification of surface energy in nuclear multifragmentation”. In: *Phys. Rev. C* 74 (4 2006), p. 044609.
- [59] V. F. Weisskopf and D. H. Ewing. “On the Yield of Nuclear Reactions with Heavy Elements”. In: *Phys. Rev.* 57 (6 1940), pp. 472–485.

- [60] A. Gilbert and A. G. W. Cameron. “A COMPOSITE NUCLEAR-LEVEL DENSITY FORMULA WITH SHELL CORRECTIONS”. In: *Canadian Journal of Physics* 43.8 (1965), pp. 1446–1496. eprint: <https://doi.org/10.1139/p65-139>.
- [61] R. Capote et al. “RIPL – Reference Input Parameter Library for Calculation of Nuclear Reactions and Nuclear Data Evaluations”. In: *Nuclear Data Sheets* 110.12 (2009). Special Issue on Nuclear Reaction Data, pp. 3107–3214.
- [62] B. D. Wilkins, E. P. Steinberg, and R. R. Chasman. “Scission-point model of nuclear fission based on deformed-shell effects”. In: *Phys. Rev. C* 14 (5 1976), pp. 1832–1863.
- [63] *INCL Geant4 physics lists*. <https://irfu.cea.fr/dphn/Spallation/physlist.html>.
- [64] Alfredo Ferrari et al. *Po-production in lead: A benchmark between Geant4, FLUKA and MCNPX*. 2018.
- [65] Tatsuhiko Sato et al. “Features of Particle and Heavy Ion Transport code System (PHITS) version 3.02”. In: *Journal of Nuclear Science and Technology* 55.6 (2018), pp. 684–690. eprint: <https://doi.org/10.1080/00223131.2017.1419890>.
- [66] Luis Alvarez-Ruso et al. “Recent highlights from GENIE v3”. In: *Eur. Phys. J. ST* 230.24 (2021), pp. 4449–4467. arXiv: 2106.09381 [hep-ph].
- [67] C.H. Llewellyn Smith. “Neutrino reactions at accelerator energies”. In: *Physics Reports* 3.5 (1972), pp. 261–379.
- [68] Tomasz Golan. “Modeling nuclear effects in NuWro Monte Carlo neutrino event generator”. PhD thesis. University of Wroclaw, 2014.
- [69] R. Bradford et al. “A New parameterization of the nucleon elastic form-factors”. In: *Nucl. Phys. B Proc. Suppl.* 159 (2006). Ed. by F. Cavanna, J. G. Morfin, and T. Nakaya, pp. 127–132. arXiv: hep-ex/0602017.
- [70] G. T. Garvey, W. C. Louis, and D. H. White. “Determination of proton strange form factors from  $\nu p$  elastic scattering”. In: *Phys. Rev. C* 48 (2 1993), pp. 761–765.
- [71] T Golan. “What is inside MC generators. And why it is wrong”. NuSTEC School. 2015.



# 5

## FSI modelling with INCL and NuWro cascade models

This chapter is dedicated to comparing the cascade FSI mechanisms of INCL and NuWro in the simulation of neutrino and antineutrino interactions. INCL does not have a neutrino vertex implemented, so in section 5.1, we describe how we use the neutrino vertex simulated with NuWro as input for INCL. To isolate the effects of final state interactions (FSI) from the initial state, we utilize the Single Transverse Variables, whose description and comparison for INCL and NuWro are covered in section 5.2, along with simulation results of the leading proton kinematics. In section 5.3, we repeat the study for the antineutrino reaction, where the leading nucleon is a neutron. Lastly, section 5.4 provides a glimpse into the simulation that goes beyond the factorization approach.

### 5.1 Implementation of the NuWro input

Since INCL does not have an implemented neutrino interaction vertex yet, we use the result of the NuWro simulation as an input at the starting point of the INCL cascade. We focus on modeling the CCQE neutrino interaction. The Feynman diagram corresponding to this process is shown in Fig. 5.1. In this interaction, the neutrino interacts with the neutron. The products in the final state are the muon and proton. In the nucleus generated by INCL, we choose a neutron with the closest modulus and direction of the momentum to the neutron momentum from the NuWro simulated event. This neutron is replaced by the

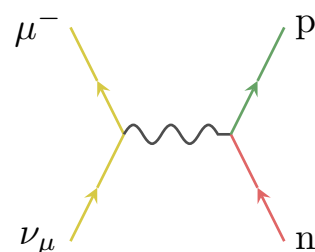


Figure 5.1 Neutrino CCQE interaction.

proton and muon from NuWro (see fig. 5.2). This way, we choose the neutron inside the INCL nucleus, on which we will force the interaction. We use the NuWro Spectral Function (SF) model with a disabled "SF FSI" option (that is described in Chapter 3) as a primary choice. In order to compare only INCL and NuWro cascades, we have disabled all the excitation models, including the Fermi breakup. The impact of the de-excitation on the FSI modeling will be discussed in the following chapter. The "back-to-spectator" option in INCL described in Chapter 4 has improved the agreement with some sets of data: for example, the neutron multiplicity in proton-induced reactions on  $^{208}\text{Pb}$ , as shown in [1]. The modeling of the very low-energy nucleons, which is affected by this feature, is still an open issue for cascade mechanisms, and there are no compelling arguments for utilizing such an option. In the scope of this work, we have disabled the "back-to-spectator" option thus allowing all the low momentum protons to participate to the cascade. Fermi momentum is mass-dependent and equal to 210 MeV for the carbon nucleus in the INCL model.

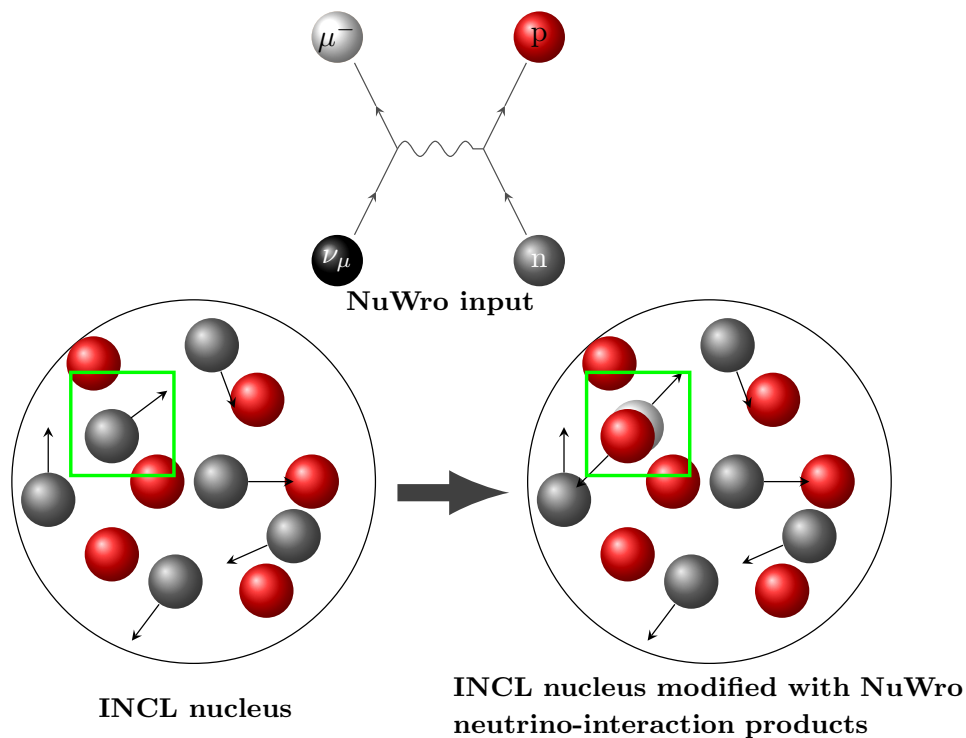


Figure 5.2 The scheme of neutrino-nucleus reaction implementation.

As described in Chapter 3, the default Pauli blocking (PB) model in INCL is strict-statistical, where strict PB is applied to the first interaction and statistical to the subsequent ones. Since the first interaction, in this case, is the neutrino interaction taken from NuWro, we use just a statistical model in INCL for the cascade re-interactions.

INCL and NuWro nuclear models are quite different. One can see the position-momentum correlation dictated by the Hartree-Fock-Bogoliubov formalism implemented in INCL and

the LFG model used in the NuWro cascade simulation in Fig. 5.3. These two models have an opposite trend of the position-momentum correlation. For INCL, high-momentum particles tend to occur on the outskirts of the nucleus, while for NuWro, they tend to be closer to the center. Another difference between the models stems from a long tail in the NuWro SF model that one can see in fig. 5.4. This tail corresponds to the short-range correlations (SRC) that are absent in INCL (the work is ongoing to include them in the model). Thus, the position distribution of the neutron sampled from NuWro is slightly different from other protons in INCL (right plot of fig. 5.4).

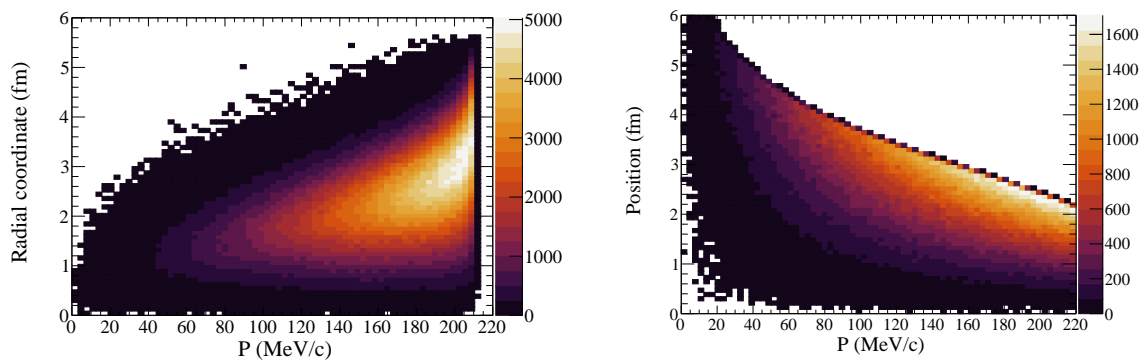


Figure 5.3 Radial coordinate and momentum distribution inside the nucleus for INCL (left), and NuWro LFG (right) nuclear models ( $z$  axis in arbitrary units).

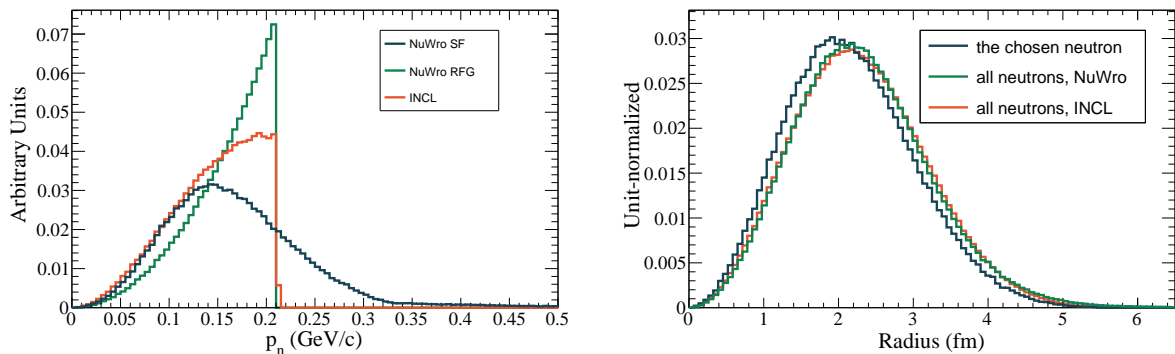


Figure 5.4 Left: Momentum distribution of neutrons in the nucleus for NuWro SF and RFG and INCL nuclear models (shape comparison). Right: Position distribution of neutrons in INCL and NuWro and of the INCL neutron chosen to match the SF neutron simulated in NuWro in our matching algorithm.

To ensure the robustness of the FSI characterization conclusions, we have performed similar studies using the NuWro Relativistic Fermi Gas (RFG) model instead of SF as a neutrino vertex input to INCL. The details of this study can be found in Appendix A, where we show that all the main conclusions on FSI comparisons between INCL and NuWro stays unchanged.

Due to SRC, in NuWro, the neutrino vertex in 15% of events has two outgoing protons. In the INCL vertex, we keep only the leading proton—the proton with the highest momentum—that triggers the cascade. We tested that removing all instances of 2-proton events from the neutrino vertex has no impact on the conclusions on how to characterize the FSI cascade of the leading proton in NuWro and INCL. We have also tested that the complete removal of the second nucleon does not impact the final results of the characterization of the FSI cascade of the leading proton in NuWro and INCL.

## 5.2 Proton FSI modelling

We simulated about 350000 CCQE events with NuWro SF model using T2K neutrino energy flux. We analysed the results of the NuWro and INCL simulations using ROOT software version 6.22/02 [2]. To characterize the proton FSI, we use the following channels classification:

- **No cascade FSI:** no change of energy of the highest momentum proton, no extra final state particles;
- **One proton:** change of energy of the highest momentum proton, no extra final state particles;
- **Multiple nucleons:** production of extra nucleons but no pions in the final state. For the INCL simulation, we distinguish the channel with only additional nucleons produced and the one featuring the production of nuclear clusters;
- **Proton + pion;**
- **0 proton events:** NuWro channel with no proton in the final state. For INCL we subdivide this channel:
  - $\mu$  only: full proton absorption;
  - $\mu$ ,  $n$ ,  $\pi$  and cluster emission ( $\alpha$ , deuterons, tritons...), but no proton in the final state.

We present the fractions of different channels for different models in table 5.1. INCL has a larger fraction of events with no proton in the final state. Such events contribute to the 7.7% of total events in INCL against less than 0.1% in NuWro. In the NuWro cascade, if particles are not Pauli blocked, most likely, they will leave the nucleus. The INCL nuclear model features a higher probability of reabsorbing particles in the nucleus during FSI. This tendency is also confirmed by the smaller fraction of events with more than 1 proton in the final state (multinucleon production by FSI results in 25.6% of total events in NuWro and 9% in INCL).

Events with no proton in the final state also differ by their nature between INCL and NuWro. While in NuWro, the dominant channel is charge exchange (events feature neutron in the final state), INCL has multiple equally probable scenarios. Proton can be absorbed by the nucleus, can leave as a neutron, or can leave the nucleus as a nuclear cluster.

Table 5.1 Fractions of the different FSI channels, i.e. fraction of events with different final state particles after the FSI cascade, in CCQE events with T2K neutrino energy flux. Fractions of events with and without protons in the final state are quoted separately.

	<b>Channel</b>	<b>NuWro SF</b>	<b>INCL+NuWro SF</b>
	no protons	1.4%	19.5%
	protons	98.6%	80.5%
<b>No proton</b>	absorption	4.4%	39.5%
	neutron + $\pi$ production	3.4%	0.6%
	$\pi$ production	0.2%	0%
	neutron knock-out	92%	29.6%
	cluster knock-out	0%	30.3%
<b>Proton</b>	1 proton, no FSI	70.4%	68.5%
	1 proton only with FSI	2.4%	19.2%
	1p + other nucleons or clusters	26.2%	11.7%
	proton(s)+ $\pi$ production	1%	0.6%

We have also studied the transparency depending on the coordinate of the neutrino vertex inside the nucleus. The *transparency* is an experimental measure defined as the probability of a struck nucleon escaping the nucleus without significant re-interactions. For the used simulations, we define "Monte-Carlo transparency" as a fraction of events without FSI interaction on the leading proton exiting from the interaction vertex. It is a commonly used definition of transparency that is also used, for example, in Ref. [3]. Fig. 5.5 shows that both models agree with data while having a divergence in their prediction. Especially for the low momentum protons, INCL features smaller transparency. The predictions vary the most in the region of interest for the present study (0.2—1 GeV of proton momentum). At the same time, there are very sparse data and no clear preference for one model over the other.

Fig. 5.6 shows the transparency depending on the position of the neutrino interaction. We calculate the transparency in the frame where the neutrino direction is along the Z axis (left plot on fig. 5.6). As expected, the less nuclear matter the proton passes through, the higher the transparency. The nuclear transparency is, as expected, symmetric around the axis of the neutrino direction.

### 5.2.1 Leading proton kinematics

Figure 5.7 shows the distributions of the leading proton momentum before and after FSI. Since we take the neutrino vertex from NuWro, the shape of the distribution of the proton

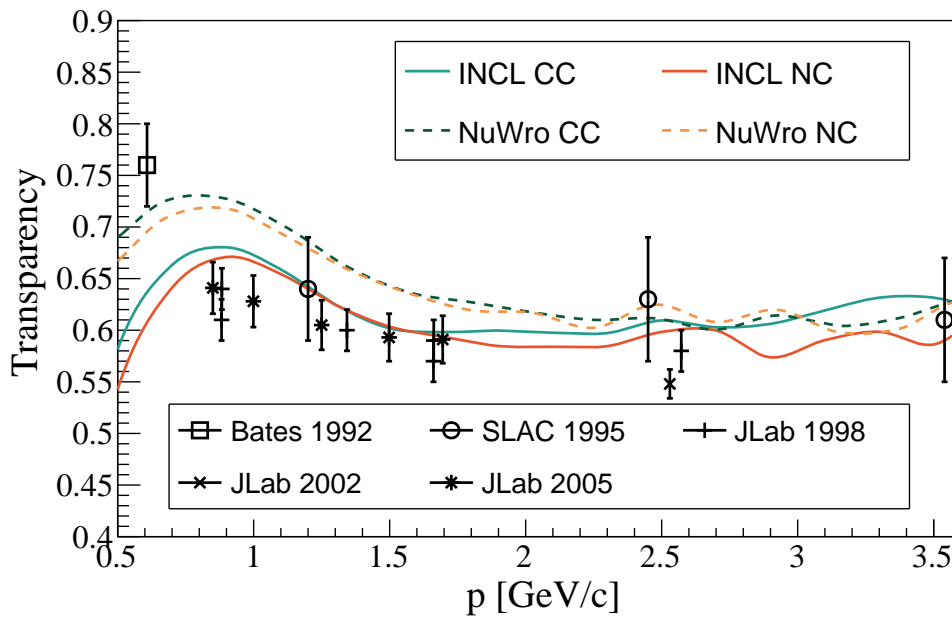


Figure 5.5 Nuclear transparency of  $^{12}\text{C}$  (percentage of events without FSI) as a function of proton momentum modelled by NuWro and INCL.

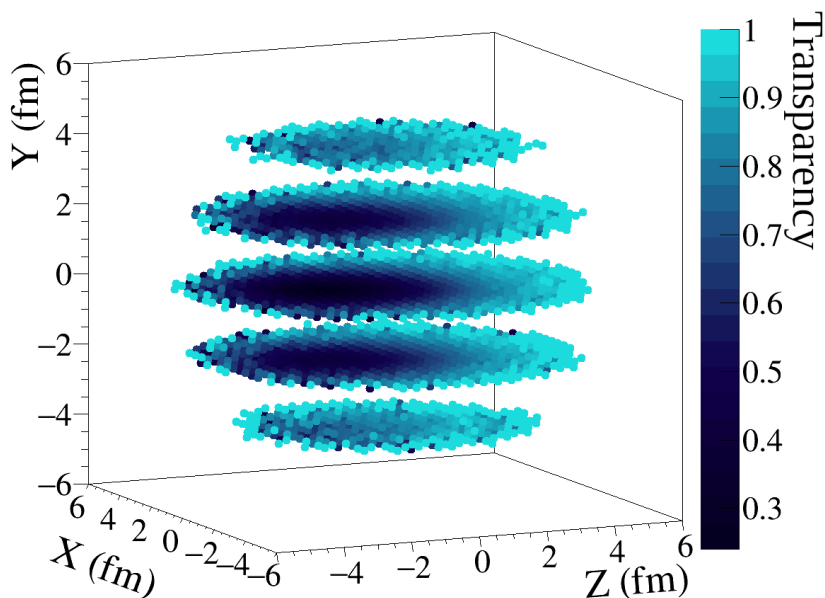


Figure 5.6 Nuclear transparency of  $^{12}\text{C}$  (ratio of number of events without FSI to all events) dependence on the position of the neutrino interaction inside the nucleus. Y-coordinate is averaged out to the 5 slices. The Z-coordinate corresponds to the initial neutrino direction.

momentum before FSI is identical for both INCL and NuWro. Figure 5.7 also shows the relative fraction of the different final states as a function of proton momentum before and after FSI. INCL features a broader spectrum of FSI channels. Smaller transparency of INCL leads to fewer events with at least one proton in the final state. In particular, proton absorption events concentrate in the region of low proton momentum before FSI. At the same time, events in which the proton leaves the nucleus as a nuclear cluster populate the distribution right before the peak of the distribution ( $\sim 350$  MeV/c). In NuWro, protons at low momenta after FSI are consistently accompanied by other produced nucleons. INCL features mostly events with only one proton in the final state. Additionally, the peak of the FSI part of the proton momentum after FSI distribution for NuWro is lower than that of INCL. This is due to the fact that the INCL Pauli blocking is more strict than the one in NuWro.

To directly quantify FSI effects, we compare the proton kinematics before and after FSI, as shown in fig. 5.8. Predictably, FSI decelerates leading protons and smears the angular distribution compared to the pre-FSI one (this effect is less evident in INCL). A compelling feature of INCL is that it tends to decelerate protons more on an event-by-event basis. In contrast, the total momentum distribution after FSI of all the protons leaving the nucleus is larger in INCL than in NuWro. This effect is because low-momentum protons are absorbed in the nucleus.

### 5.2.2 Single Transverse Variables

We use Single Transverse Variables (STV) to disentangle FSI effects from the physics of the initial nuclear state. Ref. [4] provides an extensive description of STV; we present the illustration of the STV definition in fig. 5.9. STV are defined in the transverse plane with respect to the neutrino direction.

The first variable of interest is the  $\delta p_T$ :

$$|\delta \vec{p}_T| = |\vec{p}_T^p + \vec{p}_T^\mu|, \quad (5.1)$$

where  $\vec{p}_T^p$  is the transverse component of the leading proton and  $\vec{p}_T^\mu$  is the transverse component of the muon momentum.  $\delta p_T$  can be considered as the “missing transverse momentum” and, in the absence of FSI in quasi-elastic events, represents the Fermi motion of the initial nucleon. If neutrino interacted with a the nucleon at rest,  $\delta p_T$  would equal zero. FSI might smear this distribution by shifting the peak position and contributing to the long tail in the high  $\delta p_T$  region.

The second variable we will focus on is the transverse boosting angle  $\delta \alpha_T$ :

$$\delta \alpha_T = \arccos \frac{-\vec{p}_T^\mu \cdot \delta \vec{p}_T}{p_T^\mu \cdot \delta p_T}. \quad (5.2)$$

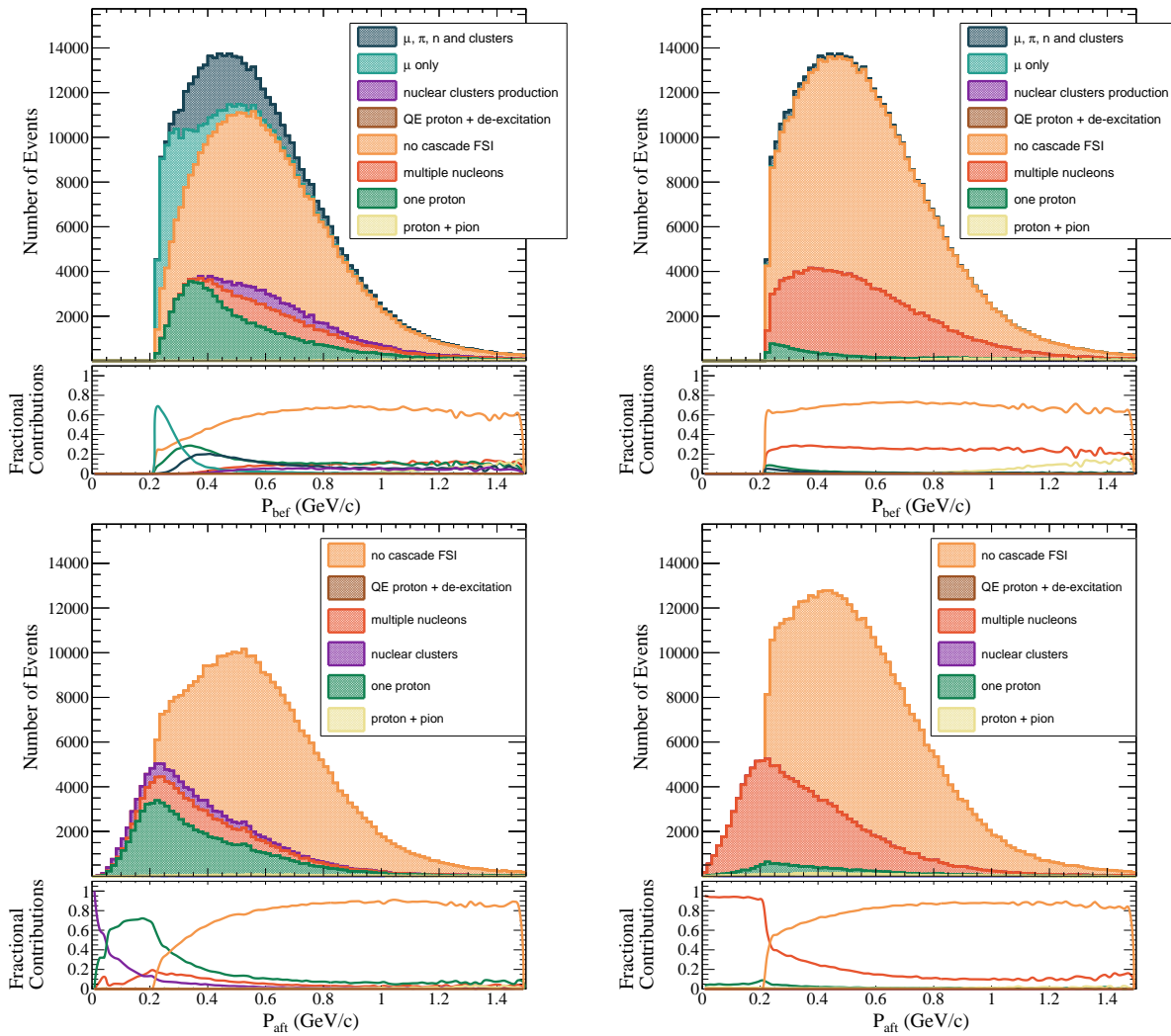


Figure 5.7 Top: proton momentum before FSI for INCL (left), and NuWro (right) cascade models in CCQE events with T2K neutrino energy flux. Sub-processes correspond to the fate of the proton after FSI. The shape of proton momentum before FSI is by definition identical for INCL and NuWro cascades. Bottom: leading proton momentum after FSI for INCL (left), and NuWro SF (right) nuclear models. The fractions of different FSI sub-processes as listed in Tab. 5.1 are also shown. The 0 proton channel in NuWro includes muon only and pion and neutron production. There is no cluster production in NuWro.

Events with strong FSI, where the proton is strongly decelerated, will tend to feature larger  $\delta\alpha_T$  values. For transparent events, there is no preferred angle, and the  $\delta\alpha_T$  distribution is uniform.

Figure 5.10 confirms the STV behaviour described above. The distribution of  $\delta\alpha_T$  for transparent events is uniform. Channels with FSI (one proton, multiple nucleons, and multiple nucleons with pions production) feature large values of  $\delta\alpha_T$ . This behavior is similar for both INCL and NuWro models. However, the shape of the FSI part in the region of interest diverges between the two simulations: INCL tends to suppress the high  $\delta\alpha_T$  values that are populated

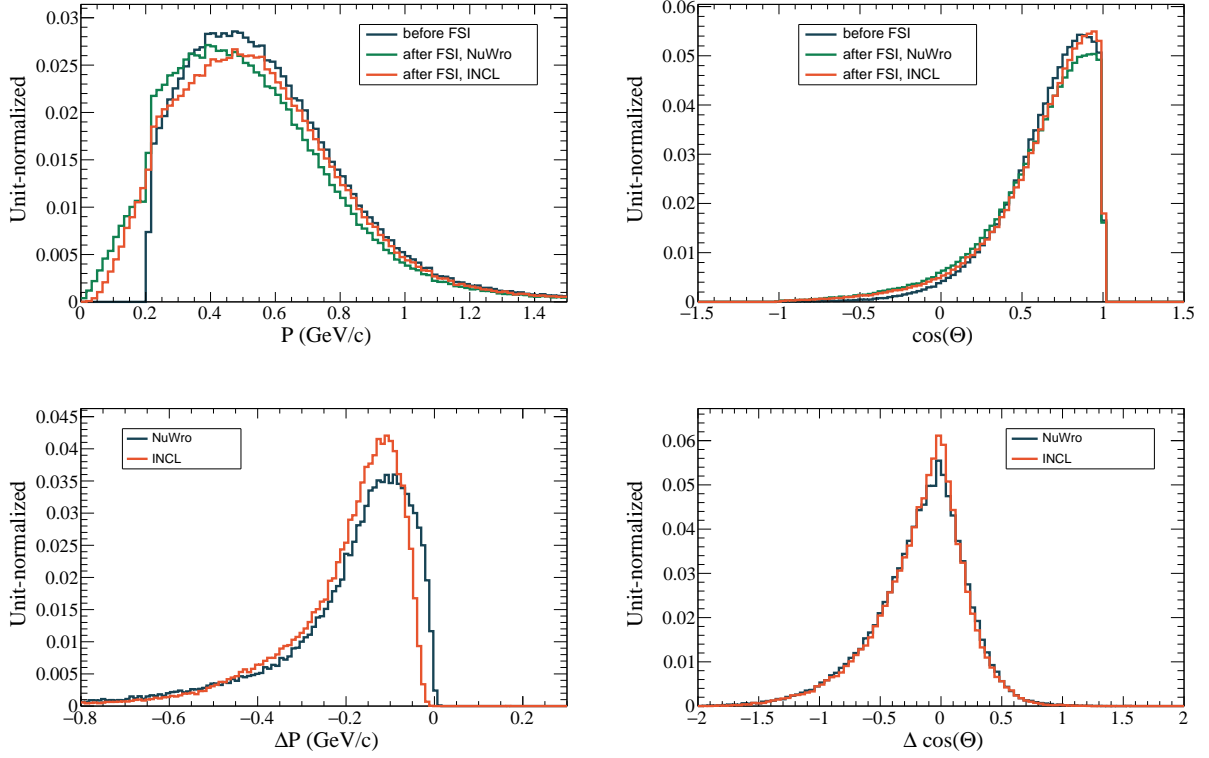


Figure 5.8 Distribution of leading proton's momentum in NuWro SF and NuWro+INCL before and after FSI (top left, shape comparison). Distribution of difference in proton's momentum before and after FSI ( $\Delta P = P_{after} - P_{before}$ ) in NuWro SF and NuWro+INCL (bottom left, shape comparison). Distribution of leading proton  $\cos(\theta)$  in NuWro SF and NuWro+INCL before and after FSI (top right, shape comparison). Distribution of difference in proton's  $\cos(\theta)$  before and after FSI ( $\Delta \cos(\theta) = \cos\theta_{after} - \cos\theta_{before}$ ) in NuWro SF and NuWro+INCL (bottom left, shape comparison). The "no FSI" channel is excluded. CCQE events with T2K neutrino energy flux are simulated.

by low momentum protons. Such difference is explained by the different Pauli Blocking models used in INCL and NuWro. For the  $\delta p_T$ , the bulk of the distribution corresponds to the channel with no FSI, and FSI channels significantly contribute to the high-energetic tail. The overall  $\delta p_T$  distribution is very similar for both INCL and NuWro, which is expected since the vertex simulation and Fermi motion modeling comes from NuWro. This conclusion is robust, independently of the nuclear model used for the fundamental interaction: we observe a similar behavior using the RFG model, as shown in Appendix A in Fig. A.3.

Part of the low-momentum protons did not enter the STV distributions since they were emitted as nuclear clusters. Such clusters will not create the same detector response as protons, as discussed in chapter 7. Fig. 5.11 shows the shape of the  $\delta \alpha_T$  distribution reconstructed with the leading hadron (proton or nuclear cluster). Nuclear cluster production corresponds to strong FSI and contributes to the high  $\delta \alpha_T$  region, but still does not fill the suppression at

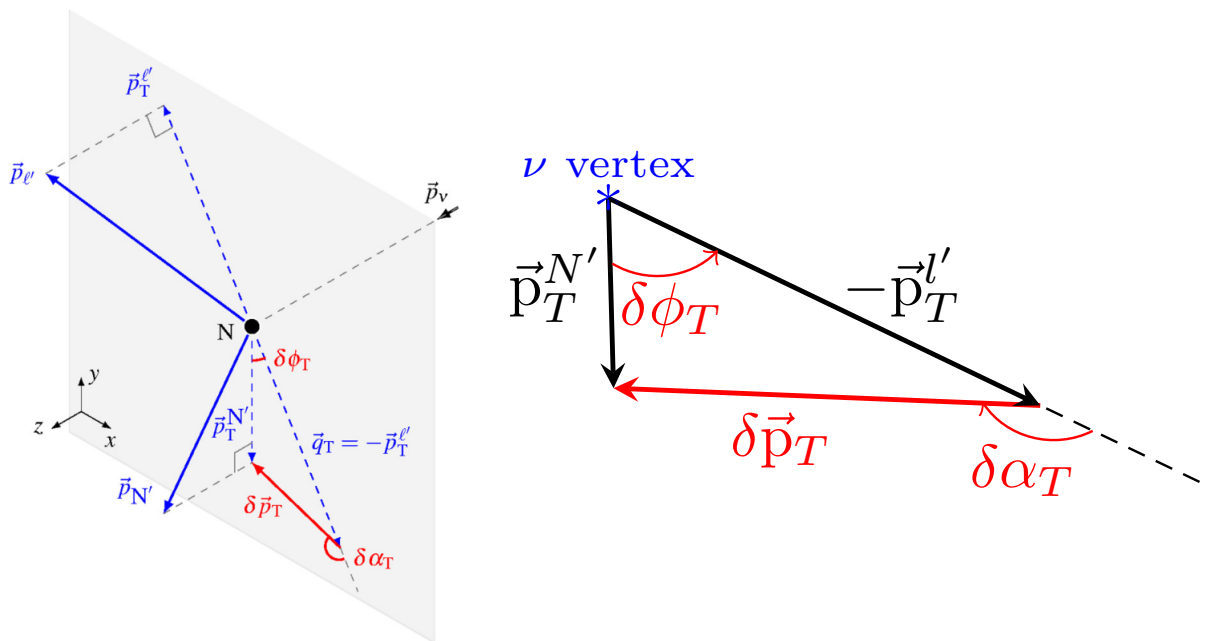


Figure 5.9 Schematic illustration of the single-transverse kinematic imbalance.  $\vec{p}_N$  and  $\vec{p}_{l'}$  are momenta of the outgoing nucleon and lepton (in the neutrino CCQE case proton and  $\mu^-$ , in the antineutrino case—neutron and  $\mu^+$ ).  $\vec{p}_T^{N'}$  and  $\vec{p}_T^{l'}$  are their projection on the transverse plane. On the right side of figure, the two-dimensional projection on the transverse plane is shown. The figure is adapted from [4].

very large values of  $\delta\alpha_T$ . But at the same time, there is still a sizable fraction of events with total proton absorption and only a muon in the final state at low proton momenta.

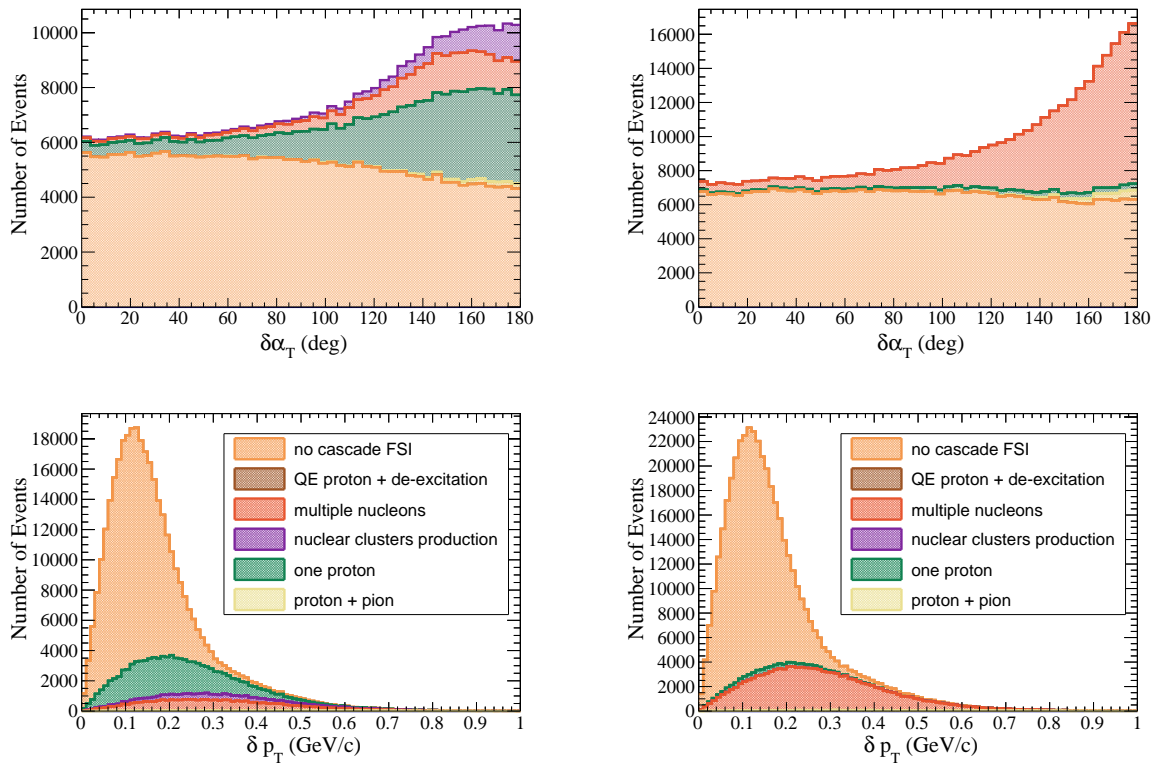


Figure 5.10 Top:  $\delta\alpha_T$  simulated with the INCL+NuWro SF (left), and NuWro (right) cascade models in CCQE events with T2K neutrino energy flux. Bottom:  $\delta p_T$  for the INCL+NuWro SF (right) and Nuwro SF(left) nuclear models.

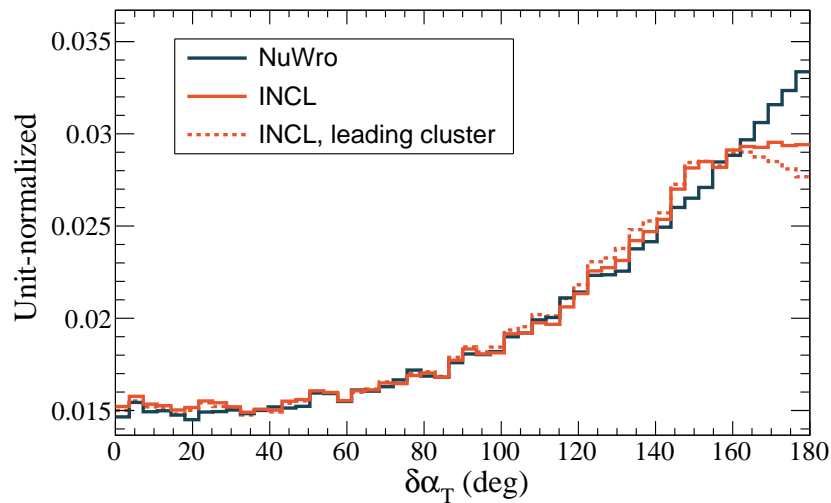


Figure 5.11  $\delta\alpha_T$  distribution in NuWro SF and NuWro+INCL (shape comparison). The effect on  $\delta\alpha_T$  shape of including also the leading nuclear cluster in INCL events is shown.

### 5.3 Neutron FSI modelling

For the antineutrino reaction modeling, we will use similar NuWro options. We simulate CCQE interactions with a neutron and a  $\mu^+$  in the final state, as shown in Fig. 5.12. The statistics used here is 1 million events. Antineutrinos are capable of interacting with both carbon and hydrogen. Since we are interested in FSI, we will simulate only interactions on carbon (since interactions with hydrogen are equivalent to those with the free proton without FSI). There are fundamental differences in the neutrino and antineutrino CCQE interactions. Fig. 5.13 shows the neutrino and antineutrino CCQE reaction cross section and energy transfer simulated with NuWro. The energy transfer distribution is narrower for antineutrinos and shifted to lower values. Cross sections in our region of interest ( $\sim 1$  GeV) differ more than three times. These intrinsic discrepancies in the initial state of neutrinos and antineutrinos will propagate to the final state characterization. On top of the nature of the neutrino and antineutrino interactions, the T2K flux data we use as an input of the simulation also varies, but these distinctions are minor.

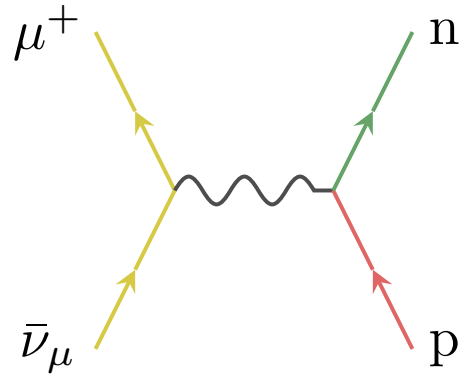


Figure 5.12 Antineutrino CCQE interaction.

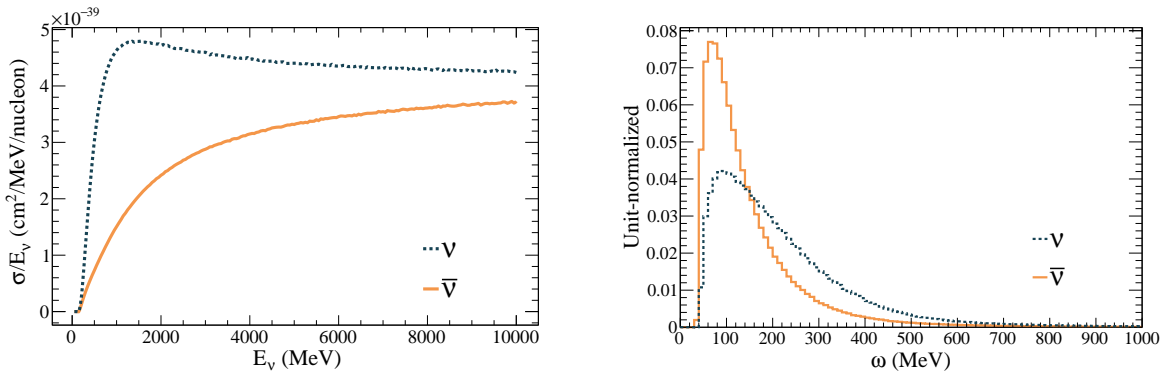


Figure 5.13 Left: Neutrino and antineutrino CCQE reaction cross sections modeled with NuWro. Right: energy transfer for neutrino and antineutrino CCQE interactions simulated with NuWro with T2K neutrino and antineutrino flux.

In order to characterize the leading neutron kinematics, we will use the same channels classification introduced in Section 5.2 with the difference that here the leading nucleon is a neutron. The fractions of the different FSI channels are shown in Table 5.2. In INCL, there are more events with no leading nucleon in the final state for the antineutrino interaction than for the neutrino interaction (31.15% vs. 19.47% for neutrinos). This effect comes from

the shape difference of the energy transfer: the peak of the leading neutron momentum distribution before FSI shifts towards the low momentum region, where absorption is a dominant channel. A similar effect is visible in INCL events without neutrons in the final state: unlike the neutrino interaction, where absorption, charge exchange, and clusterization are equally probable, absorption is prevalent in the antineutrino interaction. The NuWro FSI simulation does not feature such dependence on the transferred energy. It thus exhibits a similar probability of events without a nucleon in the final state for neutrino and antineutrino simulations.

Table 5.2 Fractions of the different FSI channels, i.e. fraction of events with different final state particles after the FSI cascade, in CCQE events with T2K neutrino energy flux. Fractions of events with and without protons in the final state are quoted separately.

	Channel	NuWro SF	INCL+NuWro SF
	no neutrons	2.4%	31.2%
	neutrons	97.6%	68.8%
<b>No neutron</b>	absorption	4.5%	62.2%
	proton + $\pi$ production	0.7%	0.1%
	$\pi$ production	0.01%	0%
	proton knock-out	94.8%	19.7%
	cluster knock-out	0%	18%
<b>Neutron</b>	1 neutron, no FSI	72.5%	68.1%
	1 neutron only with FSI	4.1%	25.8%
	1n + other nucleons or clusters	23.1%	5.8%
	neutron(s)+ $\pi$ production	0.3%	0.3%

Concerning the channels with the neutron in the final state, the NuWro simulation has a more similar behavior between protons from neutrino and neutrons from antineutrino interactions. In INCL, the shift to lower energy transfer for antineutrino interactions also reduces the probability of producing multiple nucleons in the final state (5.7% for neutrons and 11.7% for protons).

### 5.3.1 Leading neutron kinematics

Figure 5.14 supports the conclusions about the channel distributions discussed above. The shape of the neutron momentum before FSI reflects the shape of the energy transfer: the neutron momentum before FSI distribution is shifted to lower momentum values and is narrower than for protons. Lower energy transfer also leads to a larger impact of Pauli blocking on the distribution: it is responsible for the sharp edge of the proton momentum after FSI distribution. Apart from that, the conclusions about the leading neutron momentum before and after FSI are similar to the ones extracted in Section 5.2 for the leading proton.

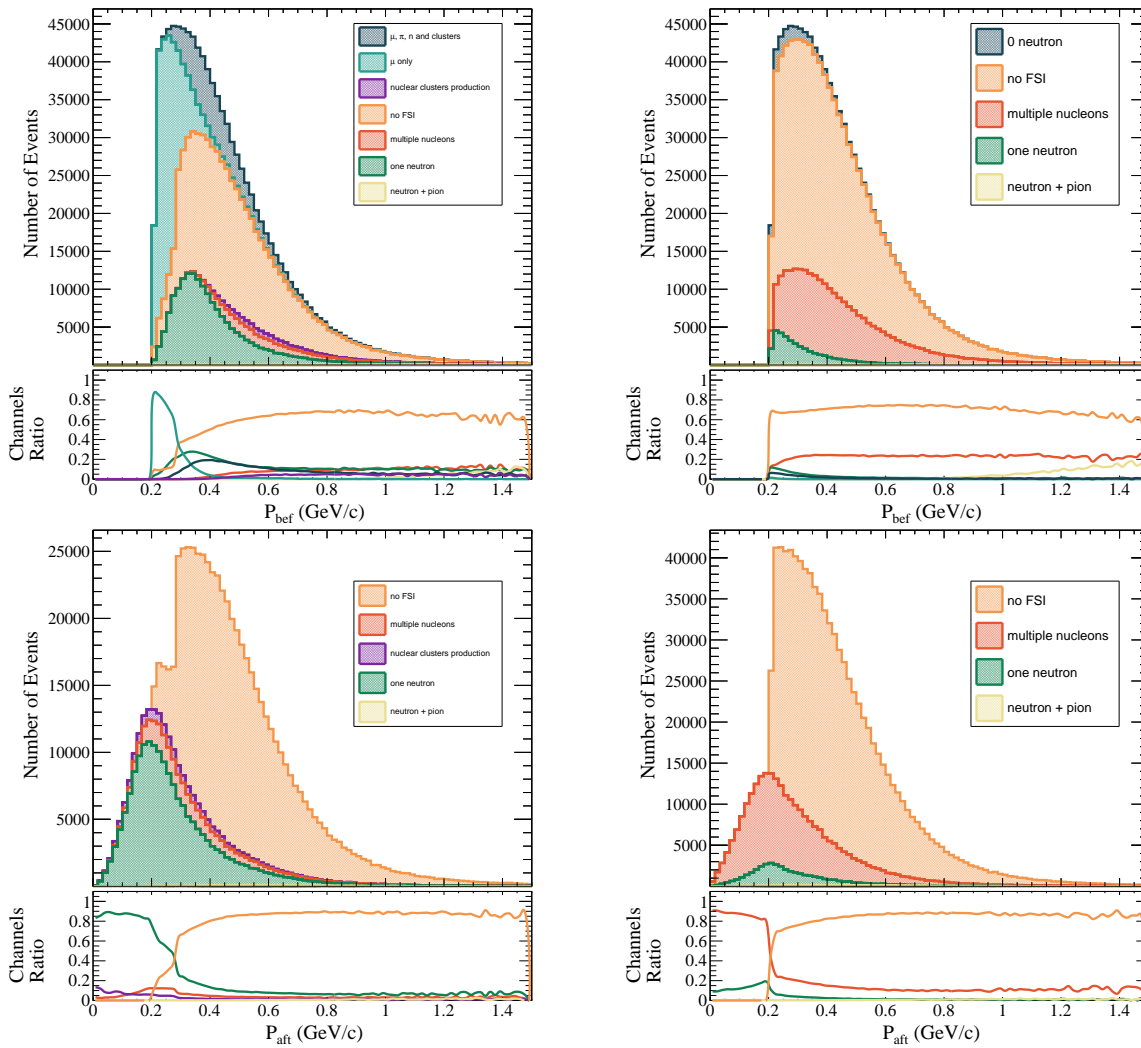


Figure 5.14 Top: neutron momentum before FSI for INCL (left), and NuWro (right) cascade models in CCQE events with T2K antineutrino energy flux. Sub-processes correspond to the fate of the neutron after FSI. The shape of neutron momentum before FSI is by definition identical for INCL and NuWro cascades. Bottom: leading neutron momentum after FSI for INCL (left), and NuWro SF (right) nuclear models. The fractions of different FSI sub-processes as listed in Tab. 5.2 are also shown. The 0 neutron channel in NuWro includes muon only and pion and proton production. There is no cluster production in NuWro.

Fig. 5.15 shows the difference between the leading nucleon kinematics. INCL tends to decelerate leading neutrons, as leading protons, event-by-event more than NuWro. The proton momentum after FSI differs a lot between INCL and NuWro since in INCL, the large fraction of events with no neutron in the final state did not enter the distribution. A more intriguing variable is the forward angle. One can spot two peaks in the NuWro  $\Delta \cos(\theta)$  distribution.

The two-peaked structure of the  $\Delta \cos(\theta)$  distribution simulated with NuWro deserves extra attention. To understand it, we need to understand better the behavior of the forward an-

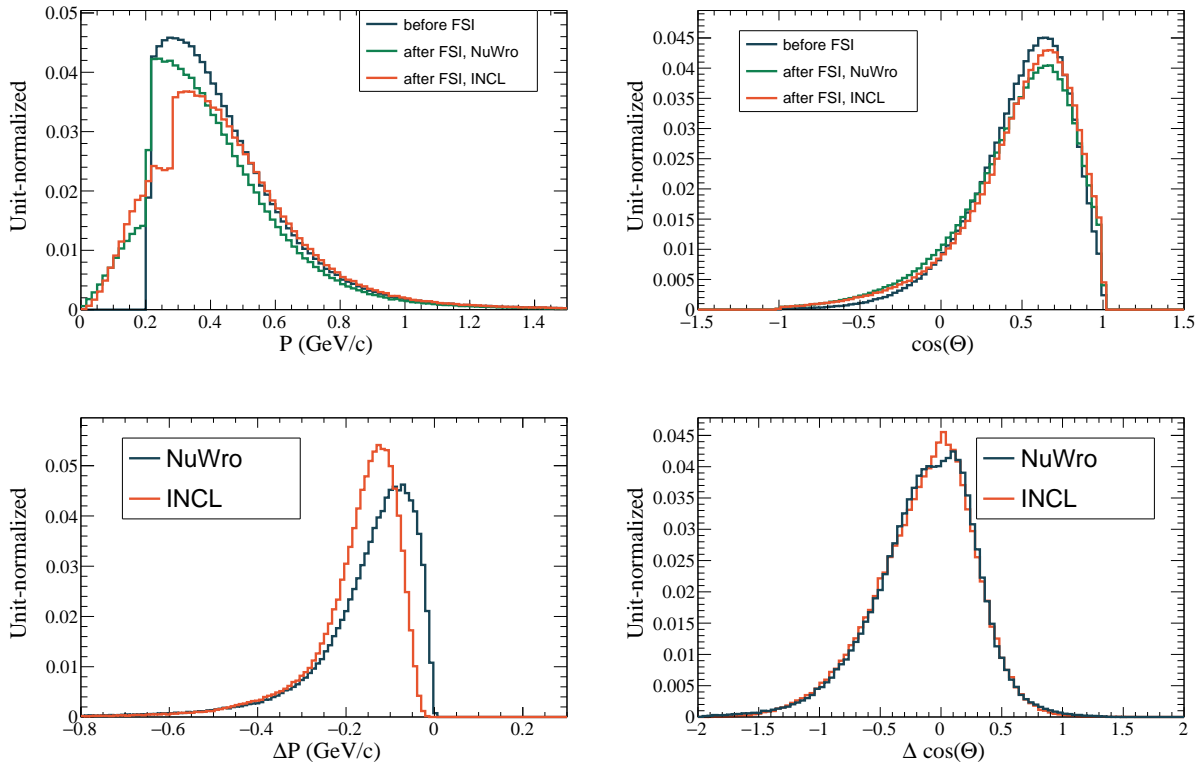


Figure 5.15 Distribution of leading neutron's momentum in NuWro SF and NuWro+INCL before and after FSI (top left, shape comparison). Distribution of difference in neutron's momentum before and after FSI ( $\Delta P = P_{after} - P_{before}$ ) in NuWro SF and NuWro+INCL (bottom left, shape comparison). Distribution of leading neutron  $\cos(\theta)$  in NuWro SF and NuWro+INCL before and after FSI (top right, shape comparison). Distribution of difference in neutron's  $\cos(\theta)$  before and after FSI ( $\Delta \cos \theta = \cos \theta_{after} - \cos \theta_{before}$ ) in NuWro SF and NuWro+INCL (bottom left, shape comparison). The "no FSI" channel is excluded. CCQE events with T2K antineutrino energy flux are simulated.

gle before and after FSI. The transparent events do not contribute to the  $\Delta \cos(\theta)$  distribution, so we plot the forward angle before and after FSI for proton and neutrons without the "no FSI" channel in Fig. 5.16. One can see a fundamental difference between the forward angles before FSI for leading protons and neutrons: the former peaks at  $\cos(\theta) \sim 1$ , and the latter is shifted to larger opening angles. It is an intrinsic feature of the neutrino and antineutrino interaction nature. Concerning the forward angle after FSI, its shape differs only slightly for protons and neutrons. Thus, when subtracting the distributions  $\cos \theta_{after} - \cos \theta_{before}$ , that peak in two different values, we obtain a final two-peaked  $\Delta \cos(\theta)$  distribution. This effect is less pronounced for the INCL simulation: we observe the one-peaked distribution slightly wider than the one for the neutrino interaction.

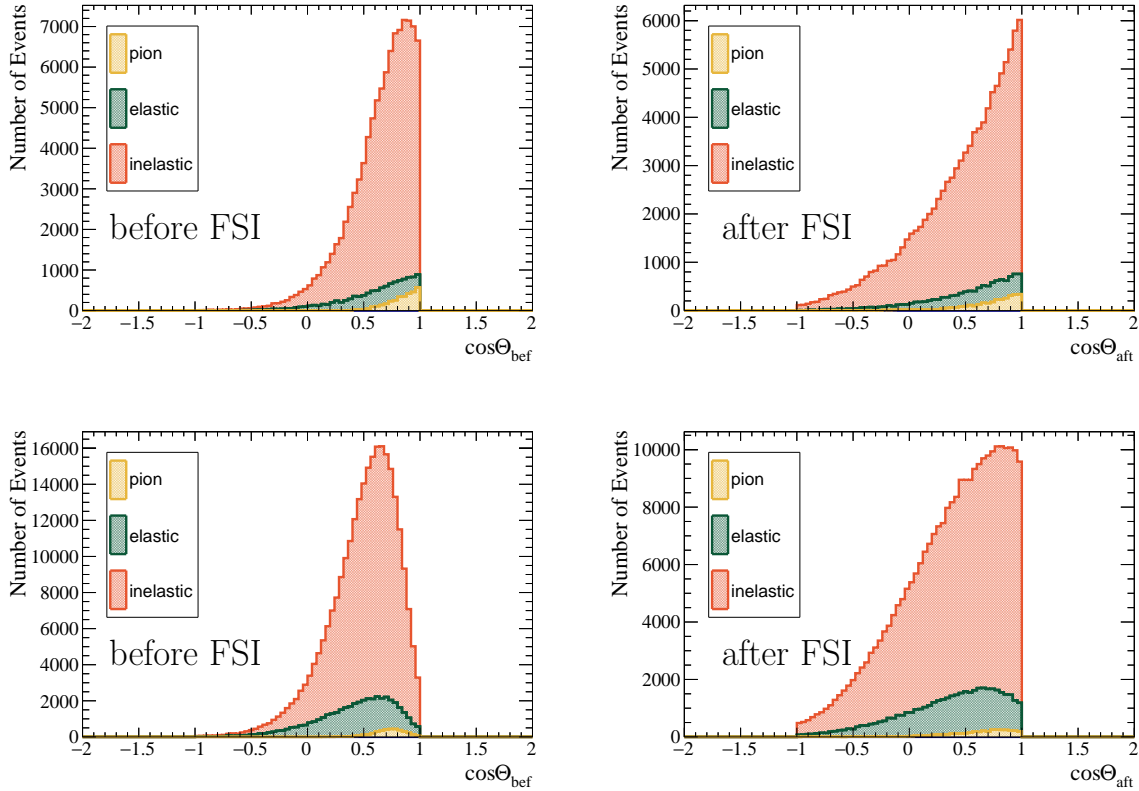


Figure 5.16 NuWro simulation of the  $\cos(\theta)$  before (left) and after (right) FSI for protons (top) and neutrons (bottom).

### 5.3.2 Single Transverse Variables

Fig. 5.17 shows the  $\delta\alpha_T$  and  $\delta p_T$  distributions obtained with INCL and NuWro. While, as we described in Section 5.2.2, we expect the  $\delta\alpha_T$  distribution to be uniform for non-transparent events, on fig. 5.17 we observe, instead, that the "no FSI" part of the  $\delta\alpha_T$  distribution is not constant and has a dip in the high  $\delta\alpha_T$  region that persists in both models. Many factors can potentially affect the  $\delta\alpha_T$  shape: energy transfer, Pauli blocking, Coulomb correction for protons, etc.

In order to disentangle all possible effects, we have performed a test simulation of the antineutrino CCQE interaction with the cross section prediction of the neutrino interaction. For simplicity, we used the RFG model and the Llewellyn-Smith formula for the  $\nu/\bar{\nu}$  cross section, where it is sufficient to change one sign to go from antineutrino cross section to neutrino. We focus on the NuWro simulation.

When we use the same cross-section, we effectively impose the same energy transfer distribution for neutrino and antineutrino interactions. Fig. 5.18 shows that  $\delta\alpha_T$  for neutrinos and antineutrinos is the same for the same energy transfer. Applying the Pauli blocking constrains the high  $\delta\alpha_T$  region for both neutrino and antineutrino simulations, as one can

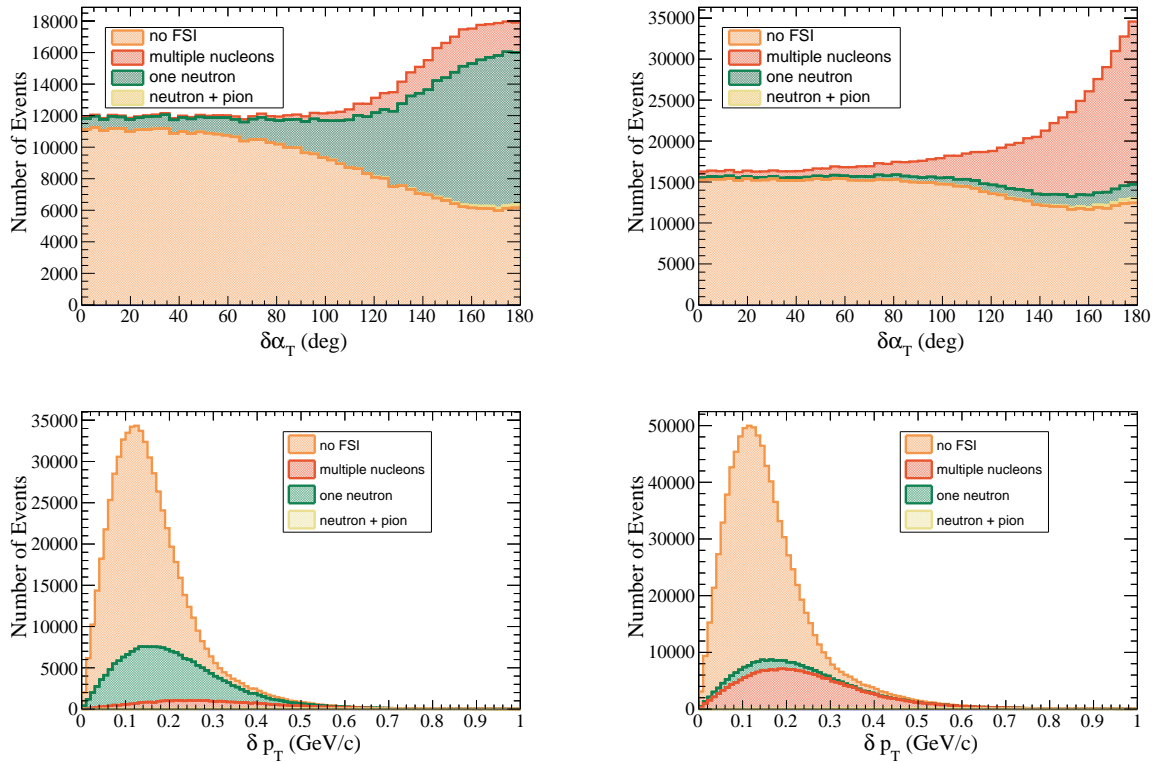


Figure 5.17 Top:  $\delta\alpha_T$  simulated with the INCL+NuWro SF (left), and NuWro (right) cascade models in CCQE events with T2K antineutrino energy flux. Bottom:  $\delta p_T$  for the INCL+NuWro SF (right) and Nuwro SF(left) nuclear models.

notice on the right plot of fig. 5.18. Therefore, the impact of the Pauli blocking is the same for the same energy transfer. Since energy transfer distribution differs for neutrino and antineutrino interactions, the Pauli blocking also acts on them differently. Considering that antineutrino CCQE interaction features lower energy transfer, the effect of the Pauli blocking is stronger than for the neutrino case. Therefore, the  $\delta\alpha_T$  distribution for transparent events is not uniform in antineutrino interactions due to the Pauli blocking. For FSI events, the conclusions are similar for neutrons and protons. For example, the suppression of the high  $\delta\alpha_T$  values in INCL.

## 5.4 Beyond factorization approach: spectral function FSI

As mentioned in Chapter 3, the NuWro generator incorporates a feature to go beyond the factorization approach [5]. In this section, we enable the "SF FSI" option to study its impact on FSI. SF FSI allows for events with a very low energy transfer that goes almost to zero. The INCL nucleus naturally absorbs such low-momentum protons, as shown in fig. 5.19.

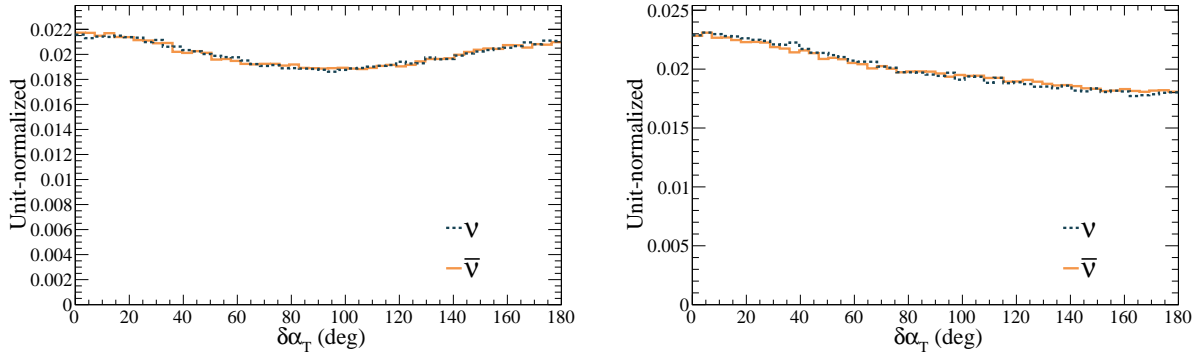


Figure 5.18  $\delta\alpha_T$  simulated with NuWro using the Llewellyn-Smith formula without (left) and with (right) Pauli Blocking.

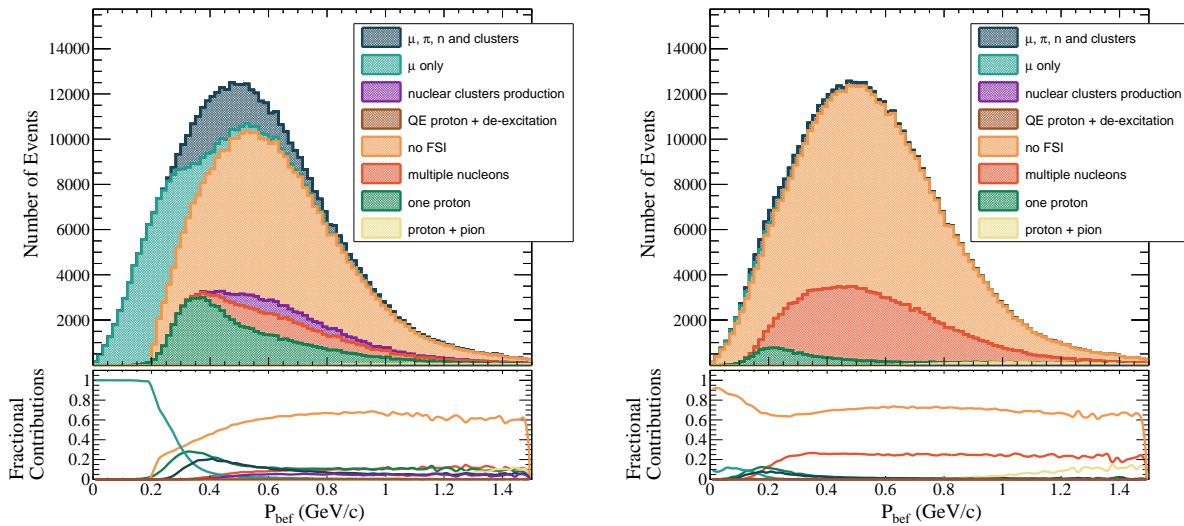


Figure 5.19 Proton momentum before FSI simulated with INCL+NuWro SF (left) and NuWro SF (right). "SF FSI" option in NuWro simulation was used.

SF FSI option alters the definition of the "no FSI" channel. In this case, some of the effects induced by the nuclear potential on the outgoing particles are already incorporated into the vertex simulation. Such option induces not only a modification on the kinematics of the hadronic final state but also of the lepton kinematics (through a modification of the cross-section as a function of the transferred energy). Fig. 5.20 shows the  $\delta\alpha_T$  simulated with INCL and NuWro SF using the "SF FSI" option. As explained above, the  $\delta\alpha_T$  distribution should be uniform in the case of transparent events. Here, we witness the enhancement of the high  $\delta\alpha_T$  region for "no FSI" events. Therefore, we cannot call such events transparent and must redefine the final state channels.

This is a first glimpse into the non-factorization problems, which will have to be addressed in the future. It is important to realize that all the FSI study presented above strongly relies on

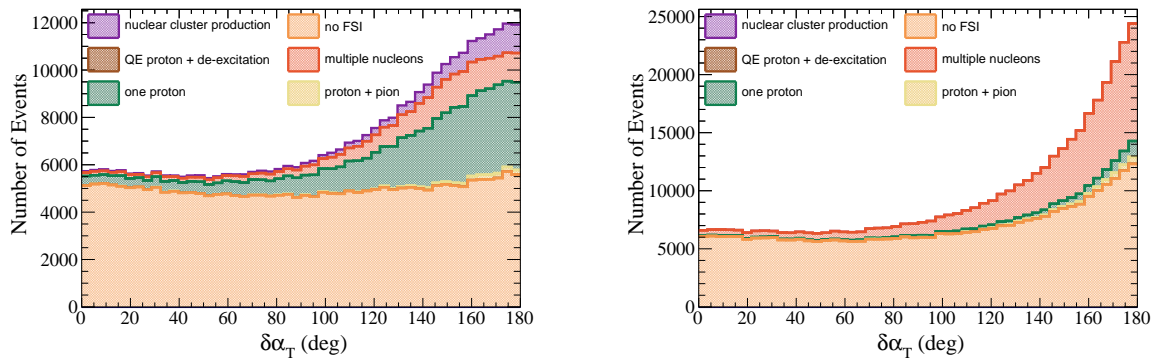


Figure 5.20  $\delta\alpha_T$  simulated with INCL+NuWro SF (left) and NuWro SF (right).

the factorization approach. This is what could be done today with present tools. In future, more advanced models based on distorted waves approximation will include "FSI" effects already at the vertex level. In this case, the simulation of the FSI cascade will have to be modified by different methods to avoid double-counting of FSI effects.

## 5.5 Summary

We compared the simulation results of INCL and NuWro cascade models of protons and neutrons for the neutrino and antineutrino CCQE reactions. Our analysis focused on the produced particles and the kinematics change of the leading nucleon induced by FSI. In particular, we used STV to compare the effects of the different cascade models. One significant difference between the two models is that INCL simulates nuclear cluster production in the FSI of neutrino interactions (this feature will be further discussed in Chapters 6 and 7). Regarding the impact of FSI on the leading nucleon, INCL's nuclear model features much lower transparency than NuWro. Transparency is a measure that allows estimating the FSI strength in a given model. Such results originate in a characteristic combination of the nucleon-nucleon cross sections, Pauli blocking, and the specifics of the used nuclear model. In particular, INCL FSI simulation features a significant fraction of events without a proton in the final state, especially while propagating low-momentum protons from the primary vertex. Additionally, the INCL model tends to reabsorb other particles produced during the FSI cascade: events with low momentum protons are mostly accompanied in NuWro with additional nucleons but not INCL. We also discussed the fundamental differences between the neutrino and antineutrino interactions and their impact on the leading neutron distribution. Featuring lower energy transfer, antineutrino interactions are more affected by the Pauli blocking. Furthermore, we analyzed the behavior of STV for the "SF FSI" simulation option. For such simulation, the  $\delta\alpha_T$  distribution for transparent events is not uniform, demonstrating the

impact of the initial state simulation on the final state variables that breaks the factorization picture.

## References

- [1] Alain Boudard et al. “New potentialities of the Liège intranuclear cascade model for reactions induced by nucleons and light charged particles”. In: *Phys. Rev. C* 87.1 (2013), p. 014606. arXiv: 1210.3498 [nucl-th].
- [2] R. Brun and F. Rademakers. “ROOT: An object oriented data analysis framework”. In: *Nucl. Instrum. Meth. A* 389 (1997). Ed. by M. Werlen and D. Perret-Gallix, pp. 81–86.
- [3] V. R. Pandharipande and Steven C. Pieper. “Nuclear transparency to intermediate-energy nucleons from (e,e’p) reactions”. In: *Phys. Rev. C* 45 (2 1992), pp. 791–798.
- [4] X.-G. Lu et al. “Measurement of nuclear effects in neutrino interactions with minimal dependence on neutrino energy”. In: *Phys. Rev. C* 94 (1 2016), p. 015503.
- [5] Artur M. Ankowski, Omar Benhar, and Makoto Sakuda. “Improving the accuracy of neutrino energy reconstruction in charged-current quasielastic scattering off nuclear targets”. In: *Phys. Rev. D* 91.3 (2015), p. 033005. arXiv: 1404.5687 [nucl-th].



# 6

## De-excitation role in $\nu$ -nucleus scattering

In the previous chapter, we have shown the results of the leading nucleon kinematics in CCQE events when FSI are simulated with INCL and NuWro. We have seen that INCL features a sizable fraction of events with no hadrons in the final state. What happened to the energy of the absorbed particles? How much energy remains in the nucleus due to all the reinteractions of the participants? In order to handle the residual energy, a further de-excitation stage is needed. The results of the INCL cascade without the subsequent de-excitation are incomplete. The de-excitation routine must follow the cascade to handle the release of the residual excitation energy. As discussed in chapter 4, we will couple INCL to ABLA since it proved its application for light nuclei [1].

In section 6.1, we calculate the excitation energy. Moving on to section 6.2, we delve into a discussion on the particles that are produced during the de-excitation process. In section 6.3, a comparison between the leading proton kinematics and STV simulated with INCL+ABLA and the INCL and NuWro results from Chapter 5 is presented. Lastly, in section 6.4, we present the neutrino energy reconstruction using only proton kinematics and the calorimetric method for INCL, INCL+ABLA, and NuWro simulations.

### 6.1 Excitation energy calculation

In order to calculate the excitation energy, we first calculate the energy and momentum of the residual nucleus:

$$\begin{aligned} E &= E_\nu + \frac{1}{2} M - \sum_i E_i \\ \vec{p} &= \vec{p}_\nu - \sum_i \vec{p}_i, \end{aligned} \tag{6.1}$$

where  $E_\nu$  is the initial neutrino energy,  ${}^{12}_6M$  is the mass of the target carbon nucleus,  $\sum_i E_i$  and  $\sum_i p_i$  are the sums of the kinetic energy and momentum of the all  $i$  outgoing particles.

Then, the excitation energy is calculated as follows:

$$E^* = \sqrt{E^2 - p^2} - M_{rem}, \quad (6.2)$$

where  $M_{rem}$  is the mass of the remnant.

In the following, we discuss the features of calculating excitation energy for the Spectral function. The Spectral Function is calculated in terms of the experimentally observable missing energy, that is defined from electron scattering experiments as:

$$E_m \equiv \omega - T_P - T_{A-1}, \quad (6.3)$$

where  $\omega$  is energy transfer,  $T_P$  is the kinetic energy of the outgoing proton and  $T_{A-1}$  is the kinetic energy of the residual nucleus. To study the excitation energy, we need to establish the relationship between the missing energy and the excitation energy. For simplicity, let us, for now, consider the transparent events where the proton from the fundamental neutrino-nucleus interaction leaves the nucleus:

$$E_m - \epsilon = M_{A-1} - (M_A - M_N), \quad (6.4)$$

here  $E_m$  is the missing energy,  $\epsilon$  is the excitation energy,  $M_N$  is the mass of a neutron,  $M_A$  and  $M_{A-1}$  are the masses of the initial and final nucleus, respectively. Taking into account that:

$$M_A = M_{A-1} + M_N - E_s, \quad (6.5)$$

where  $E_s$  is the separation energy, we can conclude that

$$E_m - \epsilon = E_s. \quad (6.6)$$

Therefore, to obtain the excitation energy from the missing energy, we need to shift the missing energy distribution, obtained with the spectral function, by the separation energy.

As described in Chapter 3, the spectral function (SF) used in NuWro is based on O. Benhar et al. calculation [2] that takes into account the electron scattering input to the single-particle wave functions and adds the correlated part evaluated within the local density approximation. Therefore, Benhar's spectral function consists of the mean-field and correlated parts. In the case of the model where nucleons in the nucleus do not interact with each other explicitly, the nuclear levels are precisely defined, and there is no smearing. The mean-field is no longer sufficient to describe the entire nucleus in a more realistic model that includes local

nucleon-nucleon interactions. The energy levels are no longer described by the  $\delta$ -functions and require additional smearing. We must consider that the shells are not fully occupied and introduce spectroscopic factors [3, 4].

For carbon, the shallowest shell corresponding to the smallest missing energy is the  $1p_{3/2}$  (the shell model is covered in Chapter 3). It gives a fair prediction of the missing energy. However, due to the smearing that is modelled as symmetric, we obtain negative values while calculating the corresponding excitation energy for some transparent events.

Currently, we try to account for that by changing the definition of the mass of the remnant calculation. For the transparent events, we do not use the experimental mass from the nuclear mass table but calculate the mass of the remnant under the assumption that the potential of the remnant did not change during the cascade and is equal to the initial  $^{12}\text{C}$  potential (*constant potential*):

$$M_{rem} = \frac{M_{^{12}\text{C}} A_{rem}}{A_{^{12}\text{C}}}, \quad (6.7)$$

where  $A_{rem}$  is the mass of the remnant and  $A_{^{12}\text{C}} = 12$  is the mass number of the  $^{12}\text{C}$ . Fig. 6.1 contains the excitation energy distributions calculated with both mass of the remnant from the nuclear mass table and with mass calculated according to equation 6.7 for the simulated with NuWro transparent events. We no longer have the negative excitation with the new  $M_{rem}$  calculation. This treatment, while not completely satisfactory, palliates the problem related with the limitations of the spectral function approach and allows to avoid nonphysical values of excitation energy.

Fig. 6.2 represents the final distribution of the excitation energy calculated for INCL and NuWro simulations for all events. INCL FSI features larger excitation energy than NuWro.

## 6.2 Particle production in de-excitation

In MC generators, neutrino interaction is always forced to happen, so the computation time is not lost for simulation of the numerous transparent events. INCL has a different philosophy and also simulates if the projectile interacted with the target nucleus. If event is transparent, INCL does not record it. In the case of the neutrino interaction simulation, INCL defines if the event was "transparent" according to the fate of the leading proton. For such events, we need to force INCL to compute the excitation energy according to the calculations in section 6.1. For the "non-transparent" it happens automatically, and the calculated value is an input of INCL to the ABLA de-excitation process. ABLA features a large production of protons, neutrons and nuclear clusters. Fig. 6.3 shows the average number of particles per event produced by INCL, INCL+ABLA, and NuWro. NuWro produces more protons than INCL, but ABLA enhances proton production almost by factor 3. Also, ABLA increases the production of  $\alpha$  particles by a factor of 10. These particles carry lower momentum than the ones produced

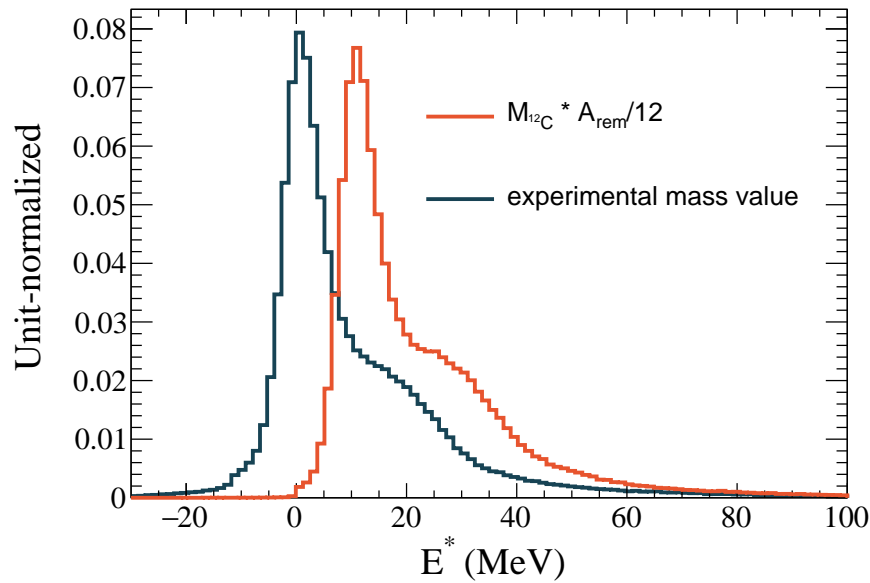


Figure 6.1 Excitation energy calculated for transparent events simulated with NuWro. The mass of the remnant is simulated with constant potential and with the mass table.

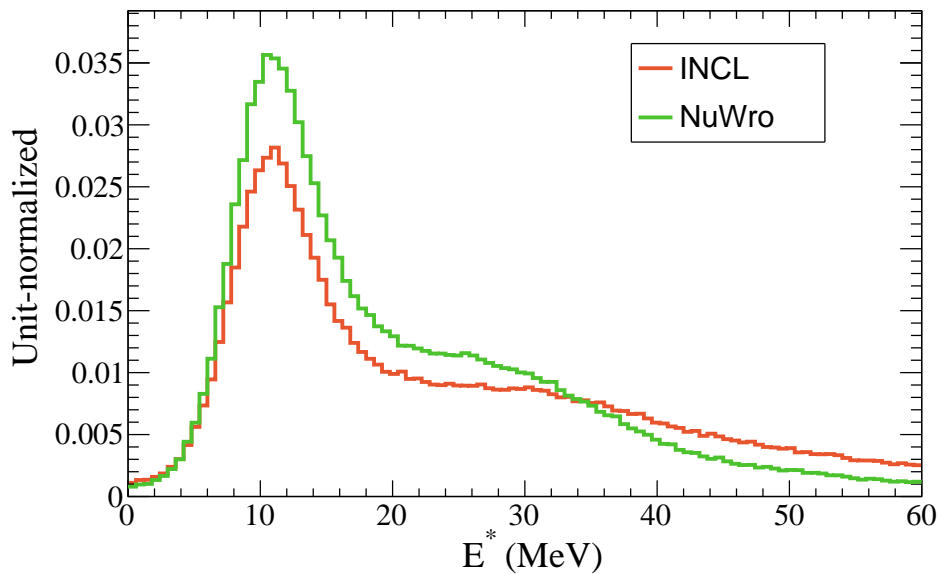


Figure 6.2 Excitation energy after INCL and NuWro cascades.

during the cascade. Fig. 6.4 shows the momentum distribution of  $\alpha$ , deuterons, and protons produced during cascade and de-excitation and the energy spectrum of the most frequently produced particles and  $\gamma$ -rays. More information about  $\gamma$ -ray emission can be found in Chapter 4. This sporadic process starts competing with nucleon emission if the excitation

energy is too low to emit nucleons (for example, as the last stage of the de-excitation process). Low-energy  $\gamma$ -rays are not crucial for the ND scintillators, where nuclear clusters and protons dominate the VA. However, they are essential for other neutrino applications, for example, the Super-Kamiokane NCQE measurement [5] and the recent Kamland measurement [6]. As mentioned in Chapter 4, ABLA does not simulate the discrete  $\gamma$ -ray emission from the lower-lying nuclear levels since this requires specific nuclear structure databases. Another code—FIFRELIN [7], specializing in gamma de-excitation—can be employed for such a low-energetic  $\gamma$ -ray emission. It proved useful for neutrino applications, as was shown by the STEREO collaboration in Ref. [8].

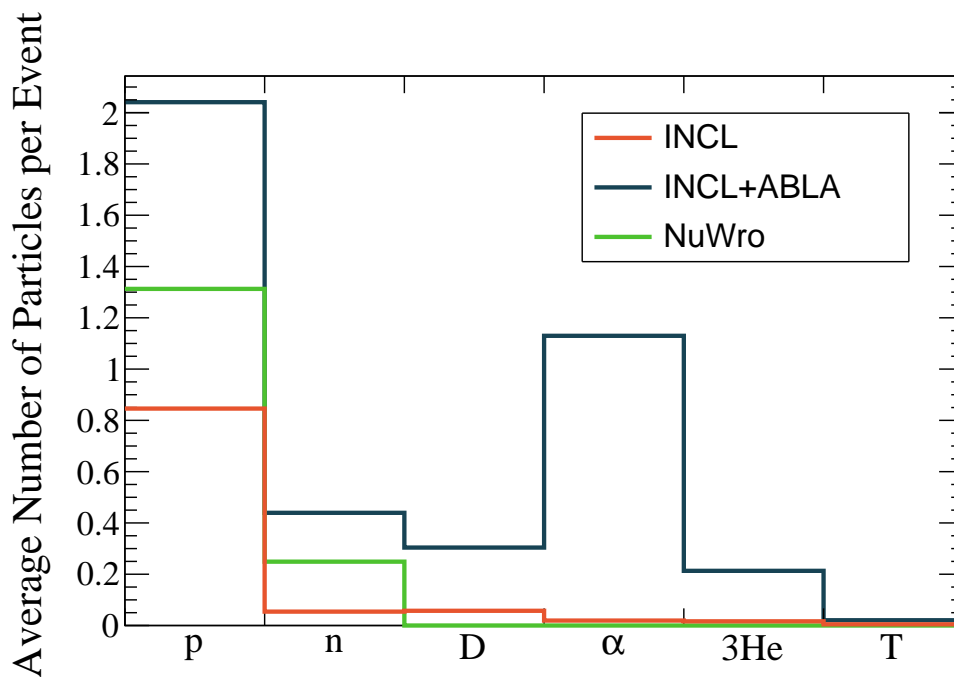


Figure 6.3 Average number of different particles in NuWro, INCL and INCL+ABLA simulations.

### 6.3 Proton kinematics

As in Chapter 5, we study the proton momentum before and after FSI, including the effects of de-excitation after the cascade. Fig. 6.5 shows these distributions simulated with INCL+ABLA, INCL, and NuWro. The INCL+ABLA simulation, unlike the bare INCL simulation, does not have such a distinctive fraction of events with no proton in the final state. However, even though we have recovered some events with a proton in the final state, the kinematics of these protons is very different from those of protons simulated by NuWro since they were produced in the nuclear de-excitation and not by the FSI cascade. In the events where

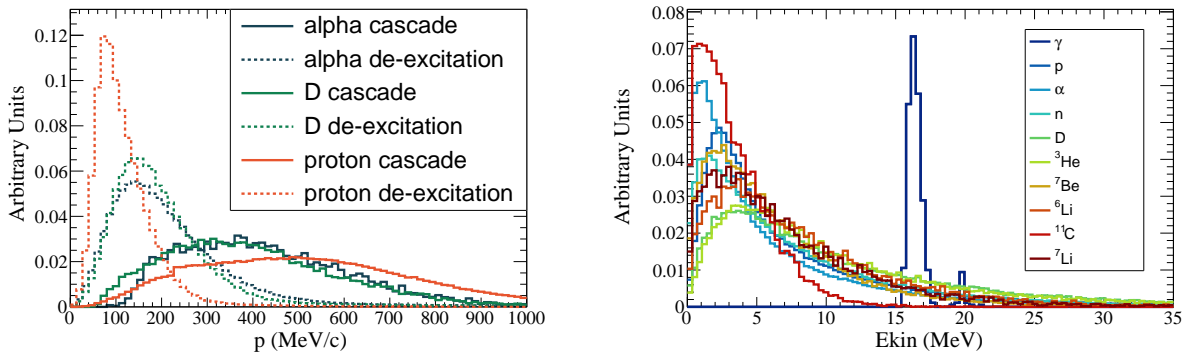


Figure 6.4 Comparison of the momentum distribution of  $\alpha$ , deuterons and protons produced during cascade and de-excitation (left) and energy spectrum of the top 9 produced particles during de-excitation (right). The  $\gamma$ -ray distribution was additionally scale down to 25%, so its peak is comparable to the energy spectra peaks of the emitted hadrons.

proton was absorbed, which were labeled as "proton absorption" and " $\mu, \pi, n$  and clusters," a significant amount of energy was left in the nucleus, which is then released during de-excitation, therefore in INCL+ABLA simulation we have production of nuclear clusters and protons in those events. For INCL, "nuclear clusters production" are of the same order as "multiple nucleons." In contrast, after enabling de-excitation, the fraction of events with only nucleons produced becomes negligible (less than 2%). The channel featuring the production of nuclear clusters becomes one of the dominant ones. NuWro has an approximated treatment of the cascade coupled to the de-excitation based on energy conservation and not an actual de-excitation model. Therefore, it looks in between INCL and INCL+ABLA, in some sense. However, we need a complete de-excitation simulation like ABLA to get the kinematics of the outgoing particles correctly.

An exclusive feature of coupling INCL to ABLA is the "QE proton + de-excitation" channel: a former "no FSI" channel, where the cascade featured only one outgoing proton that left the nucleus without interaction. However, the excitation energy due to the fundamental neutrino interaction was emitted via additional nuclear fragments. There is a small fraction of the "no FSI" events in the INCL+ABLA simulation. These are events with very low excitation energy; in reality, this energy should be emitted with  $\gamma$  rays. Nevertheless, as mentioned in Chapter 5, this process is not simulated in ABLA, so no other particles are produced during the de-excitation process.

### 6.3.1 Single Transverse Variables

Fig. 6.6 shows  $\delta\alpha_T$  and  $\delta p_T$  simulated with INCL+ABLA. The  $\delta p_T$  shape is very similar to the results from Chapter 5. At the same time,  $\delta\alpha_T$  features a massive difference in these two

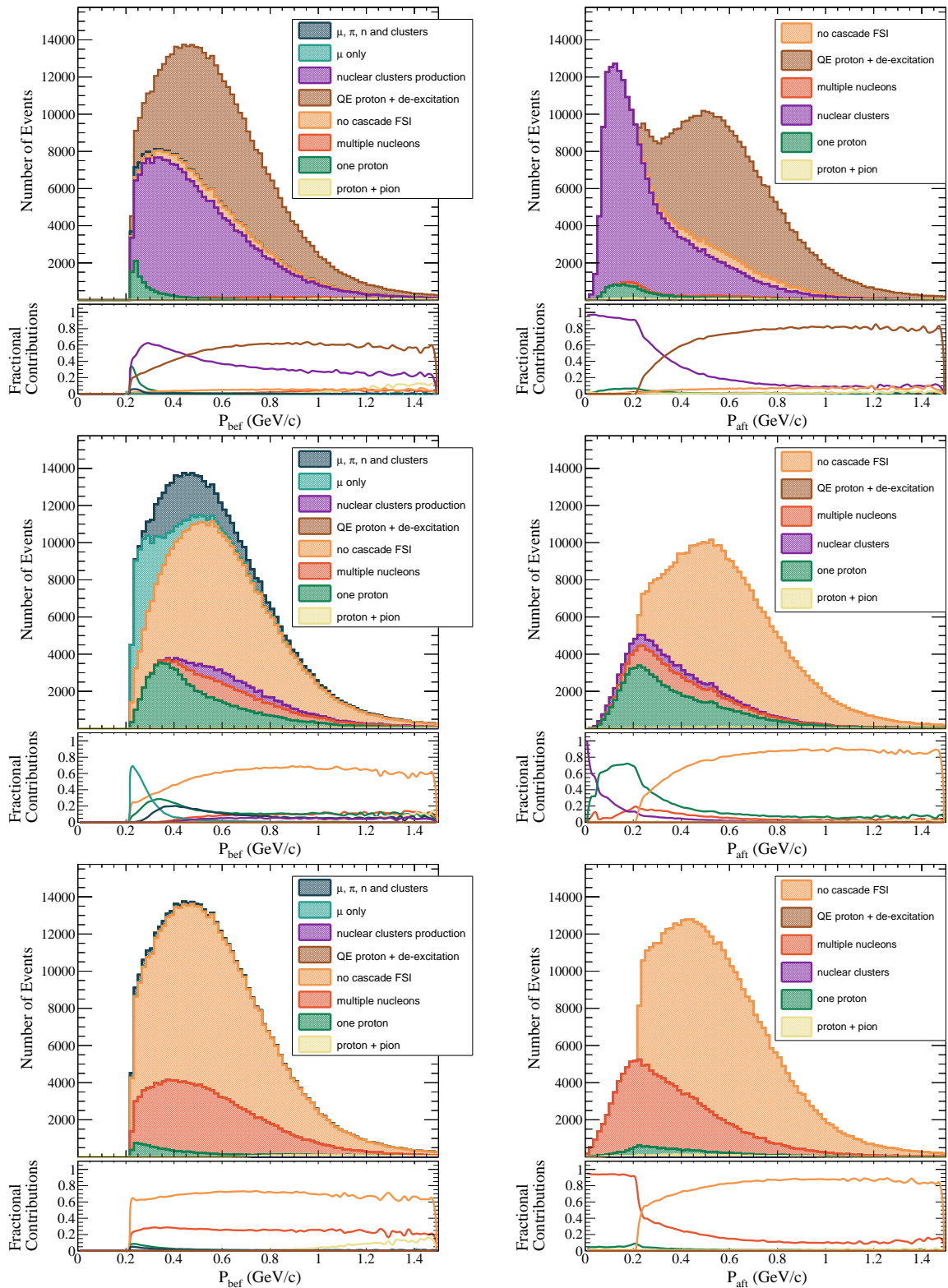


Figure 6.5 Proton momentum before (left) and after (right) FSI. Simulated with INCL+ABLA (top), INCL (center), and NuWro (bottom) cascade models in CCQE events with T2K neutrino energy flux. Sub-processes correspond to the fate of the proton after FSI. The shape of proton momentum before FSI is by definition identical for INCL and NuWro cascades. The plots with the INCL and NuWro results are the same as in Chapter 5.

simulations in the high  $\delta\alpha_T$  region. As described in subsection 5.2.2, the high  $\delta\alpha_T$  values correspond to low momentum protons, typically strongly decelerated by FSI. ABLA produced low-momentum protons that, in case of absence of the cascade-produced protons, populate the high  $\delta\alpha_T$  region. As a consequence, we have a massive difference in  $\delta\alpha_T$  distribution with bigger fraction of events at high  $\delta\alpha_T$  in presence of de-excitation. If the proton was created during the cascade, it will have higher momentum than the proton produced during de-excitation, so de-excitation does not change the leading proton kinematics in events where the leading proton comes from the cascade. Meanwhile, if no protons were produced during the cascade, the de-excitation proton will become a leading proton, and STV will be reconstructed for such event. The very high  $\delta\alpha_T$  values in INCL+ABLA simulation are suppressed by the Pauli blocking in the FSI cascade which forbids events with low momentum protons.

## 6.4 Neutrino energy reconstruction

Currently, the neutrino energy is reconstructed using muon kinematics only or the formula considering the total muon energy and kinetic energy of the leading proton (both methods were discussed in Chapter 2). We can also consider a more inclusive calorimetric energy reconstruction where all the energy released in the detector by all the final state products is taken into account [9]. The first step towards utilizing the *calorimetric method* is to study the vertex activity [10, 11], which will be further discussed in Chapter 7.

We reconstruct the neutrino energy using the NuWro, INCL, and INCL+ABLA simulations. Fig. 6.7 presents the neutrino reconstruction resolution calculated with leading proton only and with the calorimetric method. In the presence of de-excitation, there is a large multiplicity of particles in the final state, and the leading proton carries a smaller fraction of total energy. Therefore we have a larger tail of small  $E_{rec}$  when we consider only the muon and the proton. However, de-excitation plays a crucial role if we include the kinetic energy of all the final state particles for the reconstruction of the neutrino energy. Without the de-excitation simulation, the separation energy does not produce any observable signature (i.e., it corresponds to missing energy), so the reconstructed energy is biased. In the presence of the de-excitation simulation, the separation energy translates into excitation energy, following equation 6.4, and it is released in the form of additional nucleons and nuclear clusters. In this case, the energy could be reconstructed unbiasedly when all the final state particle's kinematics are included.

Figure 6.8 contains more detailed information about the resolution of neutrino energy reconstruction using INCL+ABLA simulation. On the left plot containing all events, the reconstruction improvement using all produced hadrons is already discussed in Fig. 6.7. The center and right plots contain this distribution separated by FSI and no-FSI events,

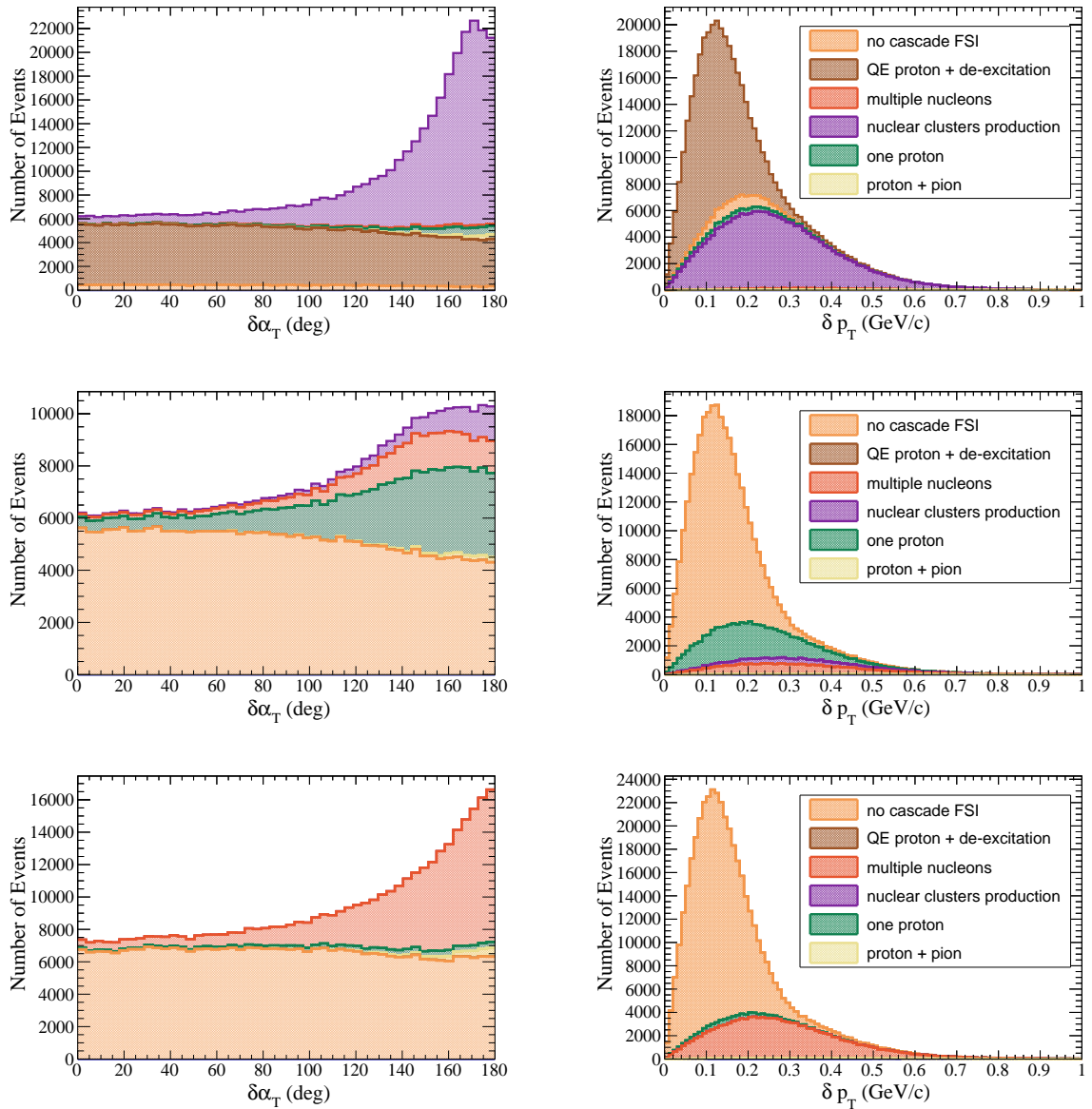


Figure 6.6  $\delta\alpha_T$  (left) and  $\delta p_T$  (right) simulated with INCL+ABLA (top), INCL (center) and NuWro (bottom) cascade models in CCQE events with T2K antineutrino energy flux. The plots with the INCL and NuWro results are the same as in Chapter 5.

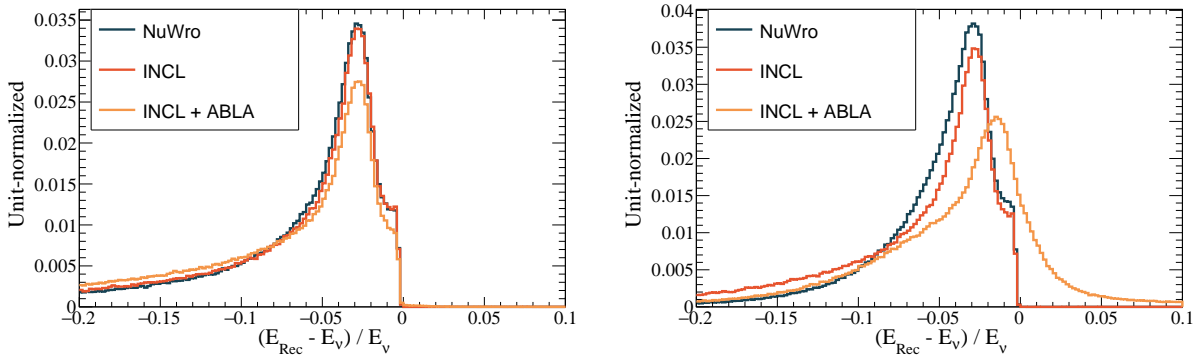


Figure 6.7 Shape comparison of the neutrino energy reconstruction resolution using proton and muon only (left) or the sum of the kinetic energy of all the final state particles (right).

respectively. Since there is always some excitation energy from the fundamental neutrino interaction, de-excitation produces extra particles, considering all the particles in the final state improves the resolution even for no-FSI events. Since we use the constant-potential mass for the excitation energy calculation, in some events, our calculation is higher than the actual excitation energy, so we overestimate the reconstructed neutrino energy.

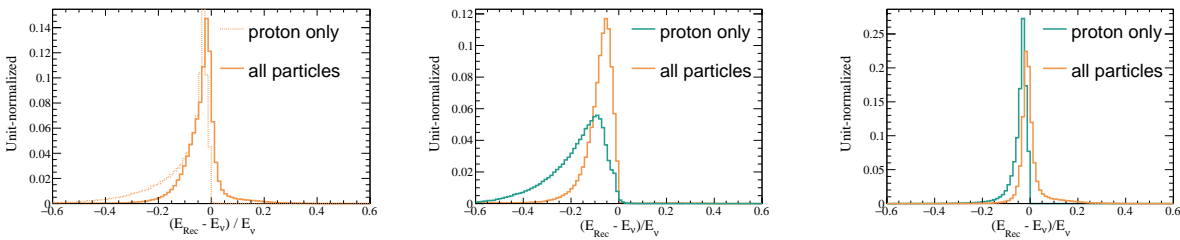


Figure 6.8 Shape comparison of the neutrino energy reconstruction resolution using with proton and muon only and with all outgoing particles. Left: all events simulated with NuWro, INCL and INCL+ABLA; center: INCL+ABLA simulation of the FSI events; right: INCL+ABLA simulation of the no FSI events.

## 6.5 Summary

We have discussed the role of nuclear de-excitation in neutrino-nucleus interactions. Even if the hadrons outgoing from the neutrino vertex do not undergo any FSI, nonetheless, the nucleus will have non-zero excitation energy resulting from the fundamental neutrino interaction. FSI will further increase the energy stored in the nucleus, especially in case of nucleon absorption, and such energy will be then released during the de-excitation stage. During de-excitation, ABLA generates a significant amount of various particles, mainly protons and

alpha particles. INCL+ABLA simulation shows almost three times increased production of protons and ten times that of alphas.

De-excitation induces proton production also in some of events where the FSI cascade proton was absorbed, but the kinematics of these protons differ drastically from those produced by FSI. The presence of de-excitation simulation causes the separation energy to convert into excitation energy, which is released as additional particles. As a consequence, all particles produced in the neutrino events should be considered, so the neutrino energy can be reconstructed unbiasedly.

The precise neutrino energy reconstruction is a vital step for the new generation of oscillation experiments. The calorimetric method of the neutrino energy reconstruction, which considers all emitted particles after the neutrino interaction, allows for better neutrino energy resolution but also demands better modeling of the hadronic compound of the neutrino-nucleus interactions. Understanding the production and kinematical properties of nuclear clusters is crucial for improving the existing neutrino-nucleus interaction models and controlling the corresponding systematic uncertainties. We present a detailed study of the nuclear clusters' behavior in the next Chapter 7.

## References

- [1] Benjamin Braunn et al. “Assessment of nuclear-reaction codes for proton-induced reactions on light nuclei below 250 MeV”. In: *The European Physical Journal Plus* 130.7 (2015), p. 153.
- [2] O. Benhar et al. “Spectral function of finite nuclei and scattering of GeV electrons”. In: *Nuclear Physics A* 579.3 (1994), pp. 493–517.
- [3] C. Bisconti, F. Arias de Saavedra, and G. Co’. “Momentum distributions and spectroscopic factors of doubly closed shell nuclei in correlated basis function theory”. In: *Phys. Rev. C* 75 (5 2007), p. 054302.
- [4] F. Arias de Saavedra et al. “Renormalized Fermi hypernetted chain approach in medium–heavy nuclei”. In: *Physics Reports* 450.1 (2007), pp. 1–95.
- [5] K. Abe et al. “Measurement of neutrino and antineutrino neutral-current quasielastic-like interactions on oxygen by detecting nuclear deexcitation  $\gamma$  rays”. In: *Phys. Rev. D* 100.11 (2019), p. 112009. arXiv: 1910.09439 [hep-ex].
- [6] S. Abe et al. “First measurement of the strange axial coupling constant using neutral-current quasi-elastic interactions of atmospheric neutrinos at KamLAND”. In: (Nov. 2022). arXiv: 2211.13911 [hep-ex].
- [7] D. Regnier, O. Litaize, and O. Serot. “An improved numerical method to compute neutron/gamma deexcitation cascades starting from a high spin state”. In: *Computer Physics Communications* 201 (2016), pp. 19–28.
- [8] H. Almazan et al. “Improved FIFRELIN de-excitation model for neutrino applications”. In: (July 2022). arXiv: 2207.10918 [hep-ex].
- [9] Artur M. Ankowski et al. “Comparison of the calorimetric and kinematic methods of neutrino energy reconstruction in disappearance experiments”. In: *Phys. Rev. D* 92.7 (2015), p. 073014. arXiv: 1507.08560 [hep-ph].
- [10] G. A. Fiorentini et al. “Measurement of Muon Neutrino Quasielastic Scattering on a Hydrocarbon Target at  $E_\nu \sim 3.5$  GeV”. In: *Phys. Rev. Lett.* 111 (2 2013), p. 022502.
- [11] L. Fields et al. “Measurement of Muon Antineutrino Quasielastic Scattering on a Hydrocarbon Target at  $E_\nu \sim 3.5$  GeV”. In: *Phys. Rev. Lett.* 111 (2 2013), p. 022501.

# 7

## Experimental observables

While in previous chapters we discussed the variables at the MC generator level (for example, proton momentum before FSI is a very interesting variable to study, but it is not experimentally observable), this chapter is dedicated to discussing variables observable in the detector. Section 7.1 compares the studied simulations with available measurements of STV and anticipates the possible sensitivity of the next generation of detectors to the nuclear effects due to FSI. Section 7.2 details the study of the nuclear clusters' behavior in the detector using Geant4 simulation. Section 7.3 reports the neutron secondary interactions simulation results with Bertini and INCL cascades implemented in Geant4.

### 7.1 Proton kinematics: comparison to the available data

Given their new capabilities, the developed models will be crucial for future detectors, such as the T2K ND280 upgrade and the LAr TPC technology. The models presented in this thesis can also already be validated against available data on STV measurements. Here, we compare INCL, INCL+ABLA, and NuWro simulation results to the STV measurements performed by T2K [1] and MINERvA [2] in the samples without pions in the final state ( $CC0\pi$ ). The  $CC0\pi$  sample contains events not only from the CCQE channel but also from 2p2h, where the second nucleon is considered undetected, and from resonant pion production, where the pion is produced in the fundamental neutrino-nucleus interaction but then it is reabsorbed by FSI. Our INCL and INCL+ABLA Monte-Carlo samples consist of only CCQE events. We add the contribution of non-QE interactions from NuWro to compare to experimental data. Moreover, the experimental acceptance and thresholds lead to constraints on the phase space where detectors have adequate sensitivity. Table 7.1 presents the acceptance cuts of the T2K and MINERvA STV measurements.

Table 7.1 Signal phase space restriction for the T2K and MINERvA measurements. For T2K, the cuts apply to the proton with the highest momentum. For MINERvA, event passes the cuts if any proton corresponds to the allowed phase space.

<b>Experiment</b>	<b><math>p_\mu</math></b>	<b><math>p_p</math></b>	<b><math>\theta_\mu</math></b>	<b><math>\theta_p</math></b>
T2K	$p_\mu > 250$	$450 < p_p < 1000$	$\cos(\theta_\mu) > -0.6$	$\cos(\theta_p) > 0.4$
MINERvA	$1500 < p_\mu < 10000$	$450 < p_p < 1200$	$\cos(\theta_\mu) > 0.93$	$\cos(\theta_p) > 0.34$

We apply these experimental cuts to the prediction of NuWro and INCL and compare to STV measurements of T2K and MINERvA in Figs. 7.1 and 7.2. Such acceptance cuts, notably requiring large enough proton momentum to be reconstructed, tend to suppress the difference between the models. We look forward to measurements with a lower tracking threshold, as expected, for instance, with ND280 upgrade [3] and the detectors of the SBN program [4]. The different shape in  $\delta\alpha_T$  is washed out. Still, due to proton absorption, the lower overall normalization of INCL is visible. Such feature tends to slightly improve the data-MC agreement. MINERvA neutrino flux has higher energy than the T2K flux. It is therefore more affected by the contributions of the non-QE channels.

For the INCL sample, we also reconstruct STV including nuclear clusters. In this case, the nuclear cluster or the proton with the highest momentum is chosen as a proton candidate. We assume the same acceptance cuts for protons and nuclear clusters for simplicity. As previously seen in generator-level studies in Chapters 5 and 6, nuclear clusters distribute at high  $\delta\alpha_T$ , similarly to protons affected by FSI. Given the relatively high momentum threshold for proton tracking, the different proton momentum distributions after FSI in the two cascade models (even including nuclear clusters) have a subleading effect.

As Chapter 6 shows, de-excitation significantly modifies the leading proton kinematics and STV, particularly  $\delta\alpha_T$  prediction. Fig. 7.3 shows the superimposed prediction of  $\delta\alpha_T$  and  $\delta p_T$  of INCL, INCL+ABLA and NuWro. Since ABLA mostly produces low-momentum particles, these events are not accepted by the experimental cuts. In the end, the current detector threshold is too large to see the impact of the de-excitation.

Trying to mimic the acceptance of the next generation of experiments, we have modified the current T2K cuts and applied them to our simulations. The result is shown in Fig. 7.4. Firstly, we removed the cut on the  $\theta_\mu$  to mimic the  $4\pi$  acceptance. Then we gradually lowered the leading proton momentum threshold. As one can see, depending on the data precision, it is possible to distinguish the prediction of the different models starting from 200 MeV/c cut on the leading proton momentum.

Spotting differences between the models by looking only at the reconstructed protons requires a very low threshold and, thus, is very challenging. On the other hand, a sizable fraction of energy goes into nuclear clusters and protons below tracking threshold, and, as shown in Chapters 5 and 6, there are significant distinctions between the models in that

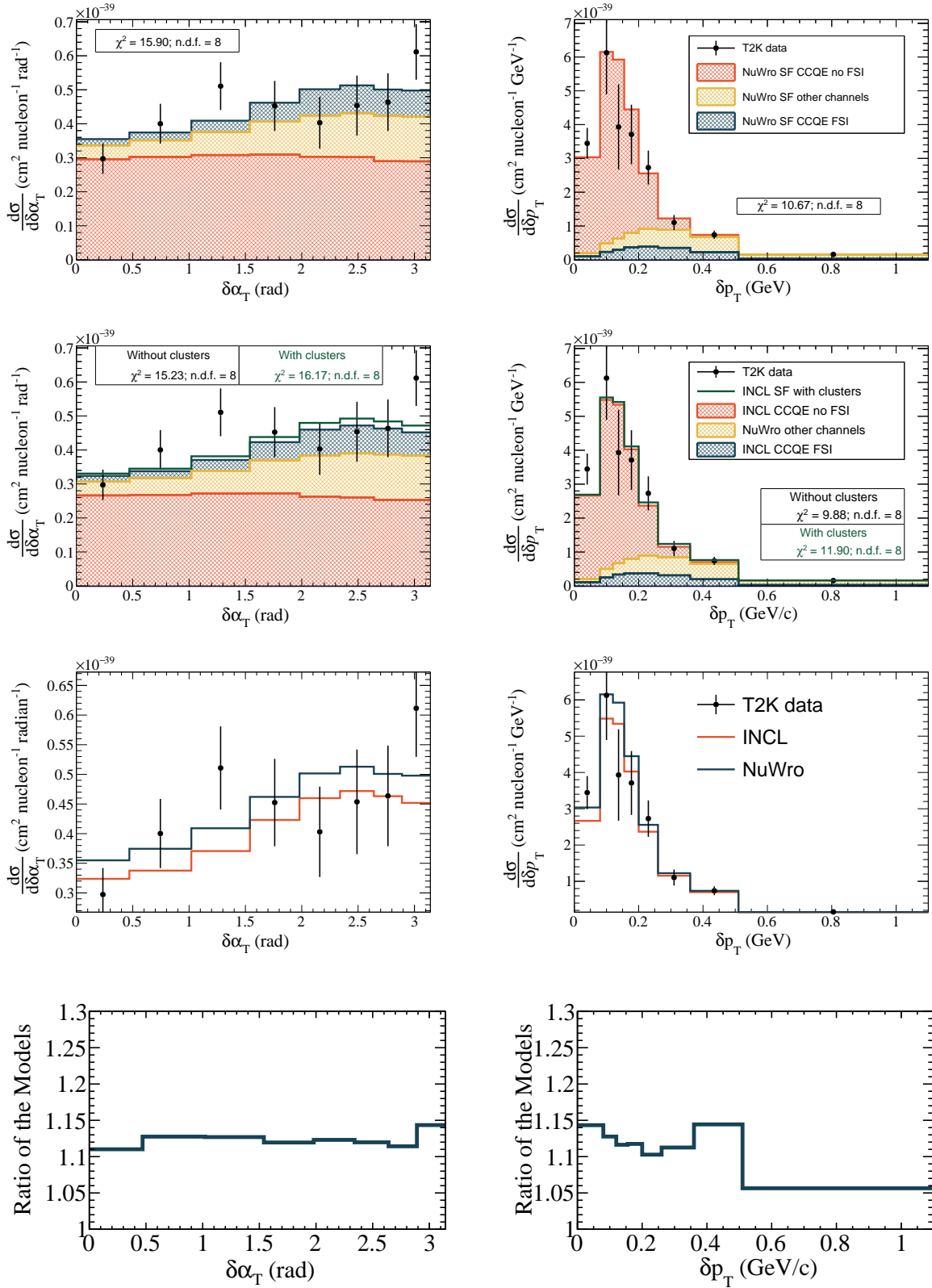


Figure 7.1 Top to bottom: NuWro SF comparison to T2K data; INCL + NuWro SF comparison to T2K data; comparison of NuWro, INCL + NuWro SF and data; ratio of NuWro SF and INCL + NuWro SF models of QE channel. Left:  $\delta\alpha_T$ , right:  $\delta p_T$ .

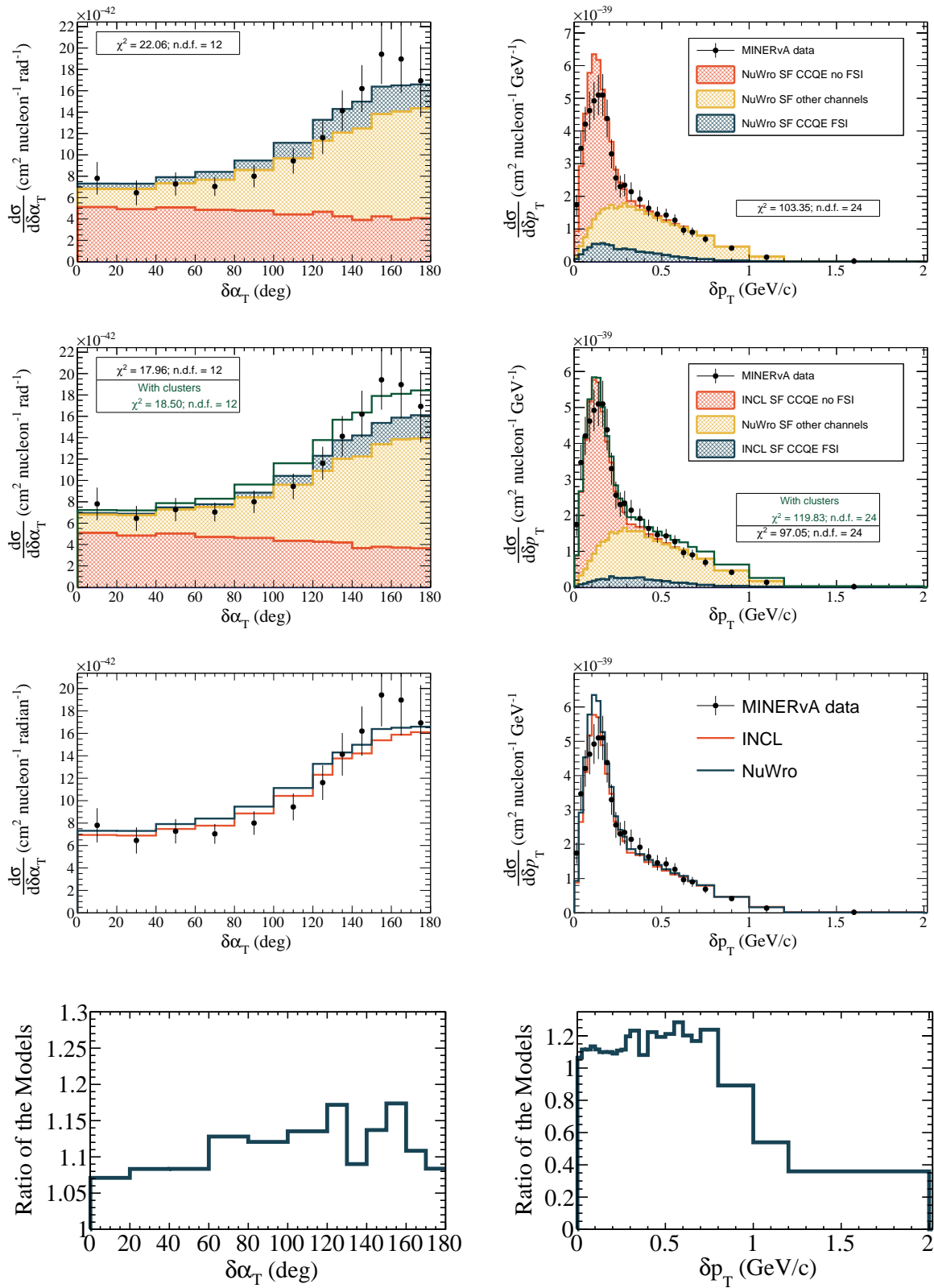


Figure 7.2 Top to bottom: NuWro SF comparison to MINERvA data; INCL + NuWro SF comparison to T2K data; comparison of NuWro, INCL + NuWro SF and data; ratio of NuWro SF and INCL + NuWro SF models of QE channel. Left:  $\delta\alpha_T$ , right:  $\delta p_T$ .

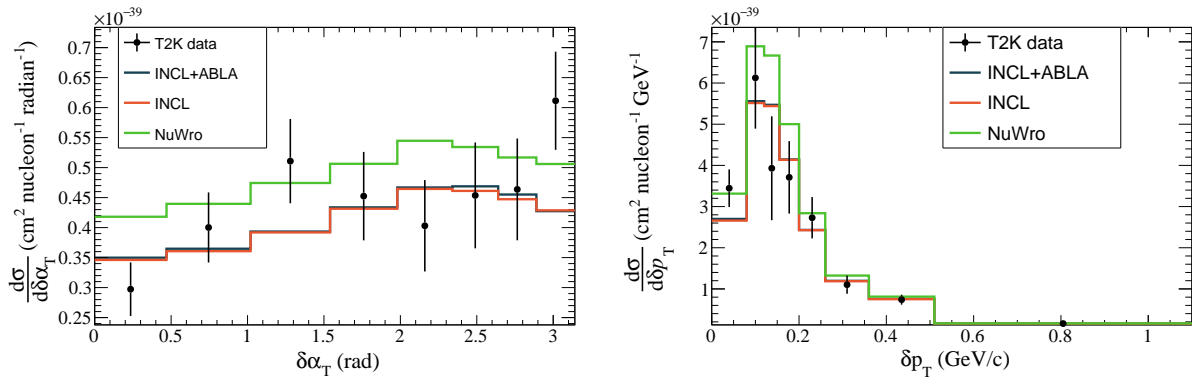


Figure 7.3 INCL, INCL+ABLA and NuWro comparison to the T2K data, superimposed. Left:  $\delta\alpha_T$ , right:  $\delta p_T$ .

region. Therefore it is essential to examine other variables, like vertex activity discussed below, to recollect experimentally the energy below the proton tracking threshold.

## 7.2 Nuclear clusters and vertex activity

The novelty of the nuclear cluster production in neutrino-nucleus interactions poses new various questions. Can nuclear clusters be seen in the detector? Can we misidentify them with the leading proton? Can we reconstruct their tracks, or will they contribute to the energy deposited around the vertex (vertex activity)? We will try to answer these questions in the following two sections.

### 7.2.1 Modelling of clusters using Geant4

In order to study the behavior of nuclear clusters in the detector, we have built a simple Geant4 [5–7] model. Here we focus on the hydrocarbon (CH) target, but a similar study could be as well performed for argon. We modeled a uniform, fully active block of hydrocarbon (with  $1.06 \text{ g/cm}^3$  density corresponding to polystyrene) with dimensions big enough to contain a whole track ( $1900 \times 1900 \times 3000 \text{ cm}^3$  size). Geant4 allows to control the precision and accuracy of the interaction modeling in the energy region of interest by specifying the needed model in the physics list. For coherence between the generator of primary neutrino interactions and of secondary interactions in the detector, we selected the physics list based on INCL implemented in Geant4: G4HadronPhysicsINCLXX and G4IonINCLXXPhysics. Primary particles are generated inside the CH block along the Z axis. We simulate in Geant4 the most frequently produced particles in INCL neutrino interactions: protons, deuterons, tritons,  $\alpha$  particles, and the  $^3\text{He}$  isotope. We generate nuclear clusters with energy distribution as simulated by INCL FSI production. This energy distribution is shown in Fig. 7.5. The proton

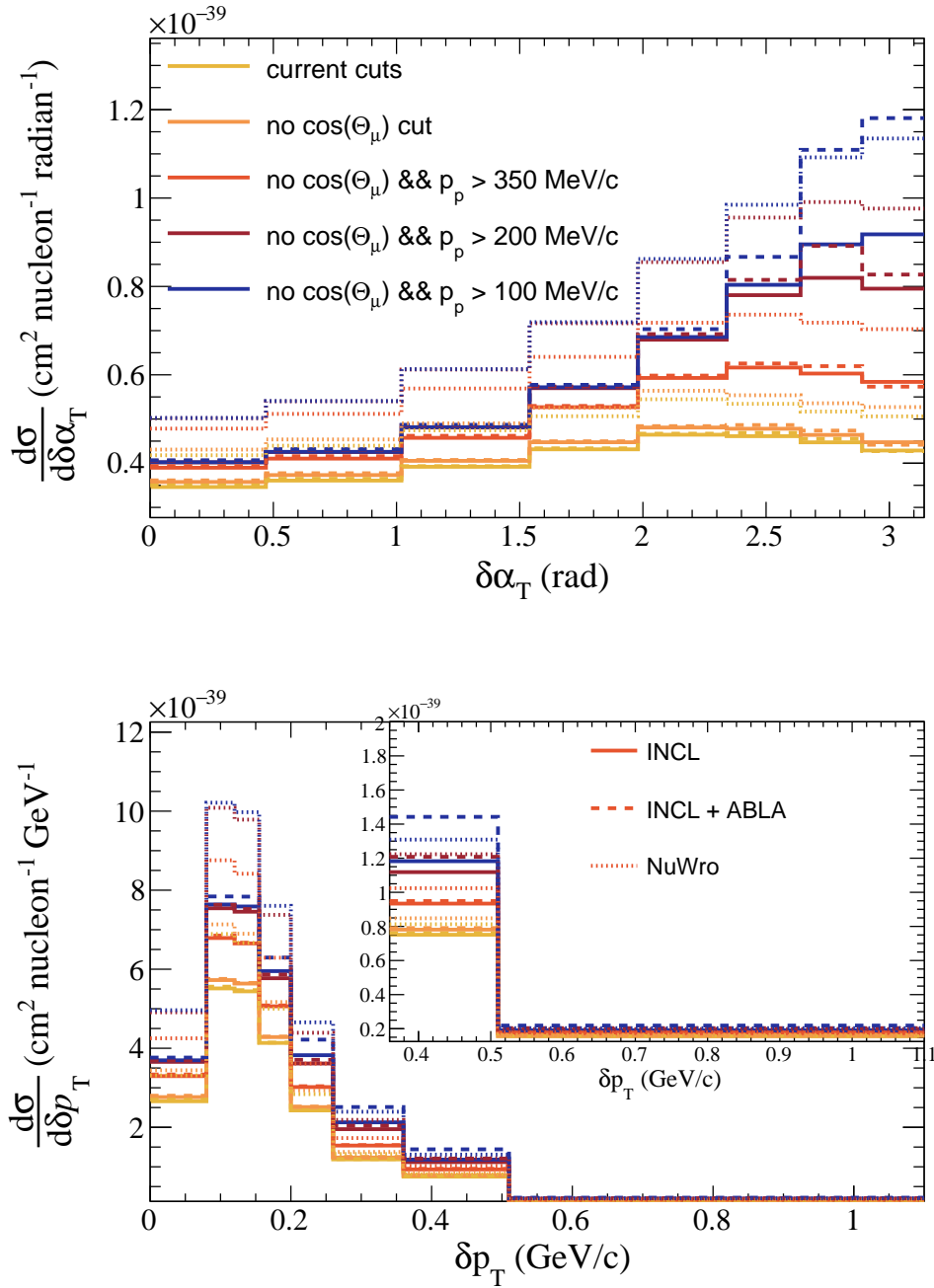


Figure 7.4 INCL, INCL+ABLA and NuWro predictions if various cuts applied. Left:  $\delta\alpha_T$ , right:  $\delta p_T$ .

energy distribution is different than others since it comes mostly from the direct neutrino-nucleus interactions while clusters are produced by FSI.

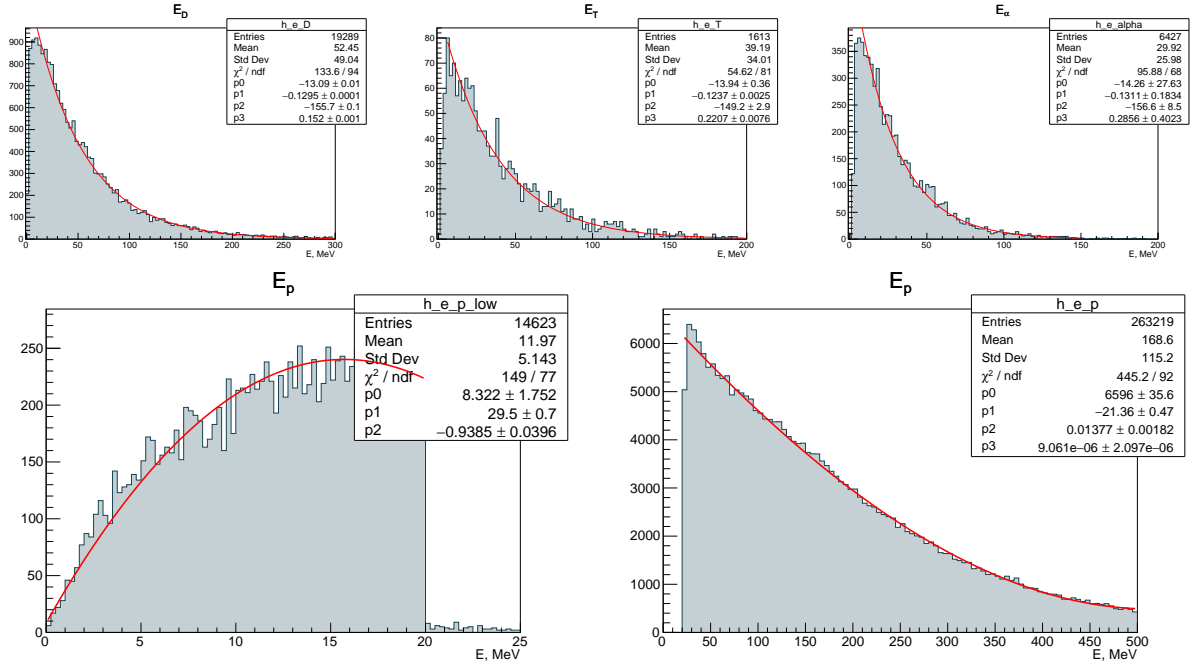


Figure 7.5 Energy distributions used for particle gun. Fit function is  $\exp(p_0 + p_1 \cdot E) + \exp(p_2 + p_3 \cdot E)$ , for low energies of the proton: 2 order polynomial.

In this study, we consider only the energy deposited by the primary particle by ionization, and we apply Birks quenching. Depending on the scintillator material, an additional suppression factor should be considered in converting energy to scintillation light. However, since this is strongly detector-dependent, it is not included in the present study to stay as general as possible. Visible energy in a given simulation step (that was limited in this simulation to 0.5 mm) is therefore calculated as

$$E^{vis} = \frac{E^{dep}}{1 + k_B \cdot \frac{E^{dep}}{L_{step}}}, \quad (7.1)$$

where  $E^{dep}$  is the energy deposited in the simulation step,  $k_B$  is the Birks coefficient, and  $L_{step}$  is the path length defined by the step of the simulation. Birks coefficient depends on the material and the type of particle traversing such material. To obtain its value, dedicated test beams are needed, but not always available, for all particles and materials. We take the Birks coefficient for protons from Ref. [8], where  $k_B = 0.0208$  (cm/MeV). According to Ref. [9], the coefficients for protons and deuterons are assumed to be the same. We also assume the same Birks coefficient for tritium. For  $\alpha$  particles, we use the results from Ref. [10], where  $k_B = 0.0085$  (cm/MeV).

In the left plot of Fig. 7.6, we can see the deposited ionization energy with Birks correction as a function of the particle's momentum. The right plot presents the length of the tracks produced by different particles as a function of their visible energy obtained with the simulation described above. The momentum of the initial nuclear clusters is superimposed with the  $dE/dx$  dependence. The  $dE/dx$  distribution of  $\alpha$  particles and  ${}^3\text{He}$  significantly differs from that of protons, deuterons, and tritons. As an example, tracks can be reconstructed in the upgraded T2K near detector if their length is more than 3 cm. Tracks of  $\alpha$  particles and  ${}^3\text{He}$  never exceed this cut, as seen on the right plot of figure 7.6. Therefore, tracks of the  $\alpha$  and  ${}^3\text{He}$  particles cannot be reconstructed in the detector, and they contribute to the vertex activity. At the same time, 36% of tritons, 53% of deuterons, and 75% of protons exceed the 3 cm cut. The  $dE/dx$  plot gives the impression that other clusters also can be distinguished from protons. However, to establish this, we must employ a particle identification algorithm based on the path traversed by clusters and the energy deposited in the detector.

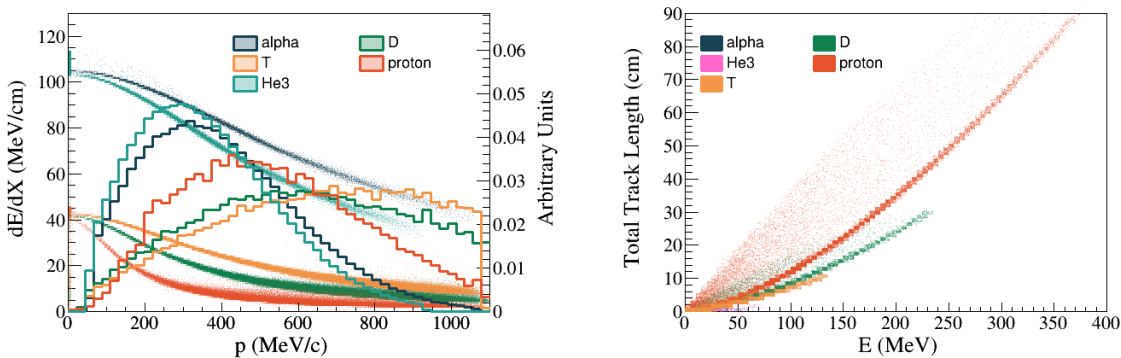


Figure 7.6 Left: momentum distribution of clusters produced by FSI in INCL (solid line) and visible energy loss by ionization (with Birks correction) as a function of their momentum (scatter plot). Right: total track length of nuclear clusters as a function of visible energy of the particles. The  ${}^3\text{He}$  distribution overlaps with the  $\alpha$  distribution and almost cannot be seen on the plot.

## 7.2.2 Identification of the nuclear clusters as tracks

Fig. 7.7 represents schematically the particle identification algorithm we developed. The main idea of this algorithm is to try to identify the type of particle based on its ionization curve. The measured deposited energy is used to estimate the particle momentum along its trajectory. The measured local energy deposits ( $dE/dx$ ) along the track are compared to the expected ones for different clusters  $\{\alpha, D, T, {}^3\text{He}, p\}$  at the estimated momenta. Finally, the algorithm selects the cluster hypothesis that best matches the observed  $dE/dx$  along the track.

Actual identification capabilities in any given experiment highly depend on the detector geometry, granularity, and scintillator material. Here, we consider a detector granularity of

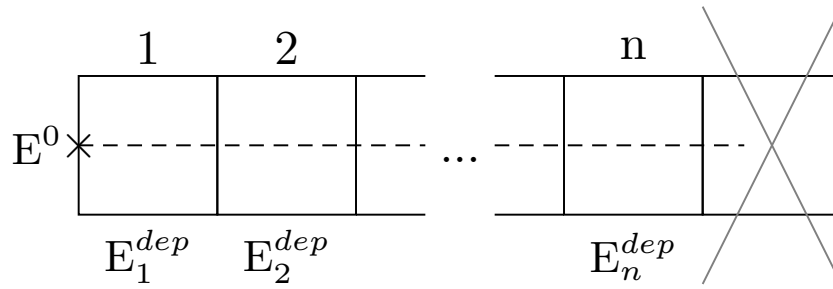


Figure 7.7 Scheme of the particles simulation and identification algorithm in a segmented scintillating detector. The shaded line indicates the cluster track traversing multiple scintillating cubes. The cluster has initial kinetic energy  $E^0$  and deposits energy  $E_i^{dep}$  in each cube. The last cube, where the cluster stops, is not considered in the identification algorithm.

1 cm<sup>3</sup> cubes, corresponding, for instance, to the geometry of the ND280 upgrade scintillating target superFGD [3]. We do not take into account any reflecting material or border effects between the cubes.

We simulate tracks as straight lines parallel to one of the cube faces and starting from the cube boundary. The last part of the track, which is shorter than 1 cm, is not used in the analysis since the exact length of the last step is unknown, given the simulated granularity. Thus we effectively remove the Bragg peak from this simplified identification algorithm. If the total particle track is shorter than 1 cm, such particles do not participate in this analysis. Moreover, at the end of the track, a fraction of events undergoes inelastic interactions with the creation of secondary particles. We do not include the energy of secondary particles in the analysis since we remove the last cube. We also modify the ionization energy plot in a way that the step of the energy deposit corresponds to 1 cm.

The total visible energy is evaluated as the sum of the visible energy in each cube

$$E^{vis} = \sum_{i=1}^n E_i^{vis}, \quad (7.2)$$

This visible energy is a proxy to the total kinetic energy of the particle, but it is not a perfect estimator since the energy lost in the last cube, where inelastic events may happen, is not included. As an analogous estimator of the remaining kinetic energy of the cluster at each step along the track, the total ‘residual’ visible energy is estimated as

$$E_i^{vis,res} = E^{vis} - \sum_{m=1}^i E_m^{vis}. \quad (7.3)$$

The distribution of the visible energy deposited in each step  $E_i^{vis}$ , as a function of the left visible energy  $E_i^{vis,left}$ , is used to build the expectations for each of the 5 particle hypotheses  $\{\alpha, D, T, {}^3\text{He}, p\}$ . For each particle  $k$ , the mean of the simulated visible energy at a given step

is estimated ( $E_i^{exp,k}$ ) for the corresponding value of remaining visible energy ( $E_i^{vis,left}$ ). The width of such distribution is also evaluated ( $\sigma_i^k$ ). Finally for each step of the simulated cluster track, the visible energy is compared to the expected one for each particle hypothesis: a  $\chi^2$  is built for each particle hypothesis

$$\chi_k^2 = \sum_{i=1}^n \frac{(E_i^{vis} - E_i^{exp,k})^2}{(\sigma_i^k)^2} \quad (7.4)$$

and the hypothesis with lowest  $\chi^2$  is chosen to identify the particle.

We have applied the procedure described above to the INCL and INCL+ABLA simulations. Table 7.2 shows the percentage of particles with a track length of more than one and three cm for the standalone INCL simulation and INCL+ABLA. As one can see, if we couple INCL and ABLA, this percentage drastically drops. Indeed, while ABLA de-excitation adds a lot more nuclear clusters in the final state, nevertheless, they have typically lower momentum than the ones produced during the cascade. Consequently, most nuclear clusters originated in de-excitation will not leave visible tracks inside the detectors.

Table 7.2 Percentage of clusters travelling more than 1 and 3 cm, for INCL only and INCL+ABLA simulations.

INCL					
	$\alpha$	${}^3\text{He}$	T	D	proton
Travels more than 1 cm, %	0.3	1.3	60	72	87
Travels more than 3 cm, %	0	0	34	51	74

INCL+ABLA					
	$\alpha$	${}^3\text{He}$	T	D	proton
Travels more than 1 cm, %	0.05	1	7.5	12.5	18.5
Travels more than 3 cm, %	0	0	2	5	12

The primary source of misidentification is secondary interactions through inelastic processes, which typically happen at the end of the cluster track. In such inelastic interactions, the cluster loses a sizable portion of energy and breaks the nucleus. The observed energy released by ionization along the cluster track before the end of the track does not include the energy released by secondary interactions. It is, therefore, smaller than expected for a cluster of that energy. As a consequence, particles could be misidentified with less ionizing ones. Tables 7.3 and 7.4 contain the misidentification percentages for all types of the studied particles.

${}^3\text{He}$  and  $\alpha$  rarely travel more than 1 cm. When they do, they can be easily identified due to their large energy deposit. Tritons are mostly misidentified as deuterons and protons, while deuterons are misidentified as protons, as for the INCL simulations.

Table 7.3 Percentage of misidentified clusters simulated with INCL.

	$\alpha$	${}^3\text{He}$	D	T	proton	total misidentification
$\alpha$	-	0	0	0	0	0
${}^3\text{He}$	0	-	0	0	0	0
D	0	0	-	0	18%	18%
T	0	0	5%	-	6%	11%
proton	0	0	0	0	-	0

Table 7.4 Percentage of misidentified clusters simulated with INCL+ABLA.

	$\alpha$	${}^3\text{He}$	D	T	proton	total misidentification
$\alpha$	-	0	-	0	0	0%
${}^3\text{He}$	0	-	0	0	0	0%
D	0	0	-	0	1%	1%
T	0	0	4.5%	-	0.3%	4.8%
proton	0	0	0	0	-	0

### 7.2.3 Vertex activity

The previous section was dedicated to the particles producing a visible track inside the detector. Particles below the tracking threshold are also interesting to study: they contribute to the total energy deposited around the vertex, called a *vertex activity* (VA). To compute the contribution of clusters to the vertex activity, we calculate the visible energy deposited by ionization in a sphere of 1 (3) cm radius around the vertex using ionization curves with the corresponding step. When the particle travels less than 1 (3) cm, we calculate its energy deposit directly using equation 7.1, where the distance  $L_{step}$  is calculated using the right plot of Fig. 7.6.

The distributions of the contribution to the vertex activity of each particle type are shown in Fig. 7.8. These distributions have two components depending if the particles leave the sphere or release all their energy inside the sphere. The long tail of INCL comes from the energy deposits due to  $\alpha$  particles and  ${}^3\text{He}$  (as can be seen on the inset panel of the right plot in Fig. 7.8).

Fig. 7.9 presents contributions to the vertex activity of all particles event-by-event. INCL+ABLA simulation features the highest nuclear cluster production, and these clusters rarely leave the vertex activity sphere. The whole kinetic energy of these clusters is left as a vertex activity. Consequently, INCL+ABLA simulation features the highest vertex activity prediction. The bare INCL cascade and NuWro simulations predictions are similar, with INCL featuring a slightly larger tail due to nuclear cluster production.

For the INCL simulation, there are 8 (11)% of the events, while for the INCL+ABLA there are 39 (51)% of the events with more than 15 (20) MeV energy deposited in the 1 (3) cm sphere.

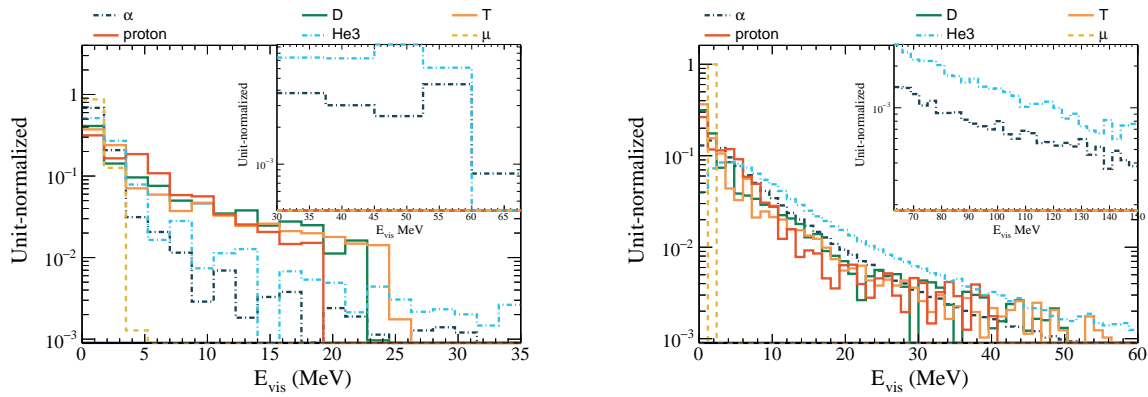


Figure 7.8 Visible energy deposited by ionization by different particles in a sphere of 1 (left) and 3 cm (right) radius around the vertex in events simulated with INCL+ABLA.

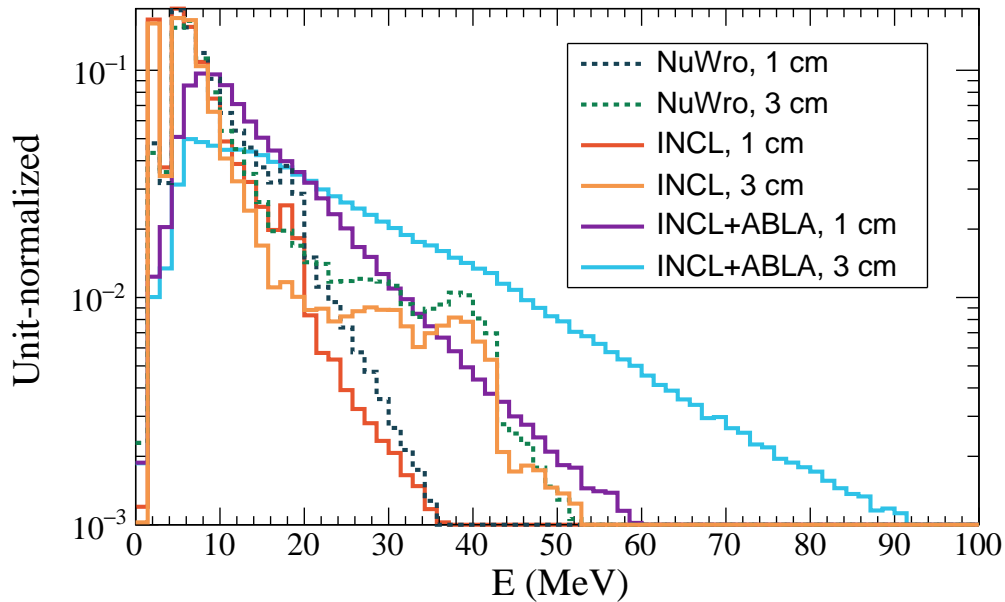


Figure 7.9 Total visible energy deposited by ionization by all the particles in a sphere of 1 (3) cm radius around the vertex. Distributions from events simulated with INCL and NuWro are compared with the same overall normalization. The tail with low statistics is not shown.

There are 10 (10)% of the events with more than 15 (20) MeV energy deposited in the 1 (3) cm sphere for NuWro. The tail of the NuWro distribution comes from multinucleon neutrino interactions and FSI inelastic processes with a production of multiple protons. The energy deposited by inelastic interactions is not included since its observability depends on the particles produced by such interactions. Inelastic interactions happen within 1 (3) cm from the primary vertex in about 3% (8%) of tritium and deuteron events and 1% (3%) of proton events. In contrast, they happen in a negligible fraction of events with  $\alpha$  and  $^3\text{He}$ . The study is

ongoing to use INCL+ABLA simulation results as an input to the official T2K near detector simulation to obtain a complete calculation of the expected vertex activity.

In present experimental neutrino measurements, the vertex activity is typically not considered in the neutrino energy reconstruction. Fig. 7.10 shows which fraction of the neutrino energy goes to the vertex activity as a function of the true neutrino energy. Here we consider only the energy lost by ionization and do not take into account the secondary interactions. The band corresponds to the asymmetric one-sigma uncertainty that contains 68% of all events. These plots show that in order to reach a precision on neutrino energy reconstruction at percent level (as requested for precise oscillation measurements), the vertex activity plays a relevant role up to several hundreds of MeV, especially when the energy released by de-excitation is considered. The more particles are produced during FSI, the less energy has the leading proton. These particles have a low momentum, so they mostly deposit all their energy as a vertex activity. Therefore, the vertex activity pulls the energy from the leading proton.

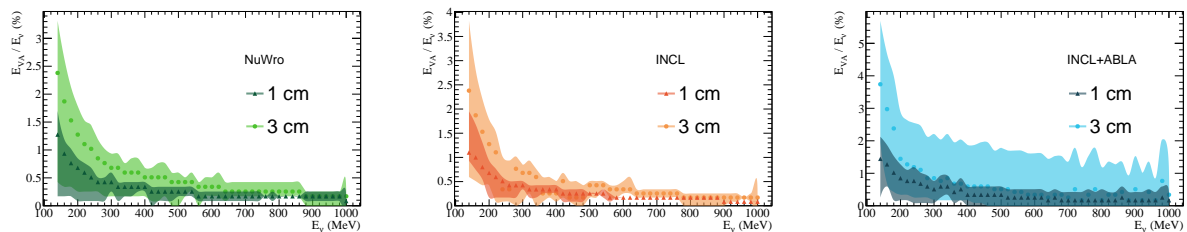


Figure 7.10 Vertex activity as a fraction of the initial neutrino energy depending on the neutrino energy simulated with NuWro, INCL and INCL+ABLA. The bands correspond to the  $1\sigma$  uncertainty. ABLA does not shift the mean ratio much but gives a larger spreading of this ratio distribution for the given neutrino energy.

Fig. 7.11 presents the ratio of the total kinetic energy of all clusters, neutrons, and non-leading protons produced in the event  $E_{clus}$  to the true neutrino energy. The actual fraction of neutrino energy going to the kinetic energy of the subleading hadrons is non-negligible (at percent level), especially if correctly considering the energy release via de-excitation. However, the fraction of visible energy in vertex activity (after Birks and removal of secondary interactions) tends to be lower. It is, therefore, a tough experimental challenge to measure VA and correct back to the total kinetic energy of the initial particles. Hence, it is crucial to have models that can adequately describe such a fraction of energy, which needs to be corrected back for a precise reconstruction of the total neutrino energy but is so difficult to observe.

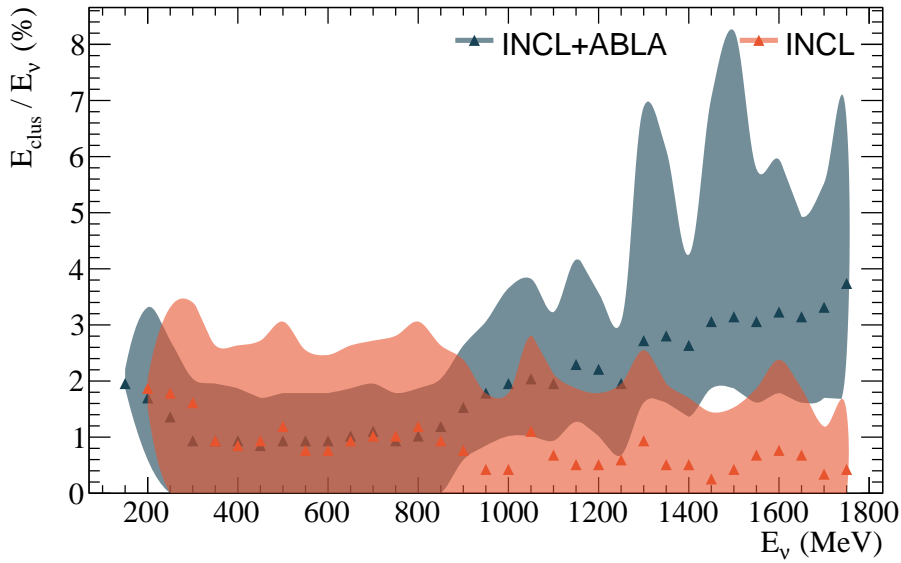


Figure 7.11 Sum of the kinetic energy of all clusters, neutrons and non-leading protons in the event as a fraction of the initial neutrino energy depending on the neutrino energy simulated with INCL and INCL+ABLA. The bands correspond to the  $1\sigma$  uncertainty.

### 7.3 Neutron measurements

Neutrons are the primary products of the antineutrino interactions. Therefore, a precise measurement of the outgoing neutron kinematics from the antineutrino vertex is essential for the correct antineutrino energy reconstruction. Knowledge of neutron kinematics can also improve the understanding of nuclear effects, for instance, by studying 2p-2h events with neutron-proton or neutron-neutron final states. A notable feature of the antineutrino interactions occurring on hydrogen is that such interactions are not subject to nuclear effects. Therefore, the neutron reconstruction from such a neutrino interaction is helpful for flux determination. The recent study of the  $\bar{\nu}_\mu p \rightarrow \mu^+ n$  reaction on hydrogen conducted by the MINERvA collaboration has led to the breakthrough measurement of the nucleon transition axial form factor [11].

In Ref. [12], such features are exploited to propose a new method for antineutrino energy reconstruction with improved resolution. The method is based on the precise measurement of the outgoing neutron kinetic energy and the momentum imbalance on the transverse plane. The method from Ref. [12] is further used to estimate the improved precision on uncertainties in the oscillation analysis as described in Ref. [13].

The ability to detect neutrons is a crucial novelty for the future detectors such as ND280 upgrade [3]. The SuperFGD detector of the upgraded ND280 has sufficient size and granularity to

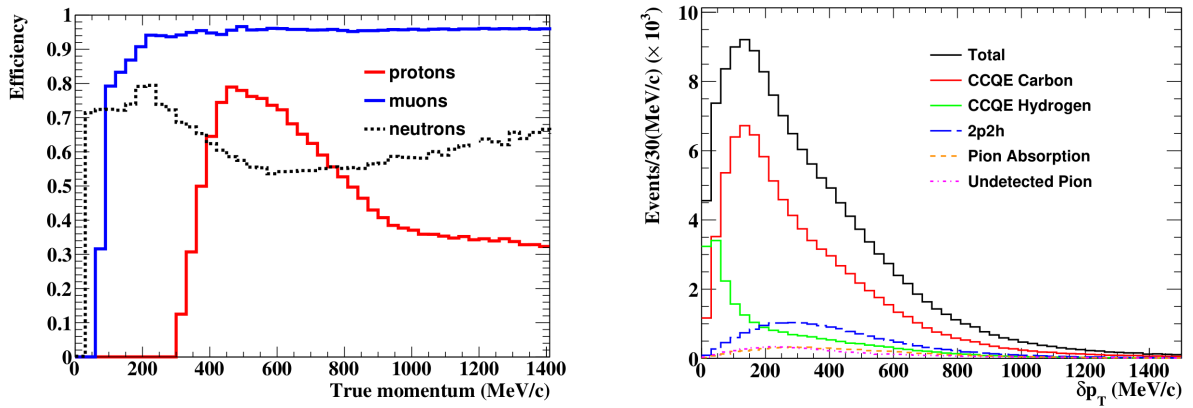


Figure 7.12 Left: the efficiency to detect protons, muons and neutrons in ND280. Right: the reconstructed  $\delta p_T$  distribution for selected CC0 $\pi$  and anti-neutrino interactions split by interaction mode and target for  $1 \times 10^{22}$  POT. The plots are taken from [13].

tag and reconstruct neutrons produced in antineutrino interactions. The measurement of the time delay between the primary antineutrino interaction and the detection of the first neutron-induced interaction (also called secondary interaction, SI) can provide information about the nucleon energy. Moreover, the uncertainty associated with the neutron secondary interaction in the detector is identified as the dominant uncertainty in the MINERvA measurement of the axial vector form factor from antineutrino–proton scattering [11]. It is, therefore, essential to study the secondary interactions of neutrons to control the uncertainties associated with the tagging of the neutron interactions.

To study the behavior of neutrons inside an abstract near detector, we simulated the antineutrino interactions with the leading neutron as a final state particle. We utilized a Geant4 simulation that contains the two physics lists: the default Bertini intranuclear cascade model [14, 15] and the one with the Liège cascade model INCL++ [16]. Using these two different physics models, we can estimate the uncertainty of the neutron interaction modeling.

We simulated the CCQE neutron production from an antineutrino flux with GENIE [17]. Some muon neutrino contamination, as expected in a real antineutrino beam, is included. To select antineutrino events only, we demanded production of  $\mu^+$  in the vertex. The data files contain almost 1 million events. A 5 MeV cut on the initial momentum of the primary neutrons was applied to remove low energetic non-physical particles. This non-realistic simulation is a known problem of the GENIE model, related to the absence of proper de-excitation modeling. To conserve the total energy in the interaction, GENIE produces many very low-energy nucleons to evacuate the residual excitation energy of the nucleus.

While tracking a particle in Geant4, the old particle is destroyed in every interaction point, independent of the process type, and a new particle is created. Even if the particle participated in elastic interactions that changed only its energy and direction, it would look like a generation of a new particle. This Geant4 technicality must be properly considered

and corrected to evaluate the neutron multiplicity properly. In order to estimate the actual multiplicity of neutrons produced in the neutrino vertex and secondary interactions, we employed an algorithm to reduce the number of artificially created particles. Fig. 7.13 shows the result of such a procedure. If only one neutron was created in the neutron interaction vertex, the algorithm would merge the initial and new tracks of the incoming and outgoing new particle, keeping the ID of the initial one. Suppose multiple particles are produced in the vertex. In that case, we cannot associate one of the final particles with the initial one, and we leave all the created tracks untouched. The features of the merging algorithm and Geant4 simulation are such that it is highly improbable that the primary neutron will produce a particle and will remain (as shown in Fig. 7.14). Therefore the secondary neutron multiplicity distribution will have a dip around one neutron.

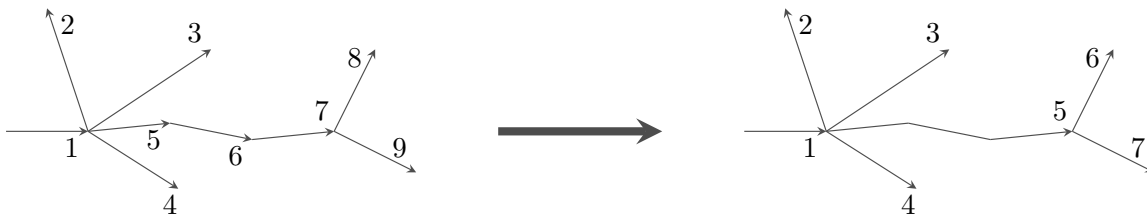


Figure 7.13 The scheme of merging trajectories to estimate the neutron multiplicity. The primary particle has track 1. It produced particles with tracks 2, 3, 4, and 5. Assigning new tracks to the initial particles is impossible, so no merging is applied. The particle with track 5 has participated in interaction with no production of extra particles, but its track number has changed to 6 and then to 7. In this case, the algorithm merges all these trajectories into one trajectory 5. Then, this neutron 5 interacts and produces two more particles. Again, no merging is applied. In the end, out of 9 tracks in the event, after applying the algorithm, there will be only 7.

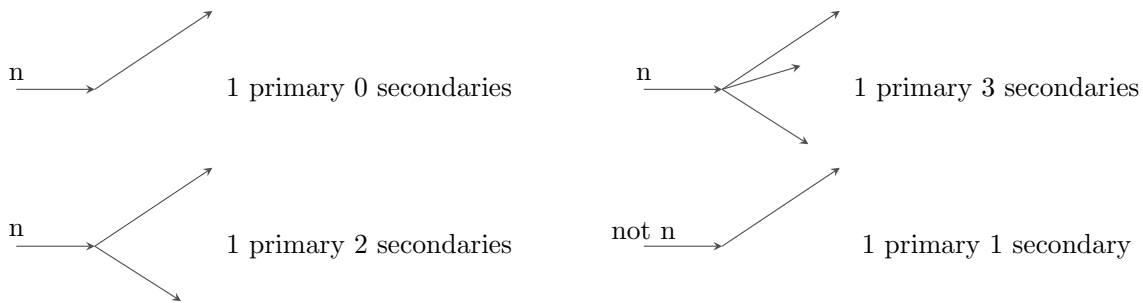


Figure 7.14 Possible scenarios of the neutron interaction with a potential number of secondary neutrons.

Fig. 7.15 shows the obtained multiplicity of the secondary neutrons. From the right plot of Fig. 7.15, one can see that the tail of the multiplicity distribution consists of low-energetic neutrons (less than 5 MeV).

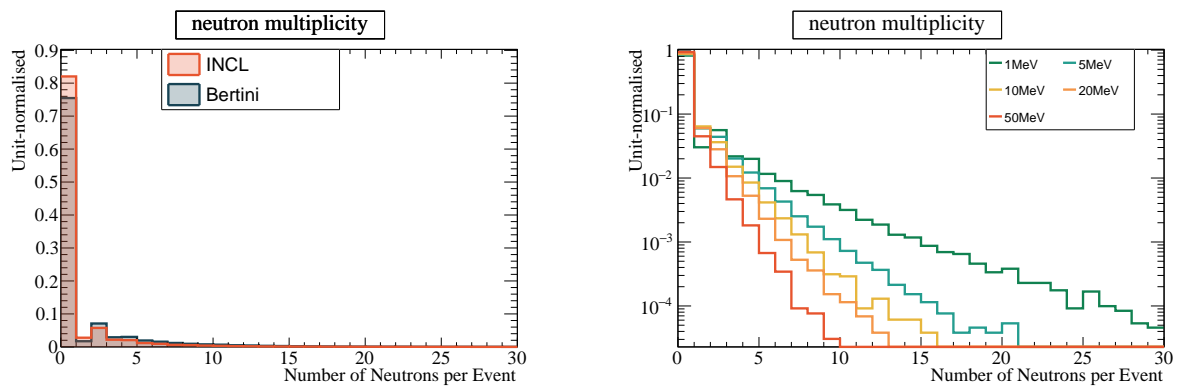


Figure 7.15 Left: secondary neutrons multiplicity simulated with Bertini and INCL. Right: secondary neutrons multiplicity with various energy cuts applied for the Bertini simulation.

It is also essential to understand which particles might produce neutrons and which particles might be produced by neutrons inside the detector. The left plot of Fig. 7.16 shows particles that produce neutrons. Most of the neutrons are generated by other neutrons. INCL features a wider variety of particles, which might produce neutrons while interacting. The particles produced by neutrons are shown on the right plot of Fig. 7.16. For the INCL simulation, the particles produced by neutrons are more diverse.

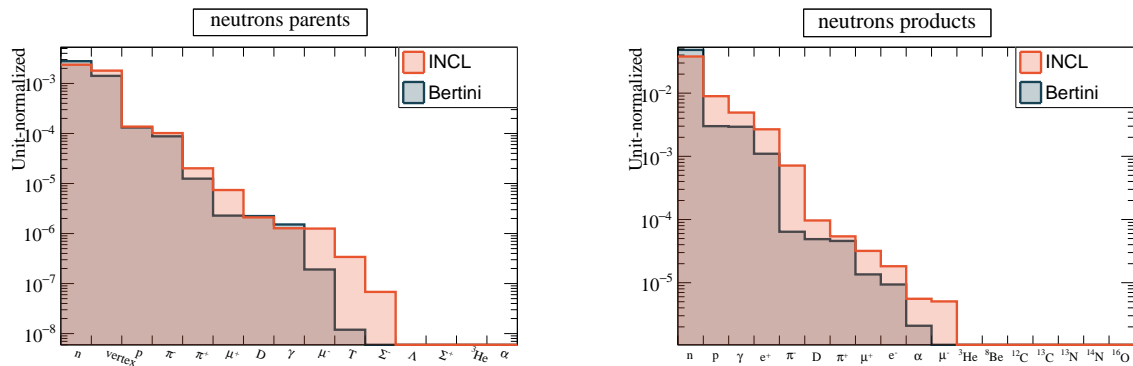


Figure 7.16 Neutron parents (left) and neutron daughters (right) simulated with INCL and Bertini. "Vertex" means that the neutron was produced in the neutrino interaction vertex.

The next question is about the physical processes in which neutrons can participate. Geant4 classifies processes and subprocesses, where processes describe various physical interactions (e.g., hadron process that includes hadron elastic, inelastic, and at rest processes) and subprocesses are responsible for a more defined type of interaction (e.g., scintillation or annihilation). Fig. 7.17 presents which processes and subprocesses participate primary and secondary neutrons in the INCL simulation. Primary neutrons have higher energy than secondary ones. Consequently, the interaction channels of primary neutrons are more diverse.

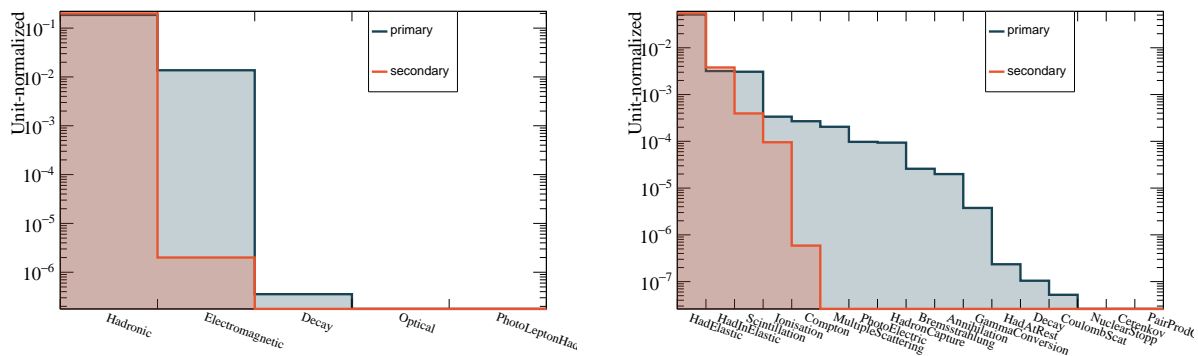


Figure 7.17 Geant4 processes (left) and sub-processes (right) in which participate primary and secondary neutrons. The simulation is performed with the physics list that includes INCL.

The cross section of the different processes depends on the energy of the neutron. Fig. 7.18 shows the probability of the main processes as a function of the neutron momentum for Bertini and INCL simulations. The most crucial difference between Bertini and INCL is the inelastic hadron process. On the contrary, the elastic process is mostly the same. The electromagnetic process is relevant only for primaries. In conclusion, the probabilities of different processes are pretty similar for both simulations.

We study the number of interactions, energy deposits, and direction changes for the primary and secondary neutrons. Fig. 7.19 contains these distributions simulated with INCL and Bertini physics lists. The energy deposit distribution has an exponential behavior that peaks at zero, demonstrating that most interactions are very soft. The same can be noticed for the direction changes: it peaks at zero, so the particle tends to have small direction changes in most interactions. For all variables, both INCL and Bertini predictions are similar.

Fig. 7.20 shows the  $\Delta E$  vs.  $\Delta \cos(\theta)$  distribution for primary and secondary neutrons. The spread of this distribution is large, but after applying the 5 MeV cut on the kinetic energy, it becomes more narrow, suggesting that the low-energy particles that scatter on high angles cause the spread. Not all the reinteractions inside the sensitive volume are visible in the detector, and not all reinteractions cause a sizable change in the neutron kinematics (and thus a sizable impact on time-of-flight measurement). We consider a neutron interaction to be visible if the energy deposit is larger than 1 MeV, or the change of particle direction is larger than  $1^\circ$ . Fig. 7.21 compares the number of interactions distributions from Fig. 7.19 to the ones obtained with the described cuts applied.

Understanding the visible and invisible neutron interactions is crucial for the correct neutron energy reconstruction: we need to tag the first relevant interaction of the primary neutron from the vertex. This procedure is not experimentally straightforward. First, the first visible interaction might come from a secondary neutron, which constitutes a background

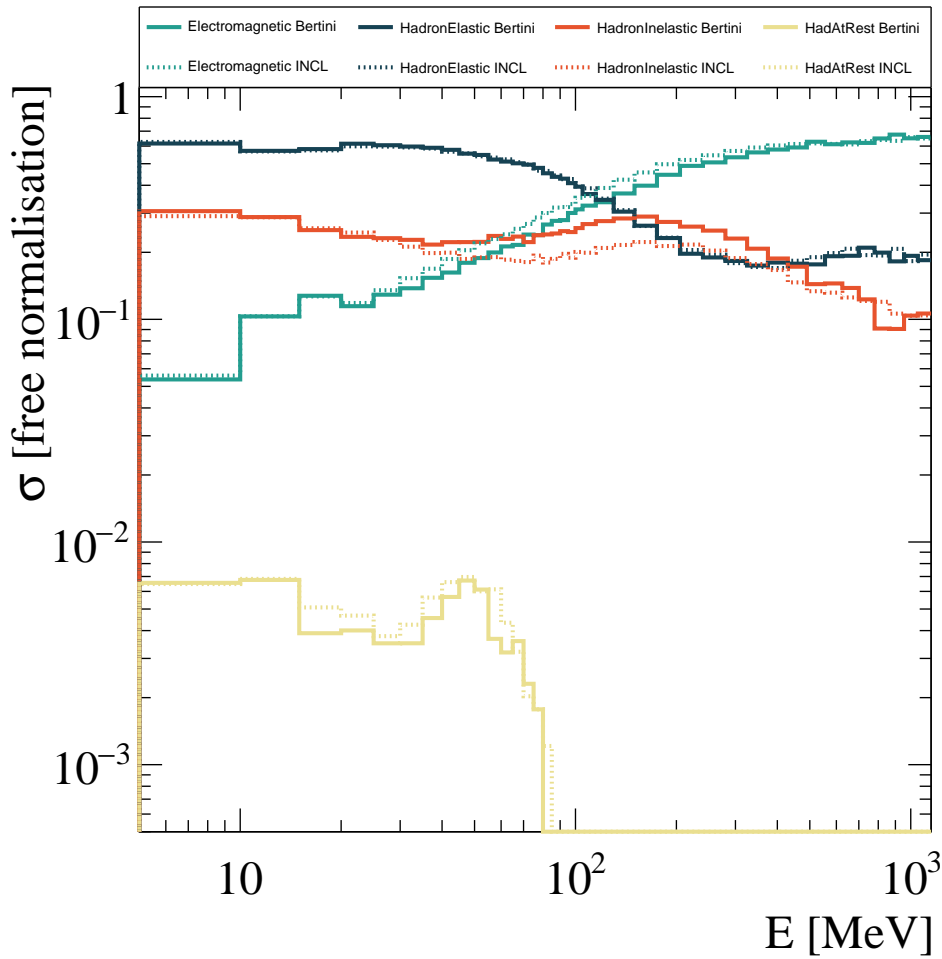


Figure 7.18 Probability of different neutron processes as a function of neutron energy. These processes were simulated with INCL and Bertini physics lists.

source. Another possibility is that we correctly tag an interaction from the primary neutron but not its first one, which could be invisible (below the detecting threshold).

We have calculated the efficiency of signal detection. In order to calculate efficiency, we considered interactions with energy deposits larger than 1 MeV. If the first such a deposit came from the primary neutron, we consider it a signal event, and it is from the secondary neutron—background event. The INCL and Bertini simulations' efficiencies are  $74.9 \pm 0.8\%$  and  $70.9 \pm 1.1\%$ , respectively. Therefore we can estimate a systematic uncertainty on neutron detection efficiency of 7%. It is the first time that such an uncertainty is estimated for this type of neutron detection and it is of relatively large size.

We have also tried to reconstruct the kinetic energy of the signal primary neutrons using time and distance until the first interaction. Fig. 7.22 shows the kinetic energy resolution for INCL and Bertini simulations. The distributions are similar (for Bertini, the mean value of the distribution is  $-0.067$  with standard deviation of  $0.064$ , and for INCL the mean value is

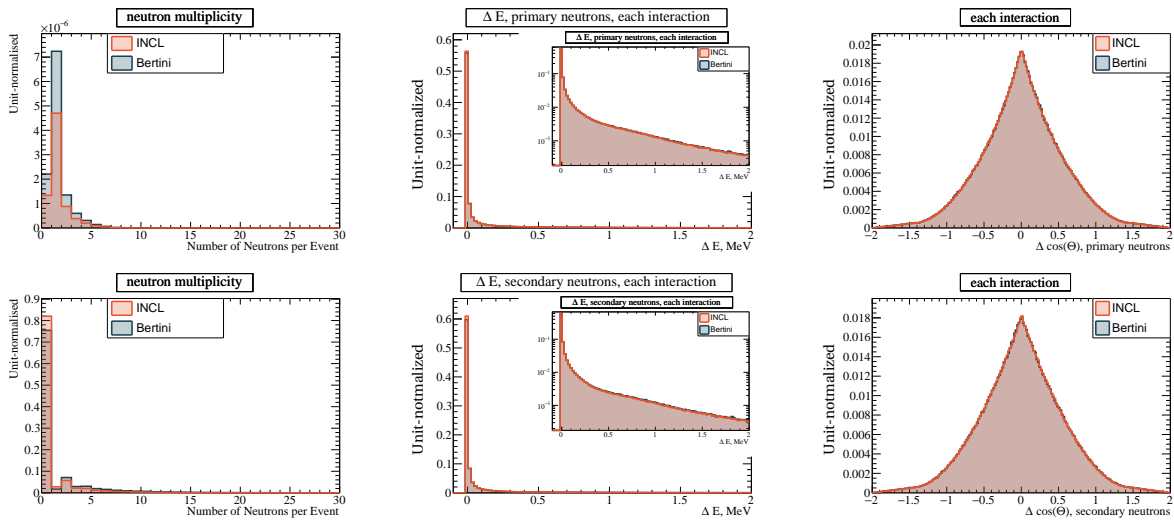


Figure 7.19 Number of interactions (left),  $\Delta E$  (middle) and  $\Delta \cos \Theta$  (right) for primary (top) and secondary (bottom) neutrons.

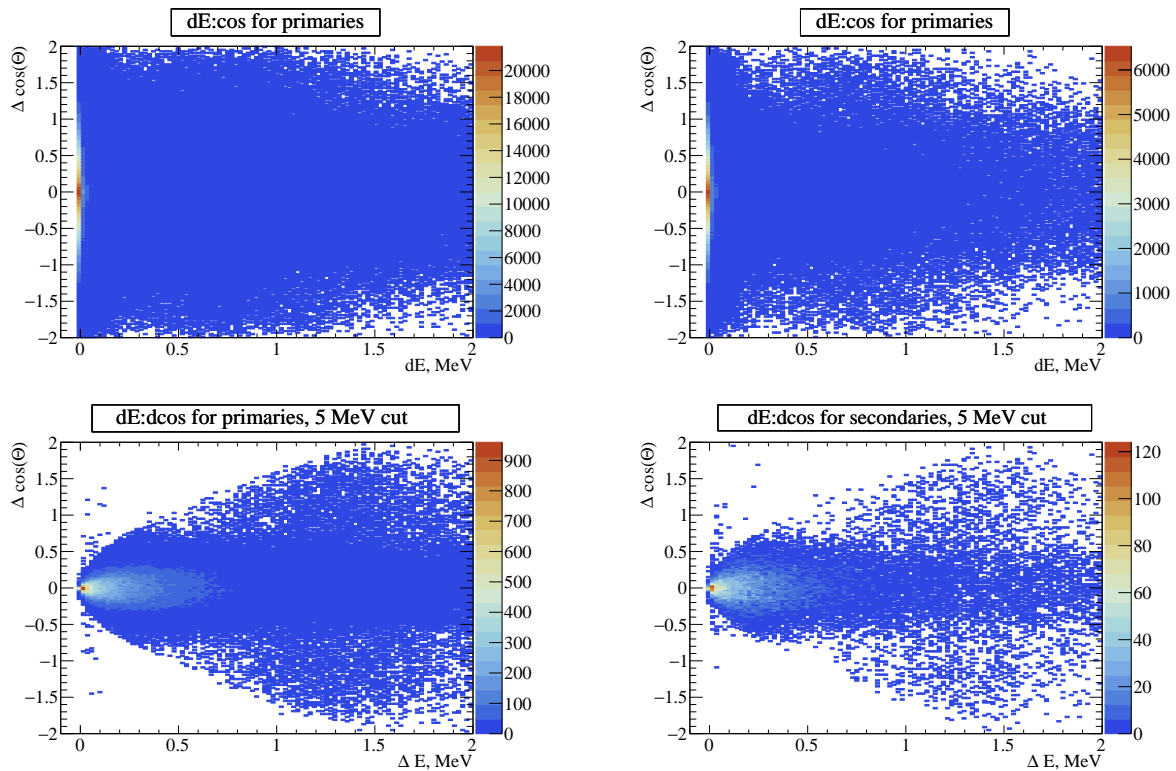


Figure 7.20  $\Delta E$  vs.  $\Delta \cos(\theta)$  for primary (left) and secondary (right) neutrons. For the bottom plots, the cut on the kinetic energy  $E > 5$  MeV is applied. Such a cut application suggests that large scattering angles correspond to the low-energy particles.

-0.069 with the standard deviation of 0.065), which allows us to conclude that the systematic uncertainty associated with utilizing different models is small.

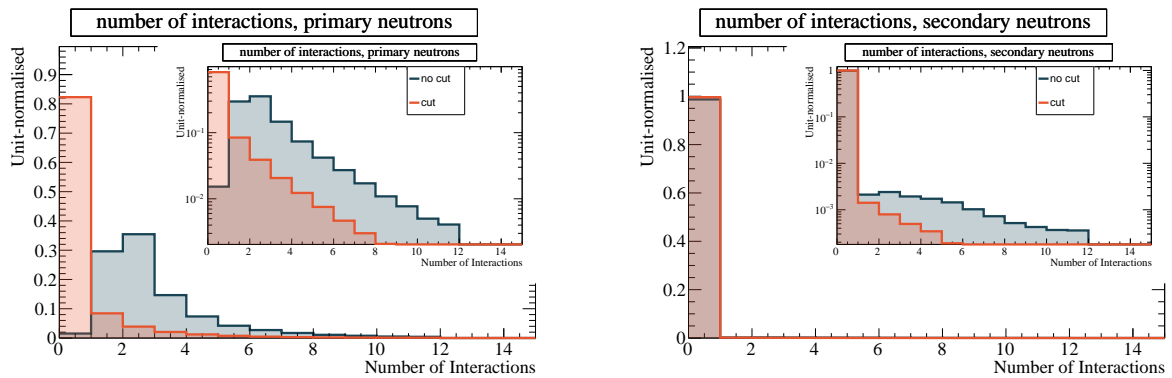


Figure 7.21 Number of visible interactions for primary (left) and secondary (right) neutrons; INCL cascade model.

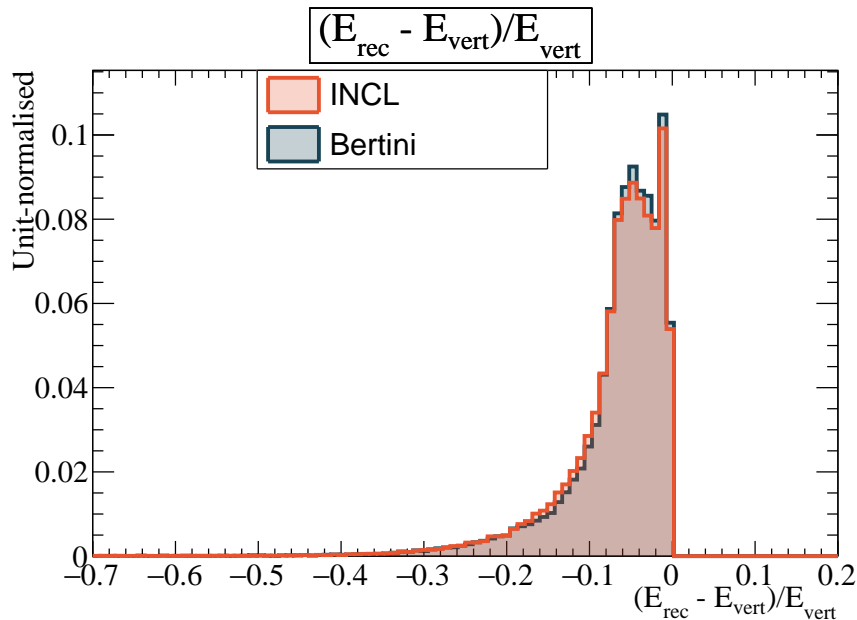


Figure 7.22 Kinetic energy reconstruction resolution of the primary neutrons, simulated with INCL and Bertini cascades.

## 7.4 Summary

We compared the simulation results with the experimental data provided by T2K and MINERvA collaborations. It is difficult to differentiate between the two FSI models due to the limited sensitivity of the available data and the proton momentum threshold of present detectors. We are looking forward to the next generation of experiments and their next-generation precision measurements.

Nuclear clusters can be detected as highly ionizing tracks or contribute to the energy deposited around the vertex (vertex activity) if they are below the tracking threshold. These

clusters behave differently than protons in many aspects, as they release more energy through ionization. To be reconstructed, these clusters must have larger momentum than protons. When identified as tracks, their momentum can be measured by their curvature, and their corresponding kinetic energy depends on the actual particle mass. The kinetic energy of a cluster leaving the nucleus differs from that of the initial proton producing the cluster. We presented the results of our particle identification algorithm, which showed that protons cannot be misidentified as nuclear clusters. However, a complete simulation considering secondary interactions and electronics response is necessary. INCL+ABLA features a significant production of multiple nucleons and nuclear fragments contributing to vertex activity. The proportion of neutrino energy transferred to the kinetic energy of the secondary hadrons is not negligible, especially when considering de-excitation. At the same time, the portion of energy that is visible in the detector is smaller due to quenching effects. Therefore, it is essential to have models that can accurately model such a fraction of energy, which must be corrected to achieve a complete neutrino energy reconstruction.

We also studied neutron secondary interactions by simulating neutron propagation in the detector using the two models. Our results showed that the Bertini and INCL models feature a consistent prediction of the neutron kinematics, while the efficiency has a difference which would correspond to an important systematics on neutron detection.

## References

- [1] K. Abe et al. “Characterization of nuclear effects in muon-neutrino scattering on hydrocarbon with a measurement of final-state kinematics and correlations in charged-current pionless interactions at T2K”. In: *Phys. Rev. D* 98.3 (2018), p. 032003. arXiv: 1802.05078 [hep-ex].
- [2] X.-G. Lu et al. “Measurement of Final-State Correlations in Neutrino Muon-Proton Mesonless Production on Hydrocarbon at  $\langle E_\nu \rangle = 3$  GeV”. In: *Phys. Rev. Lett.* 121 (2018), p. 022504.
- [3] K. Abe et al. “T2K ND280 Upgrade - Technical Design Report”. In: (Jan. 2019). arXiv: 1901.03750 [physics.ins-det].
- [4] R. Acciarri et al. *A Proposal for a Three Detector Short-Baseline Neutrino Oscillation Program in the Fermilab Booster Neutrino Beam*. 2015.
- [5] S. Agostinelli et al. “Geant4—a simulation toolkit”. In: *Nuclear Instruments and Methods in Physics Research Section A: Accelerators, Spectrometers, Detectors and Associated Equipment* 506.3 (2003), pp. 250–303.
- [6] J. Allison et al. “Geant4 developments and applications”. In: *IEEE Transactions on Nuclear Science* 53.1 (2006), pp. 270–278.
- [7] J. Allison et al. “Recent developments in Geant4”. In: *Nuclear Instruments and Methods in Physics Research Section A: Accelerators, Spectrometers, Detectors and Associated Equipment* 835 (2016), pp. 186–225.
- [8] P. A. Amaudruz et al. “The T2K Fine-Grained Detectors”. In: *Nucl. Instrum. Meth. A* 696 (2012), pp. 1–31. arXiv: 1204.3666 [physics.ins-det].
- [9] F. Saiho et al. “Light Output Response of GSO(Ce) Scintillator to Deuterons”. In: *Proceedings of the 2002 Symposium on Nuclear Data (JAERI-Conf 2003-006)* (2002), pp. 232–236.
- [10] Xavier Sarazin. “Recherche de la double désintégration beta sans émission de neutrino. Le détecteur BiPo”. HDR. Orsay, LAL, 2012.
- [11] T. Cai et al. “Measurement of the axial vector form factor from antineutrino–proton scattering”. In: *Nature* 614.7946 (2023), pp. 48–53.
- [12] L. Munteanu et al. “New method for an improved antineutrino energy reconstruction with charged-current interactions in next-generation detectors”. In: *Phys. Rev. D* 101 (9 2020), p. 092003.

- 
- [13] S. Dolan et al. “Sensitivity of the upgraded T2K Near Detector to constrain neutrino and antineutrino interactions with no mesons in the final state by exploiting nucleon-lepton correlations”. In: *Phys. Rev. D* 105 (3 2022), p. 032010.
- [14] M.P. Guthrie, R.G. Alsmiller, and H.W. Bertini. “Calculation of the capture of negative pions in light elements and comparison with experiments pertaining to cancer radiotherapy”. In: *Nuclear Instruments and Methods* 66.1 (1968), pp. 29–36.
- [15] J. J. Griffin. “Statistical Model of Intermediate Structure”. In: *Phys. Rev. Lett.* 17 (9 1966), pp. 478–481.
- [16] Davide Mancusi et al. “Extension of the Liège intranuclear-cascade model to reactions induced by light nuclei”. In: *Phys. Rev. C* 90.5 (2014), p. 054602. arXiv: 1407.7755 [nucl-th].
- [17] Luis Alvarez-Ruso et al. “Recent highlights from GENIE v3”. In: *Eur. Phys. J. ST* 230.24 (2021), pp. 4449–4467. arXiv: 2106.09381 [hep-ph].

# 8

## New detectors: the case of the High-Angle TPC for the ND280 upgrade

As introduced in Chapter 2, the next generation of LBL experiments will feature more powerful beams and enlarged far detector masses. To cope with the increased precision enabled by such enlarged statistics, a better control of the systematic uncertainties will be needed. To this aim, an effort is ongoing to improve the near detector capabilities using modern technologies such as liquid Argon Time Projection Chambers in the SBN program [1] or the highly granular scintillator detector and the new TPCs in the T2K near detector upgrade [2].

In this chapter, we present the work done in the scope of the T2K ND280 upgrade described in Chapter 2. Here we focus on the new HA-TPC production. As mentioned in Chapter 2, the HA-TPC readout is done with MicroMegas modules. These modules are connected to the electronics and the cooling planes, as shown in Fig. 8.1. The readout electronics is based on the AFTER Application Specific Integrated Circuit (ASIC) [3]. The entire ERAM module is read out by the 2 Front-End cards (FECs), each containing 8 ASICs. The FECs capture the analog signal of the 1152 detector pads and digitalize them using an octal-channel analog-to-digital converter (ADC). A Front-End Mezzanine (FEM) card for each ERAM module is located on top of the FECs. The FEM performs the control, synchronization, and data aggregation. The data from all the 16 ERAMs of a HA-TPC is collected via optical fibers to a Trigger, and Data Concentrator Module (TDCM) used for the clock synchronization, trigger and data concentration and transfer [4]. A TPC prototype has been tested at DESY Test Beams in 2019 [5] and 2021 [6] that proved that the ERAM performances entirely fulfill the demands of T2K.

We present the calibration of the electronics response of the AFTER ASICs in Section 8.1. This study was published in Ref. [7]. In section 8.2, we present the  $E \times B$  studies performed with the DESY Test Beam 2021 data partially published in Ref. [6].

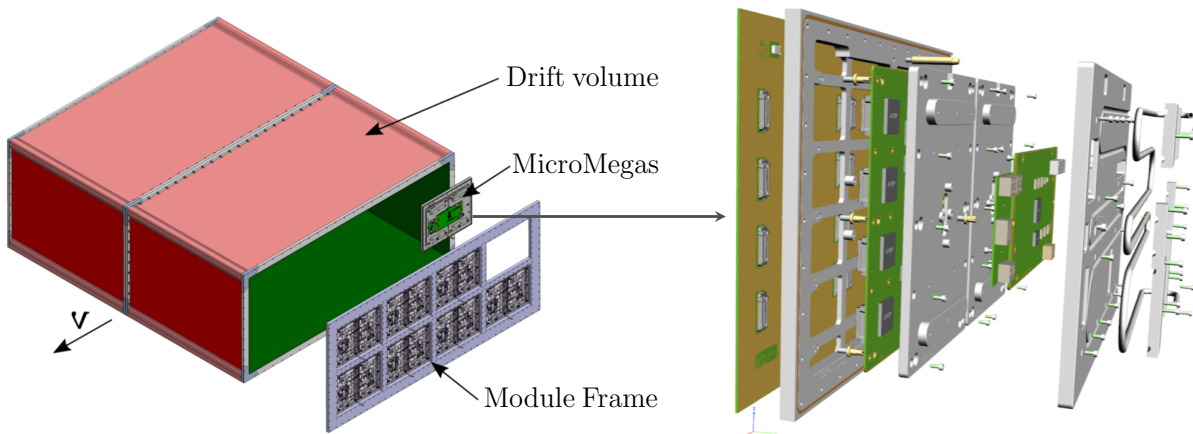


Figure 8.1 The HA-TPC structure and the structure of a Micromegas module with its associated electronics and mechanical structure.

## 8.1 Electronics calibration

We use the electronics calibration data to study the electronics response linearity between the channels, which is needed for precise charge measurement. The calibration data was collected with an onboard pulser with peaking times of 200 and 412 ns and various amplitudes. The picture of the setup is shown in Fig. 8.2.

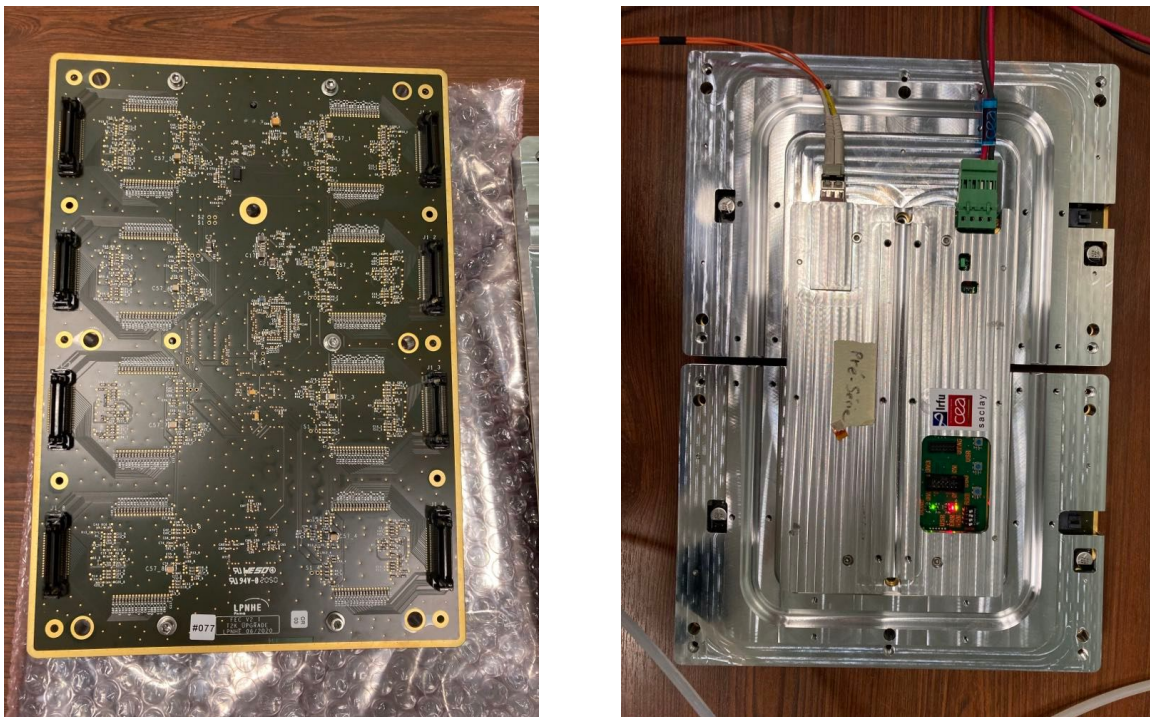


Figure 8.2 Photographs of the setup.

Fig. 8.3 represents a view of an ERAM with each bin being a pad, and an example of the injected calibration peaks. The left figure corresponds to the data taking for one channel of each ASIC (therefore there are 16 pads with the injected signal). Each pad was exposed to the 24 different signal amplitudes, as shown on the right.

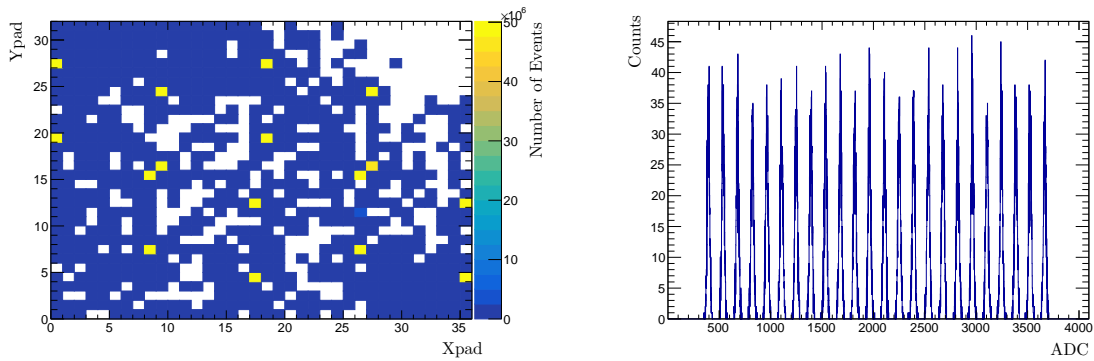


Figure 8.3 Example of calibration signals: signals on an ERAM (each bin represents a pad) (left) and distribution of all signals collected in a single pad (right).

During the data taking, we also checked the pedestal value (the baseline of the signal) for all ASICs (figure 8.4). A precise pedestal estimation is important for further proper extraction of the signal amplitude. We recorded the readout of the electronics with no injected signal. One can see that some ASICs (corresponding to channels 5—8) had a bit higher noise, but it is within the expected values (the maximal accepted RMS of the pedestals is 6).

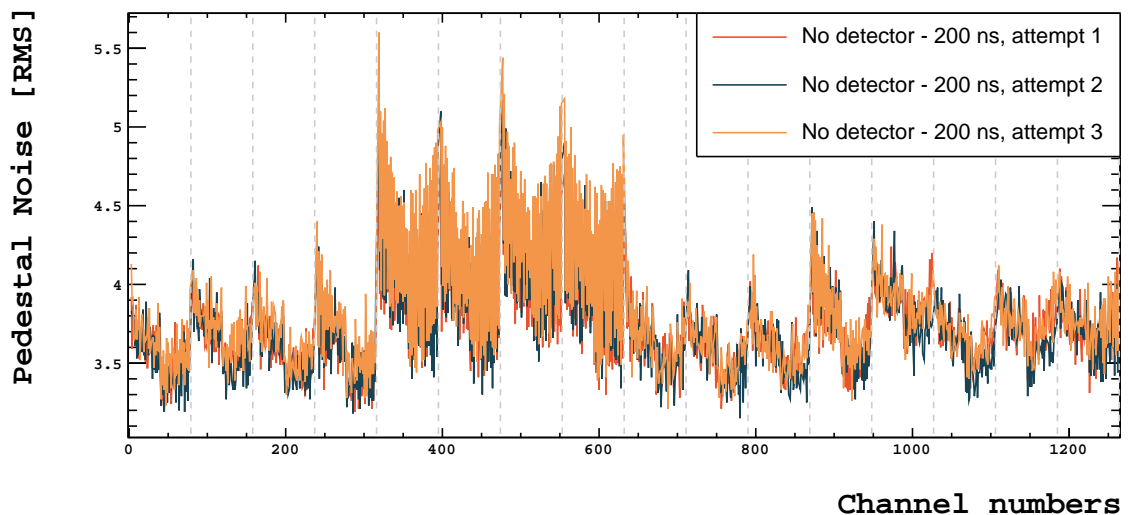


Figure 8.4 Pedestal test. ASICs are separated with gray dashed lines.

Figure 8.5 shows the peaks of the calibration signal at different amplitudes. One can notice the 2%—2.5% displacement of the position of the peaks at higher injected amplitude for

different ASICs. The magnitude of this shift is in agreement with expectations and should be corrected with calibration data to equalize the response of the channels in different ASICs and have a uniform energy scale in the detector.

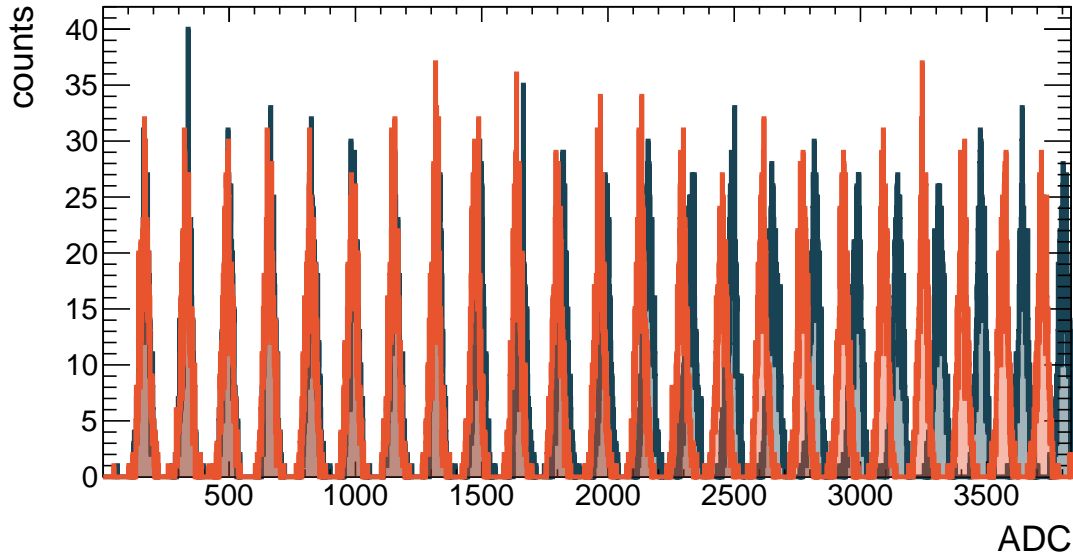


Figure 8.5 Example of the maximum of amplitude of injected signals in two different channels.

To perform calibration, we demand at least ten empty bins between subsequent peaks and at least 100 events inside each peak. We also subtract a pedestal of 250 ADC. We do not consider amplitudes above 3800 ADC to avoid saturation effects. We fit each peak with a Gaussian distribution and plot the mean value of each Gaussian distribution as a dependence on the peak number. The example of the obtained calibration line is shown in Fig. 8.6.

Fig. 8.7 shows the map of the electronic linearity coefficients  $p_1$ , and fig. 8.8 shows the 1-dimensional overall distributions of the electronic linearity coefficients (intercepts  $p_0$  that provide the dispersion for the pedestals and slopes  $p_1$ ) for all pads of the two FECs used for the readout of a single tested ERAM. As one can see, the distribution of the linearity coefficients within one ASIC is homogeneous, between the neighbor ASICs there is a smaller than 3% difference in linearity. The overall non-linearity within all the pads might be up to 7%.

The electronics calibration was performed for multiple FECs showing consistent results. The software to perform the electronics calibration described above was distributed within T2K GitLab and is ready to be used by the collaboration.

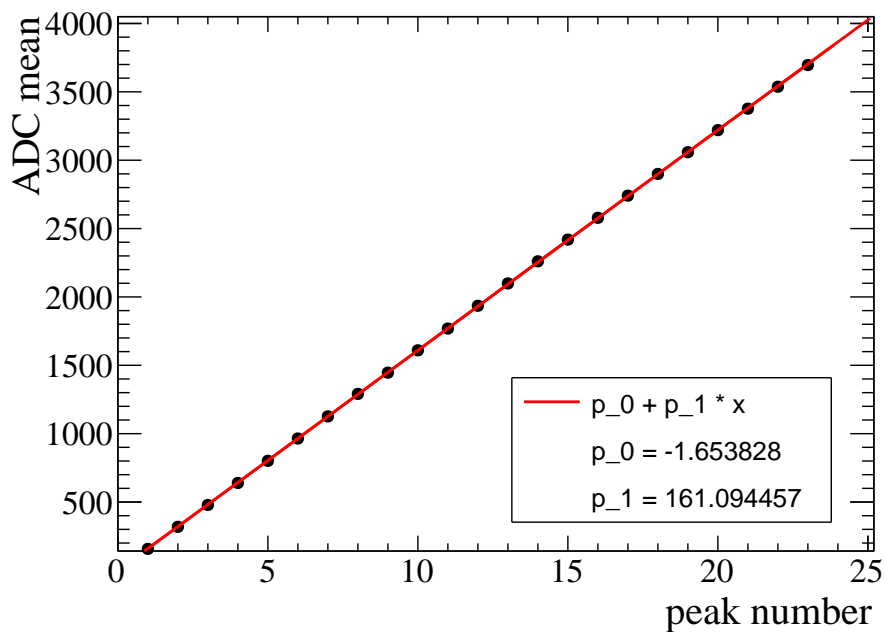


Figure 8.6 Example of the calibration line. After subtracting the pedestal, its intercept must be around zero.

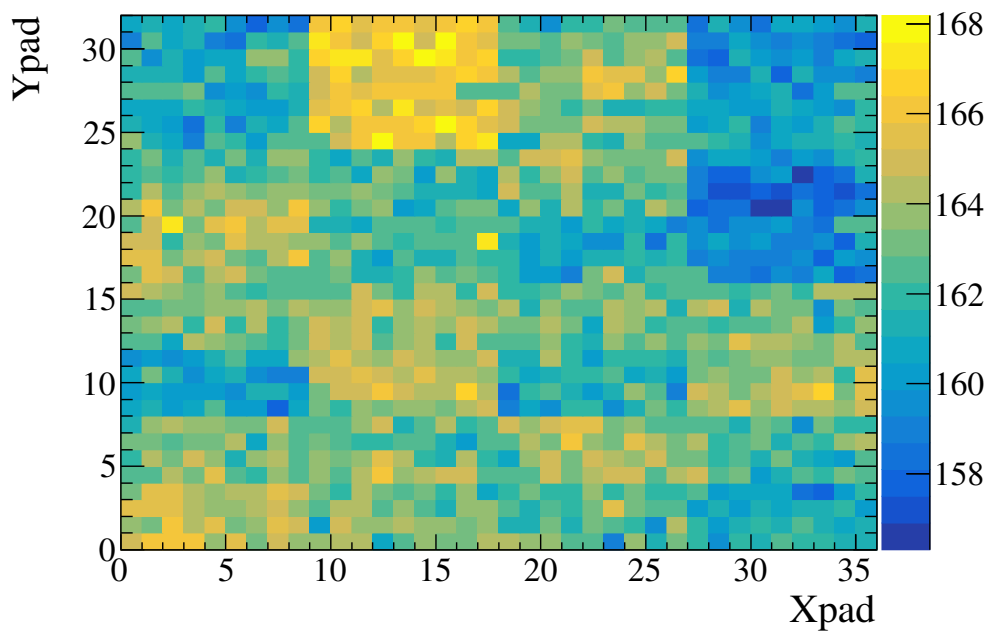


Figure 8.7 Map of the electronic linearity coefficients.

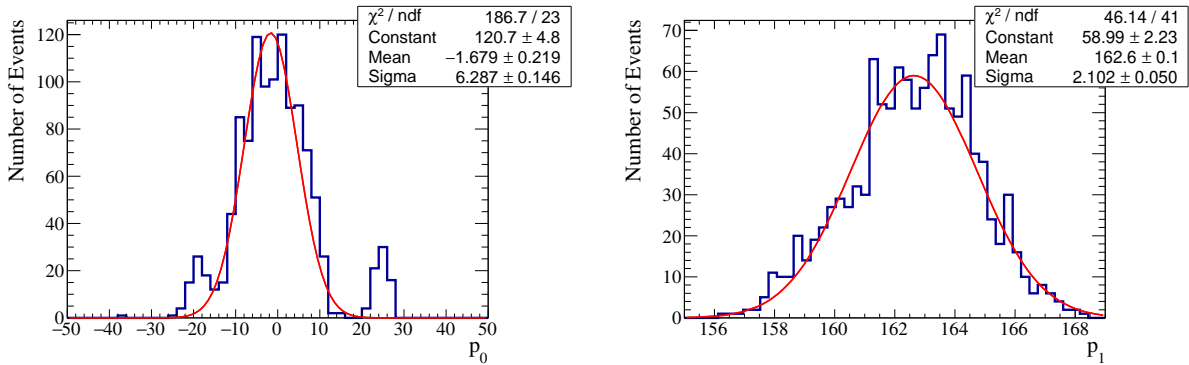


Figure 8.8 Left: 1D distribution of the pedestal dispersion of two FECs. Right: 1D distribution of the electronic linearity coefficients of two FECs.

### 8.2 The $E \times B$ effect

The scheme showing the working principle of a TPC is shown in Fig. 8.9. In the case of the absence of the magnetic field, electrons drift along the electric field to the anode and produce on it an image of the track.

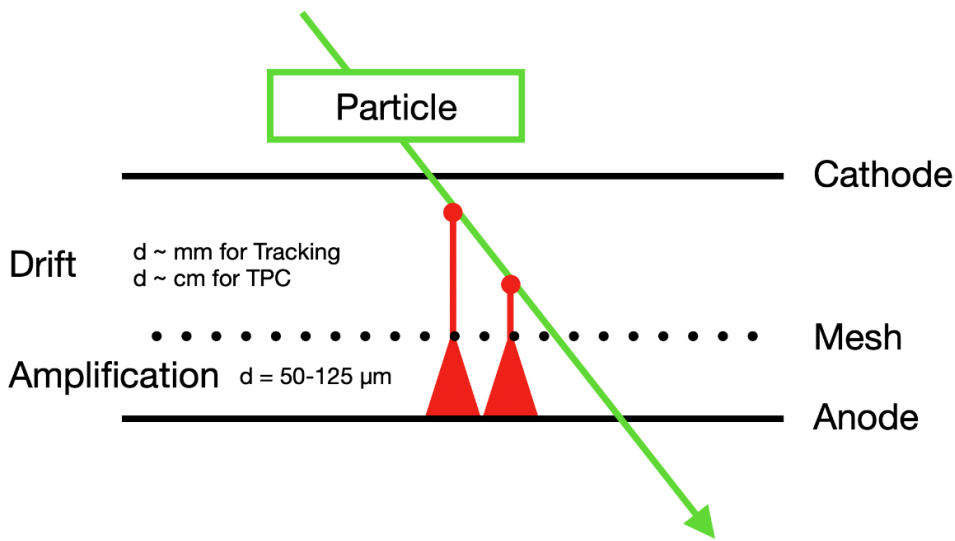


Figure 8.9 When a particle passes through the Micromegas detector, it ionises several atoms in the conversion volume, and the primary electrons drift to the amplification region. In the amplification region, an electron avalanche is formed. The picture and description are taken from [8].

In order to extract momentum measurements from track curvature, the TPCs are typically embedded in a magnetic field. The particle momentum  $\vec{p}$  is measured by the curvature radius  $\rho$  of the track [9]:

$$|\vec{p}| = q\rho|\vec{B}|, \tag{8.1}$$

where  $q$  is the charge of the particle, and  $B$  is the magnetic field.

In order to keep a regular and uniform drift of the electrons, the magnetic field must be oriented parallel to the electric field. The electrons drift therefore with an helicoidal trajectory around the field lines.

A non-uniform magnetic field can cause distortions of the track image projected on the ERAM. Particularly dangerous non-uniformities are the ones which give a non-zero magnetic component perpendicular to the electric field: this effect is called  $E \times B$ , since it's present when the vector product  $E \times B$  is not zero. These distortions might introduce bias in the reconstructed momentum. Therefore, if the curvature is not correctly reconstructed, the momentum reconstruction will be biased.

The schematic view of the DESY test beam setup is shown in Fig. 8.10. The electric and magnetic fields are oriented along the Z-axis. The electron beam with tunable momenta between 1 and 4 GeV/c passes along the X-axis. The TPC is not placed symmetrically with respect to the X-axis. The magnetic field map is shown in Fig. 8.11.

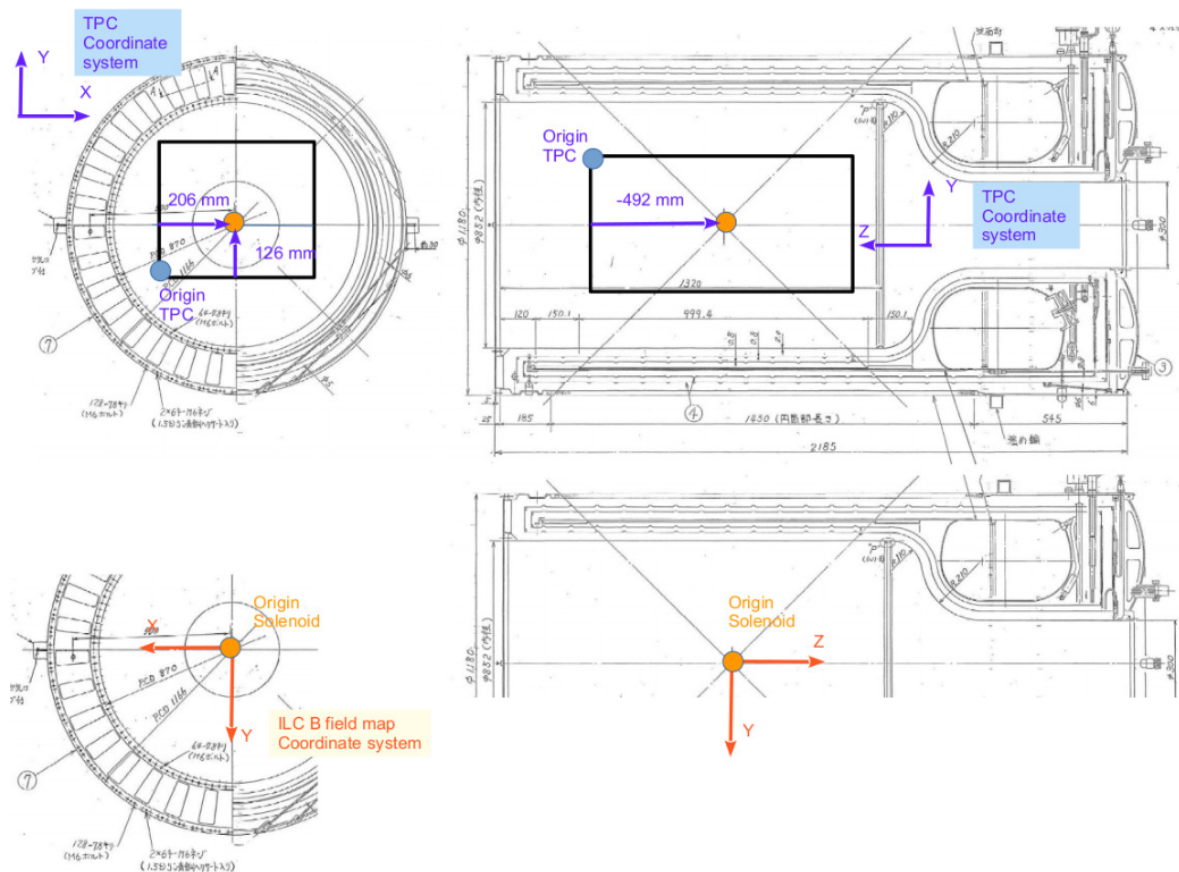


Figure 8.10 Scheme of the DESY test beam setup. The figure is adapted from Ref. [10].

Inside the ND280 volume, the magnetic field was measured with a dedicated campaign [11], and the  $E \times B$  effect is expected to be small. The effect seen in the DESY Test Beam data is

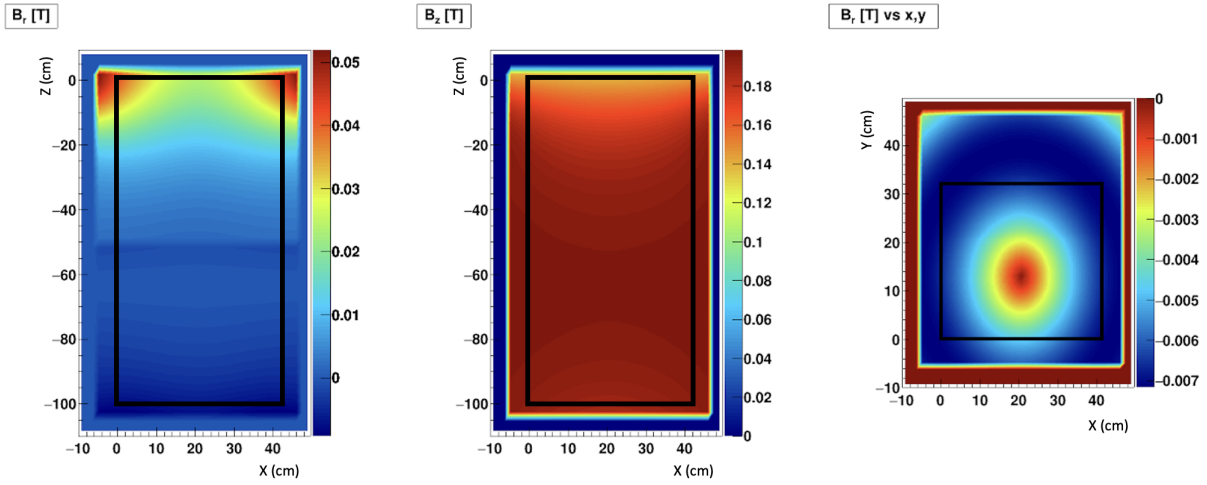


Figure 8.11 Map of the magnetic field. Left: radial component, top view. Central: longitudinal component, top view. Right: radial component, front view. The black boxes represent the contours of the TPC’s drift volume. Notice the non-negligible radial component of the field, especially in the rear of the TPC. The figure and description are adapted from Ref. [6].

more prominent due to the small magnet used during the test beam, which was not providing a uniform magnetic field.

The effect is well visible in the inclination of the reconstructed tracks shown in Fig. 8.12. We expect perfect horizontal tracks from the beam, so the angle directly shows the  $E \times B$  effect. The track inclination cannot be explained by the curvature induced by the magnetic field since this effect is negligible for the magnetic field and the electron momenta used in the test beam (most data are taken at  $B = 0.2$  T, as used in T2K, and electron momenta between 1 and 4 GeV/c).

Below we present the quantification of the  $E \times B$  effect for the particle with mass  $m$  and charge  $q$  moving with velocity  $\vec{V}$  in an electric field  $\vec{E}$  and a magnetic field  $\vec{B}$ . The equation of motion of this particle is:

$$q \cdot \vec{E} + q \cdot (\vec{V} \times \vec{B}) - \vec{k} \cdot \vec{V} = 0, \quad (8.2)$$

where  $k > 0$  is a phenomenological constant. The quantity  $\frac{m}{k} = \tau$  has a time dimension. It describes the average time between two collisions of the particle with the gas molecules. Following Ref. [12], this equation can be solved for the velocity  $\vec{V}$ , and the result will be the Langevin equation:

$$\vec{V} = \frac{\mu}{1 + (\omega\tau)^2} \left( \vec{E} + (\omega\tau) \frac{\vec{E} \times \vec{B}}{|\vec{B}|} + (\omega\tau)^2 \frac{\vec{B} \cdot (\vec{E}\vec{B})}{|\vec{B}|^2} \right), \quad (8.3)$$

where  $\mu = \frac{q}{m}\tau$  is the mobility of the particle (velocity per unit electric field strength),  $\omega = \left| \frac{qB}{m} \right|$  is the cyclotron frequency,  $\vec{E} \times \vec{B} = EB \sin(\delta)$  with  $\delta$  being an angle between the magnetic and

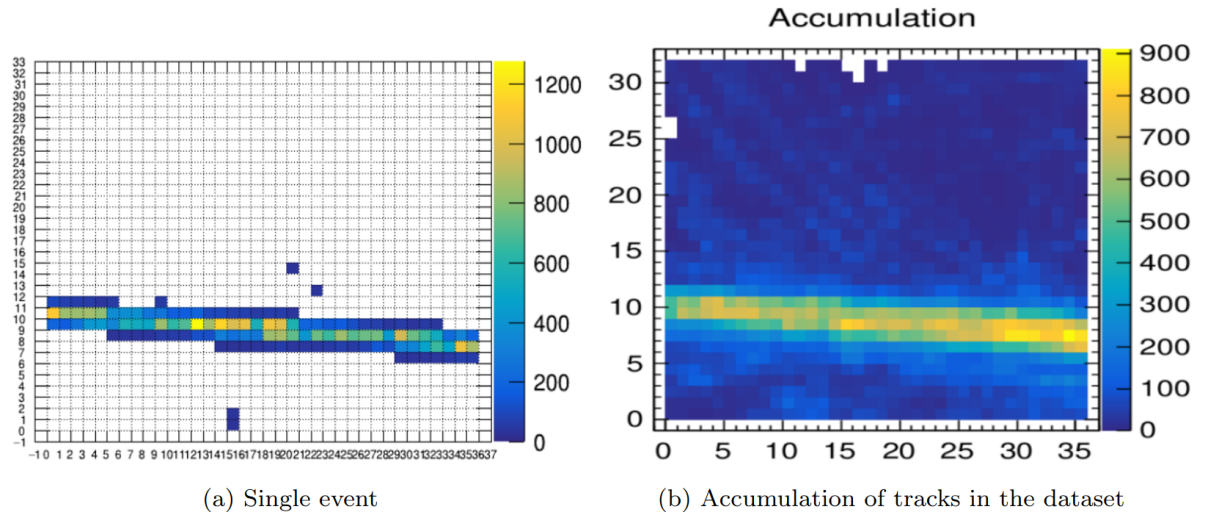


Figure 8.12 Event display of nominally horizontal beam. (a) single track; (b) accumulation plot of the tracks from the same dataset ( $B = 0.2$  T). The figure and description are adapted from Ref. [6].

electric fields. Let us also define the components of the vector  $\vec{V}$ :

$$\begin{aligned}
 \vec{V}_0 &= \frac{\mu}{1 + (\omega\tau)^2} \cdot \vec{E} \\
 \vec{V}_1 &= \frac{\mu}{1 + (\omega\tau)^2} \cdot (\omega\tau) \frac{\vec{E} \times \vec{B}}{|\vec{B}|} \\
 \vec{V}_2 &= \frac{\mu}{1 + (\omega\tau)^2} \cdot (\omega\tau)^2 \frac{\vec{B} \cdot (\vec{E}\vec{B})}{|\vec{B}|}
 \end{aligned} \tag{8.4}$$

The scheme visualizing the velocity components is shown in Fig. 8.13.

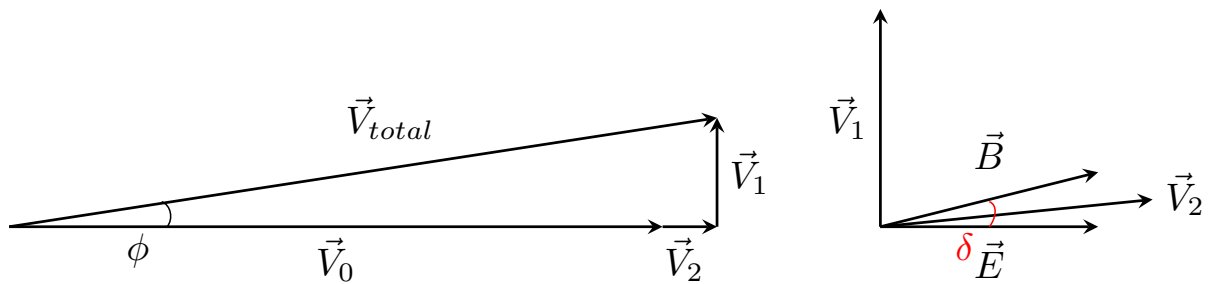


Figure 8.13 Schematic view of the drift velocity components according to the Langevin equation.

We assume that  $\delta$  is very small, the  $\vec{V}_2$  component is almost directed along the electric field and is parallel to  $\vec{V}_0$ . In such a case, the drifting electrons will move along the  $\vec{V}_1$  perpendicular

to the electric field, introducing the shift  $\Delta$  for the projection on the ERAM:

$$\Delta = Z_{drift} \cdot \tan\left(\frac{\vec{V}_1}{\vec{V}_0 + \vec{V}_2}\right), \quad (8.5)$$

where  $Z_{drift}$  is a drift distance. Assuming the small-angle approximation

$$\Delta = Z_{drift} \cdot \left(\frac{\langle\delta\rangle\omega\tau}{1 + (\omega\tau)^2}\right), \quad (8.6)$$

where  $\langle\delta\rangle$  is the average value of  $\delta$  along the trajectory of the drifting electron.

From equation 8.6, one can see that the  $E \times B$  effect is small at low and high magnetic field limit, and the maximal inclination due to the  $E \times B$  effect is reached for  $\omega\tau = \mu B = 1$ . For the DESY setup, the expected value of mobility is  $\mu = 2.8 \text{ T}^{-1}$ , corresponding to a maximal  $E \times B$  effect for  $B \simeq 0.36 \text{ T}$ .

To experimentally measure the  $E \times B$  effect, we used the B field scan data collected from the DESY test beam, which provides data with magnetic fields equal 0, 0.1, 0.2, 0.4, 0.7, and 1 T for the electric field of 275 V/cm. The tracks were reconstructed using the package for the DESY beam test data analysis [13] based on the DBSCAN algorithm [14] for track reconstruction. This algorithm is efficient for removing discontinuous tracks. However, it will still accept, for example, events with two intersected tracks or tracks with kinks. Therefore, the reconstructed tracks need to be further selected to identify clean single-track events. We fitted tracks using scikit-learn linear regression algorithm [15]. As metrics, we chose maximal error:

$$MaxError(y, \hat{y}) = \max(|y_i - \hat{y}_i|), \quad (8.7)$$

here  $y$  and  $\hat{y}$  are the arrays of the actual and predicted by the linear fit values, respectively. The track is accepted if the maximal error for the given track is smaller than the mean maximal error for this data set (that equals 3 for most files). Figure 8.14 presents examples of accepted and rejected tracks. One can notice that all these tracks lack data points in row number 25. This row contains a dead pad and therefore was removed from the analysis.

Fig. 8.15 shows the slope coefficients of the accepted tracks for the various magnetic field values. One can notice the two-peaked structure of some distributions, especially for the magnetic field values corresponding to the more significant  $E \times B$  effect. The peaks correspond to the different drift distances at which the data was collected. The distribution without a magnetic field acts as a reference of what is expected in the absence of the  $E \times B$  effect due to the intrinsic beam angular distribution. The smaller  $E \times B$  effect, as expected and explained above, is observed for the large magnetic field  $B = 1 \text{ T}$ . The effect is most visible for the values of magnetic field around 0.2—0.4 T, which is in excellent agreement with the expectations.

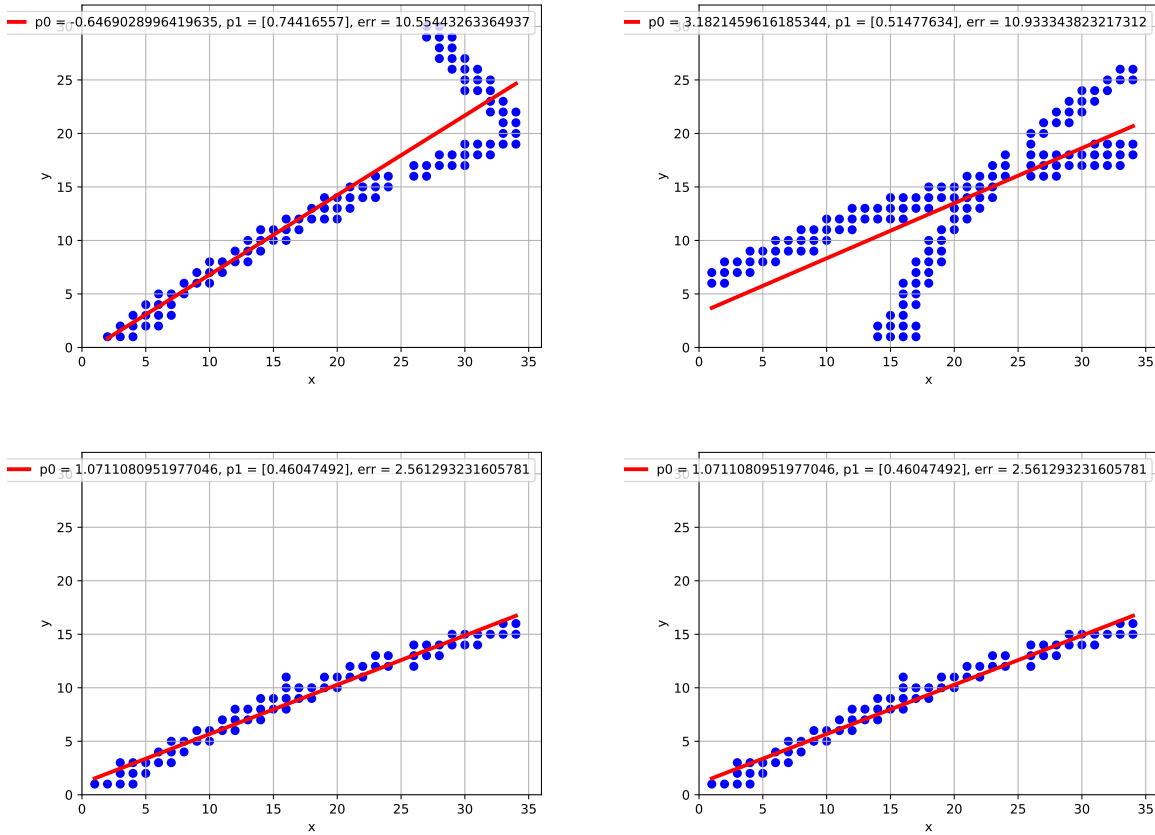


Figure 8.14 Top: examples of rejected tracks; bottom: examples of accepted tracks.

### 8.3 Summary

This chapter describes the calibration of the electronics response for the HA-TPC readout system used in the T2K near detector upgrade. This calibration aims to ensure precise charge measurement and linearity of response between the channels. The electronic linearity coefficients are homogeneous within one ASIC, and there is a smaller than 3% difference in linearity between neighbor ASICs. The overall non-linearity within all the pads is up to 7%.

The  $E \times B$  effect studies using data from the DESY Test Beam were performed to study the distortions of the track image projected on the ERAM. The magnitude of the effect in data and theoretical calculations are coherent. This analysis was essential to confirm the non-uniformity of the magnetic field in the DESY test beam and help to extract proper TPC performance from those data, as published in Ref. [6].

Overall, the work presented in this chapter shows the successful development and testing of the HA-TPC detector for the T2K ND280 upgrade.

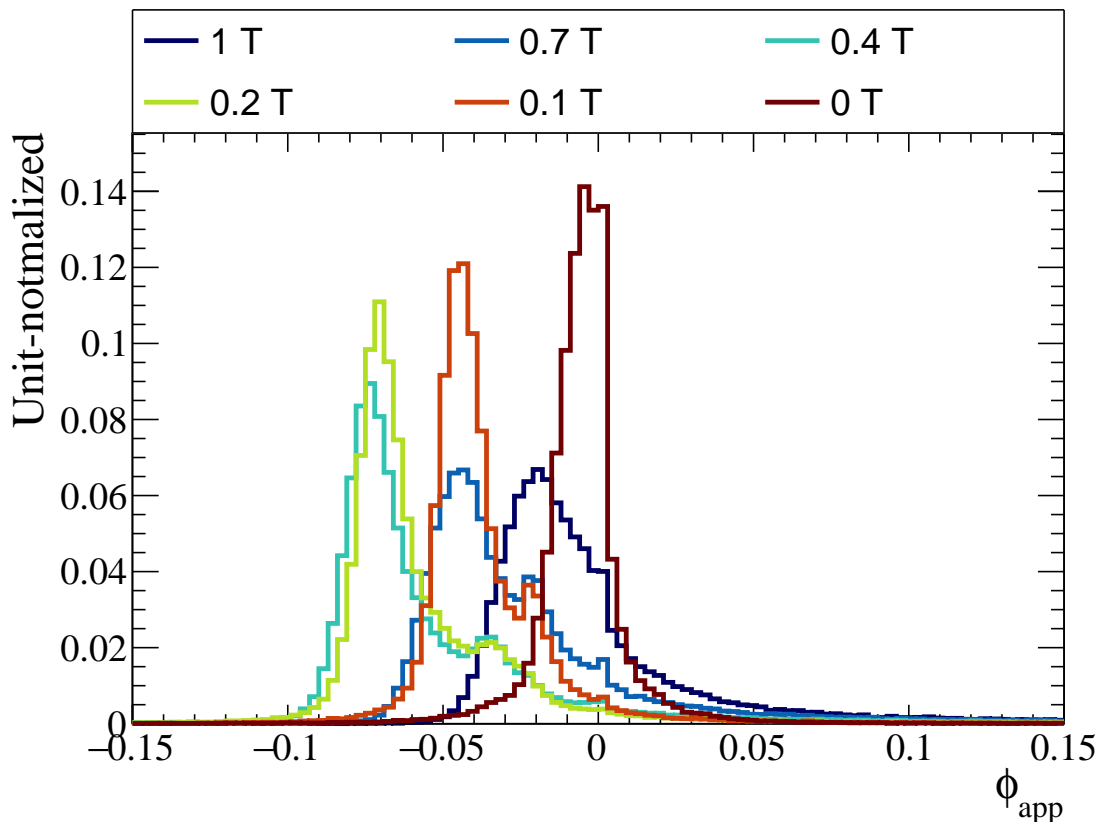


Figure 8.15 Slope coefficients depending on the value of the magnetic field, superimposed.

## References

- [1] Jonathan Asaadi et al. “A New Concept for Kilotonne Scale Liquid Argon Time Projection Chambers”. In: *Instruments* 4.1 (2020).
- [2] K. Abe et al. “T2K ND280 Upgrade - Technical Design Report”. In: (Jan. 2019). arXiv: 1901.03750 [physics.ins-det].
- [3] P. Baron et al. “AFTER, an ASIC for the readout of the large T2K time projection chambers.” In: *2007 IEEE Nuclear Science Symposium Conference Record*. Vol. 3. 2007, pp. 1865–1872.
- [4] Denis Calvet. *Back-end Electronics for Low Background and Medium Scale Physics Experiments Based on an Asymmetric Network*. 2018. arXiv: 1806.07618 [eess.SP].
- [5] D. Attié et al. “Characterization of resistive Micromegas detectors for the upgrade of the T2K Near Detector Time Projection Chambers”. In: *Nucl. Instrum. Meth. A* 1025 (2022), p. 166109. arXiv: 2106.12634 [physics.ins-det].

- [6] D. Attié et al. “Analysis of test beam data taken with a prototype of TPC with resistive Micromegas for the T2K Near Detector upgrade”. In: (Dec. 2022). arXiv: 2212.06541 [physics.ins-det].
- [7] D. Attié et al. “Characterization of Charge Spreading and Gain of Encapsulated Resistive Micromegas Detectors for the Upgrade of the T2K Near Detector Time Projection Chambers”. In: (Mar. 2023). arXiv: 2303.04481 [physics.ins-det].
- [8] David Attié et al. “Current Status and Future Developments of Micromegas Detectors for Physics and Applications”. In: *Applied Sciences* 11.12 (2021).
- [9] Claus Grupen and Boris Shwartz. *Particle Detectors*. 2nd ed. Cambridge Monographs on Particle Physics, Nuclear Physics and Cosmology. Cambridge University Press, 2008.
- [10] Pierre Granger. “Studies of Time Projection Chambers using micro-pattern detectors for the DUNE experiment”. PhD thesis. Saclay, 2022.
- [11] K. Abe et al. “The T2K Experiment”. In: *Nucl. Instrum. Meth. A* 659 (2011), pp. 106–135. arXiv: 1106.1238 [physics.ins-det].
- [12] F. Dydak. “On distortions of TPC coordinates: inhomogeneities of electric and magnetic field”. In: (2003). revised 10 June 2003.
- [13] *DESY beam test data analysis*. [https://gitlab.com/t2k-beamtest/desy\\_testbeam/-/tree/feature/desy\\_2021](https://gitlab.com/t2k-beamtest/desy_testbeam/-/tree/feature/desy_2021).
- [14] M Ester et al. “A density-based algorithm for discovering clusters in large spatial databases with noise”. In: *Proceedings of 2nd International Conference on Knowledge Discovery and Data Mining (KDD-96)* (Dec. 1996).
- [15] Fabian Pedregosa et al. “Scikit-Learn: Machine Learning in Python”. In: *J. Mach. Learn. Res.* 12.null (2011), 2825–2830.



# 9

## Conclusion

The field of neutrino physics has been rapidly evolving in the past 20 years. The neutrino oscillation physics enters the precision era: notably, the NOvA [1] and T2K [2] long-baseline experiments feature measurements of the neutrino mixing angle  $\theta_{23}$  and the largest mass splitting in the atmospheric sector at a few percent precision. The next-generation experiments DUNE [3] and Hyper-Kamiokande [4] aim to establish the mass ordering and possibly discover charge-parity violation with  $5\sigma$  significance, as well as to measure the value of the CP-parameterizing phase  $\delta_{CP}$  with a precision better than 15 degrees. Such results will be enabled by unprecedented statistics of produced and detected neutrinos, requiring an exceptionally robust and precise control of systematic uncertainties.

Modern neutrino acceleration experiments employ a two-detector scheme, placing the near detectors close to the neutrino source before any standard neutrino oscillation can occur. This detector aims to characterize the neutrino flux and to measure the neutrino-nucleus cross section to tune the interaction models and minimize the corresponding uncertainties. To cope with the increasing need for precision, a new generation of near detectors is being developed based on a precise and exclusive reconstruction of all the final-state particles produced in neutrino-nucleus interactions. This concept is at the core of the design of the upgrade of T2K near detector ND280 [5]. The upgraded near detector will allow for the 3-dimensional reconstruction of the neutrons, low-momentum protons, and high-angle muons.

On the other hand, studying the exclusive final states demands a complete understanding of the hadronic part of the neutrino interaction and reliable simulation models. Neutrino-nucleus interaction modeling constitutes a challenging source of systematic uncertainty. Along with future detector technologies, we must develop a corresponding modeling framework to fully benefit from the improved detector capabilities.

Many neutrino interaction models utilize the plane-wave impulse approximation approach that allows for factorization of the lepton-nucleus cross section, meaning that the cross section is modeled as a convolution of the cross section of the interaction on the single nucleon and a nuclear model describing the dynamics of these target nucleons, and further reinteractions in the nuclear medium are simulated independently. Typically, final-state interactions of resulting hadrons, which are the main focus of this thesis, are simulated with a cascade mechanism.

This thesis focuses on the simulation of the CCQE (anti)neutrino reaction with the Intranuclear Cascade Liege code. INCL is a nuclear physics model primarily designed to simulate nucleon-, pion- and light-ion-induced reactions on nuclei. It shows a remarkable agreement with an exhaustive list of experimental data [6, 7]. The excitation energy left after INCL is emitted with the further de-excitation modeled with ABLA, which emits various particles after the cascade putting the nucleus in the ground state. The simulation results of INCL and INCL+ABLA are compared to the results of the NuWro generator. This is the first time that a comprehensive de-excitation simulation is interfaced with neutrino interaction and FSI simulations. The role of all the three aspects (primary neutrino interaction, FSI and de-excitation) could be compared and studied for the first time.

This study of INCL and INCL+ABLA in the framework of neutrino interactions highlights various novelties in the modeling of the neutrino-induced reaction, including the production of nuclear clusters (e.g., deuterons,  $\alpha$  particles) in the final state. Nuclear clusters behave differently than protons in the detector, having a different kinetic energy than the initial nucleon forming the cluster. The production of nuclear clusters in neutrino interactions was never simulated before (since this feature of INCL is absent in the other widely used neutrino MC generators) and it is here studied in full details for the first time. Moreover, thanks to ABLA, for the first time we could simulate the release of removal/binding energy in form of de-excitation energy visible in the detector. Such predictions may significantly impact the analysis and interpretation of the experimental data, notably for identifying low-momentum particles and measuring energy deposits around the neutrino vertex (also known as vertex activity). We show that considering all the particles leaving the nucleus improves the neutrino energy reconstruction. For all these reasons, the accurate modeling and identification of particles in the final state, including nuclear clusters, are crucial to estimate correctly all the energy leaving the nucleus and the FSI corrections to it. We discuss the behavior of nuclear clusters in the detector. The actual fraction of neutrino energy going to the kinetic energy of the subleading hadrons is relatively large, especially considering the energy released via de-excitation. However, the fraction of visible energy is much lower, making it a tough experimental challenge to measure and correct back to the total neutrino energy. Therefore, it is crucial to have models that can adequately model such a fraction of energy to accurately

reconstruct the total neutrino energy. The work is ongoing to include INCL+ABLA predictions into the complete official T2K detector simulation.

We compare the production of INCL+ABLA for the leading proton kinematics with present measurements from T2K and MINERvA. We focus on Single Transverse Variables which correspond to transverse kinematic imbalance and have enhanced sensitivity to different nuclear effects. The thresholds of the current experiments are too large to be sensitive to the differences between the models and to the impact of the de-excitation. The needed sensitivity for the leading proton momentum threshold is possible starting from 200 MeV/c, which will be achievable with DUNE LAr TPCs and the T2(H)K SuperFGD detector.

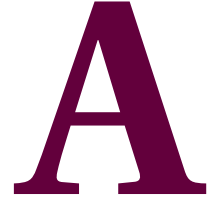
A completely new capability of the T2K SuperFGD detector consists in the measurement of neutrons produced in (anti)neutrino interactions. While such technique has the potential to be a game-changer in terms of precision measurements, it is crucial to evaluate the systematic uncertainties related with the neutron detection mechanism. In this thesis, we focus on the simulation of the neutron secondary interactions, as they constitute the major source of systematic uncertainty in neutron detection. We estimated uncertainties associated with utilizing the two simulation models, Bertini and INCL, on the kinetic energy reconstruction of the primary neutrons and on the neutron detection efficiency. These studies are the first ones conducted which such level of precision (preliminary and more simplified estimations were conducted by MINERvA [8]).

In this thesis we focused on the CCQE interactions, the main reaction channel for the T2K experiment. The resonance production and deep inelastic scattering channels become more crucial for other experiments operating at different neutrino energies, for example, for the future experiment DUNE. INCL can significantly contribute to the simulation of the other channels, notably RES since INCL features the proper handling of the  $\Delta$ -resonance decay. It is moreover of crucial importance to perform FSI and secondary interaction (SI) studies for pions also, where INCL could bring interesting new effects. While we focused on the carbon target, it is also interesting to repeat the studies with other targets, e.g. argon, which is the target material of the near and far detectors of DUNE. It is also important to continue the work initiated within this thesis on the CCQE neutrino interaction implementation in INCL to obtain a consistent description of the neutrino interaction and to use INCL independently of the external models.

During this thesis, we contributed to the development of the ND280 upgrade. In this document, we describe the electronics calibration for the new HA-TPC and the studies of the  $E \times B$  effect in test beam data. We show that the electronic non-linearity within all pads is within 3 % for the neighbor ASICs, which satisfies the requirements for the HA-TPCs. The observed  $E \times B$  effect is shown to agree with the expected theoretical values and is expected to be small in ND280.

## References

- [1] D. S. Ayres et al. “NOvA: Proposal to Build a 30 Kiloton Off-Axis Detector to Study  $\nu_\mu \rightarrow \nu_e$  Oscillations in the NuMI Beamline”. In: (Mar. 2004). arXiv: hep-ex/0503053.
- [2] K. Abe et al. “The T2K Experiment”. In: *Nucl. Instrum. Meth. A* 659 (2011), pp. 106–135. arXiv: 1106.1238 [physics.ins-det].
- [3] B. Abi et al. *Deep Underground Neutrino Experiment (DUNE), Far Detector Technical Design Report, Volume II: DUNE Physics*. 2020.
- [4] Hyper-Kamiokande Proto-Collaboration: K. Abe et al. *Hyper-Kamiokande Design Report*. 2018.
- [5] K. Abe et al. “T2K ND280 Upgrade - Technical Design Report”. In: (Jan. 2019). arXiv: 1901.03750 [physics.ins-det].
- [6] J. C. David. “Spallation reactions: A successful interplay between modeling and applications”. In: *The European Physical Journal A* 51.6 (2015).
- [7] S. Leray et al. “Results from the IAEA Benchmark of Spallation Models”. In: *J. Korean Phy. Soc.* 59.2 (2011), pp. 791–796.
- [8] T. Cai et al. “Measurement of the axial vector form factor from antineutrino–proton scattering”. In: *Nature* 614.7946 (2023), pp. 48–53.



## Initial state nuclear model

In chapter 5, we describe the implementation of the neutrino vertex simulated with NuWro to the INCL simulation. Such an approach might introduce biases in the final simulation results. To prove that the characterization of FSI in INCL and the differences between NuWro and INCL FSI are robust against assumptions on the initial nuclear state, we repeat the study using relativistic Fermi gas (RFG) in NuWro to model the initial state.

It is well known that the RFG-based models fail to reproduce the measured distributions of proton kinematics and STV [1, 2]. We also show it in Fig. A.1 where we compare STV simulated with NuWro RFG and INCL+NuWro RFG with the T2K data. We use the RFG model only as a diagnostic tool to test the robustness of the FSI results. In this case, the nucleon momentum and position are provided by NuWro RFG, and the INCL nuclear state is built around that nucleon. Fig. A.2 shows the differences between the momentum-position correlation for the INCL neutrons and the neutron taken from the NuWro RFG simulation.

We also test a more coherent simulation where the initial and final-state nuclear effects are simulated with the INCL model. To this aim, we reweigh the NuWro RFG simulation to represent the INCL distribution of nucleon momenta and the position shown in Fig. A.2. The binding energy (for each nucleon position and momentum) and the total cross section are kept as in the original NuWro RFG model.

In Tab. A.1, the fractions of different FSI channels are similar to those observed with SF simulation in Tab. 5.1. The fractions change slightly due to the different momentum distributions of proton before FSI, but similar trends are observable.

In Fig A.3,  $\delta\alpha_T$  distributions are shown. RFG features an enhancement of small  $\delta\alpha_T$  values due to the large fraction of protons with large momentum, just below the Fermi limits. Still, the characteristic suppression of such region induced by FSI in INCL is visible.

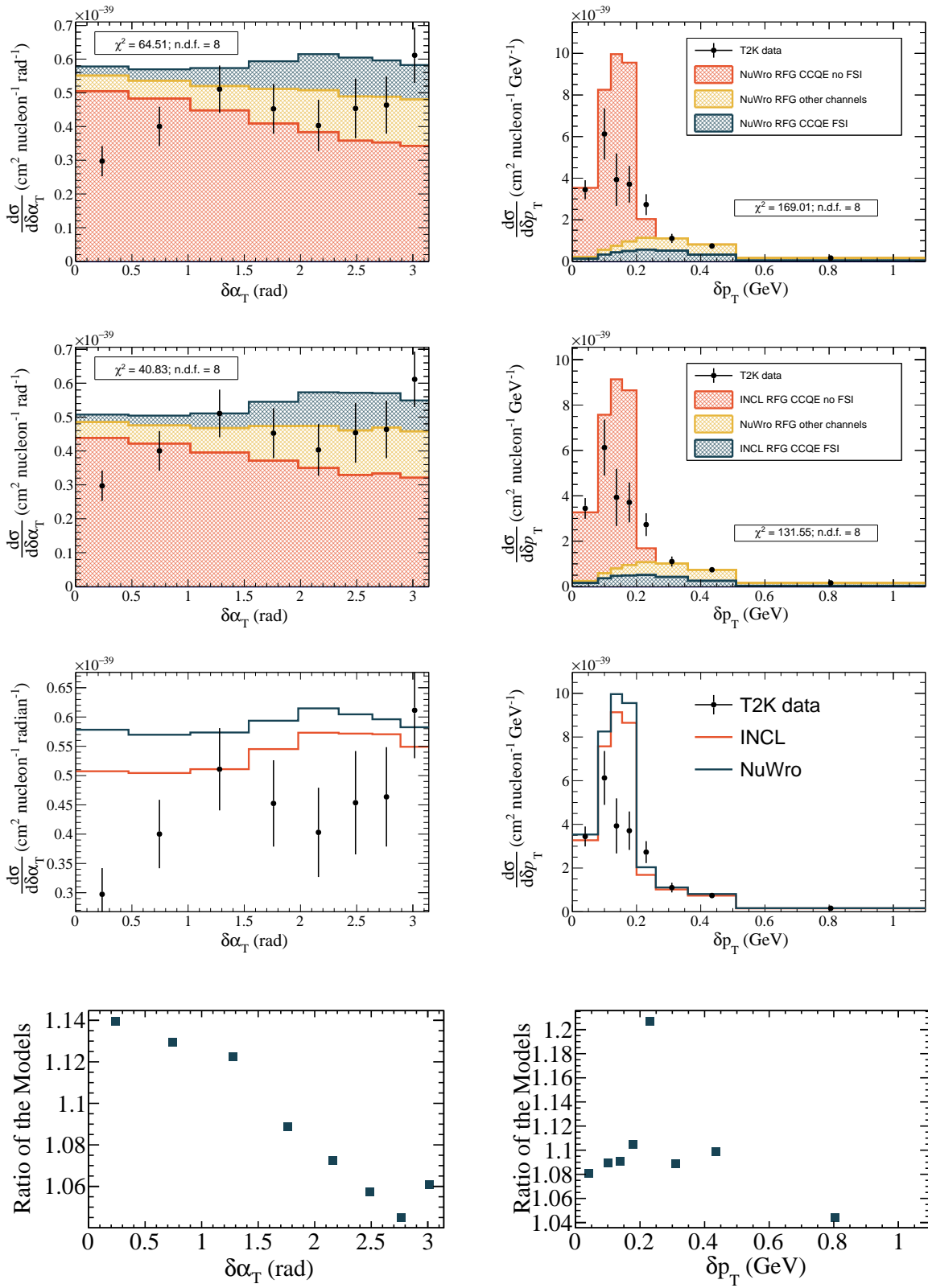


Figure A.1 Top to bottom: NuWro RFG comparison to T2K data; INCL + NuWro RFG comparison to T2K data; comparison of NuWro RFG, INCL + NuWro RFG and data; ratio of NuWro RFG and INCL + NuWro RFG models of QE channel. Left:  $\delta\alpha_T$ , right:  $\delta p_T$ .

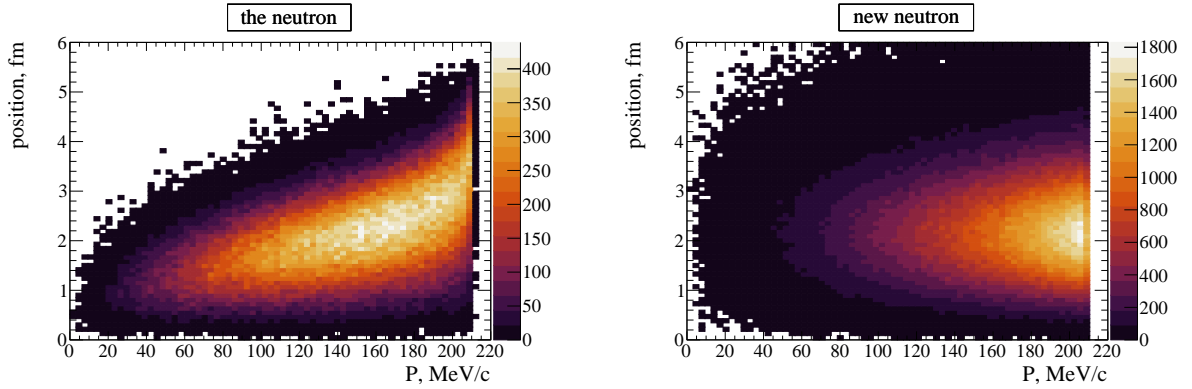


Figure A.2 Neutron momentum distribution inside the nucleus: standard INCL nucleus (left) and INCL nucleus built around NuWro neutron (right) as a function of radius.

Table A.1 Fractions of events with and without protons in the final state, fractions of different channels in events with and without protons in the final state.

	Channel	NuWro RFG	INCL+ NuWro RFG	INCL+ NuWro reweighted
<b>No proton</b>	no protons	0.9%	14.9%	14.7%
	protons	99.1%	85.1%	85.3%
	absorption	1.1%	25.8%	25.9%
	neutron + $\pi$ production	4.7%	0.8%	0.9%
	$\pi$ production	0.04%	0%	0%
	neutron production	94.2%	36.7%	36.5%
	cluster production	0%	36.7%	36.7%
<b>Proton</b>	no FSI	71.9%	72%	72.5%
	1 proton	2.0%	16.1%	15.8%
	multiple nucleons	24.6%	11.3%	11.1%
	$\pi$ production	1.9%	0.6%	0.6%

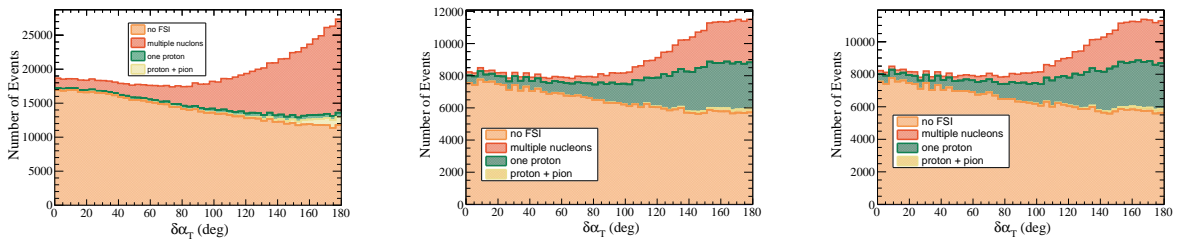


Figure A.3  $\delta\alpha_T$  for NuWro RFG (left), INCL+NuWro RFG (middle) and INCL+NuWro RFG reweighted to INCL initial momentum and position (right).

## References

- [1] K. Abe et al. “Characterization of nuclear effects in muon-neutrino scattering on hydrocarbon with a measurement of final-state kinematics and correlations in charged-

current pionless interactions at T2K”. In: *Phys. Rev. D* 98.3 (2018), p. 032003. arXiv: 1802.05078 [hep-ex].

- [2] X.-G. Lu et al. “Measurement of Final-State Correlations in Neutrino Muon-Proton Mesonless Production on Hydrocarbon at  $\langle E_\nu \rangle = 3$  GeV”. In: *Phys. Rev. Lett.* 121 (2018), p. 022504.